SEARCH FOR EXTENDED GALACTIC SOURCES OF ASTROPHYSICAL NEUTRINOS WITH THE ICECUBE NEUTRINO OBSERVATORY

By

Devyn Rysewyk Cantu

A DISSERTATION

Submitted to
Michigan State University
in partial fulfillment of the requirements
for the degree of

Physics – Doctor of Philosophy

2021

ABSTRACT

SEARCH FOR EXTENDED GALACTIC SOURCES OF ASTROPHYSICAL NEUTRINOS WITH THE ICECUBE NEUTRINO OBSERVATORY

By

Devyn Rysewyk Cantu

The IceCube Neutrino Observatory — a cubic-kilometer of instrumented ice at the geographic South Pole — has been observing a high-energy astrophysical neutrino flux since 2010. However, a steady source of these neutrinos is yet to be identified. Possible candidates contributing to the high-energy neutrino flux include extended sources (spanning a few degrees) originating from within the Milky Way. Such sources have been discovered in the very-high-energy gamma-ray sky along the galactic plane with experiments such as HAWC and H.E.S.S. If the emission from these extended sources is of a hadronic origin, an associated flux of neutrinos from the decay of pions is also expected to be observed. Therefore, an observation of neutrino emission from these extended gamma-ray sources would provide direct insight into cosmic-ray acceleration in the galaxy. Two approaches to performing dedicated searches for extended sources along the galactic plane with nine years of IceCube data will be discussed. With these two approaches, no significant sources were found and the results are consistent with background.

While IceCube has revealed the existence of sources of high-energy astrophysical neutrinos, the identification of the sources is challenging because astrophysical neutrinos are difficult to separate from the background of atmospheric neutrinos produced in cosmic-ray-induced particle cascades in the atmosphere. The efficient detection of air showers in coincidence with detected neutrinos can greatly reduce those backgrounds and increase the sensitivity of neutrino telescopes. Imaging Air Cherenkov Telescopes (IACTs) are sensitive to gamma-ray-induced (and cosmic-ray-induced) air showers in the 50 GeV to 50 TeV range, and can therefore be used as background-identifiers for neutrino observatories. The feasibility of an array of small scale, wide field-of-view, cost-effective IACTs as an air shower veto for neutrino astronomy will be discussed. A surface array of 250 to 750 telescopes would significantly improve the performance of a cubic kilometer-scale detector

like IceCube, at a cost of a few percent of the original investment. The number of telescopes in the array can be optimized based on astronomical and geometrical considerations.

For my family.
I would not be who I am today without you.
I love you, always and forever!

ACKNOWLEDGMENTS

"It takes a village to raise a child."

-African Proverb

I believe most people, if they are honest with themselves, can resonate with this proverb; however, I can only speak for myself to its truth. It would be impossible for me to write down the gratitude that I have for every single person who has helped me along this journey. The support I have received has been lifelong and immense! For this reason, I would love to thank those that have been pivotal in my life and who, without them, I would not have made where I am today.

My scientific curiously started well before elementary school. Actually, it has always been such a part of me, that I wonder if it is in the construct of my DNA. Once I reached school-age, I was lucky enough to have some of the most amazing teachers in the world.

Mrs. Shephard, Mrs. Detweiler, and Ms. Robinson (now Mrs. Storer) – my elementary school teachers. The three of you gave me the freedom to grow and learn beyond my years and supported me the entire way. I'm so thankful for you giving me a space filled with opportunity and encouragement. It made all the difference for me at such a young age and starting my journey.

Mr. A, Mr. Reese, and Mr. Hale – my aviation teachers. I came into high school already with a passion for flying. But the three of you fueled that passion like gasoline to a flame with every class and every day after school or during lunch where I would hang out with you in the aviation lab. I loved hearing your stories. They deepened my love for my biggest passion. You transformed the mystery of flight into reality as I graduated with my single-engine pilot's license. I cannot thank you enough!

USAF Sgt. Stradford and USAF Sgt. Rossi – my AFJROTC instructors. You taught me how to be a leader, how to be strong, and the importance of teamwork. Thank you for challenging me and encouraging me to go beyond my limits.

Mr. Siekerman – my AP Government teacher. I was always the biggest pain to you as a student, bugging you all the time because government wasn't my strongest subject. Thank you for

always being there for me, not taking it easy on me, and always pushing me to go past my comfort zones of my academic interests. You taught me that my comfort zone is not always where I belong.

Mrs. Corbett – my Calculus teacher. I have no words for all that I owe to you. You pushed me not just in math, but in life as well. Math always came easy to me, but the lessons I took from you extended far beyond academics. I learned how to be a good partner, how to persevere through the tough times in life, and how to stay positive through it all. Thank you for everything you've done for me. Just keep swimming!

Mrs. Santana – my physics teacher of three years. I found you in my sophomore year, and I just could not leave you! To say that you nourished my love for physics would be an understatement. You have the most beautiful heart and soul, and you gave me a place to be my nerdy self. You showed me that scientists do not have to fit in a box. You have more spunk than anyone I have ever met, and you showed me that I should strive to stand out rather than fit in.

Five days after graduating high school, I moved over 2,500 miles across the country, starting over in a new city without knowing anyone and becoming a part of the MIT community. MIT can be a daunting place, but it is filled with wonderful people. Out of everyone, I am eternally grateful for my research advisor of four years, Joesph Formaggio.

Joe Formaggio, I cannot begin to tell you how thankful I am to have met you as my first physics professor at MIT during the fall. I always loved your personality and your ways of teaching physics. Then you gave one lecture discussing your research about these wonderfully mysterious particles called neutrinos, and I knew then I had to work with you. That day after class, I just walked up to you and that is where it all began! The support and drive you gave me throughout my four years at MIT were immeasurable. You opened up a whole new world to me I never knew existed, and you found ways for me to connect the passions I already had with it. You were there for me during my best and worst times at MIT. You were there when I was happy and laughing and you were there when I needed to vent and cry. Thank you for being such a wonderful role model and pivotal person in my life.

The thought of going to graduate school in physics at MSU was equally daunting as the previous

four years at MIT. But I have been surrounded with a village of people that have made it a wonderful six and a half years. In some aspects it felt long, but in other ways too short.

Joshua Hignight and J.P.A.M. de Andre, thank you for being the best postdocs a student could ever ask for when they are just starting grad school. Thank you for all the help you gave me, even though I didn't work on your area of IceCube. Thank you for encouraging me to spend quality time with you instead of being a workaholic in the office all the time. Time management and balance are essential skills to both a professional and personal life. Those lessons I owe to both of you!

Kim Crosslan and Brenda Wenzlick, thank you for always being there to answer what seems like the millions of questions I have. You have made navigating grad school and the HEP department a breeze. You both are invaluable in BPS!

Jessie Micallef, you are so much more than just a colleague to me. I know when you met me, I was super quiet and unsociable. But you've helped me break out of that shell. We found out we share so many of the same interests, and we have become great friends. Thank you for helping me open up, for being there when I had dumb questions about coding, for comic-cons and movie premieres, for being the most awesome cat-sitter ever, and for whenever I needed to vent. But most of all, for being such a dear friend.

Brian Clark, Robert Halliday, Claudio Kopper, Hans Niederhausen, Nathan Whitehorn, thank you for being there for the countless questions and debugging sessions throughout the past few years. You always seemed to drop everything to help when I needed you. I'm so grateful to have had you around MSU during my last few years here. All of you are the amazing!

Mehr Un Nisa, you are a force of nature! I admire your ability to juggle so many tasks, which includes me being the most obnoxious grad student ever. Seriously, all the questions I've asked you, all the times I came to you freaking out over something, it never stopped. But you were always there, helping me and reassuring me along the way, no matter how busy you were or how many things you were balancing on your ever-growing plate. Thank you from the bottom of my heart!

Martin Rongen and Matt Kauer, thank you for making the trip down to Antarctica so

memorable. Martin, you were so fun to work with and I will never forget that trip, including our “Triathalon" of ping-pong, darts, and pool while waiting for flights North. Matt, we had an incredible time connecting on our shared interests. Every time I hear a motorcycle pass by, I am reminded of the times we spent oogling over motorcycles while waiting for flights. It is strange how little things can become such lifelong memories.

Tyce DeYoung – my MSU advisor. Finally, my time at MSU would have never happened without the support from my advisor, Tyce DeYoung. Thank you Ty, for taking me in and teaching me how I could mesh my love for neutrinos and my love for space together. Thank you for helping me make one of my lifelong dreams of going to Antarctica a reality. Thank you for teaching me communication skills that will be invaluable as I move up in my career.. I’m confident moving forward in life because of the lessons you’ve taught me while at MSU.

Last and greatest, to my loving family and friends. You mean more to me than words can tell. You have my heart. Everything I do is for you. Thank you for loving me and being there for me.

Cyndi Clough – my mom. Mom, there hasn’t been a moment in my life where you did not support me. You let me follow my dreams even if they were dangerous. We practically lived in the emergency room! You supported me so much that you faced your biggest fear of flying and allowed me to take you up in a small plane when I got my pilot’s license. You were at every soccer game and every science fair. You bought me space and physics books, even when you thought I was insane to love them so much. You have taught me to be strong and independent and how it feels to be loved by a mother. There is nothing compared to it. Mom, I am reaching my dreams because of you. You say you do not understand what I am doing but the most important thing for you to know is. . . I love you so much!

Robb Clough – my dad. There has not been a moment in my life that you were not there for me. You have stuck with me from when I was a stubborn little toddler to now when I am a stubborn full-grown woman. Some things never change! You have shown me what it means to be a selfless, loving person who would do anything for their family. I would not be here today if it were not for you. I could never thank you enough for loving me unconditionally.

Brytni Rysewyk-Jorgensen – my sister. Sis, we are polar opposites except when it comes to the thing that matters most. Family. Thank you for being there for me my entire life. I will never forget the fun times picking on mom, throwing strawberry milkshake malt balls at each other, the time we spend in the Ice Hotel and our dogsled run, and the list goes on. I love you.

Zach Cantu – my husband. Thank you for putting up with me all these years and for your undying support for my dreams and aspirations. Thank you for letting me be myself, and for loving me for the ridiculously nerdy person I am. I love you! Always and forever!

I have truly been blessed with so many wonderful people during this chapter of my life, too many to acknowledge all of them. But they know who they are and what they mean to me and how they have touched my life. I just hope that I have given them some of what they have given me and that we will continue to share rich and rewarding lives.

I thank all of you for being a part of my village!

TABLE OF CONTENTS

LIST OF TABLES

LIST OF FIGURES

CHAPTER 1

NEUTRINO ASTRONOMY

1.1 Cosmic Rays

Charged particles are created from unknown sources and propagate throughout the universe, ultimately reaching Earth's atmosphere. These charged particles are called cosmic rays. The discovery of cosmic rays was fueled by a series of experiments with electroscopes. In the presence of ionizing radiation (like cosmic rays), electroscopes will discharge. Around 1900, improvements were made to the insulation of electroscopes, allowing measurements of spontaneous discharge to be made with high sensitivity. Charles Thomson Rees Wilson and others found a decrease in radiation when an electroscope was placed inside an insulating box [24]. This meant that the radiation was coming from somewhere outside the box, either from terrestrial origins or extra-terrestrial origins.

In order to test where the penetrating radiation was coming from, Theodor Wulf came up with the idea to measure the radiation at a location farther off of the ground [4]. In 1909, Wulf traveled to Paris and conducted measurements at the top of the Eiffel Tower, 300 m above the ground. If the radiation was coming from the ground, Wulf expected to see a decrease in radiation at the top of the Eiffel Tower as compared to the ground. However, Wulf found that the radiation levels were similar to the level of radiation on the ground. To further investigate Wulf's results, it was clear that going to a higher altitude was necessary.

In 1911 and 1912, Victor Hess conducted a series of air balloon flights, reaching an altitude of 5.3 km above sea level. After an initial decrease in radiation, Hess saw the level of radiation increase significantly as he increased in altitude [25]. He concluded that this radiation must be coming from outer space. Hess also saw that his measurements did not vary based on what time of day he recorded them and ruled out the Sun as a significant source of this radiation. Hess's results were confirmed by Werner Kolhörster [26] and Hess was awarded the Nobel Prize in Physics in 1936 for the discovery of cosmic rays.

1.1.1 Cosmic Ray Composition

The term “cosmic ray" can apply to many different particles with origins from outer space. *Primary* cosmic rays are particles that are created in astrophysical sources out in the universe. *Secondary* cosmic rays refer to particles that are created when primary cosmic rays interact within their producing source or interstellar gas within the universe (also known as spallation). Primary cosmic rays are composed of around 85% protons, 12% α particles (He nuclei), and 3% heavier nuclei [2].

The chemical composition of cosmic rays compared to the composition of the solar system can be seen in Figure 1.1. The largest differences between the composition of cosmic rays and the solar system are the relative abundance of two groups of elements: Li, Be, B ($Z = 3, 4, 5$ respectively) and Sc, Ti, V, Cr, Mn ($Z = 21, 22, 23, 24, 25$ respectively). These elements are low in abundance within the solar system since they are not typically end products of stellar nucleosynthesis [27]. Carbon and oxygen spallation populates elements such as Li, Be, B and iron spallation populates elements such as Sc, Ti, V, Cr, Mn, which result as elements within the composition of cosmic rays. Another notable feature of Figure 1.1 is the abundance of elements for even Z and odd Z. When Z is even, the nucleus is more tightly bound, and therefore more stable and abundant than the elements with odd Z.

1.1.2 Cosmic Ray Energy Spectrum

Distributions of cosmic rays are often discussed in terms of the differential and integral flux of cosmic rays. The differential flux is given by [4]

$$\Phi(E) \equiv \frac{d^2\varphi}{dE\,d\Omega} \equiv \frac{dN}{A \cdot T \cdot d\Omega \cdot dE} \quad \left[\frac{\text{particles}}{\text{cm}^2\ \text{s sr GeV}}\right] \tag{1.1}$$

where N is the number of particles, A is the detector surface area, $d\Omega$ is the solid angle and dE is the energy interval. At energies larger than a few GeV, the differential flux of cosmic rays can be approximated as a power law [4]:

$$\Phi(E) \propto \left(\frac{E}{\text{GeV}}\right)^{-\alpha} \tag{1.2}$$

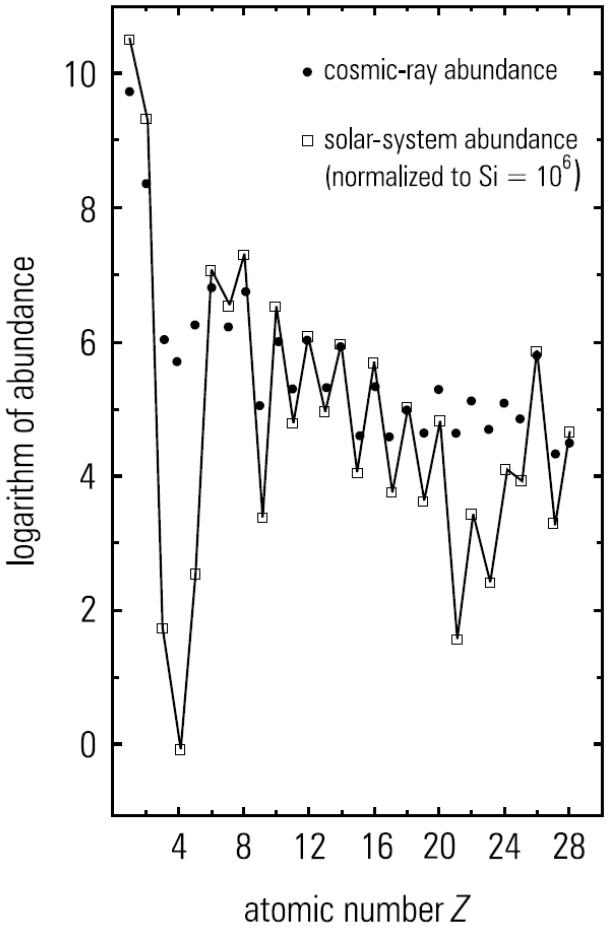

Figure 1.1: Chemical abundance of cosmic rays as compared to the solar-system abundance in terms of the atomic number of the element Z. Figure taken from [2].

The differential all-particle cosmic-ray flux can be seen in Figure 1.2. The spectrum has been observed over several orders of magnitude in energy by many different air-shower experiments. The spectrum in Figure 1.2 is multiplied by $E^{2.6}$ in order to highlight prominent features in the spectrum.

From around several GeV to $\sim 10^{15}$ eV, the energy spectrum is well described by a power law with $\alpha = 2.7$ [4]. Above that energy range, four prominent features appear. At an energy $\sim 10^{15}$ eV, a softening occurs in the power law spectrum. This is referred to as the “knee". Above the knee, the power law index softens to $\alpha \approx 3.1$ [4]. The knee is believed to be caused by particles reaching their maximum energy in cosmic-ray accelerators within the Galaxy [3]. Also, at energies above

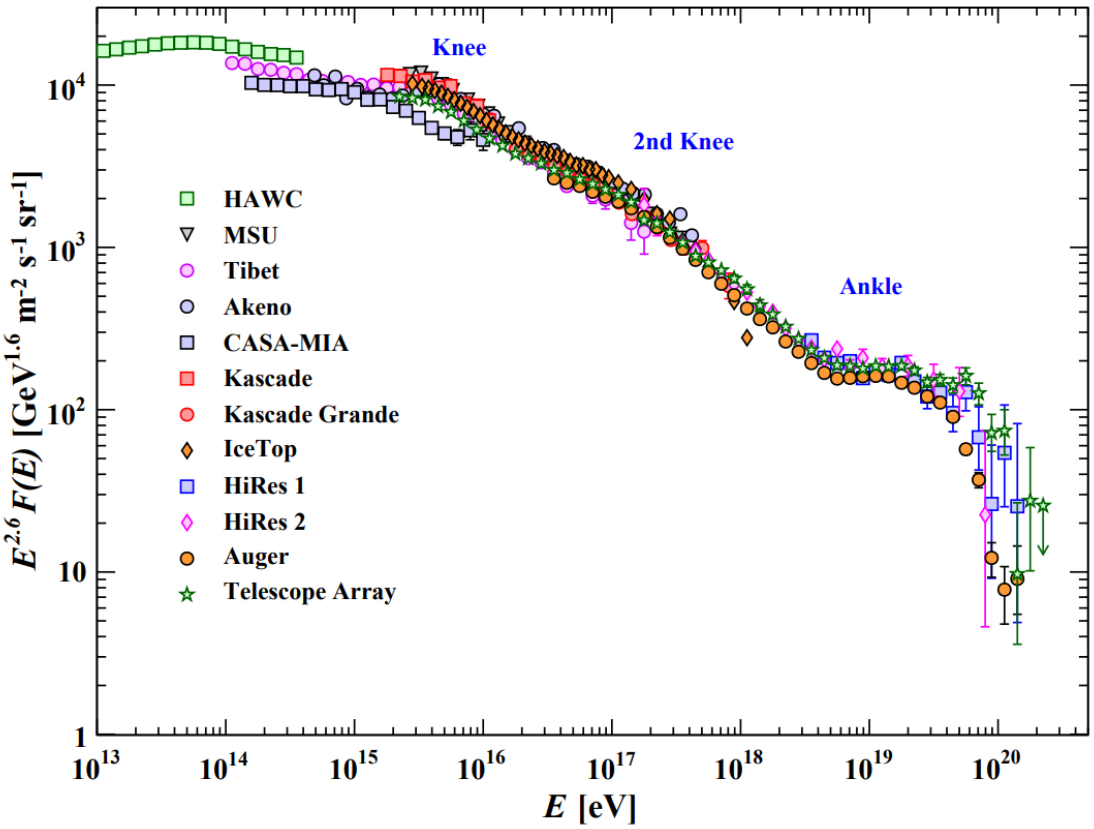

Figure 1.2: The differential all-particle cosmic-ray flux, $\Phi(E)$, over several orders of magnitude of energy. The spectrum is multiplied by $E^{2.6}$ in order to highlight features better. Figure from [3].

the knee, protons are more likely to escape the magnetic field of the Galaxy because of their higher energy. Heavy primary nuclei are still confined because their heavy masses require more energy to escape the Galaxy's magnetic field. The softening at the knee continues to about 8×10^{16} eV, where another kink appears, called the "second knee", and the spectrum softens again to $\alpha \approx 3.3$ [3, 28]. This is believed to be caused by heavier nuclei reaching their maximum energy before being able to escape the Galaxy's magnetic field [29]. The next prominent feature is the spectral hardening at $\sim 4 \times 10^{18}$ eV. This feature is called the "ankle". The spectrum hardens due to extra-galactic acceleration now being dominant over galactic acceleration, assuming extra-galactic accelerators are more powerful than Galactic accelerators [3]. At these energies, the Galaxy's magnetic field is no longer strong enough to contain cosmic rays. Another explanation for the ankle is the cosmic-ray protons and photons from the cosmic microwave background (CMB) are suffering radiative energy

losses from pair production ($p + \gamma_{\mathrm{CMB}} \rightarrow p + e^+ + e^-$) [30].

Finally, the last prominent feature is the rapid steepening of flux above energies of 5×10^{19} eV. This is likely caused by the interaction of cosmic rays with photons from the CMB. This is also called the Greisen-Zatsepin-Kuzmin (GZK) cut-off [31, 32]. When cosmic rays and CMB photons collide at high enough energies, they can produce a resonant Δ^+ which immediately decays [4]:

$$p + \gamma \rightarrow \Delta^+ \rightarrow \begin{cases} \pi^+ + n \\ \pi^0 + p \end{cases} \tag{1.3}$$

This cut-off effectively limits the distance to the sources of cosmic rays $>10^{20}$ eV to be within $\sim$ 100 Mpc, the GZK horizon [33]. Every time a cosmic ray collides with CMB photons, it loses 10% of its energy [4]. Within a few interactions with the CMB, the cosmic rays will drop below the GZK threshold of 5×10^{19} eV, which can explain the sharp cut-off of the cosmic-ray energy spectrum.

1.1.3 Cosmic-Ray Acceleration

A proposed method for how particles can be accelerated to such high energies is called the first-order Fermi acceleration mechanism [34, 4]. The idea behind this mechanism is that particles are bouncing back and forth between upstream and downstream materials in a shock wave. This process assumes collisionless interactions, with the particles bouncing back and forth due to inhomogeneities in the magnetic fields on either side of the shock wave [4]. The shock wave dynamics can be seen in Figure 1.3. The shock wave is considered to be moving at velocity v_s with respect to the surrounding interstellar media. As it moves, particles on either side will have different velocities depending on the rest frame that is being evaluated. The relative velocities in each frame of reference can be seen in Figure 1.3.

Every time a particle crosses the shock wave, it gains energy. The average energy gain per cycle can be defined as [4]

$$\left\langle \frac{\Delta E}{E} \right\rangle = \frac{4}{3}\beta = \frac{v_s}{c} = \beta_s \tag{1.4}$$

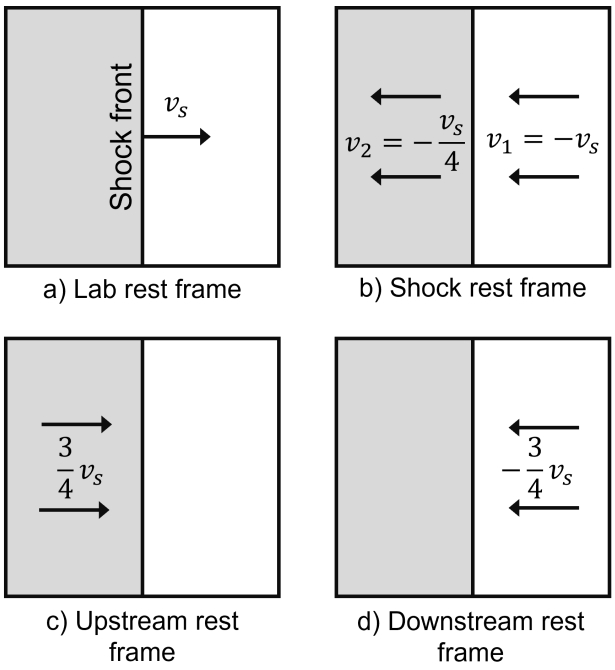

Figure 1.3: Diagrams of the shock wavefront in different frames of reference: a) the laboratory frame, b) the rest frame of the shock wave, c) the rest frame of the upstream medium, and d) the rest frame of the downstream medium. Figure adapted from [4].

where β is the the velocity of the particle, v_s is the velocity of the shock wave, and E is the energy of the particle before it crosses the shock wave boundary. After n cycles, the particle will have a final energy of

$$E = E_0 \, (1 + \beta_s)^n \tag{1.5}$$

where E_0 is the original particle energy. There is also the probability that particles will be left behind, leaving the shock front. This can simply be calculated as $P_{\text{esc}} = \beta_s$ [4], which allows the probability of a particle remaining after n cycles to be $P = (1 - P_{\text{esc}})^n$. The probability can easily be transferred to the ratio of particles remaining:

$$N = N_0 \, (1 - P_{\text{esc}})^n = N_0 \, (1 - \beta_s)^n \tag{1.6}$$

Solving Equation 1.5 for n and expressing Equation 1.6 in differential form gives a power-law spectrum [4]:

$$\frac{dN}{dE} \propto E^{-1+\frac{\ln(1-\beta_s)}{\ln(1+\beta_s)}} \tag{1.7}$$

For non-relativistic shock speeds, $\beta_s \ll 1$ and the above expression can be simplified to $dN/dE \propto E^{-2}$ given the Taylor expansion of the logarithms. This approximation is for the most efficient situation, where the escape probability remains constant for the non-relativistic shock wave. If the conditions in the shock wave environment become inefficient, the spectral index will soften to a value between 2.0 and 2.4 [4]. The measured spectral index of 2.7 discussed in Section 1.1.2 can be explained by the energy dependence of particles escaping the confinement of the Galactic magnetic field.

1.1.4 Hillas Criteria

Cosmic rays will continually accelerate in their source environment until they are energetic enough to escape the magnetic field of their source region. The maximum energy that a particle can obtain in a source region before escaping can be defined as [4]

$$E_{\max} = Ze\beta_s BR \simeq 10^{18} Z\beta \left(\frac{B}{\mu\text{G}}\right)\left(\frac{R}{\text{kpc}}\right) \quad \text{eV} \tag{1.8}$$

where Ze is the charge of the particle, β_s is the speed of the shock wave, B is the magnetic field, and R is the radius of the source. This maximum energy is known as the Hillas criterion [35]. The magnetic field strength and source size required to contain cosmic rays, as well as the size and magnetic field profile of several different possible sources of cosmic rays is shown in the Hillas diagram in Figure 1.4.

1.2 Neutrino Astronomy

The origin of cosmic rays has remained a mystery since they were discovered over a century ago. The problem that arises when trying to trace cosmic rays back to their source is the fact that cosmic rays are charged particles. As charged particles move through magnetic fields, their paths bend. So as cosmic rays propagate through the magnetic fields in the universe, their paths are bent and they no longer point back to where they originate. However, if cosmic rays interact with the medium near their source, that interaction can produce particles such as photons and neutrinos.

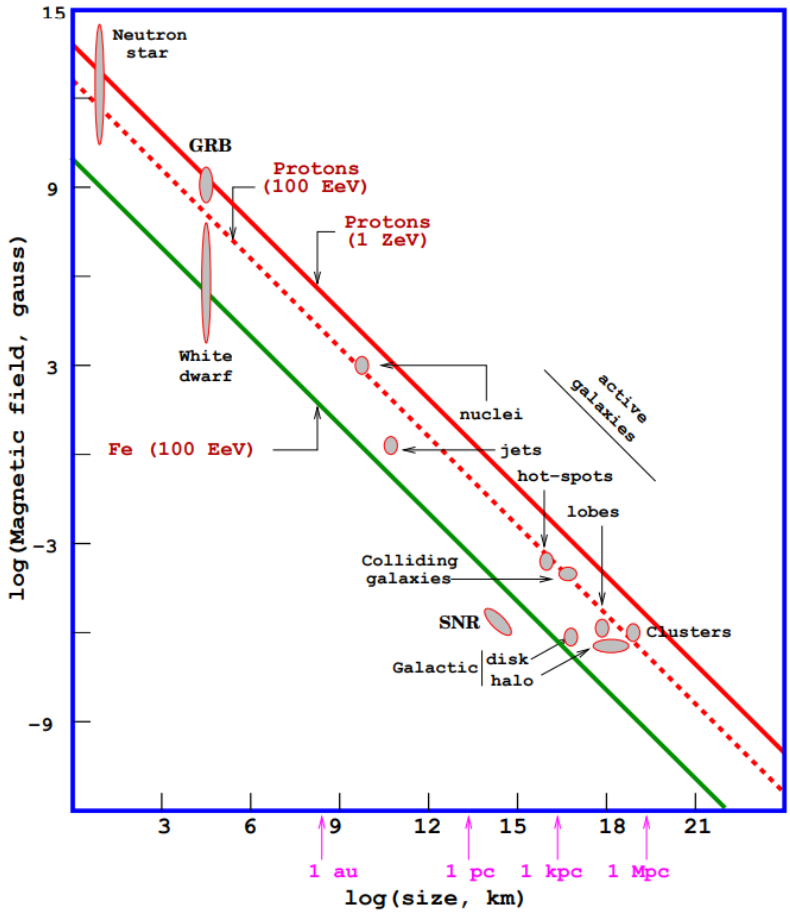

Figure 1.4: The magnetic field strength and source size required to contain cosmic rays of certain energies and charge. A 1 ZeV proton is shown in the solid red line. A 100 EeV proton is shown in the dashed red line. A 100 EeV iron nuclei is shown in the solid green line. Additionally, the size and magnetic field profiles of possible sources of cosmic rays is also shown. Figure from [5].

The photons used in observational astronomy were primarily in the visual wavelengths until the 1900s, when astronomy branched out into different wavelengths of light. Photons are now used to observe the sky across the electromagnetic spectrum, ranging from radio waves to gamma rays. Photons are neutral particles, so they can propagate through the universe unperturbed by magnetic fields. This means that if a very-high-energy photon is observed, it will point back to where it originated. However, several problems arise when one attempts to observe photons to determine the origins of cosmic rays. Photons can be absorbed by dense environments or radiation fields in the source, never reaching Earth to be detected. In addition, very-high-energy photons can be produced

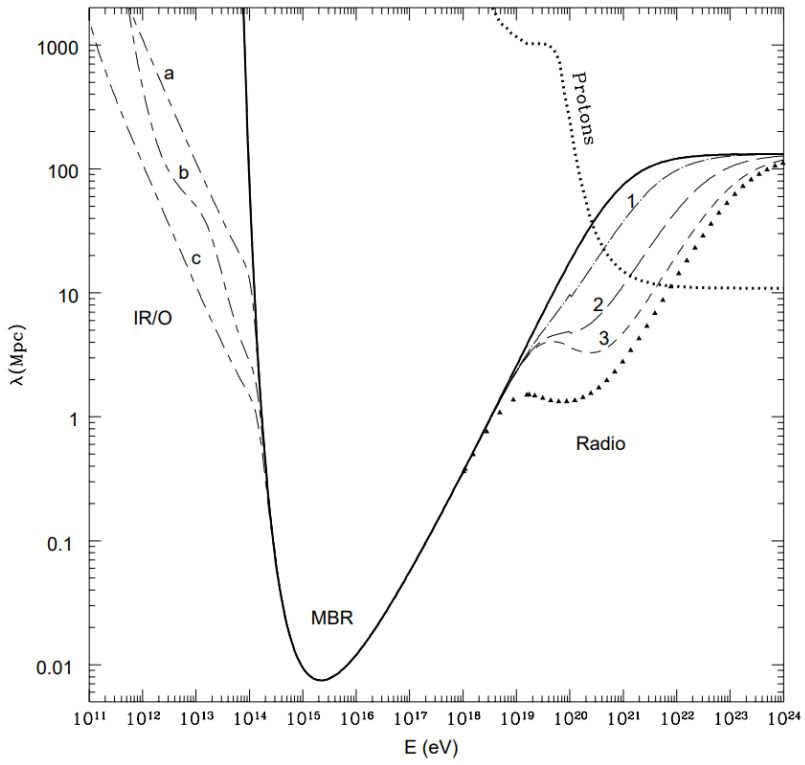

Figure 1.5: The mean free path of very-high-energy photons before interacting and producing electron-positron pairs through pair production. Below 10^{14} eV, VHE photons interact with inrared or optical (IR/O) photons. Above 10^{19} eV, VHE photons interact with radio photons. In between, VHE photons interact with the CMB photons (labeled as MBR). Figure from [6].

by both leptonic (such as inverse Compton scattering and pair production) and hadronic processes (such as π^0 decay), while cosmic rays can only be produce particles via hadronic processes [4]. Therefore, observing photons from a source does not necessarily prove that source is an origin of cosmic rays.

Finally, at high enough energies, the universe becomes opaque to gamma rays due to interaction with background photons and undergoing pair production: $\gamma + \gamma_{\text{bkg}} \rightarrow e^+ + e^-$. This can be seen in Figure 1.5. For energies below 10^{14} eV, high-energy photons interact with background infrared or optical photons. Above energies of 10^{19} eV, the limiting factor becomes radio photons. However, in the energy range of 10^{14} eV to 10^{19} eV, high-energy photons can interact with photons from the cosmic microwave background (denoted as MBR in Figure 1.5). At an energy around 100 TeV, the mean free path of that gamma ray becomes on the order of tens of Mpc. For even higher energies

at around 1 PeV, the mean free path becomes less than 10 kpc. With the radius of our Galaxy at roughly 16 kpc, this limits observational astronomy even within our own Galaxy at certain energies.

For unambiguous proof of cosmic-ray acceleration from sources both within and outside of our Galaxy, other approaches must be developed. Neutrinos are typically thought of as the ideal messenger particle in the search for origins of cosmic rays. These particles are neutral, like photons, and are not deflected by magnetic fields. They are rarely absorbed due to only interacting via the weak force. Finally, neutrinos can only be produced through hadronic processes. Thus, observing high-energy neutrinos from a source provides evidence of a source of cosmic rays. However, neutrinos are called “ghost" particles for a reason. They can travel through entire planets without interacting. So how does one observe astrophysical neutrinos? Chapter 2 discusses the principle of detecting neutrino interactions at high energies and Chapter 3 describes a detector that was designed especially to observe these high-energy ghost particles.

1.2.1 A Brief Introduction of Neutrinos

Neutrinos were first postulated in the early 1930s by Wolfgang Pauli as a solution to the beta decay problem. At the time, beta decay seemed to defy conservation laws of energy and angular momentum. A light, neutral particle would hold the laws of conservation true. In 1933, Enrico Fermi proposed a theory of beta decay that included Pauli’s particle, which Fermi coined the term “neutrino" [36]. It wasn’t until 1956 when the neutrino was confirmed by Clyde Cowan and Frederick Reines by conducting experiments using a nuclear reactor [37, 38]. Since then, many properties of neutrinos have been discovered, such as the different flavors of neutrinos and neutrino oscillations. Due to all of their properties, neutrinos make an ideal messenger for astronomy.

1.2.2 Neutrino Production

Cosmic rays can interact with matter or photons near the sources where they were produced. In these hadronic interactions, charged and neutral pions are produced, which then decay into neutrinos. For cosmic-ray proton interactions with photons, the primary interaction is through the resonance

of the Δ^+ meson [3]:

$$p + \gamma \rightarrow \Delta^+ \rightarrow \begin{cases} n + \pi^+ \\ p + \pi^0 \end{cases}$$

For cosmic-ray interactions with matter, mesons are produced in proton-nucleon interactions such as:

$$p + p \rightarrow \begin{cases} p + n + \pi^+ \\ p + p + \pi^0 \end{cases}$$

$$p + n \rightarrow \begin{cases} p + n + \pi^0 \\ p + p + \pi^- \end{cases}$$

The pions produced in these interactions have extremely short lifetimes (2.6×10^{-8} s for charged pions and 8.5×10^{-17} s for neutral pions). With a branching ratio of 99.98%, charged pions will decay into muons and neutrinos, where the muon with decay further into more neutrinos. Neutral pions will decay into photons with a branching ratio of 98.82%. These decays and their secondary neutrinos are:

$$\begin{aligned} \pi^+ &\rightarrow \mu^+ + \nu_\mu \\ \mu^+ &\rightarrow e^+ + \nu_e + \bar{\nu}_\mu \\ \pi^- &\rightarrow \mu^- + \bar{\nu}_\mu \\ \mu^- &\rightarrow e^- + \bar{\nu}_e + \nu_\mu \\ \pi^0 &\rightarrow \gamma + \gamma \end{aligned}$$

These processes produce neutrinos with the flavor ratio of $\nu_e : \nu_\mu : \nu_\tau = 1 : 2 : 0$. However, neutrinos will oscillate over the distance they travel from their source to Earth, resulting in a flavor ratio at Earth of $\nu_e : \nu_\mu : \nu_\tau = 1 : 1 : 1$ [39]. In these decay models, the resulting gamma rays and neutrinos closely follow the energy spectrum of the primary cosmic rays [4]. The typical energy of neutrinos resulting from primary protons in the above interaction and decay modes is directly

related to the primary proton energy by $E_\nu \simeq 0.05 E_p$ [4]. Observing gamma rays and neutrinos from sources would shed light on the cosmic-ray spectrum of that source.

1.3 Possible Sources of Astrophysical Neutrinos

The following sections will discuss some of the astrophysical events or sources that could be origins of cosmic rays; and thus, high energy neutrinos. These events or sources have the possibility of accelerating cosmic rays to the energies seen in Section 1.1.2. If these cosmic rays interact with matter or photon fields near their sources, the mechanisms discussed in Section 1.2.2 will produce high-energy neutrinos and photons that are needed to observe origins of cosmic rays. The astrophysical neutrino flux has been measured by IceCube [40], with assumptions that the neutrino flux is isotropic and has an equal flavor ratio at Earth.

1.3.1 Galactic Origins

As discussed in Section 1.1.2, Galactic cosmic rays are expected to hit a maximum energy of around 10^{15} eV before extra-Galactic emissions starts to dominate, though it is still unclear where extra-galactic accelerators enter in the cosmic-ray energy spectrum. If Galactic cosmic rays interact near their sources, the secondary neutrinos created in those interactions and decays will have maximum energies around 100 TeV. The total Galactic contribution to the astrophysical neutrino flux measured by IceCube has been limited to be no more than 14% above 1 TeV [41]. The following are several different possible sources within the Galaxy that could produce these cosmic rays.

Supernova Remnants (SNRs): SNRs are believed to be one of the most probable sources of cosmic rays in the Galaxy. When stars of $M > 8 M_\odot$ reaches the end of its life, the star explodes into a supernova. In this supernova explosion, most of the energy is emitted in MeV neutrinos [42]. In addition, the matter in and around the star when it explodes is ejected, forming a shock wave that expands into space traveling at speeds $v \simeq 0.01c$ for thousands of years [43]. This expanding shell of matter after a supernova explosion is called an SNR. Shock acceleration is expected to occur in these SNR shells. Pion decay, the origin of high-energy neutrinos and gamma rays and a signature

for proton acceleration, has already been detected in two SNRs within the galaxy (IC 443 and W44) [44, 45]. However, maximum energy of neutrinos that is expected from SNRs is $E_\nu < 10$ TeV, which is an order of magnitude lower than the maximum energy expected of neutrinos from within the Galaxy [42]. Whether or not SNRs would be able to accelerate protons up to the energy of the knee region is still an active area of research [46, 47].

Microquasars: Microquasars are binary systems that contain 1) a compact remnant of a collapsed star, such as a neutron star or a black hole ($M > 3M_\odot$), and 2) a star that is still alive. The two objects in microquasars are gravitationally linked and orbit around each other. The compact object accretes mass from the star, possibly producing a relativistic jet that is perpendicular to the accretion disk. Shocks produced in microquasars could possibly accelerate protons to ~PeV energies, resulting in ~TeV photons and neutrinos. TeV gamma rays were observed from the microquasar LS 5039 by H.E.S.S. [48]. If the LC 5039 gamma rays are of hadronic origin, a TeV neutrino flux could possibly be seen as well [49]. It is difficult to use gamma-ray emission for proof of proton acceleration since gamma rays can be produced by leptonic mechanisms as well. It has also been discussed whether observed gamma-ray fluxes from microquasars are affected by absorption, resulting in a reduced observed flux than the true produced flux. An associated neutrino flux could potentially be 100 times higher than the observed gamma-ray flux from a microquasar [49]. It has been shown that neutrinos ranging from 1-100 TeV could be produced by proton interactions with photons in the relativistic jet or accretion disk of microquasar systems [50, 51].

Pulsars and Pulsar Wind Nebulae (PWNe): A neutron star is often a remnant of supernovae when the mass of the collapsed star is $M > M_\odot$ [4]. In the case where the neutron star is rotating and is highly magnetized, it is classified as a pulsar. Pulsars emit a beam of radiation along its magnetic axis; and therefore, it can only be observed when the magnetic axis is pointed at Earth. A pulsar can be surrounded by material left over from the supernova explosion as well. This matter can be accelerated to relativistic speeds due to the proximity to the pulsar. The accelerated matter forms a wind, which is called the Pulsar Wind Nebula (PWN). PWNe interact with SNRs or the interstellar medium, creating a shock wave that is believed to accelerate particles to high energies.

Pulsars and PWNe are known to emit in radio, X-rays, and gamma rays [4]. Many PWNe have been detected in the gamma-ray sky; however, it is generally believed that the emission is produced by leptonic mechanisms in the electromagnetic fields associated with pulsars and PWNe. There is a possibility that hadronic mechanisms can be present, and the predicted neutrino fluxes for known PWNe for these scenarios have been calculated in [52, 53].

Galactic Diffuse Emission: If cosmic rays escape the immediate surroundings of their source and are at low enough energies not to escape the confinement of the Galactic magnetic field, these cosmic rays have the possibility of interacting with the interstellar medium within the Galaxy. These cosmic-ray interactions produce gamma rays and neutrinos diffusively throughout the Galactic plane. Diffuse gamma-ray emission in the TeV energy range along the plane has been observed by several experiments such as H.E.S.S. [54], Milagro [55], and HAWC [56]. Diffuse gamma-ray emission was also discovered in regions above and below the plane, called the Fermi bubbles [57, 58]. If the Fermi bubbles are caused by the star-forming regions in the center of the Galaxy, hadronic mechanisms in these regions are expected to produce neutrinos as well [59, 60, 61]. Galactic diffuse emission has been shown to not only trace the interstellar medium, but also in dense regions of matter where sources are located. H.E.S.S. found that the diffuse emission observed in the center of the Galaxy follows dense matter distributions and points to a cosmic ray accelerator in the region [62]. Therefore, diffuse emission could also possibly be elevated near sources of cosmic rays.

1.3.2 Extra-Galactic Origins

In regions above the ankle of the cosmic-ray energy spectrum, extra-galactic emission of cosmic rays is expected to dominate over Galactic emission. There are several potential sources of cosmic rays outside of the Galaxy, which are discussed below.

Active Galactic Nuclei (AGNs): AGNs are extremely luminous compact regions in the center of galaxies, with accretion disks that surround a supermassive black hole. Galaxies that host AGNs in their centers are called Active Galaxies. The supermassive black hole accumulates matter from

the accretion disk, and two relativistic jets are formed perpendicular to the accretion disk. These jets are ideal locations for shock acceleration of cosmic rays with the ability to produce high-energy gamma rays and neutrinos. The classification of AGNs depends on the the orientation of the AGNs to Earth [63]. In the case where the relativistic jet is pointed directly at Earth, AGNs are classified as blazars. Blazars are considered one of the most powerful astrophysical objects known, and in 2017, IceCube and several other observatories around the world detected neutrinos and photons originating from the location of the blazar TXS 0506+056 [64, 65]. The observation of both neutrinos and gamma rays indicates TXS 0506+056 as a likely source of cosmic rays. However, IceCube has demonstrated that blazars alone cannot account for the total neutrino flux seen [66], leaving the mystery of the origin of the majority of these neutrinos open.

Gamma Ray Bursts (GRBs): GRBs are known to be the most luminous explosions in the universe and are the brightest objects in the gamma-ray sky. GRBs are transient, lasting up to several hundred seconds. Currently, the origin of GRBs is still debated. They are believed to be from the core collapse of a massive star or the merging of compact binary systems (two neutron stars, or a neutron star and a black hole) [67, 68]. These events lead to a “fireball" of particles that create relativistic jets, in which gamma rays and neutrinos would be produced [68]. IceCube has been in search of neutrinos originating from GRBs and has determined that up to 1% of the observed astrophysical neutrino flux originate from GRBs [69, 70, 71].

Starburst Galaxies: Starburst galaxies are galaxies with a high rate of star formation and have been suggested to be a source of high-energy neutrinos [72]. Starburst galaxies are believed to be formed from the galaxy mergers, and the high rate of star formation can last for millions of years. Because of this, supernovae occur at a higher rate than typically seen in galaxies (2-4 per century in the Milky Way [43]). Gamma rays that have been observed from starburst galaxies are believed to be of hadronic origin, pointing to cosmic-ray acceleration [73]. Proton interactions with interstellar matter in the galaxy will also produce high-energy neutrinos. However, evidence points to starburst galaxies being sub-dominant producers of high-energy neutrinos [74].

Galaxy Clusters: Galaxies in the vicinity of other galaxies can become gravitationally bound

together. As galaxy clusters continue to grow through the accretion of additional galaxies and the merger with other clusters, cosmic shock waves on the scale of ~ Mpc are produced [75]. Protons are expected to be accelerated in these cosmic shock waves, then interact with interstellar media, producing high-energy photons and neutrinos [76]. Galaxy clusters are also expected to be hosts to AGN, GRBs, and starburst galaxies, which are also possible origins of high-energy neutrinos.

1.4 Background Affecting Astrophysical Neutrino Detection

When searching for astrophysical neutrinos, the main backgrounds in those searches come from atmospheric muons and neutrinos. When primary cosmic rays interact with particles in the Earth's atmosphere, they create showers of secondary particles [4]. The interaction and decay mechanisms that were discussed in Section 1.2.2 also come into play in the Earth's atmosphere. Atmospheric muons and neutrinos are produced from charged pion and kaon decays from cosmic-ray interactions in the atmosphere. Atmospheric muons typically arrive at detectors in bundles of muons with enough energy to travel through several kilometers of matter. Because of this, it is necessary to build neutrino detectors deep within a material, such as Earth or water, in order to reduce as much atmospheric muon background as possible. However, since muons have the ability to travel great distances, it is typical for neutrino experiments to only look for neutrinos in the up-going region where the entire Earth acts as a shield against atmospheric muons. Atmospheric neutrinos, on the other hand, can traverse the entire Earth, and represent an irreducible background to neutrino experiments. However, the energy spectrum of atmospheric neutrinos is a power-law spectrum with a soft index of 3.7 [4], which differs from the cosmic-ray energy spectral index of 2.7 below the knee. Further discussion on the effects of background on IceCube will be discussed in Section 4.2.

CHAPTER 2

NEUTRINO DETECTION TECHNIQUES

As discussed in Chapter 1, neutrinos provide smoking-gun evidence of cosmic-ray acceleration if a source of high-energy neutrinos is discovered. Neutrinos are neutral particles that only interact via the weak force. Because of this, they travel unperturbed from their origin to Earth. The challenge of neutrino astronomy is to observe these ghost particles once they arrive.

2.1 Neutrino Interactions in Matter

This thesis is primarily concerned with high-energy neutrinos above 100 GeV. In this energy range, the dominant neutrino interaction process is deep inelastic scattering [77]. In deep inelastic scattering, the incoming neutrino scatters off a quark in the nucleon via the exchange of either a W or Z boson. This produces a lepton and a hadronic cascade in return. The processes of deep inelastic scattering are:

$$\nu_l + N \rightarrow l^- + X \qquad \bar{\nu}_l + N \rightarrow l^+ + X \tag{2.1}$$

$$\nu_l + N \rightarrow \nu_l + X \qquad \bar{\nu}_l + N \rightarrow \bar{\nu}_l + X \tag{2.2}$$

where N is the nucleon in the medium that the neutrino is interacting in, X is the outgoing hadronic cascade, and l corresponds to a lepton flavor, either e, μ, or τ. Equation 2.1 corresponds to charged-current (CC) deep inelastic scattering. In CC interactions, a W^- or W^+ boson is exchanged and an outgoing charged lepton is produced. Equation 2.2 corresponds to neutral-current (NC) deep inelastic scattering. In NC interactions, a Z^0 boson is exchanged and an outgoing neutrino is produced. Feynman diagrams of CC and NC interactions can be seen in Figure 2.1. Due to the high energy of neutrinos > 100 GeV, the transfer of energy is too great for the nucleon to stay intact, thus a hadronic cascade is produced in return.

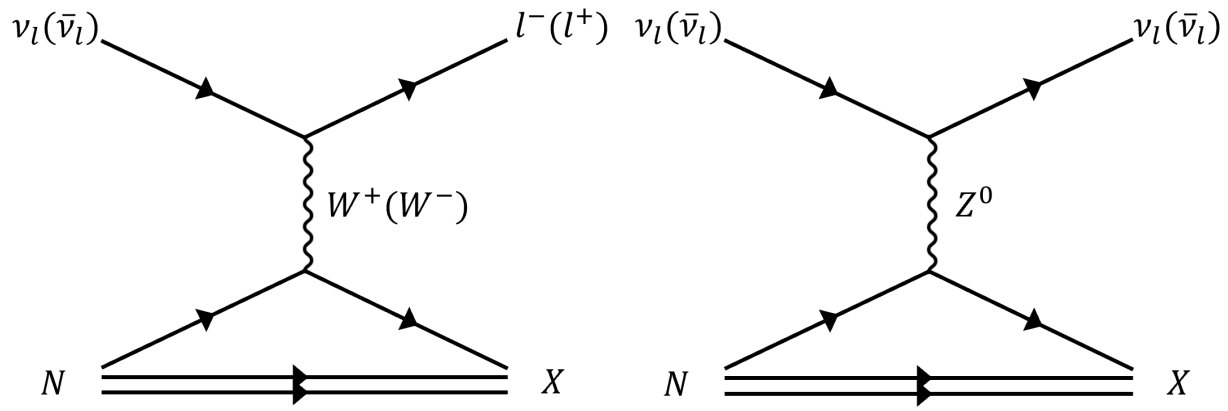

Figure 2.1: Feynman diagrams of charged-current (CC) deep inelastic scattering (left) and neutral-current (NC) deep inelastic scattering (right). In both cases, the incoming neutrino scatters with a nucleon, N in matter. For CC interactions, a W boson is exchanged and a lepton and hadronic cascade, X, is produced. For NC interactions, a Z boson is exchanged and a neutrino and hadronic cascade are produced.

Deep inelastic scattering can be completely described by three dimensionless variables [77]:

$$y = \frac{E_{\text{had}}}{E_\nu} = 1 - \frac{E_l}{E_\nu} \tag{2.3}$$

$$x = \frac{Q^2}{2M_N(E_\nu - E_l)} \tag{2.4}$$

$$Q^2 = -q^2 = (p_\nu - k_l)^2 \tag{2.5}$$

where x is the Bjorken scaling factor, y is the inelasticity, and Q^2 is the momentum transfer. E_ν is the energy of the neutrino, E_{had} is the energy of the hadronic cascade, E_l is the energy of the outgoing lepton, M_N is the mass of the nucleon, p_ν is the 4-momentum of the incoming neutrino, and k_l is the 4-momentum of the outgoing lepton. Using Equations 2.3, 2.4, and 2.5, the total neutrino and anti-neutrino cross section for deep inelastic scattering can be defined as [77]

$$\frac{d^2\sigma^{\nu,\bar{\nu}}}{dx\,dy} = \frac{G_F^2 M_N E_\nu}{\pi\left(1 + Q^2/M_{W,Z}^2\right)^2}\left[\frac{y^2}{2}2xF_1(x,Q^2) + \left(1 - y - \frac{M_N xy}{2E}\right)F_2(x,Q^2) \pm y\left(1 - \frac{y}{2}\right)xF_3(x,Q^2\right], \tag{2.6}$$

where G_F is the Fermi constant and $M_{W,Z}$ is the mass of the mediating weak force boson, either $W^\pm$ for CC interactions or Z^0 for NC interactions. The three $F_i(x,Q^2)$ are dimensionless nucleon

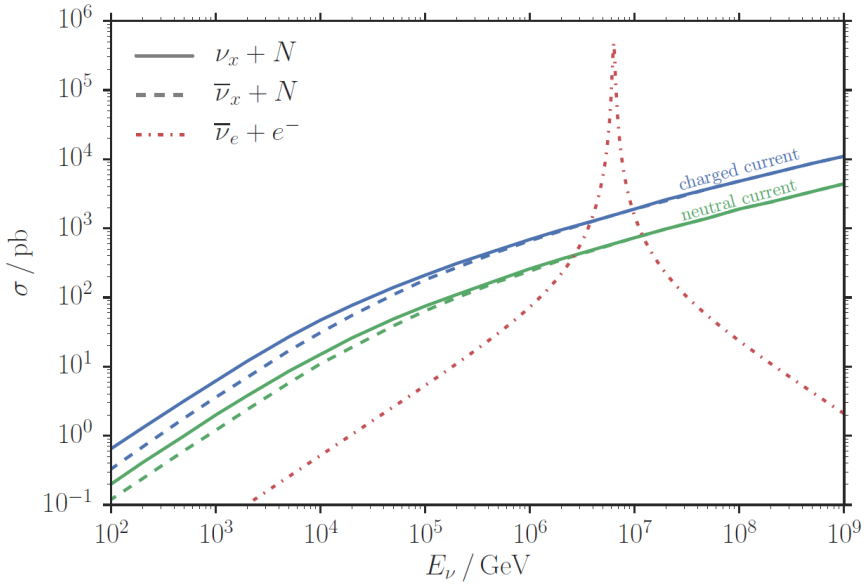

Figure 2.2: The neutrino (solid) and anti-neutrino (dashed) cross sections for charged-current interactions (blue) and neutral-current interactions (green) for deep inelastic scattering as a function of neutrino energy. The Glashow resonance cross section is shown in dashed red. Figure from [7], with data taken from [8].

structure functions that describe the structure of the medium [77]. Finally, the ± in the last part of Equation 2.6 denotes the switch between neutrino and anti-neutrino cross section.

The neutrino and anti-neutrino cross sections for CC interactions and NC interactions of deep inelastic scattering can be seen in Figure 2.2. For neutrino energies $< 10^4$ GeV, the (anti-)neutrino cross sections scale linearly with energy. However above that energy range, the momentum transfer becomes larger than $M_{W,Z}$, suppressing the cross section at higher energies [77]. At energies above 10^7 GeV, the cross sections scales as a power law, E^α, where $\alpha \simeq 0.363$ [77].

Additionally, it can be seen that the neutrino cross section is larger than the anti-neutrino cross section at low energies. This is because deep inelastic scattering is dominated by the scattering off of valence quarks at lower energies. Valence quarks are the quarks that carry the quantum numbers of the nucleon: *uud* for protons and *udd* for neutrons. The interaction of anti-neutrinos with valence quarks is less likely due to helicity suppression [78]. At higher energies, the difference between the neutrino and anti-neutrino cross sections is negligible. In this regime, scattering off of sea quarks becomes dominant. Sea quarks are equal in quarks and anti-quarks, making the neutrino

and anti-neutrino cross sections approximately equal [78].

The other notable feature from Figure 2.2 is the effect of Glashow resonance. At high energies, neutrino-nucleon cross scattering is the dominant interaction type. Neutrino-electron scattering is sub-dominant because the electron mass is so small compared to that of a proton or neutron. However, resonant production of a W^- boson can occur for $\bar{\nu}_e + e^-$ interactions. This resonance occurs when the $\bar{\nu}_e$ has an energy of $E_{\text{res}} = M_W^2/2m_e = 6.3$ PeV [77]. This can be seen in Figure 2.2 and is dominant above cross sections for neutrino-nucleon interactions at the resonant energy. This resonance was predicted by Sheldon Glashow in 1960 [79]. Recently, IceCube has been able to detect Glashow resonance in the detector [80].

Due to their small cross section, it is possible for neutrinos to travel through large bodies of matter, such as the Earth, without interacting. However, the cross section increases with energy, so the more energetic the neutrino, the more likely it is to interact with matter. The Earth is transparent to low-energy neutrinos. However, for neutrinos above $\sim$ 100 TeV, the Earth becomes unavoidably opaque. This can be seen in Figure 2.3. This plot was produced by simulating neutrino propagation through the Earth using the All Neutrino Interaction Simulation (ANIS) [81] and the Preliminary Reference Earth Model (PREM) [82] for the Earth density profile. A constant, isotropic E^{-2} neutrino flux was created at the Earth's surface at different zenith angles to the South Pole.

Figure 2.3 shows that the average survival rate of neutrinos and anti-neutrinos at the detector depends on the flavor of neutrino, the energy of the neutrino, and the amount of matter the neutrino has to travel through to get to the detector. The more energetic neutrinos are and the more matter they have to travel through, the more likely they will be absorbed before reaching the detector. For electron neutrinos, the effects of Glashow resonance can be seen to worsen the survival rate of neutrinos at the resonant energy of 6.3 PeV. For tau neutrinos, the attenuation is shifted towards higher energies due to tau regeneration. This occurs when a CC tau neutrino interacts and produces a tau lepton. Due to the short lifetime of a tau lepton of 290.3×10^{-15} s [3], the tau lepton will decay before losing much energy and produce a tau neutrino that can still travel to the detector [83].

The final outcome of the neutrino interactions discussed in this section are either a neutrino

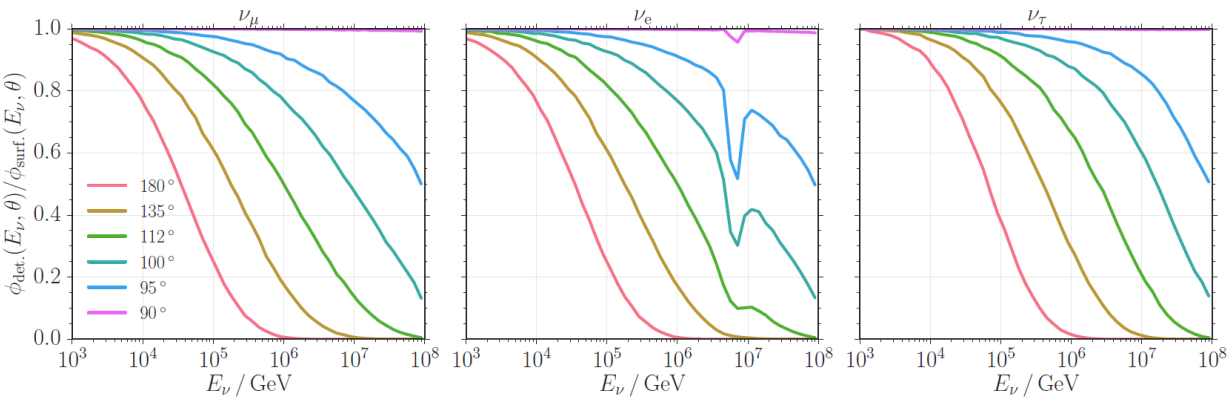

Figure 2.3: The average fraction of surviving neutrinos and anti-neutrinos at the detector after passing through the Earth at different zenith angles. 90° approaches directly from the side, with minimal travel through the Earth. 180° approaches directly from the top, with maximal travel through the Earth. The surviving flux at the detector is attenuated due to neutrino interactions with matter in the Earth. For energies below the TeV range, this effect is negligible. The effect of Glashow resonance on electron neutrino interactions can be seen by the dip in the fraction of surviving neutrinos at the resonant energy of 6.3 PeV. Figure from [7].

and a hadronic cascade for NC interactions and a charged lepton and a hadronic cascade for CC interactions. For NC interactions, since a neutrino is a neutral particle, it will escape invisibly and the only observation that can be made is of the hadronic cascade. For CC interactions, both the charged lepton and the hadronic cascade can be observed. The signature of the charged lepton depends on the flavor of charged lepton that is produced in a CC interaction. The signatures of charged leptons and hadronic cascades can be seen in Figure 2.5. The next section will discuss how these leptons and hadronic cascades create these signatures in a medium.

2.2 Cherenkov Radiation

High-energy neutrinos can be detected indirectly by observing secondary particles from deep inelastic scattering discussed in the previous section. These secondary particles include charged leptons and hadronic cascades that include charged particles discussed in more detail in the next section. When these interactions occur at high energies, the outgoing particles are traveling faster than the speed of light in the medium where the interaction occurred. When particles travel faster than the speed of light in a medium, they emit Cherenkov radiation. This is essentially the "sonic

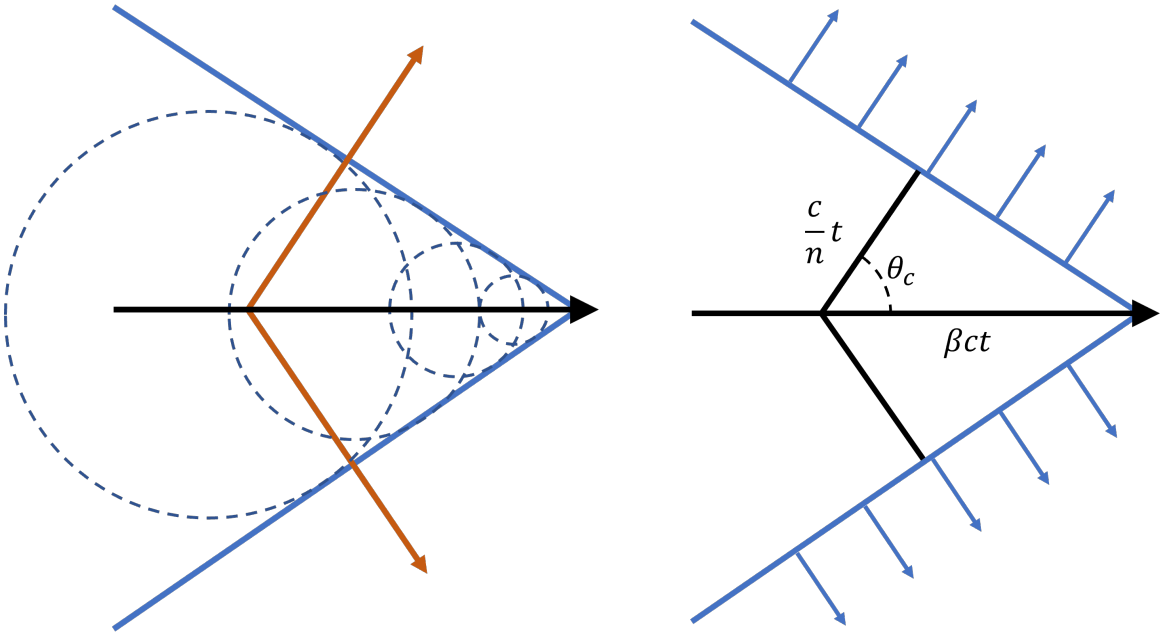

Figure 2.4: Diagrams of Cherenkov radiation that is emitted at angle θ_c when a particle moves faster than the speed of light in the medium in which it is moving. The left plot shows the emission of Cherenkov radiation at different points along the particle's path, forming the cone-like structure as the particle moves. The right plot shows the geometry of Cherenkov radiation. The Cherenkov angle can be calculated for the medium that the particle is moving in.

boom" of light. A visualization of Cherenkov radiation can be seen in Figure 2.4. It shows the emission of Cherenkov radiation at different points along the particle's path, forming the cone-like structure as the particle moves.

The geometry of Cherenkov radiation is also shown in Figure 2.4. With this geometry, it is easy to calculate the Cherenkov angle for a specific medium. The Cherenkov emission angle can be calculated as

$$\cos\theta_c = \frac{1}{\beta n}, \tag{2.7}$$

where θ_c is the Cherenkov emission angle, β is the velocity of the particle divided by the speed of light in a vacuum ($\beta = v_p/c$), and n is the index of refraction of the medium. The secondary particles that IceCube detects in ice are highly relativistic, traveling so close to the speed of light in a vacuum that $\beta \approx 1$. Light, on the other hand, travels at a speed of c/n, where c is the speed of light in a vacuum and n is the index of refraction of the medium. The index of refraction of ice is approximately 1.33 at 300 nm [84]. Given this, the Cherenkov emission angle is $\theta_c \approx 41°$.

The threshold of Cherenkov radiation is when a particle's velocity exceeds the speed of light in a medium. It can easily be described by $\beta > 1/n$. For $n = 1.33$, the Cherenkov threshold is when $\beta \gtrsim 0.75$. The Cherenkov threshold can also be expressed as a particle's energy by

$$E_c > m\left(1 - \frac{1}{n^2}\right)^{-1/2} \tag{2.8}$$

where m is the mass of the particle emitting Cherenkov radiation. For electron, muon, and tau leptons, the Cherenkov threshold is at energies of 0.78 MeV, 160 MeV, and 2.7 GeV respectively.

The number of Cherenkov photons that are emitted by a particle per unit wavelength and distance of the charged particle is given by the Frank-Tamm formula [85]:

$$\frac{d^2N}{dxd\lambda} = \frac{2\pi\alpha z^2}{\lambda^2}\left(1 - \frac{1}{\beta^2 n^2(\lambda)}\right), \tag{2.9}$$

where α is the fine structure constant, z is the charge of the particle in e, λ is the wavelength, β is the speed of the particle, and $n(\lambda)$ is the wavelength-dependent index of refraction. The index of refraction of ice can be defined as a polynomial that can be found in [84]. For a charge $z = 1$ particle traveling at $\beta \approx 1$ and approximating the index of refraction of ice to be 1.33 across all wavelengths, in the range of 300 nm to 500 nm, the particle will emit approximately 265 photons per cm.

2.3 Secondary Particles from Neutrino Interactions

As discussed in Section 2.1, CC neutrino interactions produce a secondary lepton of the same flavor of the incident neutrino while NC neutrino interactions produces a secondary neutrino. Because neutrinos travel invisibly, the only way to detect a neutrino is by observing secondary particles from neutrino interactions. The different types of signature for different types of neutrino interactions can be seen in Figure 2.5. For both CC and NC interactions, a hadronic cascade is produced from the neutrino scattering off a nucleon. This hadronic cascade is all that can be observed for NC interactions, since the outgoing neutrino escapes invisibly. For CC interactions, along with a hadronic cascade, a charged lepton is produced and creates specific signatures depending on

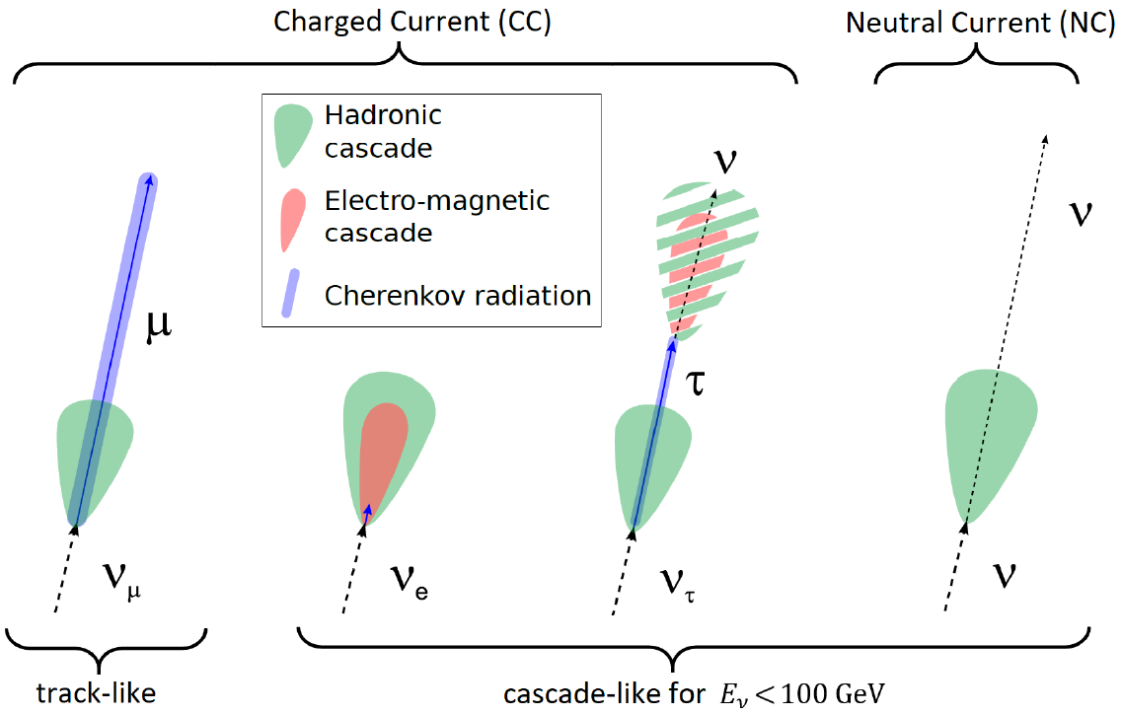

Figure 2.5: Event signatures for all types of neutrino interactions discussed in Section 2.1. Hadronic cascades, electromagnetic cascades, and Cherenkov radiation from particles that can travel long distances can be seen. If the energy of the tau neutrino is < 1 PeV, then the two cascades are indistinguishable. For neutrino energies below 100 GeV, the three cascade-like events are indistinguishable. The type of emission observed after the tau decay depends on the decay channel, which will sometimes feature an outgoing muon track as well as neutrinos and cascades. Figure from [9].

the flavor of the outgoing lepton. Details on individual scenarios are considered in the following sections.

2.3.1 Muons

CC interactions of astrophysical muon neutrinos produce high-energy muons. High-energy muons lose energy through ionization and radiative processes such as e^+e^- pair production, bremsstrahlung, and photonuclear interactions [3, 86, 87]. The average muon energy loss can be approximated as [88]

$$-\frac{dE_\mu}{dx} = a(E_\mu) + b(E_\mu) \cdot E_\mu \tag{2.10}$$

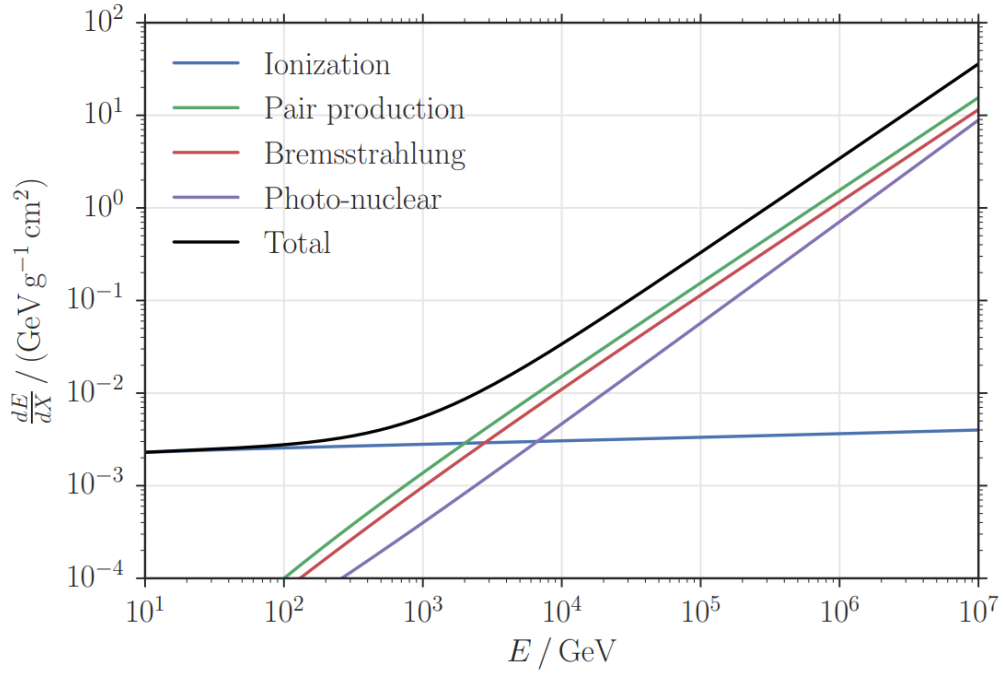

Figure 2.6: Muon energy loss in ice for multiple different processes. Ionization dominates the total energy loss at low energies, while the radiative losses dominate the total energy loss at high energies. Figure from [7], produced with data from [10].

The first term, $a(E)$, is the energy loss from ionization, which can be described by the Bethe-Bloch formula in [3]. Ionization is dominant at energies below several hundred GeV, which can be seen in the mean total muon energy loss in Figure 2.6. For ionization, energy loss rises very slowly as energy increases and can be treated as a quasi-continuous energy loss [89]. At around 1 TeV, radiative processes become dominant, which is expressed as the second term, $b(E)$, in Equation 2.10. Radiative energy loss of muons scale linearly with energy when muons are traveling in water or ice [88]. The loss due to pair production, bremsstrahlung, and photonucluear interactions are all included in the radiative loss term: $b \equiv b_{\text{pair}} + b_{\text{brem}} + b_{\text{photo}}$. For ice, $a = 0.268$ GeV/mwe and $b = 4.70\ 10^{-4}$/mwe where mwe is "meter of water equivalent" (distance normalized to water density) [86]. The radiative losses appear as electromagnetic cascades along the muon track.

Aside from energy loss, muons also have a chance to decay through the following decay mode with a branching ratio of nearly 100% [3]:

$$\mu \rightarrow e^- + \bar{\nu}_e + \nu_\mu \tag{2.11}$$

The mean lifetime of a muon is $(2.1969811 \pm 0.0000022) \times 10^{-6}$ s [3]. With this long of a lifetime, muons of high energy can travel several hundred kilometers before decaying. Therefore, the length of travel for high-energy muons is dependent on the energy loss processes discussed above.

With the energy loss rate in Figure 2.6, muons are able to travel many kilometers (depending on energy) until it is no longer able to produce Cherenkov radiation. For example, a 1 TeV muon can travel approximately 2 km in ice [86]. With the ability to travel great lengths in ice, muons provide the best opportunity for pointing resolution to determine astrophysical origins of neutrinos.

2.3.2 Electrons

CC interactions of electron neutrinos produce high-energy electrons. Energy loss for electrons is similar to that of muons, except for the fact that an electron's mass is less than 0.5% of a muon's mass; and therefore, will lose energy at a much faster rate, dropping below the Cherenkov threshold much faster than a muon. For high-energy electrons, bremsstrahlung dominates energy loss, which produces high-energy photons. These photons then undergo e^+e^- pair production, and those electrons emit photons via bremsstrahlung, and this process continues. This is called an electromagnetic cascade.

The average energy loss for electrons emitting bremsstrahlung photons is

$$\frac{dE_e}{dx} = -\frac{E}{X_0}, \tag{2.12}$$

where X_0 is the radiation length of the electron, which is $X_0 = 39.31$ cm in ice [90]. For the electromagnetic cascade, the maximum distance it can develop in ice is [3]

$$x_{max} = X_0 \cdot \left(\ln\left(\frac{E}{E_c}\right) \pm 0.5 \right). \tag{2.13}$$

E_c is the critical energy where the energy loss from ionization matches the energy loss of bremsstrahlung and the $\pm$ depends on whether a photon (+) or an electron ($-$) induced the electromagnetic cascade. The critical energy in ice is 78.6 MeV for an electron and 76.5 MeV for a positron [90]. The maximum distance an electromagnetic shower can propagate ranges from roughly 1.7 m at 10 GeV to around 6.2 m at 1 PeV.

2.3.3 Taus

CC interactions of tau neutrinos produce high-energy tau leptons. As discussed in Section 2.1, the tau lepton has an extremely short lifetime. Therefore, its travel length is often determined by relativistic kinematics rather than energy loss. For ultra-relativisitic particles where $v \gg c$, the energy can be approximated using $E \approx pc$ where p is the particle's momentum and c is the speed of light. Given this approximation, the length traveled by a tau lepton before it decays can be defined as

$$x \approx \frac{E_\tau \tau c}{m_\tau} = 50\,\mathrm{m} \cdot \frac{E_\tau}{\mathrm{PeV}} \tag{2.14}$$

for the lifetime of a tau lepton of $\tau = 2.90 \times 10^{-13}$ s and a mass of $m_\tau = 1.78$ GeV [3]. Once the tau lepton decays, there are a number of different possibilities. Tau leptons are heavy enough to decay into mesons such as π and K mesons. The total branching ratio for all hadronic or semi-leptonic modes is approximately 64.9% [3]. Two other notable non-hadronic decay modes are $\tau^- \rightarrow \nu_\tau e^- \bar{\nu}_e$ with a branching ratio of around 17.8% and $\tau^- \rightarrow \nu_\tau \mu^- \bar{\nu}_\mu$ with a branching ratio of around 17.4% [3]. If an electron or muon is emitted in the tau lepton decay, it will produce the same signatures discussed above. For all other hadronic or semi-leptonic modes, it will produce a hadronic cascade.

In IceCube, the initial cascade from the neutrino interaction can only be distinguished from the cascade from the decay of the tau lepton if it is at an energy above 1 PeV. At energies less than 1 PeV, the two cascades from the different interaction vertices cannot be distinguished. Below 1 PeV, CC tau neutrino interactions are mistaken as CC muon neutrino interactions because the tau lepton decays into a muon with a 17.4% branching ratio. The rest of the time, CC tau neutrino interactions are mistaken as either CC electron neutrino interactions or NC neutrino interactions.

2.3.4 Hadronic Cascades

In the hadronic cascades produced by all deep inelastic scattering interactions, both CC and NC, mainly pions are produced. Charged pions decay primarily into muons and neutrinos (with a branching ratio of approximately 99.99% [3]), which continue the propagation of the hadronic

cascade. However, when neutral pions decay, they mainly produce two photons (with a branching ratio of approximately 98.8% [3]). Photons will undergo pair production and start electromagnetic cascades. Hence hadronic cascades are also accompanied by electromagnetic cascades. With IceCube's separation of optical modules that observe these cascades in the ice, hadronic and electromagnetic cascades are indistinguishable.

2.4 Neutrino Source Searches

Searching for astrophysical neutrino sources relies heavily on being able to trace where the neutrino come from in the sky. While all types of events can be used in neutrino source searches, muons provide the best pointing resolution to find astrophysical neutrino sources. The extended Galactic neutrino source search in this thesis uses exclusively track-like events. This includes CC muon neutrino interactions in the ice as well as CC tau neutrino interactions that are mistaken for CC muon neutrino interactions due to the tau decay into a muon. The extended Galactic neutrino source search will be discussed in Chapter 4.

CHAPTER 3

ICECUBE NEUTRINO OBSERVATORY

IceCube is a neutrino observatory situated at the geographic South Pole in Antarctica. The IceCube collaboration started construction on the detector in 2004, with its completion coming six years later in December 2010. Even during the years of construction, IceCube began collecting data with the partial detector. IceCube's original design and purpose was to observe neutrinos from astrophysical origins and to identify the sources they originated from. In 2013, IceCube realized one of its primary objectives in observing astrophysical neutrinos [91]. However, over the years, IceCube's scientific goals have broadened into many areas of physics and science. IceCube is a versatile detector, able to probe into areas such as cosmic ray physics, dark matter, beyond Standard Model physics such as searches for exotic particles, neutrino oscillation physics, and the study of the Antarctic ice through glaciology.

Recently, IceCube has stepped into the realm of multi-messenger astronomy, where the same astrophysical source or phenomenon can be observed not only by different wavelengths of light (such as optical, X-ray, gamma-ray, and radio), but also by different messengers, such as gravitational waves, and neutrinos. Multi-messenger astronomy depends on the collaboration of many different experiments and utilizes IceCube's ability to send out alerts to fellow observatories in real-time when a high-energy event is observed. This allows other observatories to examine the area in the sky from which the high-energy event originated to see if other detections are found. This proved to be effective when IceCube and several other observatories reported both a high-energy neutrino and photons originating from the direction of the blazar TXS 0506+056 [92, 93]. The observation of this neutrino in IceCube occurred on September 22, 2017, with follow-ups from around 20 different observatories around the world. These observations from a broad range of energies of photons and neutrinos point to TXS 0506+056 as a possible source of high-energy neutrinos, and therefore, a unambiguous source of cosmic rays. The success IceCube has seen so far in reaching its original scientific objectives to branching out in other areas of science is due to the design, performance,

and reliability of the IceCube detector.

3.1 IceCube Detector Layout

The IceCube Neutrino Observatory consists of two main parts: the in-ice array and the surface array called IceTop. A diagram of IceCube can be seen in Figure 3.1. Since IceCube relies on the detection of Cherenkov radiation to observe neutrinos, the detector must be placed in an optically clear medium, dark enough to detect the light from these interactions. So IceCube instrumented the Antartic ice to observe these astrophysical neutrinos. The in-ice array is made of of 5,160 digital optical modules (DOMs) situated on 86 strings (cables) with depths in the Antarctic ice ranging from 1450 m to 2450 m below the surface at the South Pole [14]. Each DOM houses a photomultiplier tube (PMT) which detects light in the ice. There are 60 DOMs on each string, with DOMs spaced ~17 m apart from each other on the main 78 IceCube strings. The main IceCube strings have a string spacing of around 125 m, which was optimized to detect astrophysical neutrinos on the the order of $\mathcal{O}$(TeV) to $\mathcal{O}$(PeV) energies [14].

DeepCore is a more dense layout of eight strings, with the average string spacing of 72 m. The DOMs on the eight DeepCore strings have a specialized layout optimized for lower-energy observations ranging from 10 GeV to 100 GeV [14]. 50 DOMs are placed at the bottom of the detector with a spacing of 7 m, ranging from 2100 m to 2450 m. The remaining 10 DOMs are placed above the dust layer (a band of ice ranging from 2000 m to 2100 m that has significantly higher absorption and scattering than the surrounding ice [94]) at a separation distance of around 10 m. These 10 DOMs above the dust layer act as a veto array for the remaining 50 DOMs below on each string in an attempt to remove atmospheric muon background [14]. With the eight specialized DeepCore strings and the 78 IceCube strings, all 86 strings are laid out in a hexagonal array that can be seen in Figure 3.2. With all 86 strings, IceCube has instrumented ~1 cubic kilometer of Antarctic ice.

IceTop is the surface detector of IceCube at 2,835 m above sea-level [12]. It is a cosmic ray air-shower array that consists of 162 tanks of ice oriented in pairs at 81 stations across the surface

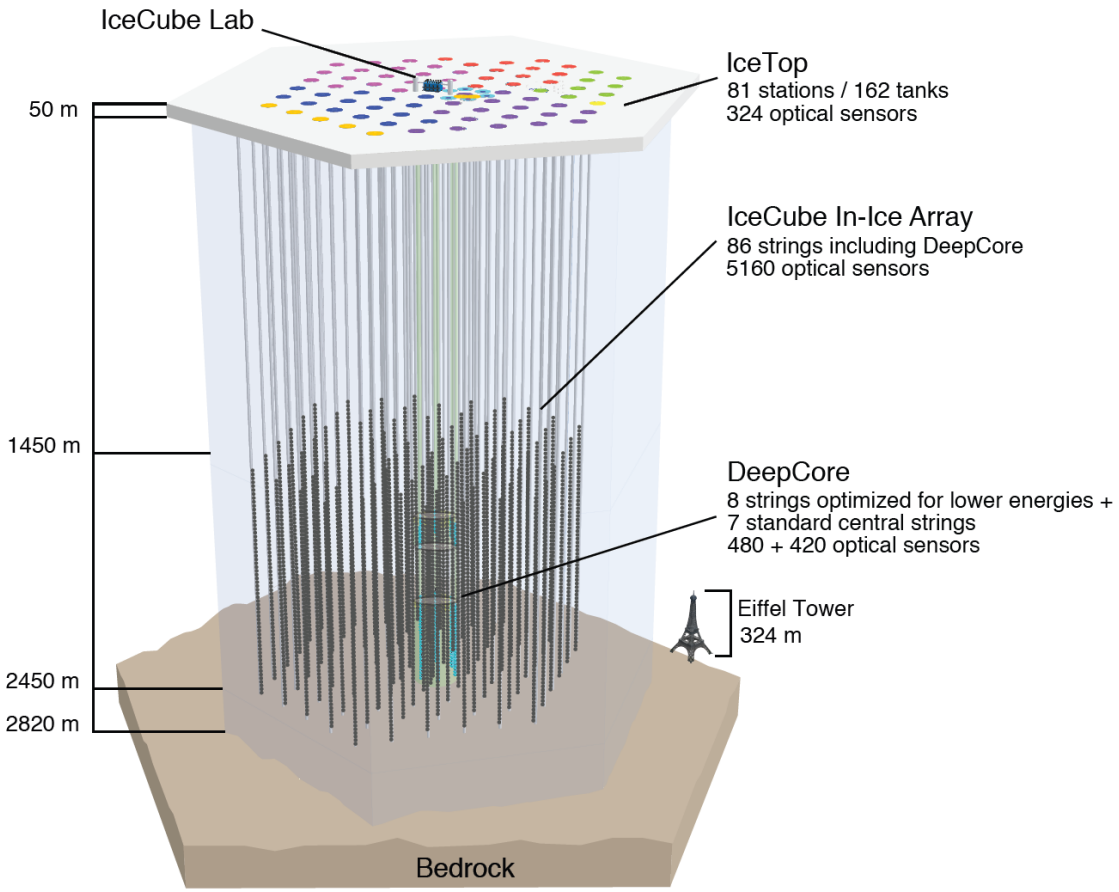

Figure 3.1: A diagram of the IceCube Neutrino Observatory, consisting of the in-ice array which includes a denser sub-array called DeepCore, and surface structures such as the IceCube Laboratory and the cosmic-ray air shower detector called IceTop. Figure taken from [11].

at the South Pole. Each tank is instrumented with two DOMs, identical to the DOMs placed in the in-ice array. IceTop operates on the same physics as IceCube. Cherenkov radiation is produced in the ice in the IceTop tanks and the DOMs detect that light. IceTop stations are roughly at the same locations of the IceCube strings, around ~125 m apart. The location of the IceTop tanks can be seen in Figure 3.2. The primary goals of IceTop are to characterize the composition of cosmic rays and to analyze the cosmic-ray energy spectrum. IceTop has shown to able to observe air-showers originating from cosmic rays on the order $\mathcal{O}$(PeV) to $\mathcal{O}$(EeV) [95]. Along with studying cosmic rays, IceTop can be used as a veto array for the IceCube detector in the ice [14]. If coincident events are seen in both IceCube and IceTop, the event in IceCube can be associated with background from

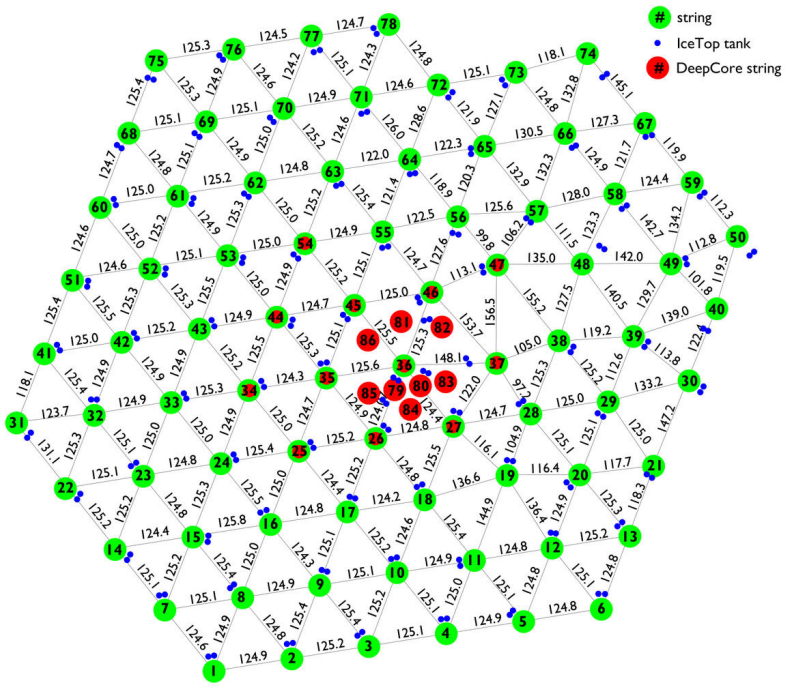

Figure 3.2: A diagram of the layout of all 86 IceCube strings as well as IceTop tanks. The distance between strings is approximately ~125 m for the main in-ice array. The strings included in DeepCore are situated closer together. Figure taken from [11].

the atmosphere.

Finally, the last major part of the IceCube Neutrino Observatory is the IceCube Laboratory (ICL). The ICL is located on the surface at the South Pole directly above IceCube. The ICL acts as the main operations building on-site at the South Pole. The first floor is dedicated to laboratory working space and storage. The second floor houses the server room. The cables from IceCube are routed up to the surface, where the surface cables are run to the two cable towers on either side of the ICL. These cable towers lead straight to the server room on the second floor. The server room contains computers that run various tasks, such as the collection of data from IceCube, monitoring systems, and online filtering systems [14].

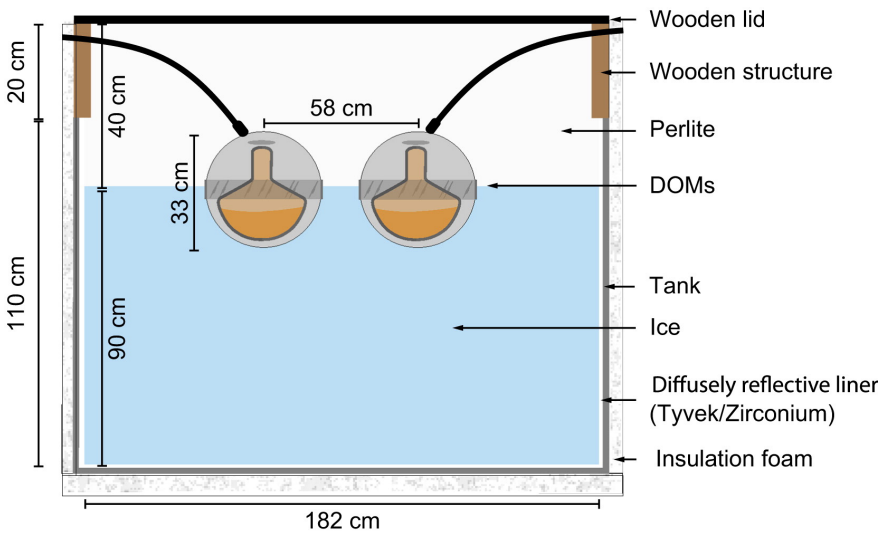

Figure 3.3: A schematic diagram of an IceTop tank. There are 162 IceTop tanks, and each tank is instrumented with two DOMs. The tank is filled with ice with the two DOMs inside. Figure taken from [12].

Figure 3.4: An image of the IceCube Laboratory (ICL) on the surface above IceCube. The ICL is the main operations building on-site at the South Pole, with laboratory working space on the first floor and the server room on the second floor. The cables from IceCube are routed along the surface to the two cable towers on each side of the ICL, which are both connected to the server room on the second floor.

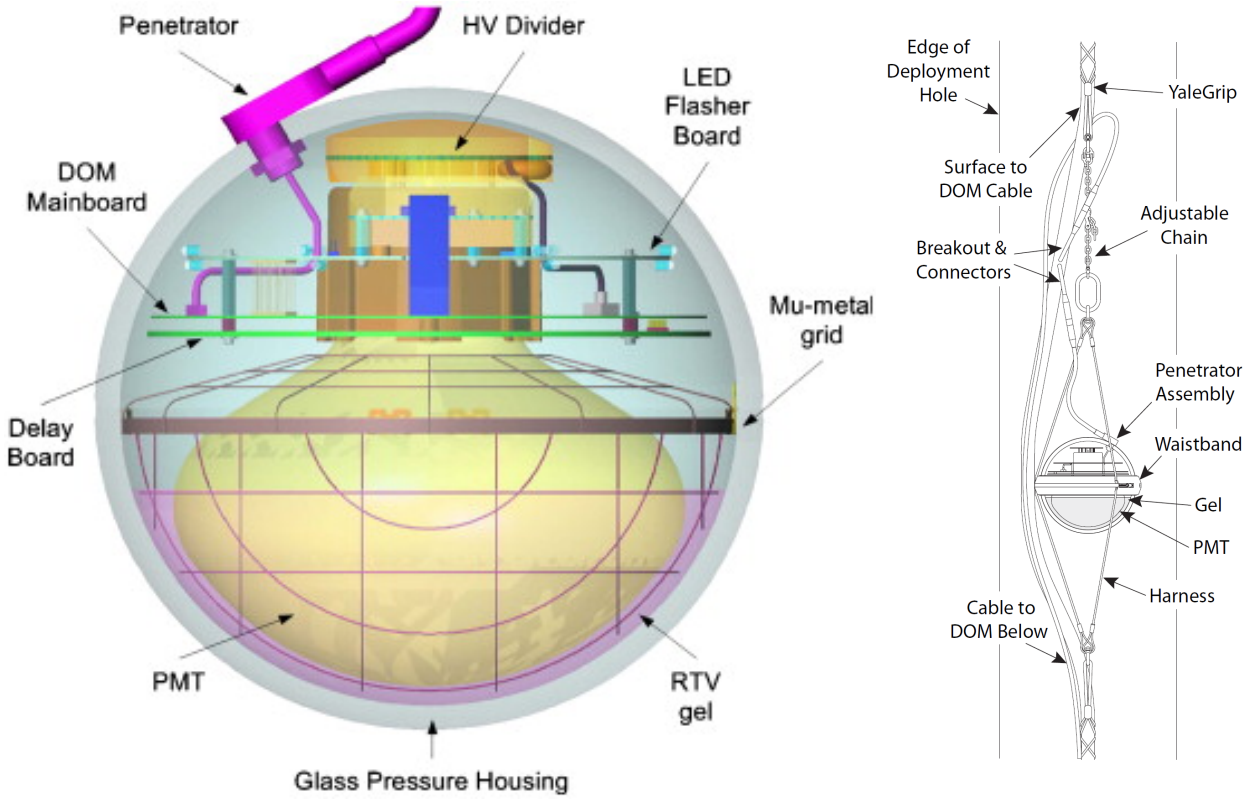

Figure 3.5: A schematic diagram of a digital optical module (DOM) (left) and the string assembly (right). Left figure taken from [13] and right figure taken from [14].

3.2 Digital Optical Module

IceCube is only able to observe astrophysical neutrinos, as well as perform studies in several different areas in physics, because of the DOMs that instrument the Antarctic ice. A schematic diagram of a DOM can be seen in Figure 3.5. The main component of a DOM is the 10"-diameter Hamamatsu R7081-02 photomultiplier tube (PMT) [96]. PMTs are sensitive enough to detect single photons in the ice. They operate based on the principle of the photoelectric effect. When a photon hits a material like alkali metals, it emits electrons, also known as photoelectrons (PEs). An illustration of how a PMT works is shown in Figure 3.6. When an incident photon strikes the material called the photocathode, it emits a photoelectron. This photoelectron then cascades down a series of dynodes of increasingly higher voltage, emitting more and more electrons as it collides with each dynode. Eventually, the collection of electrons reaches the anode and exits the PMT as a sizeable signal.

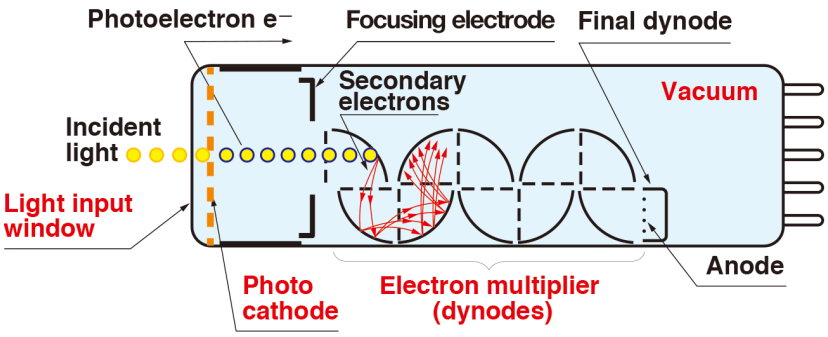

Figure 3.6: An example of a photomultiplier tube and how it works. An incoming photon interacts with the photocathode, emitting a photoelectron that gets amplified through a series of high-voltage dynodes. Figure taken from [15].

The PMT faces downward in the DOM, rests in a gel that supports the PMT and provides good optical transmission to the PMT, and is shielded by a mu-metal grid that reduces the effects of the South Pole magnetic field on the PMT's collection efficiency [14]. With the PMT, each DOM also includes a DOM Mainboard. This board is used to control every component inside of a DOM, including the digitization of waveforms from the PMT, communications with the data acquisition (DAQ) system in the ICL, and the communication with neighboring DOMs for the purpose of local coincidence (LC) triggering [14]. More details of the DOM Mainboard can be found in [13]. Each DOM also contains a LED flasher board for various calibration purposes and a high voltage supply and divider for the PMT [14]. Finally, the PMT and all internal components are encased in a glass pressure housing to withstand the pressure of being submerged under kilometers of ice. The DOM is then connected to the string via the penetrator, which safely carries the power/data cable through the pressure housing.

3.3 Data Acquisition, Triggers, and Filters

The acquisition of data begins when a DOM is "hit" by one or more photons. Waveforms of the PMT signals are digitized and read-out if the DOM registers a charge exceeding 0.25 PE [14]. However, a DOM can register a hit due to noise that is not from an interacting photon, such as spontaneously emitted electrons from the photocathode. Trigger and coincidence procedures are

set up to help distinguish whether a hit is from noise or from photons in the ice from relativistic particles. A local coincidence (LC) is checked for before data is sent. If neighboring DOMs on the same string in the ice both record hits within ± 1 μs, it is considered a hard local coincidence (HLC) and the waveforms along with the timing and charge information are sent to the surface DAQ. If neighboring DOMs do not record hits within ± 1 μs, then it is considered a soft local coincidence (SLC) and only the timing and charge information are sent to the surface.

The DAQ on the surface performs more triggers to determine if hits are from possible physics events in the ice. HLC hits are examined to see if there is evidence of any spatial or temporal clustering of HLC hits. There are a number of different types of triggers that can prompt the DAQ to form an event, which will include both HLC and SLC hits within a specific time window defined by the type of trigger [14]. The most common trigger in IceCube is called the Simple Multiplicity Trigger (SMT). If a certain number of HLC hits are seen within a sliding time window of several μs (8 within IceCube, 3 within DeepCore), then the SMT is triggered and the time window remains open until there are no more HLC hits within the initial trigger time window. The number of HLC hits and the time window required to satisfy the SMT condition depends on the sub-detector being used (main in-ice array, DeepCore, IceTop) [14]. The SMT trigger only requires temporal correlation between HLC hits. There is no requirement for spatial correlation. The SMT trigger rate for the main in-ice array is 2.1 kHz, while the SMT trigger rate for DeepCore is 250 Hz.

The triggers that do require spatial correlation are called the Volume Trigger and the String Trigger. An example of the Volume and String Triggers are shown in Figure 3.7. The number of HLC hits and the time window required to satisfy these triggers are based on the size of the volume that is being evaluated. There are cases when the time window of the SMT and the spatial triggers is too short. It is possible that a heavy, slow-moving particle can travel through the ice and hit neighboring DOMs past the time window that would satisfy the other triggers. For these cases, IceCube developed a Slow Particle (SLOP) trigger dedicated to search for slow-moving particles [14].

There are three other triggers for purposes mainly outside of searching for astrophysical neu-

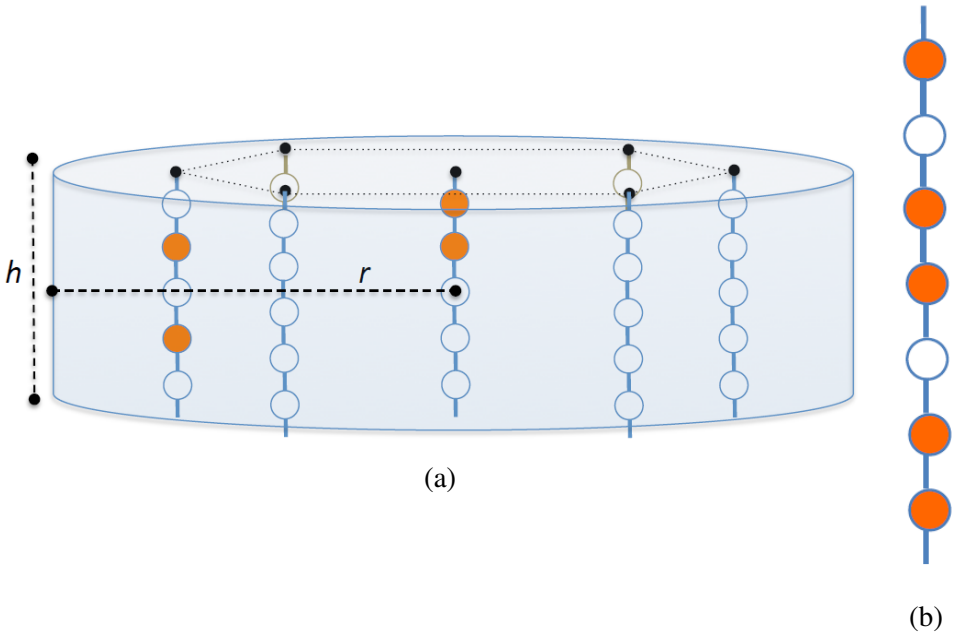

(a)

(b)

Figure 3.7: A representation of the Volume Trigger (left) and the String Trigger (right). Both figures taken from [14].

trinos. The Fixed-Rate Trigger (FRT) collects data from the entire detector in 10 ms intervals. This trigger is often used to study noise in the detector [14]. A Calibration Trigger also exists and is tunable to fit the needs of the tests to be performed. And finally, a Minimum Bias trigger records every N-th HLC hit and triggers data collection. [14]. N depends on the sub-detector being used. Details of all the different triggers and their associated time windows and number of HLC hits required per sub-detector can be found in [14]. Collectively, event rates are dominated by atmospheric muons and trigger the detector at about a rate of ~2.7 kHz and the amount of data stored from the DAQ system is about 1 TB per day [14].

Once the DAQ registers an event, it has to pass through selection filters to determine if the event information should be sent via satellite to the North. The Processing and Filtering (PnF) system passes events through 25 different filters to see if the events match signatures for different physics analyses [14]. If an event passes the filters, it is sent via satellite to data warehouses in the Northern Hemisphere. Afterward, all events are recorded on tape at the South Pole, regardless of the filter decision [14]. Tapes are then sent to the North for permanent storage.

3.4 Types of Events

Different types of events can be seen in IceCube depending on the flavor of neutrino that interacted as well as what type of interaction occurred. As explained in Section 2.1, at the energies IceCube is concerned with, neutrinos interact with matter via deep inelastic scattering. The two types of deep inelastic scattering are neutral current (NC) interactions and charged current (CC) interactions. When NC interactions occur, the outgoing particle is a neutrino. However, a hadronic cascade is produced and Cherenkov light is produced by the particles in the hadronic cascade. When CC interactions occur, the outgoing particle is a charged lepton which leaves a Cherenkov light signature in the detector. A hadronic cascade is still produced in CC interactions, but the particles in the hadronic cascade rapidly scatter or decay, leaving the light emission from a hadronic cascade in a small volume.

With CC and NC neutrino interactions in mind, there are three types of event signatures that IceCube could see in the detector. The first type is a track-like event. Tracks are created when a CC muon neutrino interaction occurs, and a high-energy muon is produced along with a hadronic cascade. Muons are able to travel long distances on the order of several kilometers before dropping below the Cherenkov threshold and decaying. Because muons travel through the ice for those long distances, the Cherenkov light that is deposited appears to be a straight line, like a track. The scattering angle between the incoming muon neutrino and the outgoing muon is small at high energies ($\Psi_{\nu\to\mu} \sim 0.7^\circ\,(E_\nu/\mathrm{TeV})^{-0.7}$ [47]). Because of this, the direction of the outgoing muon is taken as the direction of the incoming muon neutrino and an angular resolution below 1° can be obtained for neutrinos above TeV energies [20]. The signature of a track event can be seen in Figure 3.8.

The second type of event that IceCube is able to detect in the detector is a cascade, which can be seen in Figure 3.9. Cascade events can be produced in a variety of ways. If NC interactions for any flavor of neutrino occur, an outgoing neutrino is produced as well as a hadronic cascade. Since neutrinos are neutral and weakly-interacting, they do not leave a trace and they exit the detector invisibly. However, the hadronic cascade contains charged particles that will travel a short

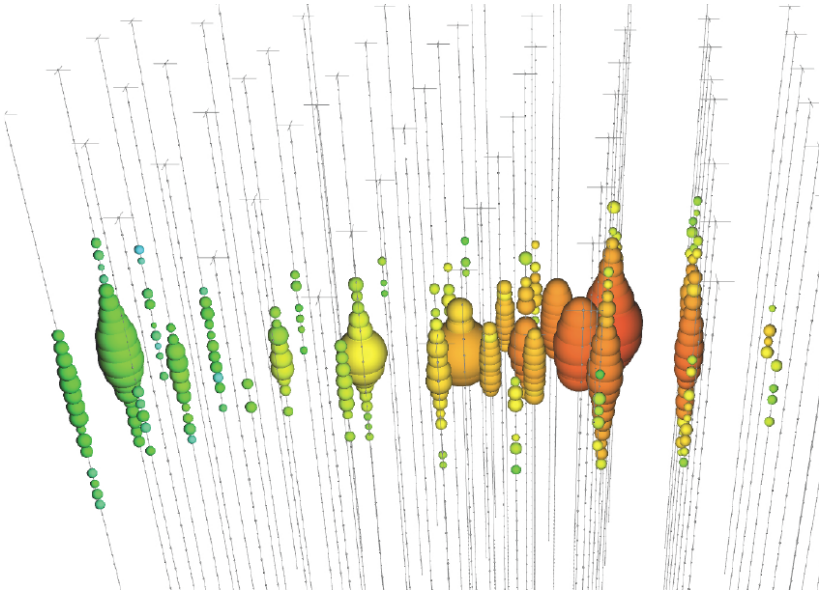

Figure 3.8: A simulation of a track-like event in IceCube. Tracks are produced when CC muon neutrino interactions occur and a muon is produced in return. The color of the DOMs represent the arrival times of the photons (red is early, green is late). The size of the DOM represents the amount of charge that is seen in that DOM. The CC neutrino interaction occurred near the red hits, with the muon exiting to the left. Figure taken from [16].

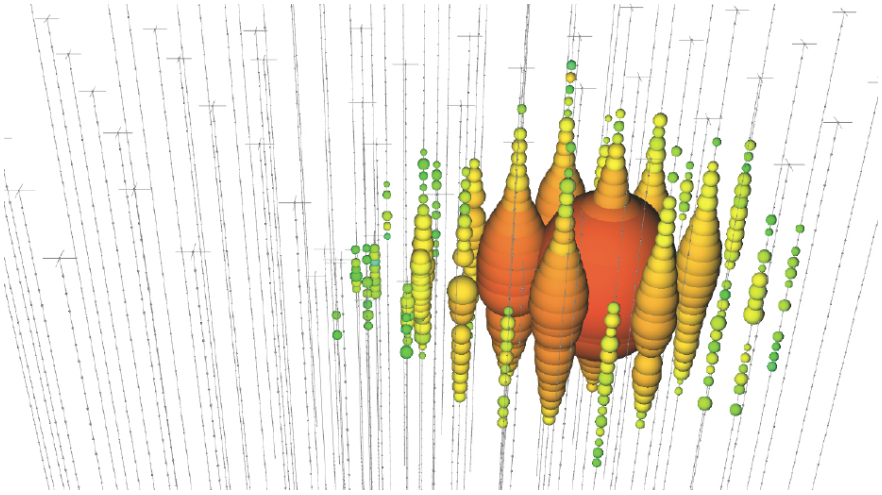

Figure 3.9: A simulation of a cascade-like event in IceCube. Cascades can be produced by NC interactions for all flavors of neutrinos, for CC interactions for electron neutrinos, and for CC interactions for tau neutrinos for energies below 1 PeV. The color of the DOMs represent the arrival times of the photons (red is early, green is late). The size of the DOM represents the amount of charge that is seen in that DOM. Figure taken from [16].

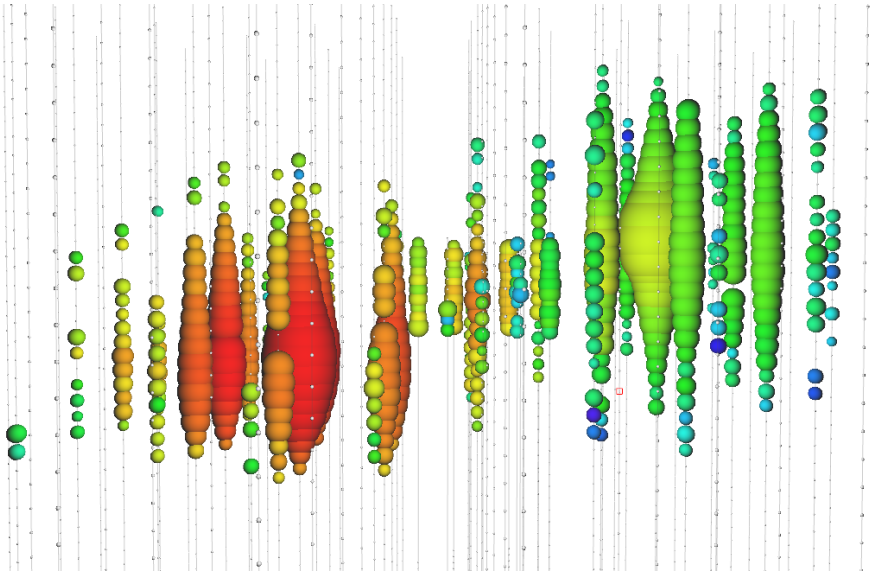

Figure 3.10: A simulation of a double-bang event in IceCube. Double-bang events occur when CC tau neutrino interactions occur above 1 PeV producing a τ lepton. When these high-energy τ leptons are produced, the τ leptons are able to travel over 50 m in IceCube before they decay. At these distances, the light emission from the decays are distinguishable from the light emission of the hadronic cascades from the initial tau neutrino interactions. The color of the DOMs represent the arrival times of the photons (red is early, green is late). The size of the DOM represents the amount of charge that is seen in the DOM. Figure taken from [16].

distance before scattering or being absorbed, emitting Cherenkov light as they move through the ice. Secondly, if a CC electron neutrino interaction occurs, the outgoing electron produces an electromagnetic cascade in addition to the hadronic cascade which cannot be distinguished from each other. Cherenkov light is emitted from the electron and the charged particles in the cascades. Another way a cascade event can be detected in IceCube is when a CC tau neutrino interaction occurs, and a tau lepton is produced. However, in this type of interaction, the signature will only appear to be cascade-like if the energy of the initial tau neutrino is $<$ 1 PeV. At these energies, the τ lepton decays quickly. Because of the spacing of the strings in IceCube, the Cherenkov light emitted in the initial interaction, during the travel of the τ lepton, and in the decay of the τ lepton are indistinguishable. The spacing of the strings and the scattering of light in the ice are why all of these interactions produce more spherically-symmetric events. The particles that emit Cherenkov light in these interactions are unable to travel far before scattering or decaying, and their emitted

light looks spherical in return. Because cascade events are rather spherical, cascade events have poor angular resolution, even at high energies. Their median angular resolution is $\sim 15^{\circ}$ [97].

The third type of event that IceCube has the ability to detect is a double-bang event, which can be seen in Figure 3.10 (though IceCube has yet to actually see this type of event in the detector). For this type of event, a tau neutrino with an energy > 1 PeV interacts in the detector and produces a τ lepton and a hadronic cascade. At these energies, the τ lepton would be able to travel more than 50 m before decaying [20], allowing the decay of the τ lepton to be differentiated from the initial neutrino interaction, resulting in two cascade events. This creates the double-bang signature in IceCube.

The energy resolution of events depends on how much energy is deposited into the detector rather than outside of the detector. Due to the spherical nature of cascade events, most, if not all, of the energy is deposited inside the detector. The energy of the event is directly proportional to the amount of light deposited into the detector, so these types of events have good energy resolutions down to ~15%. For track events, it becomes more complicated. Sometimes, tracks can be fully contained in the detector. However, for higher-energy muons, at least part of the track is outside of the detector. Because of this, the measured energy of a track is only a lower limit on the energy of the original neutrino, resulting in an energy resolution around ~30%.

3.5 Track Event Reconstruction

The IceCube events that are used in the analysis in this thesis are tracks. As discussed in the previous section, tracks are created from muons that travel through the ice that are detected by IceCube. Muons produced in high-energy neutrino interactions often travel lengths greater than the size of the IceCube detector, therefore only leaving a small amount of their energy in the detector, hampering their muon energy resolution. However, due to their track-like nature, their angular resolution is $< 0.5^{\circ}$, as compared to teh resolution of cascade-like events, which is $\sim 15^{\circ}$.

IceCube utilizes several different reconstruction algorithms for both the direction and the energy of the observed events. Directional reconstruction is especially important in discerning where

neutrinos are originating from and if there are any locations in the sky where the neutrinos are concentrated. Energy reconstruction is essential to determine the energy spectra of the incoming neutrinos. Energy signatures can be used to help determine whether the neutrino is of astrophysical or atmospheric origin. Therefore, reconstruction of these events is of vital importance.

3.5.1 Direction Reconstruction

The first step in IceCube's directional reconstruction of muon tracks is a "quick, first-guess" algorithm called LineFit [98]. LineFit does not take into account any information of the geometry of Cherenkov light emissions. It instead models the motion of the muon through the ice as a plane wave. In the beginning of IceCube data-taking, this algorithm simply found the best possible line through all the hit DOMs by doing a least squares minimum:

$$\mathcal{H} = \min\left(\sum_{i=1}^{N} |\vec{x}_i - (\vec{x}_0 + \vec{v}t_i)|^2\right), \tag{3.1}$$

where N is the total number of hit DOMs, $\vec{x}_0$ is the starting point of the track, $\vec{v}$ is the velocity of the particle, and $\vec{x}_i$ and t_i are the position and time of the i-th hit. It was shown that noise in the detector that was far away from the DOMs hit by a physics event affected LineFit's performance significantly [7]. Since then, an improved version of LineFit employs a cut on location and timing of hit DOMs to exclude noise hits, as well as utilizing the Huber penalty function to be less sensitive to noise in the detector [99]. LineFit's improved minimization of the least squares is

$$\mathcal{H} = \min\left(\sum_{i=1}^{N} \phi(|\vec{x}_i - (\vec{x}_0 + \vec{v}t_i)|)\right), \tag{3.2}$$

where $\phi(\rho)$ is the Huber penalty function defined as

$$\phi(\rho) = \begin{cases} \rho^2 & \text{if } \rho < \mu \\ \mu(2\rho - \mu) & \text{if } \rho \geq \mu \end{cases} \tag{3.3}$$

The objective of the Huber penalty function is to reduce the effects of outliers in the data. If a hit DOM is close to the track, it is more than likely a result from a physics event. If a hit DOM is far

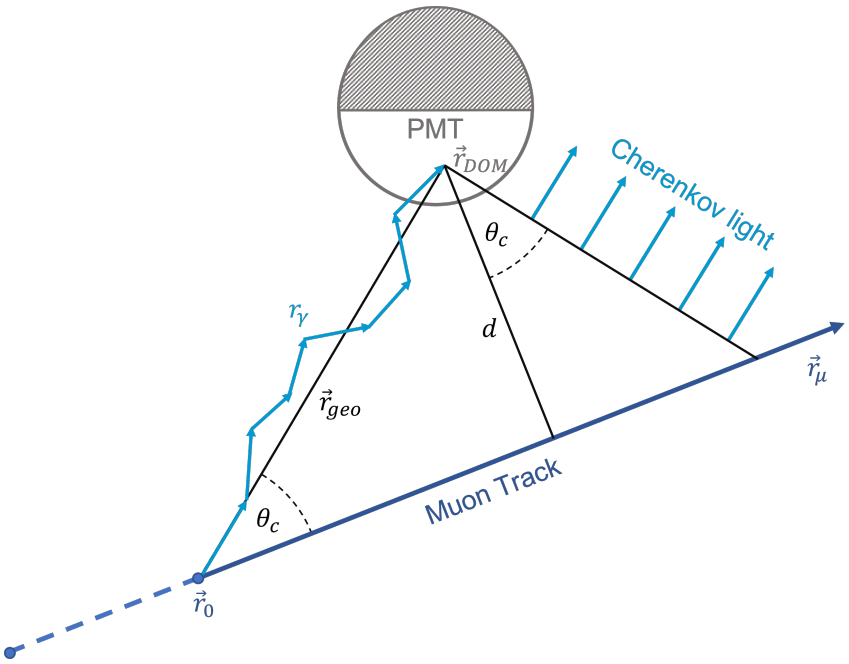

Figure 3.11: A diagram of a muon track and its associated Cherenkov light close to a DOM at position $\vec{r}_{DOM}$. The muon track begins at $\vec{r}_0$ with a direction $\vec{r}_\mu$. Cherenkov light is emitted at an angle of θ_c. When the muon is produced, the most direct path for Cherenkov light to travel to the DOM is $\vec{r}_{\text{geo}}$. The actual path traveled by the Cherenkov light is $\vec{r}_\gamma$ because the photon scatters as it moves through the ice. Finally, the closest distance the muon approaches a DOM is distance d. Figure adapted from [17].

from the track, it is more likely a result of noise. The cutoff distance, μ, has been optimized to be 153 m from the track. LineFit is able to achieve angular resolutions down to around 4° [99]. The results of LineFit are used to seed more sophisticated, likelihood-based algorithms.

The likelihood-based algorithms that IceCube utilizes to reconstruct the direction of muons are the single photoelectron (SPE) and multi photoelectron (MPE) reconstruction models. Both algorithms model muons as particles traveling through ice at the speed of light ($\beta = 1$), emitting Cherenkov light as they move through the ice. The geometry of a muon track and its emitted Cherenkov light can be seen in Figure 3.11. The muon track begins at $\vec{r}_0$ with a direction $\vec{r}_\mu$. The Cherenkov light, emitted at an angle of θ_c, scatters as it travels through the ice. Its resulting path and arrival time is $\vec{r}_\gamma$ and t_γ. If the Cherenkov photons followed the ideal path to the DOM, its path and arrival time would be $\vec{r}_{\text{geo}}$ and t_{geo}. The closest distance the track approaches a DOM is

distance d. And finally, the location of the DOM is $\vec{r}_{\mathrm{DOM}}$.

Since the photons do not take the ideal path to the DOM, the time residual can be defined as the difference in the observed arrival time of the photon and the expected time of the photon if the photon had taken the most direct route, $t_{\mathrm{res}} = t_\gamma - t_{\mathrm{geo}}$. The geometric time, t_{geo}, can be calculated based on the geometry of the track and Cherenkov light, seen in Figure 3.11. SPE determines the likelihood of observing the residual time of each of the recorded hits and can be defined for a single DOM as [98]:

$$\mathcal{L}_{\mathrm{DOM}}(\vec{r}_0, t_0, \theta, \phi) = \sum_{i=1}^{N} p(t_{\mathrm{res},i}|\vec{r}_0, t_0, \theta, \phi), \tag{3.4}$$

where N is the number of hits and p is the probability of observing a photon with a time residual $t_{\mathrm{res},i}$ given the muon track parameters of $\vec{r}_0, t_0, \theta$, and ϕ. Typically, the first photon has the smallest time residual, and therefore, the most constraining [9]. However, since only the time of the first photon is used, it has to be accounted for the fact that it is the first photon out of N photons. Thus, the MPE likelihood for a single DOM is defined as the likelihood to observe the first out of N photons [98]:

$$\mathcal{L}_{\mathrm{DOM}}(\vec{r}_0, t_0, \theta, \phi) = N p(t_{\mathrm{res},1}|\vec{r}_0, t_0, \theta, \phi) \left(\int_{t_{\mathrm{res}'}}^{N} dt_{\mathrm{res}'} p(t_{\mathrm{res}'}|\vec{r}_0, t_0, \theta, \phi) \right)^{N-1} \tag{3.5}$$

Both the SPE and MPE likelihoods have been defined in terms of the likelihood of the data recorded by a single DOM. To get the total likelihood over all DOMs, the product of the single-DOM likelihoods is taken over all DOMs:

$$\mathcal{L}(\vec{r}_0, t_0, \theta, \phi) = \prod_k \mathcal{L}_{\mathrm{DOM}_k}(\vec{r}_0, t_0, \theta, \phi). \tag{3.6}$$

To obtain the best-fit direction of the muon track, the negative logarithm of the likelihood, $-\log \mathcal{L}(\vec{r}_0, t_0, \theta, \phi)$, is minimized.

Finally, an estimate on the angular error based on the reconstructed direction of the event must be determined. The likelihood space around its minimum (which is used to determine the best-fit direction) is approximately parabolic in shape. The likelihood space is evaluated in 24 different (θ, ϕ) locations around the best-fit direction [18]. From a paraboloid fit, a 1σ angular error is

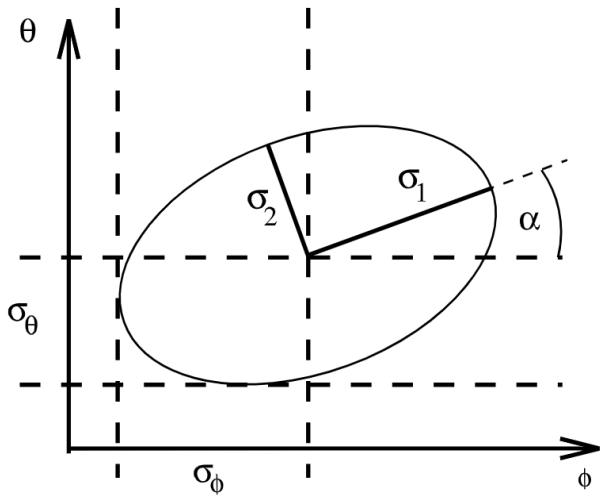

Figure 3.12: The paraboloid fit can be expressed as the major and minor axes of the paraboloid, σ_1 and σ_2, and the rotation angle, α. Figure from [18].

calculated [18]. An example of a paraboloid can be seen in Figure 3.12. The paraboloid fit can be defined as the major and minor axes of the paraboloid, σ_1 and σ_2, as well as the rotation angle, α. The final angular error used for analyses is $\sigma_{\text{paraboloid}}$, which is defined as:

$$\sigma_{\text{paraboloid}} = \sqrt{\frac{\sigma_1^2 + \sigma_2^2}{2}}. \tag{3.7}$$

3.5.2 Energy Reconstruction

For high-energy muons, energy reconstruction is difficult because only part of the track is inside the detector. At 1 TeV, a muon can travel approximately 2 km [86]. Most muons that IceCube observes travel past of the bounds of the instrumented ice. In addition, a muon could have traveled far in the ice before reaching the detector, losing most of its energy by that time. Therefore, the energy of the muon seen in the detector acts as a lower limit for the true neutrino energy. For cascades, IceCube selects events that are contained within the detector. Since cascade events are mostly contained within the detector, they deposit the bulk of their energy within the instrumented ice. While muon tracks have poor energy resolution, we can obtain an energy resolution for cascades down to ~15% [97].

The reconstruction algorithm used for the muon tracks in this analysis is called MuEX, and it is applied to the visible energy of the muon along its track [97]. MuEX splits the muon path into a series of cascades emitted along its path. Under the assumption that the event energy is directly proportional to the photon light yield, MuEX expects the number of detected photons to follow a Poisson distribution with a mean of:

$$\lambda = \Lambda E + \rho \tag{3.8}$$

where Λ is the number of photons per unit energy in the reconstruction, ρ is the expected number of noise photons, and λ is the mean number of photons for the track of energy E. The likelihood of detecting k photons from an event is:

$$\mathcal{L} = \frac{\lambda^k}{k!} e^{-\lambda} \tag{3.9}$$

In order to find the best-fit energy, the likelihood needs to be maximized. This is done by minimizing the logarithm of the likelihood, which is defined by:

$$\ln \mathcal{L} = k \ln (\Lambda E + \rho) - (\Lambda E + \rho) - \ln (k!) \tag{3.10}$$

The logarithm of the likelihood is then minimized with respect to the one free parameter, E.

Several approximations go into the estimation of λ to increase computational speed, such as spherical symmetry of cascade light emission along the track and uniform emission of Cherenkov light [97]. To better account for statistical uncertainties of λ, the likelihood is convolved with a probability distribution, G, on the mean light yield λ, giving the modified likelihood as:

$$\mathcal{L} = \prod_j \int_0^\infty d\lambda_i \; G(\lambda_i, \lambda_j) \; \frac{\lambda_i^{k_i}}{k_i!} e^{-\lambda_i} \tag{3.11}$$

where the probability distribution, $G(\lambda_i, \lambda_j)$, can be found in [97]. The final energy resolution ranges from 30-35% depending on the muon's energy. Energy resolution tends to improve as the muon energy increases [97].

3.6 Antarctic Ice Properties

The ability to detect Cherenkov light from secondary particles of neutrino interactions is highly dependent on the detector medium and its optical properties. Due to IceCube's sheer size of a

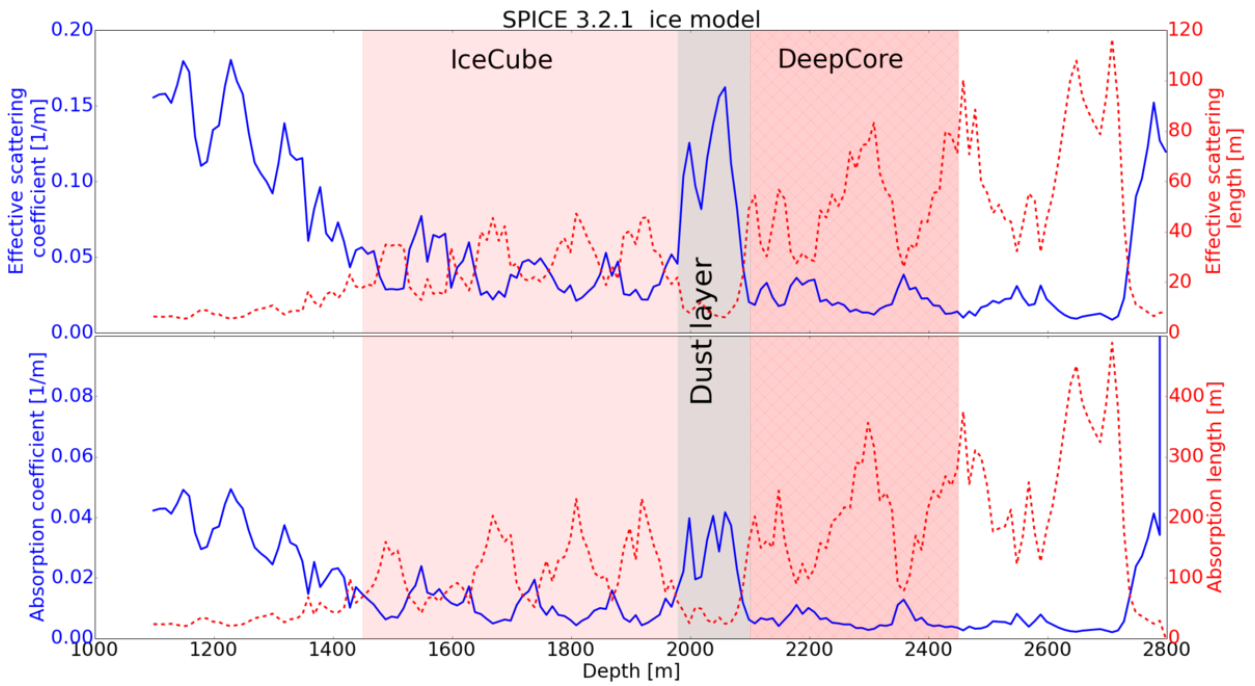

Figure 3.13: The scattering (top) and absorption (bottom) coefficients (solid blue) and lengths (dashed red) for the SPICE 3.2.1 ice model at different depths. The areas of IceCube and DeepCore are shaded red, with DeepCore hatched as well as shaded. A region of high absorption and scattering exists from ~2000 m to ~2100 m, which is called the dust layer. Figure from [19].

cubic kilometer, a laboratory environment for the detector is impossible, and therefore, a natural medium is needed. The Antarctic ice sheet is one of the purest materials on the planet, which is why IceCube instrumented the Antarctic ice for the detector.

Even though the ice is extremely clear, it is not completely free of impurities. The Antarctic ice sheet has evolved by the accumulation of snow that has gradually been compressed over thousands of years. Over the years, weather conditions or environmental influences greatly affected the purity of the snow. Thus, the properties of the ice are expected to change according to the depth which reveals the age of the ice as well as the weather conditions or environmental influences during those times [100]. The age of the ice in the detector ranges from around 40,000 years at a depth of 1500 m to around 100,000 years at a depth of 2500 m [101]. Different types of impurities include mineral grains, volcanic ash, salts, acids and soot [101]. Because of these impurities, an in-depth characterization of the ice is important to perform physics analyses.

Two important parameters to use for describing the optical properties of the ice are the absorption (λ_a) and scattering (λ_s) lengths of photons. Photons can be absorbed in the ice, reducing the number of photons detected at DOMs. This directly affects the energy resolution of events, since the number of observed photons is less than the number of emitted photons. Photons can also be scattered, changing the photon's direction and increasing its path length to a DOM. Scattering directly affects the direction reconstruction of an event due to the altered path of a photon when it scatters. The energy and direction reconstruction algorithms need to account for these effects correctly, so scattering and absorption lengths must be measured in the ice.

Scattering and absorption can be measured using the LED flashers mounted in each DOM. Photons are emitted from LED flashers in DOMs and recorded by other DOMs in terms of total charge and arrival times. This is done throughout the entire detector and a global fit for the ice parameters can be obtained. The scattering and absorption lengths/coefficients of the South Pole ice model used in this analysis (also called SPICE 3.2.1) can be seen in Figure 3.13. Scattering and absorption effects are greatest near the surface, where layers of snow are still being compacted. Because of this, there are many air bubbles in the layers near the surface. These air bubbles become air hydrate crystal structures once compressed enough at the depths that IceCube has instrumented [102]. Another region of high scattering and absorption ranges from ~2000 m to ~2100 m. This region is called the dust layer, and corresponds to one of the last colder-than-average glacial periods [103]. When a glacial period is colder than average, it tends to be dryer and windier, resulting in more impurities in the atmosphere [103].

The scattering and absorption lengths depend not only on depths, but also the horizontal position. This is because the ice layers are tilted due to the flow of the glacier over the underlying bedrock [101]. In addition, the Antarctic ice sheet is constantly sliding downhill at a rate of around ten meters per year. This introduces an azimuthal anisotropy of the ice properties because light prefers to travel with the flow of ice, believed to be caused by alignment of ice crystal grains with the direction of flow [104]. Further studies of the ice anisotropy from additional causes are currently underway, and have been documented in [103].

CHAPTER 4

SEARCH FOR EXTENDED SOURCES OF GALACTIC ASTROPHYSICAL NEUTRINOS WITH THE ICECUBE NEUTRINO OBSERVATORY

4.1 Motivation

Many extended sources along the Galactic plane have already been discovered in the gamma-ray sky with imaging air-Cherekov telescopes (such as the High Energy Stereoscopic System, or H.E.S.S. [105]) as well as water Cherenkov air shower detectors (such as the High-Altitude Water Cherenkov Gamma Ray Observatory, or HAWC [106]). An example is the third HAWC catalog of very-high-energy gamma-ray sources, where several sources are shown to have extensions up to 1° [22]. If these gamma rays are produced by cosmic-ray interactions, neutrinos should be associated with these sources as well. Observing neutrinos from these regions would be undeniable evidence of a source of cosmic rays, as only cosmic rays produce neutrinos in hadronic interactions. While it is true that most gamma-ray sources will appear to be point-like to IceCube due to IceCube's angular resolution of around 1° at 1 TeV, the analysis in this chapter focuses not just on individual sources, but also on regions of extended emission in the Galactic plane. Regions of extended emission can stretch well above a few degrees. Examples include star-formation regions such as the Cygnus cocoon [107] or the Geminga region [108], as well as cosmic rays interacting with large structures such as molecular clouds, etc.

Further motivation for a specialized search for extended neutrino sources can be seen in Figure 4.1. This plot shows IceCube's sensitivity to hypothetical extended neutrino sources if an analysis was performed using the standard point source methods used in IceCube versus a dedicated extended source search. It can be seen that as the extension of the hypothetical source increases, performing a search devoted to extended sources achieves the best sensitivity. A traditional point source search could miss the discovery of an extended neutrino source. In this chapter, a search for Galactic, extended sources of astrophysical neutrinos is discussed. The search aims to

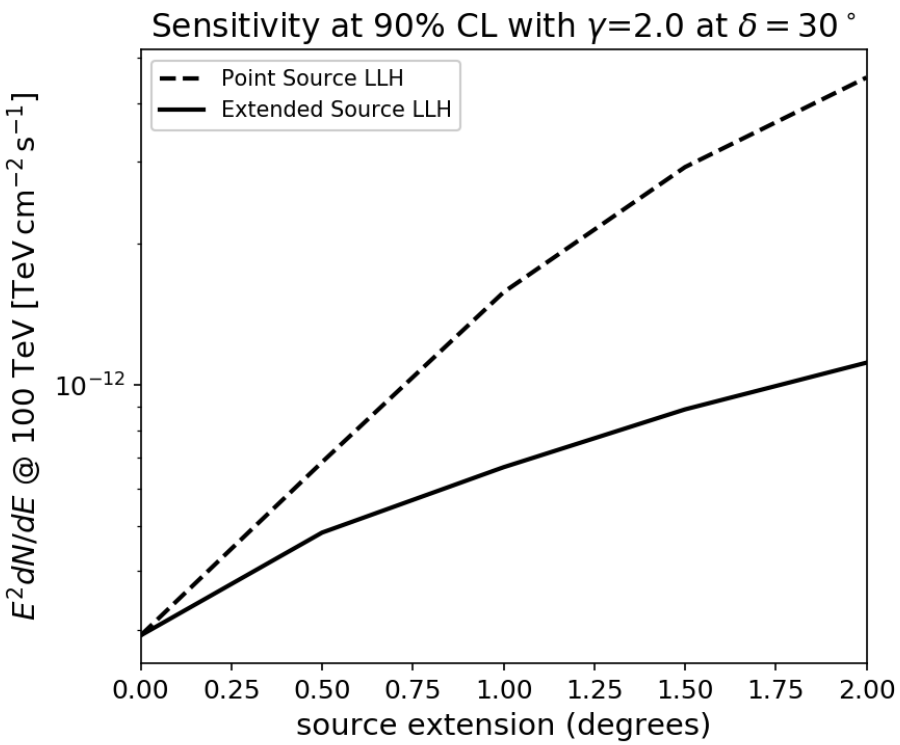

Figure 4.1: Sensitivity from an extended source with a spectral index of 2.0 at a declination of 30°. The sensitivity with the normal point source analysis (dashed line) is compared to the sensitivity with a dedicated extended source analysis (solid line).

be as model-independent as possible, not using underlying assumptions about the sources, such as their detailed morphology and spectra as observed in gamma rays [109]. A blind scan across the Galactic plane is performed, as well as a search for extended sources from a priori locations.

4.2 IceCube Point Source Samples

Since IceCube started taking data in 2007, there have been many different types of data samples produced. Data samples are constructed for specific types of analyses in IceCube. For analyses searching for sources of neutrinos, events with the best angular resolution are needed, in order to point back where the particles originate. As discussed in Section 3, muon neutrinos that create track-like events in IceCube have the best angular resolution. These track events created from muons traveling through the ice make up the IceCube Point Source (PS) sample.

In order to build a data sample, events that are seen in IceCube have to pass through several different criteria. IceCube has two different regions of background that are considered: the northern and the southern sky. With IceCube situated at the South Pole, events that come from the direction of the northern sky appear to be going up through the detector, as seen in Figure 4.2. These events are called up-going events. When cosmic rays interact in the atmosphere in the region of the northern sky, atmospheric muons and neutrinos are produced. Due to the Earth shielding IceCube from the northern sky, atmospheric muons are unable to reach the detector before decaying or interacting. However, the atmospheric neutrinos that are produced can interact inside the Earth or the detector and produce an up-going muon. These up-going muons produced from atmospheric neutrino interactions are considered the dominant background for the northern sky. The southern sky contains down-going events, which appear to descend through the detector. This region of the sky does not have the Earth to shield the detector from cosmic-ray interactions in the atmosphere. The detector is affected by both atmospheric muons and atmospheric neutrinos. However, atmospheric muons appear in the detector 10^5 times more than atmospheric neutrinos, making atmospheric muons the dominant background in the southern sky.

The boundary between the two regions lies at a declination of $\delta = -5^\circ$. Due to IceCube's location 1.5 km deep in the Antarctic ice, any events that are near the horizon have to pass through a significant amount of ice before arriving at the detector. This ice acts as a shield for the detector, moving the boundary between the northern and southern sky to $\delta = -5^\circ$ instead of the horizon. Therefore, the northern sky spans declinations in the range of $-5^\circ \leq \delta \leq 90^\circ$ and the southern sky ranges from $-90^\circ \leq \delta \leq -5^\circ$.

The atmospheric muons and neutrinos are irreducible backgrounds for the PS data sample. Several different cuts are applied in order to reduce the background as much as possible. Data samples are developed for astrophysical neutrino sources with an energy spectrum of E^{-2} base on the expectations for Fermi acceleration. The primary cosmic-ray spectrum in the energy range of several GeV to beyond 100 TeV has an energy spectrum of $E^{-2.7}$ [3]. For the northern sky, atmospheric neutrinos are expected at a rate of $\sim$ mHz and a softer energy spectrum of around

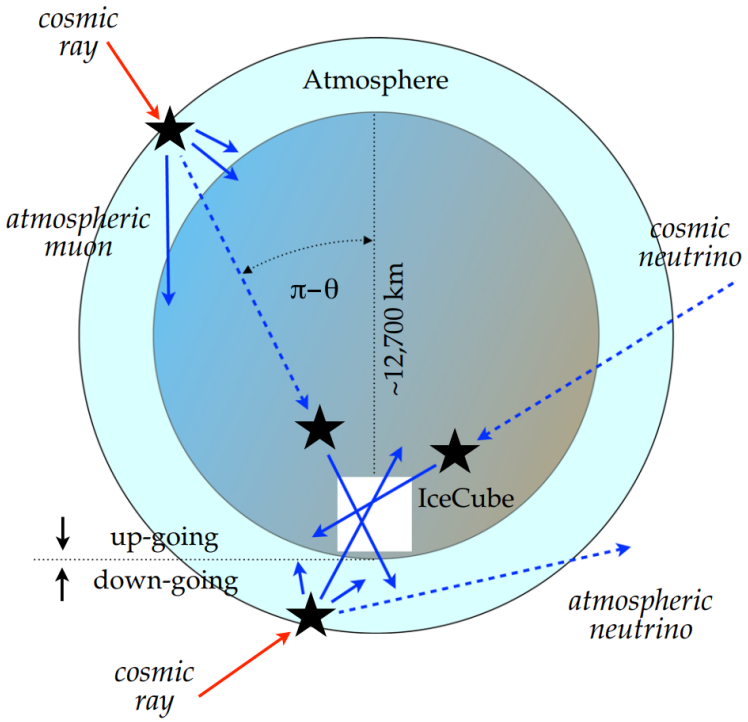

Figure 4.2: A visual representation of the different types of background IceCube is subjected to while observing astrophysical neutrinos. Cosmic rays interact in the atmosphere, producing atmospheric muons and neutrinos. In the northern sky (or up-going region), the Earth shields the detector from atmospheric muons, so atmospheric neutrinos are the dominant background. In the southern sky (or down-going region), the Earth no longer shields the detector, so atmospheric muons are the dominant background. Figure taken from [20].

$E^{-3.7}$ [110]. Energy cuts are applied to select higher energy events for the up-going northern sky sample. The southern sky is more complicated due to the increased background of atmospheric muons. Single atmospheric muons in the down-going region look identical to muons produced by astrophysical neutrino interactions in the ice. The energy spectrum of atmospheric muons are a power steeper than the primary cosmic-ray spectrum, so energy cuts are applied in the down-going southern sky sample. However, several muons can be produced in a cosmic-ray interaction in the atmosphere called a muon bundle. Atmospheric muon bundles can carry the energy signature of a single, high-energy muon produced from an astrophysical neutrino interaction in IceCube. However, the patterns in which that energy is distributed in IceCube differs between a single, high-energy muon and a muon bundle. Therefore, quality cuts are made using the output of a multivariate

machine learning technique called a Boosted Decision Tree (BDT). BDTs are trained to separate signal from background for both the northern and the southern sky with expected neutrino sources typically set to E^{-2} or $E^{-2.7}$. Since most of the events that IceCube observes are background, IceCube data is used to characterize the background.

4.2.1 Monte Carlo Simulation

To perform an analysis with an IceCube data set, IceCube's detector response needs to be understood. Several different simulation tools have been created in order to have detailed simulations of events that are prepared using physics processes and detector characteristics, including Antarctic ice and detector properties and calibration techniques. IceCube's background consists primarily of atmospheric muons and neutrinos. Atmospheric neutrinos can either be up-going or down-going. However, since only neutrinos are able to pass through the Earth and still reach the detector, atmospheric muons only need to be simulated in the down-going region.

The simulation of up-going and down-going neutrinos are handled by the IceCube internal neutrino generator software called NuGen, which is based on the All Neutrino Interaction Generator (ANIS) [81]. It simulates the propagation of a neutrino through the Earth (sampling the neutrinos from a power law spectrum with a given spectral index γ), interactions inside the Earth (if the neutrino does interact), and secondary particles from interactions. If a neutrino reaches IceCube's detector volume, NuGen forces an interaction to occur and the event is assigned a weight based on the probability of interaction. Three different types of processes are able to occur in NuGen: charged current interaction, neutral current interaction, and Glashow resonance interactions. In the case that neutrinos are produced as secondaries in these interactions, those neutrinos are also propagated. Finally, information about the neutrino and its secondaries (if an interaction occurred) are stored. For simulation of down-going atmospheric muons, the muons are generated with CORSIKA (**Co**smic **R**ay **Si**mulations for **KA**scade) which simulates particle production in cosmic-ray air showers and information from the resulting high-energy muons are stored [111].

The simulation code called PROPOSAL (**Pr**opagator with **O**ptimal **P**recision and **O**ptimized

Speed for **A**ll **L**eptons) is used to propagate those secondary particles through ice [10]. PROPOSAL simulates energy losses from processes such as ionization, pair production, and decay. Simulations of these energy losses produce expected photon yields, and photons are then propagated using another IceCube internal software called CLSim [112]. Finally, propagated photons reach a DOM, the DOM response is simulated, and the outputs of the simulation are stored.

4.2.2 Event Sample Characteristics

The PS sample has undergone several iterations since the first point source analysis that used the initial 22 strings that were deployed into the Antarctic ice in 2006-2007 [113]. Each year, IceCube collects more data to be added to the PS sample. Additionally, reconstruction of the event energy and direction has improved. With the number of events growing and reconstruction techniques refined throughout the years, IceCube has achieved improved sensitivity to neutrino sources since the first published results. Since IceCube began taking data before the detector was fully completed, data sets are labeled as "IC##", where "##" is the number of strings that were complete for that year of data-taking. For the first published results with the PS sample that used 22 IceCube strings, the data set was labeled "IC22".

Name	Events	Livetime (days)	Start	End	Reference
IC40	36900	376.4	2008-04-06	2009-05-20	[114]
IC59	107011	353.6	2009-05-20	2010-05-31	[115]
IC79	93133	316.0	2010-06-01	2011-05-13	[116]
IC86_2011	136244	333.0	2011-05-13	2012-05-15	[117]
IC86_2012_2014	338590	1058.3	2012-04-26	2015-05-18	[118]
IC86v4	1133364	3184.2	2011-05-13	2020-05-29	[1]

Table 4.1: Point Source data sample properties, including the number of events, the livetime, the start and end dates, and the associated references. The 7-year PS data sample is the top grouping of data sets (IC40, IC59, IC79, IC86_2011, and IC86_2012_2014). The final IC86v4 data set is part of the current 12-year PS data sample. The current 12-year PS data sample has no official publication, but has the same cuts and processing as the data in [1], just with an additional two years of data.

This analysis used two different iterations of the PS sample: the 7-year sample and a sample

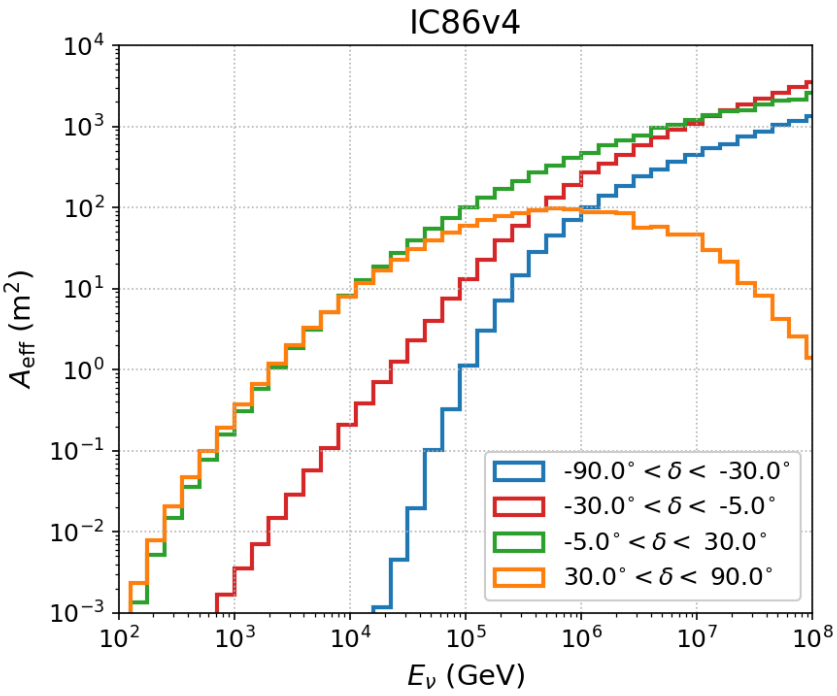

Figure 4.3: Effective area versus neutrino energy for a flux of $\nu_\mu + \bar{\nu}_\mu$ for the IC86v4 data set for different regions of the sky: down-going region of $-90^\circ < \delta < -30^\circ$ (blue), down-going region of $-30^\circ < \delta < -5^\circ$ (red), up-going region of $-5^\circ < \delta < 30^\circ$ (green), up-going region of $30^\circ < \delta < 90^\circ$ (orange).

consisting of the most recent nine years of data. For the 7-year sample, there were five subsets of data named IC40, IC59, IC79, IC86_2011, and IC86_2012_2014. The details of the 7-year data sample can be seen in the first grouping of Table 4.1. The 7-year data sample was used purely for testing with signal subtraction, which will be discussed in Section 4.4. For the actual data analysis, the most recent PS sample is used, which contains four subsets of data named IC40, IC59, IC79, and IC86v4. Given the added computational complexity of running an analysis over multiple subsets of data, and that the first three years of data contribute only 10-20% to IceCube's sensitivity, only the IC86v4 subset is used in this analysis. IC86v4 includes data using the full detector configuration for nine years. The details of the IC86v4 data set can be seen the last grouping in Table 4.1.

An important parameter to consider for IceCube data samples is their effective area. The effective area of a data sample is related to the number of observed neutrinos and the neutrino flux

by

$$N_\nu = T \int dE_\nu \int d\Omega \; A_{\text{eff}} \left(E_\nu, \Omega\right) \frac{d\Phi_\nu}{dE_\nu} \tag{4.1}$$

where N_ν is the number of observed neutrinos, T is the livetime of the data set, $d\Phi_\nu/dE_\nu$ is the differential neutrino and anti-neutrino flux, and A_{eff} is the effective area. The effective area of the IC86v4 data set is shown in Figure 4.3 and is split into up-going (green and orange) and down-going (blue and red) regions. For the down-going regions (the southern sky), the effective area is reduced for lower energies due to the dominant atmospheric muon background. Harsher energy cuts are applied to the down-going region because of this background. For the up-going region (the northern sky), especially when events become near vertical through the detector, the effective area is also lowered for higher-energy neutrinos due to the Earth's absorption of high-energy neutrinos. The overall trend of effective area increasing as the neutrino energy increases is due to the larger neutrino cross section and muon range at higher energies.

Another important quantity for data sets is angular resolution. The median angular resolution for the IC86v4 data sample can be seen in Figure 4.4. Both the energy dependence (top) and the declination dependence (bottom) of the angular resolution are shown. Angular resolution is defined as the angle between the reconstructed muon and the true neutrino directions for simulated neutrinos for a specific data set. The median angular resolution for IC86v4 is $< 1^\circ$ above 1 TeV neutrino energy in both the northern and southern sky. The angular resolution is better in the southern sky ($-1.00 \leq \sin\delta \leq -0.09$) as compared to the northern sky ($-0.09 \leq \sin\delta \leq 1.00$) due to the harsher energy cuts applied to the southern sky because of the dominant atmospheric muon background.

The last important quantity that is compared between data sets and analyses is the sensitivity. Sensitivity includes the effective area, angular resolution, livetime, event selection, etc. into one parameter to indicate IceCube's overall performance. Since sensitivity requires additional background knowledge, it will be discussed in Section 4.6.

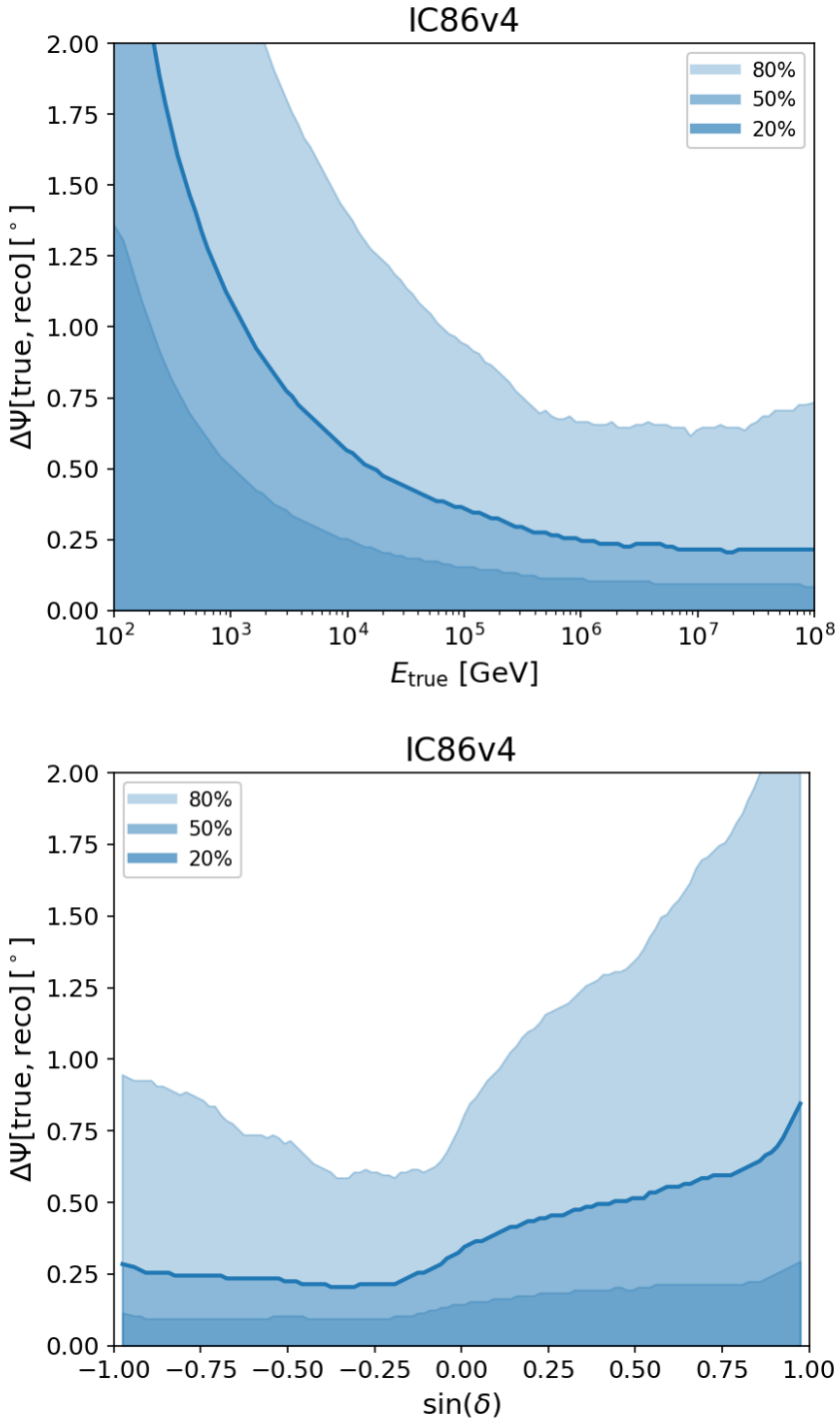

Figure 4.4: Angular resolution versus the true neutrino energy (top) and versus $\sin\delta$ of the true neutrino direction (bottom) for Monte Carlo simulation for the IC86v4 data sample. The median angular resolution is highlighted with the solid blue line, with the 20th, 50th, and 80th percentiles represented in the shaded regions.

4.3 Unbinned Maximum Likelihood Method

This analysis uses an unbinned maximum likelihood method with nine years of track data from IceCube. With the unbinned maximum likelihood method, the likelihood is formed by the product of the probability densities of each event in a data set. The likelihood can be defined as:

$$\mathcal{L}(n_s, \gamma) = \prod_{i=1}^{N} \left[\frac{n_s}{N} \mathcal{S}_i + \left(1 - \frac{n_s}{N}\right) \mathcal{B}_i \right] \tag{4.2}$$

where the fitted parameters are the number of signal events n_s and the spectral index γ. N is the number of total events in the data set, $\mathcal{S}_i$ is the signal probability distribution (PDF), and $\mathcal{B}_i$ is the background PDF. We expect signal and background to be both spatially and energetically different. Therefore, the signal and the background PDFs contain a spatial term and an energy term.

4.3.1 Signal PDF

The signal PDF can be split into the spatial part, S_i, and the energy part, ϵ_i as follows:

$$\mathcal{S}_i = S_i \left(|\vec{x}_i - \vec{x}_s|, \sigma_i, \sigma_s\right) \epsilon_i \left(\delta_i, E_i, \gamma\right) \tag{4.3}$$

where $\vec{x}_i = (\alpha_i, \delta_i)$ is the ith event direction in right ascension and declination, $\vec{x}_s = (\alpha_s, \delta_s)$ is the source location (location currently being evaluated) in right ascension and declination, $|\vec{x}_i - \vec{x}_s|$ is the angular difference between the event and the source, σ_i is the angular uncertainty of the ith event, and σ_s is the source extension.

The probability that the ith event came from an extended source at $\vec{x}_s$ is given by the spatial signal PDF, which is modeled by a 2D Gaussian:

$$S_i = \frac{1}{2\pi \left(\sigma_i^2 + \sigma_s^2\right)} \exp\left(-\frac{|\vec{x}_i - \vec{x}_s|^2}{2\left(\sigma_i^2 + \sigma_s^2\right)} \right) \tag{4.4}$$

With the 2D Gaussian representation, the source extension σ_s is defined as the standard deviation of the Gaussian. For this analysis, σ_s ranges from 0.5° to 2.0°. Many known extended gamma-ray sources have extensions close to 0.5°, with larger regions of emission extending above 2.0°. With

this analysis not only focusing on finding extended sources of neutrino emission but also on finding extended *regions* of neutrino emission, the extensions that are used for this analysis have to be larger to accommodate larger possible regions of emission.

The signal energy PDF, $\epsilon_i\left(\delta_i, E_i, \gamma\right)$ takes into account the event energy E_i and the source declination δ_i. It measures the probability of a muon of energy E_i originating from a source at declination δ_i that has a power law neutrino energy spectrum given by $E^{-\gamma}$. This includes the effects of muon range and energy loss before reaching the detector. For this analysis, γ ranges from 1 to 4. Models of Fermi acceleration depict power law energy spectra. Typical sources have a spectral index that ranges from 2 to 3. Power laws are also appropriate for narrow energy regions of sources with more complicated spectra.

4.3.2 Background PDF

Like the signal PDF, the background PDF is also split into a spatial part and an energy part as follows:

$$\mathcal{B}_i = B_i(\delta_i)\varepsilon_i(\delta_i, E_i) \tag{4.5}$$

where B_i and ε_i are the spatial and energy distributions of the IC86v4 data set that is being used for this analysis. Since this analysis is time-integrated over many years, the seasonal variations of atmospheric background are averaged out. Due to the unique location of IceCube at the South Pole, the background distributions only depend on declination. This can be seen in the visual representation of the celestial coordinate system in Figure 4.5. IceCube is situated directly under the South Celestial Pole. Due to the Earth's rotation around the axis of right ascension and IceCube's position on the axis of rotation, the background distribution is flat in right ascension if integrating over times $\gg 1$ day. At shorter time scales, the effect of the azimuthal asymmetry of the IceCube string layout on the background is non-negligible.

The spatial background probability density for the IC86v4 data set is shown in Figure 4.6. The energy probability density ratio can be seen in Figure 4.7. The energy probability density ratio is created by taking the ratio of the signal Monte Carlo energy PDF and the background

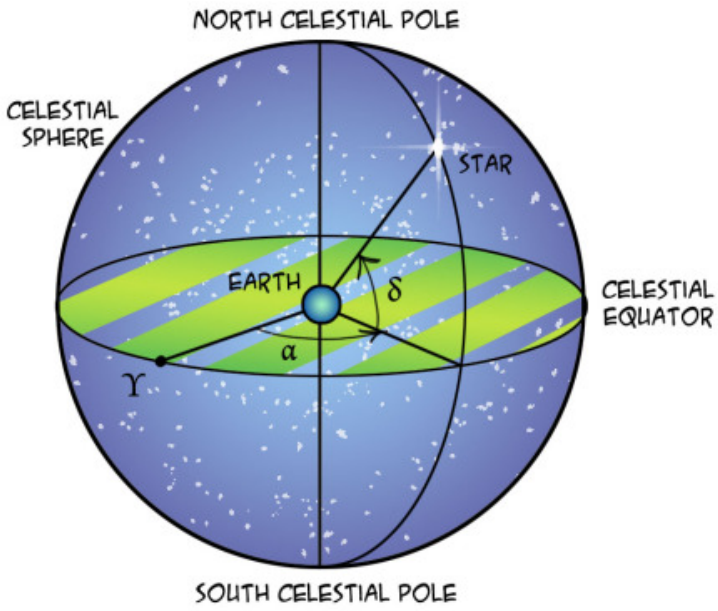

Figure 4.5: A visual representation of the celestial coordinate system. Right ascension is the angle measured along the celestial equator. Declination is the angle measured off of the celestial equator. Declination is positive in the northern hemisphere and negative in the southern hemisphere. Figure taken from [21].

energy PDF for some choice of flux. For Figure 4.7, the signal Monte Carlo was taken at an energy spectrum of E^{-2}. The southern hemisphere ranges from $-1.0 \leq \sin(\delta) \leq -0.09$ and is dominated by atmospheric muons from cosmic-ray air showers. The northern hemisphere ranges from $-0.09 \leq \sin(\delta) \leq 1.0$ and is dominated by atmospheric neutrinos from cosmic-ray air showers in the northern hemisphere. Due to the larger low-energy background in the southern sky, harsher energy cuts are applied to the southern sky to reduce the background of atmospheric muons. This is shown in the lower background probability density in the southern sky in Figure 4.6. The large jump near $\sin\delta = 0$ is the shift between the southern sky and the northern sky, which have different cuts due to their different dominant backgrounds. The harsh low-energy cuts in the southern sky can be seen in Figure 4.7, where the southern sky is concentrated in the higher energy bands.

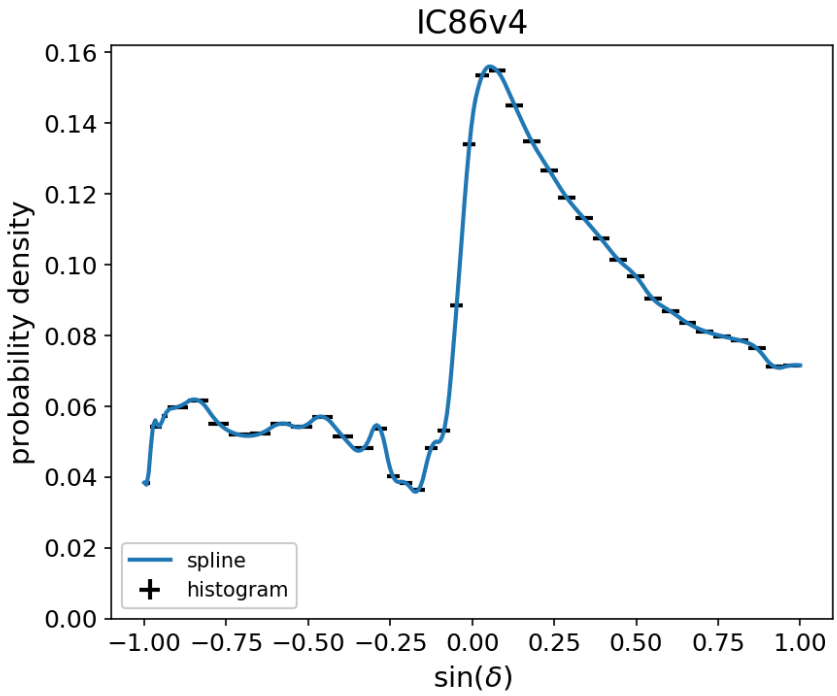

Figure 4.6: The background spatial probability density of the IC86v4 data set. Harsh cuts are applied to the southern sky ($-1.0 \leq \sin(\delta) \leq -0.09$) due to the large atmospheric muon background. This causes the low probability density in that region. The sharp jump near $\sin\delta = 0$ is the shift between the southern and the northern sky.

4.4 Signal Contamination and Source Masking

As discussed in Section 4.3, the background spatial and energy PDFs are created using the IC86v4 data set and randomizing the events in right ascension. While it is assumed that most of the data that IceCube collects is background from cosmic-ray air showers, there is a chance that some of the data come from astrophysical sources. This would be considered signal. Since all of the data is used in the creation of the background spatial and energy PDFs, this indicates there might be signal contaminating the background. Many past and current IceCube analyses use a method called signal subtraction to remove the signal contamination from the background. The analysis in this thesis utilizes a different method of removing signal contamination from the background called source masking.

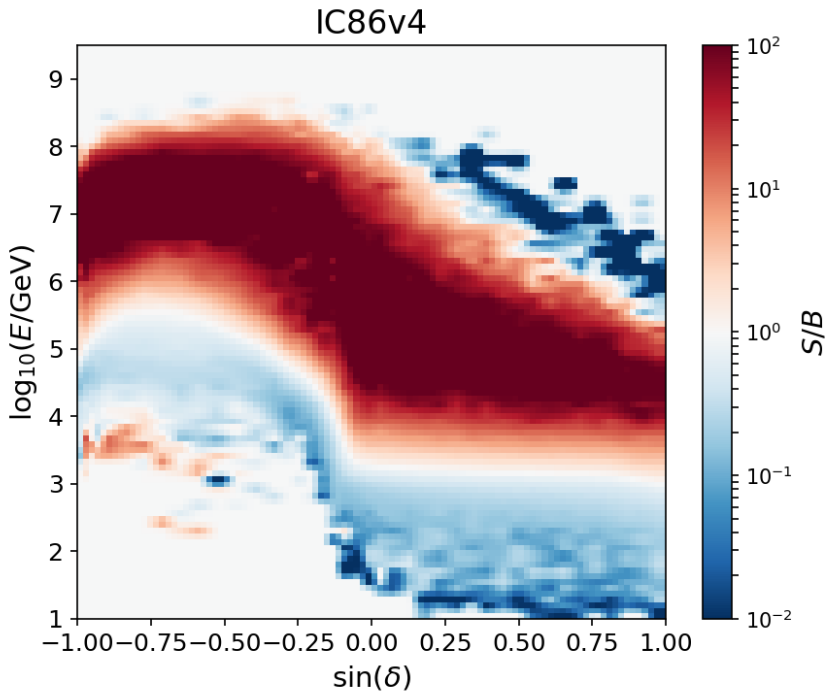

Figure 4.7: The energy probability density ratio of signal Monte Carlo at an energy spectrum of E^{-2} over the background distribution for the IC86v4 data set. Harsh low-energy cuts are applied to the southern sky ($-1.0 \leq \sin(\delta) \leq -0.09$) due to the large atmospheric muon background. This causes the low density of events in that region.

4.4.1 Signal Subtraction

The goal of signal subtraction is to correct for signal within the background PDF in the likelihood in Section 4.3. Ideally, we want $\mathcal{B}_i$ to be pure background. However, we calculate our background using scrambled data, so our likelihood actually contains the signal-contaminated, scrambled background, which is designated as $\tilde{\mathcal{D}}_i$. It can be be defined as:

$$\tilde{\mathcal{D}}_i = \frac{n_s}{N}\tilde{\mathcal{S}}_i + \left(1 - \frac{n_s}{N}\right)\mathcal{B}_i \tag{4.6}$$

where $\mathcal{B}_i$ is the pure background PDF with no signal contamination and $\tilde{\mathcal{S}}_i$ is the scrambled signal PDF which represents the contamination in the scrambled background $\tilde{\mathcal{D}}_i$. The scrambled signal PDF is essentially the projection of the standard signal PDF in declination. Since the standard signal PDF is given by a 2D normal distribution, the scrambled signal PDF is a normal distribution divided by the cosine of the declination.

Solving for $\mathcal{B}_i$ and substituting it into Equation 4.2, the signal-subtracted likelihood is as follows:

$$\mathcal{L}_{ss}\left(n_s, \gamma\right) = \prod_{i=1}^{N}\left[\frac{n_s}{N}\left(\mathcal{S}_i - \tilde{\mathcal{S}}_i\right) + \tilde{\mathcal{D}}_i\right] \tag{4.7}$$

Signal subtraction does correct for the fact that there might be signal contamination in the background PDF. However, a couple of problems emerge with implementing signal subtraction. Signal subtraction is only able to account for signal from one hypothetical source at the position that is being tested. This method is unable to account for multiple different possible sources at one time. In addition, running an analysis using signal subtraction has been proven to be more computationally expensive than running an analysis without it. Signal subtraction also introduces significant fit bias for both n_s and γ, which will be shown in Section 4.7. It is possible that the fit bias introduced when using signal subtraction is due to a bug in the IceCube source search software. This is currently being investigated.

4.4.2 Source Masking

An alternative to signal subtraction is to remove signal events from the data before calculating the background. This method is called source masking and is used in many gamma-ray astronomy analyses in the scientific community [119]. Implementing source masking involves removing events from a location in the sky, correcting the density of events in the sky due to removing events from a source location, and calculating the background PDFs with the updated data set. A major difference between source masking and signal subtraction is that source masking is able to remove signal from multiple different sources at once. Since there are possibly many different sources along the Galactic plane, source masking is ideal to use in this analysis.

An example of source masking is shown in Figure 4.8. The green dots in the figure represent events in that region of the sky and there is a source that is contributing an excess of events over the background rate. When the background PDFs are calculated, all events within a region are scrambled and parameterized. The excess of events in the source location will contribute to the background, resulting in an over-estimation of the background in that declination band. However,

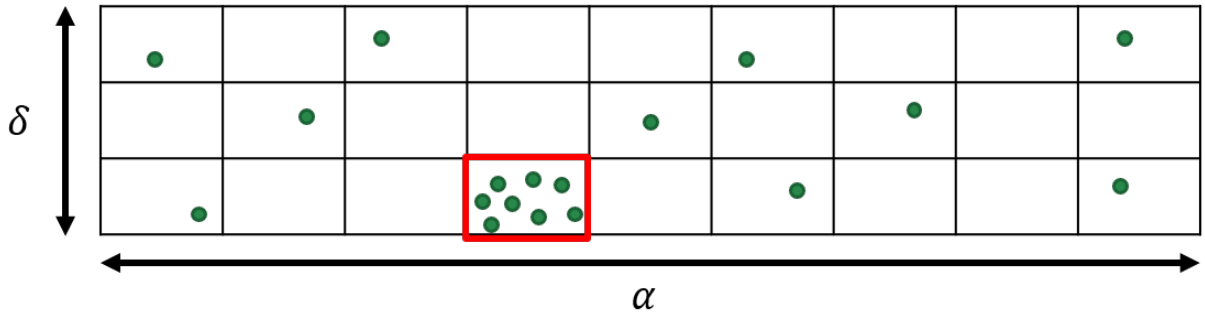

Figure 4.8: An example of the source masking method. The green dots are events in that region of the sky. The outlined red box represents a source that is contributing an excess of events in this region. Source masking removes these events, corrects for the density of the events due to removing the signal events, and then calculates the PDFs.

if the source location is masked before calculating the background PDFs and the overall density of background events is corrected, then the background in that region would not be over-estimated.

There is a balancing act required for source masking. For example, if the entire sky was masked for fear of any potential sources leaking into the background, there would be no events left to model the background behavior. The larger the masked region, the less data available to characterize the background, and the larger the statistical uncertainty of the background estimate. However, having larger statistical uncertainty is not as bad as the alternative of a biased background estimate. If the masked region is too small, it could allow signal events to leak into the background. If this is the case, the background is over-estimated in that region, which leads to decreased sensitivity. Within reason, it is always better to have a larger mask than to risk using a smaller mask with the end result of decreased sensitivity.

Since this analysis is searching for sources along the Galactic plane, the locations of any known or apparent neutrino sources (TXS 0506+056, NGC 1068) will be masked, as well as the Galactic plane (including diffuse emission) and other high energy gamma-ray sources that are associated with the Galaxy (within specified criteria). The mask described below does not cover every known Galactic source and does not explicitly include IceCube's PSF. Having too large of a mask will reduce sensitivity due to the increase in statistical uncertainty of the background estimate. We choose to remain conservative in defining the regions to be masked for this reason.

For the Galactic plane, results from multiple different experiments on Galactic diffuse emission as well as Galactic sources were taken into account.

- **High Energy Stereoscopic System (H.E.S.S.)**

  The High Energy Stereoscopic System (H.E.S.S.) is an air-Cherenkov telescope array in Namibia, South Africa that has observed Galactic diffuse gamma-ray emission at TeV energies in [54]. With their analysis, they measured the diffuse emission between Galactic latitudes of $|b| < 2^\circ$. For their background estimation, they masked out a region between $|b| < 1.2^\circ$ which was chosen to minimize contamination in the background estimate while maximizing statistics.

- **Milagro Gamma Ray Observatory**

  The Milagro Gamma Ray Observatory was a water-Cherenkov detector array in New Mexico that observed Galactic diffuse gamma-ray emission at TeV energies in [55]. They reported the spatial distribution of the Galactic diffuse emission between the latitudes of $|b| < 10^\circ$. For their background estimation, they masked out the region around the Crab Nebula as well as $|b| < 2.5^\circ$ around the plane. A mask of $|b| < 5^\circ$ around the plane was also tested, and resulted in flux variations of less than 7%.

- **High-Altitude Water Cherenkov (HAWC) Gamma Ray Observatory**

  The High-Altitude Water Cherenkov (HAWC) Gamma Ray Observatory is a water-Cherenkov detector array in Mexico that has observed both the Galactic diffuse emission at TeV energies [56] as well as Galactic gamma-ray sources [22]. HAWC's measured Galactic diffuse emission is seen between $|b| < 4^\circ$.

  The Galactic latitude of gamma-ray sources that HAWC has observed can be seen in Figure 4.9. Most of the sources that HAWC has observed are between $|b| < 5^\circ$. The two sources above $b > 20^\circ$ are extragalactic and will not be considered to determine the mask size around the Galactic plane.

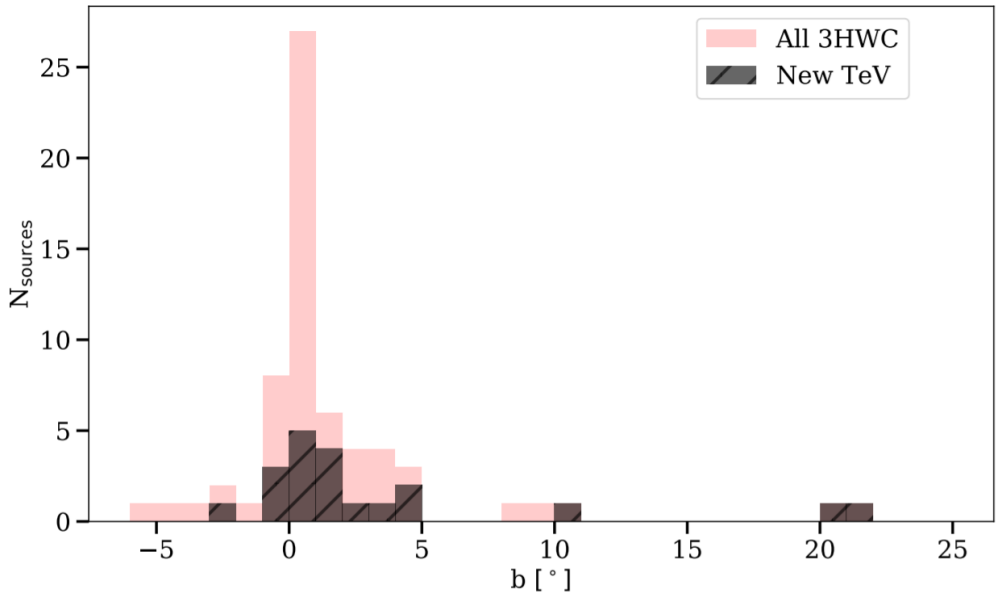

Figure 4.9: The Galactic latitudes of HAWC sources in the 3HWC source catalog [22]. The dark, shaded region represents the sources that are new and were not present in the 2HWC source catalog.

With the consideration of the Galactic diffuse emission measured by H.E.S.S., Milagro, and HAWC as well as the Galactic sources observed by HAWC, the mask size that will be used for this analysis is $|b| < 5°$. The Galactic diffuse emission is mostly contained within these bounds, and most Galactic sources can be accounted for within these latitudes.

To account for the sources that are not within $|b| < 5°$, a few sources will also have their location masked. Within the current HAWC catalog of sources in [22], there are four regions that stand out at higher Galactic latitudes than within $|b| < 5°$:

- **Crab Nebula (3HWC J0534+220)**

  Point-like source. To account for IceCube's median angular uncertainty for the IC86v4 data set, the mask radius will be set to 1.5°. 1.5° serves as the minimum mask size for point-like sources.

- **Geminga Region**

  Three sources (3HWC J0634+180, 3HWC J0631+169, 3HWC J0634+165) located on the border of the $|b| < 5°$ band. All three are point-like sources. However, with the cluster of

three different sources, the region will receive a mask radius of 5° to ensure coverage over all three sources. The location of the region will be defined as the position of 3HWC J0634+180.

- **3HWC J0621+382**

  Extended source with a radius of 0.5°. To ensure coverage and to account for angular uncertainty, the mask radius will be set to 2.0°.

- **Monogem pulsar (PSR B0656+14) region**

  Region has two 3HWC sources (3HWC J0702+147, 3HWC J0659+147). Both sources are point-like; however, due to PSR B0656+14 (also known as 2HWC J0700+143) having an extension of 1.0° [120], region will receive a mask radius of 3.0° to ensure coverage of the pulsar and two 3HWC sources and to account for angular uncertainty. The location of the region will be defined as the position of 3HWC J0702+147.

In addition, with IceCube's detection of neutrino emission from the direction of the **TXS 0506+056** blazar [64][65], the blazar's location will also be included in the mask with the point-like source mask radius of 1.5°. Finally, the last source that is included in the mask is **NGC 1068**, also known as M77. IceCube has reported the location of NGC 1068 as providing the most significant location in the Northern hemisphere [1]. Being a point-like source, NGC 1068 will have the point-like source mask radius of 1.5°. These six regions, along with their locations and the size of the mask around them, can be seen in Table 4.2.

Region	Right Ascension (°)	Declination (°)	Mask Radius (°)
Crab Nebula	83.63°	22.02°	1.5°
Geminga Region	98.75°	18.05°	5.0°
3HWC J0621+382	95.32°	38.21°	2.0°
Monogem Region	105.56°	14.75°	3.0°
NGC 1068	40.67°	0.013°	1.5°
TXS 0506+056	77.36°	5.69°	1.5°

Table 4.2: The location and mask size of the six regions that will be included in the mask along with the Galactic plane within $|b| < 5°$.

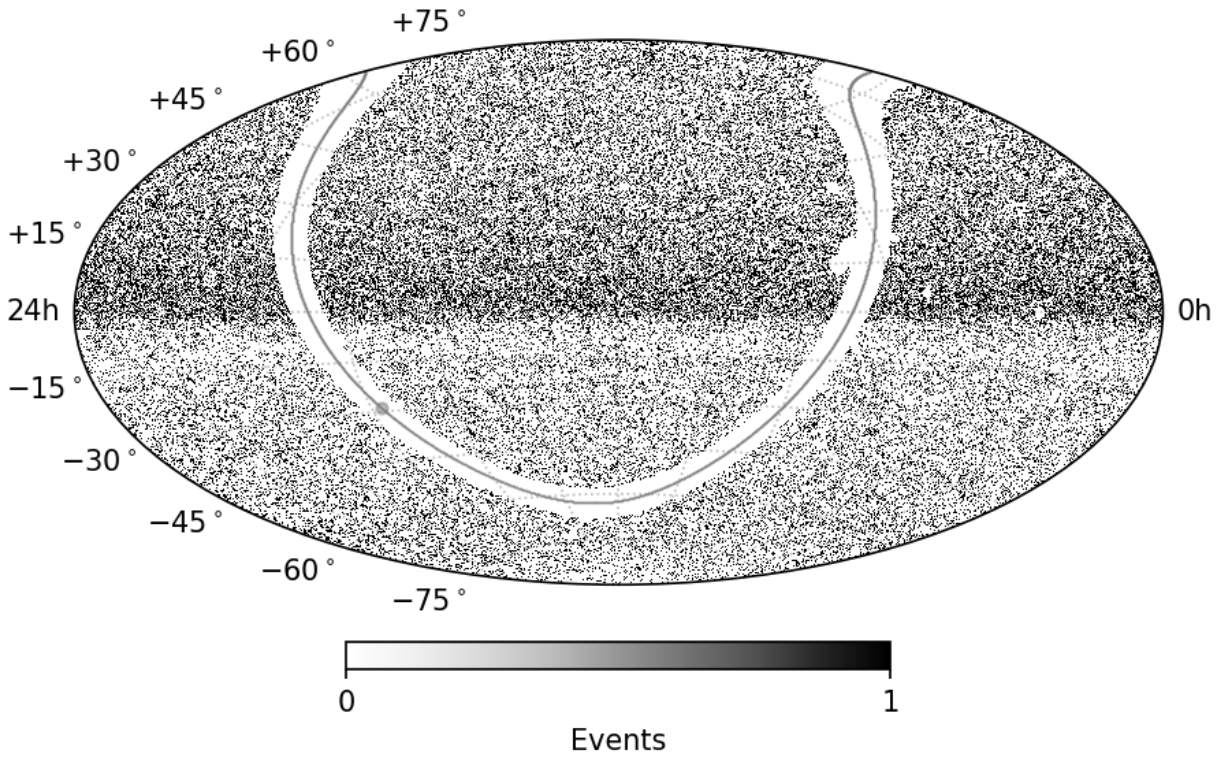

Figure 4.10: All of the events in the IC86v4 data set that are included in the background estimation after source masking is applied. The masked regions given in Table 4.2 can be seen as the empty regions in the skymap. The southern sky has a lower density of events due to the harsher cuts applied because of its larger background compared to the northern sky. The grey line and dot indicate the Galactic plane and the Galactic center respectively.

The Galactic plane and the six additional regions mentioned in Table 4.2 are the regions that will be masked out before estimating the background. The events within this mask are removed from the IC86v4 data set before the background is calculated. The events that remain can be seen in Figure 4.10. The regions of the sky that have been removed with the mask can be seen clearly. Before the background is calculated, a correction for the region of the sky that has been removed is applied.

4.5 Statistical Hypothesis Testing

4.5.1 Null and Alternate Hypotheses

As IceCube collects data from particles passing through the detector, we will not know if there is any evidence of a neutrino source in that data until it has been tested. This brings us to the topic of hypothesis testing. We want to know if the data we are seeing matches with a certain hypothesis. The two hypotheses we will be considering are the null hypothesis (H_0) and the alternate hypothesis (H_1).

The null hypothesis describes the situation where all of our observed data matches the background described in Section 4.3. On the other hand, the alternate hypothesis is when there is some difference observed. This would describe a situation where a small fraction of our observed data comes from astrophysical sources. We represent this as the number of signal particles seen, n_s. If n_s is zero, then our data matches the null hypothesis.

4.5.2 Test Statistic

When testing our data, we want to see whether the data is in agreement with the null hypothesis or the alternate hypothesis. To do this, we calculate what is called the test statistic (TS). For the unbinned maximum likelihood method, the TS is generally defined as the ratio of the likelihood under the alternate hypothesis and the likelihood under the null hypothesis. With the likelihood defined in Equation 4.2, the TS comes out to be:

$$TS = 2\log\left(\frac{\mathcal{L}\left(\hat{n}_s, \hat{\gamma}\right)}{\mathcal{L}\left(n_s = 0\right)}\right) = \log\left[\frac{\hat{n}_s}{N}\left(\frac{\mathcal{S}_i\left(\hat{\gamma}\right)}{\mathcal{B}_i} - 1\right) + 1\right] \tag{4.8}$$

where $\hat{n}_s$ and $\hat{\gamma}$ are the best-fit number of signal particles and spectral index respectively. If the signal-subtracted likelihood is used as seen in Equation 4.7, then the TS is changed to:

$$TS = 2\log\left[\frac{n_s}{N}\left(\frac{\mathcal{S}_i}{\tilde{\mathcal{D}}_i} - \frac{\tilde{\mathcal{S}}_i}{\tilde{\mathcal{D}}_i}\right) + 1\right] \tag{4.9}$$

For the maximum likelihood method, the TS is evaluated where the likelihood ratio is maximized. It has been observed empirically through simulations that a χ^2_r function, with the number

of degrees of freedom being fitted (r), describes the positive component of the TS distribution well. The probability density function of the χ^2 distribution is

$$P_r(x) = \frac{x^{r/2-1} e^{-x/2}}{\Gamma(r/2)\, 2^{r/2}} \tag{4.10}$$

where $\Gamma(n) = (n-1)!$ and r is the number of degrees of freedom. The PDF of the χ^2 distribution can be shifted and scaled as follows:

$$P = \frac{\eta}{\text{scale}} P_r(y) \tag{4.11}$$

where $y = (x - \text{loc})/\text{scale}$, loc is the shift parameter along the x-axis, scale is the shift parameter along the y-axis, and η is the fraction of positive TS values over the total number of TS values.

An example of a background-only TS distribution is shown in Figure 4.11. The background TS values are shown in the histogram, with the fitted χ^2 function as the dashed line. Since we fit for both n_s and the spectral index γ, it could be easily mistaken to expect the χ^2 to have two degrees of freedom. However, n_s and γ are not completely independent due to their relation in the differential neutrino energy spectrum. Because of this, we expect the fitted χ^2 to have the number of degrees of freedom be between 1-2. This is what is seen in Figure 4.11, where the number of degrees of freedom of the fitted χ^2 is 1.17.

4.5.3 Errors

There are two main types of errors one can make with this type of testing. If the null hypothesis is true but the test rejects the null hypothesis, this is called a Type-I error. It is also easily thought of as a false discovery. The probability of Type-I errors occurring is also called the significance level of the test, denoted by α.

The second type of error that occurs is when the alternate hypothesis is true, but the test rejects the alternate hypothesis. This is called a Type-II error and results in a false negative. The probability of making a Type-II error is denoted by β. The probability of not making Type-II errors is called the power of the test, defined as $1 - \beta$. Ideally, we would want to have both α and β small. However,

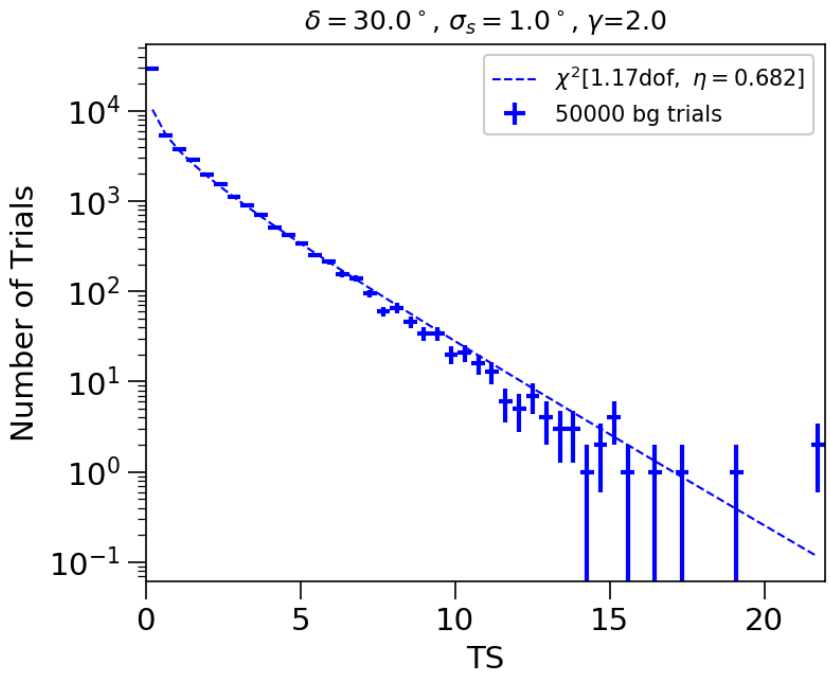

Figure 4.11: An example of a background-only TS distribution at a declination of 30°, source extension of 1° and a spectral index of 2.0. The background trials are shown in the histogram as well the fitted χ^2 distribution to the background TS distribution.

the more stringent cuts that are placed on α and β, the less chance we have of discovering any signal in the data at all.

Moving forward, the most important terms to remember in this section are:

- α: Significance level. The probability of making a Type-I error and getting a false discovery.
- $1 - \beta$: Power. The probability of not making a Type-II error and correctly accepting the alternate hypothesis.

4.6 Sensitivity and Discovery Potential

In order to see IceCube's overall performance in an analysis, sensitivity and discovery potential are calculated by performing a large amount of tests, called trials, on scrambled data. Signal events are injected into the scrambled data, and the fitted neutrino flux and the corresponding test statistics are calculated. Sensitivity represents the median 90% upper limit under the null

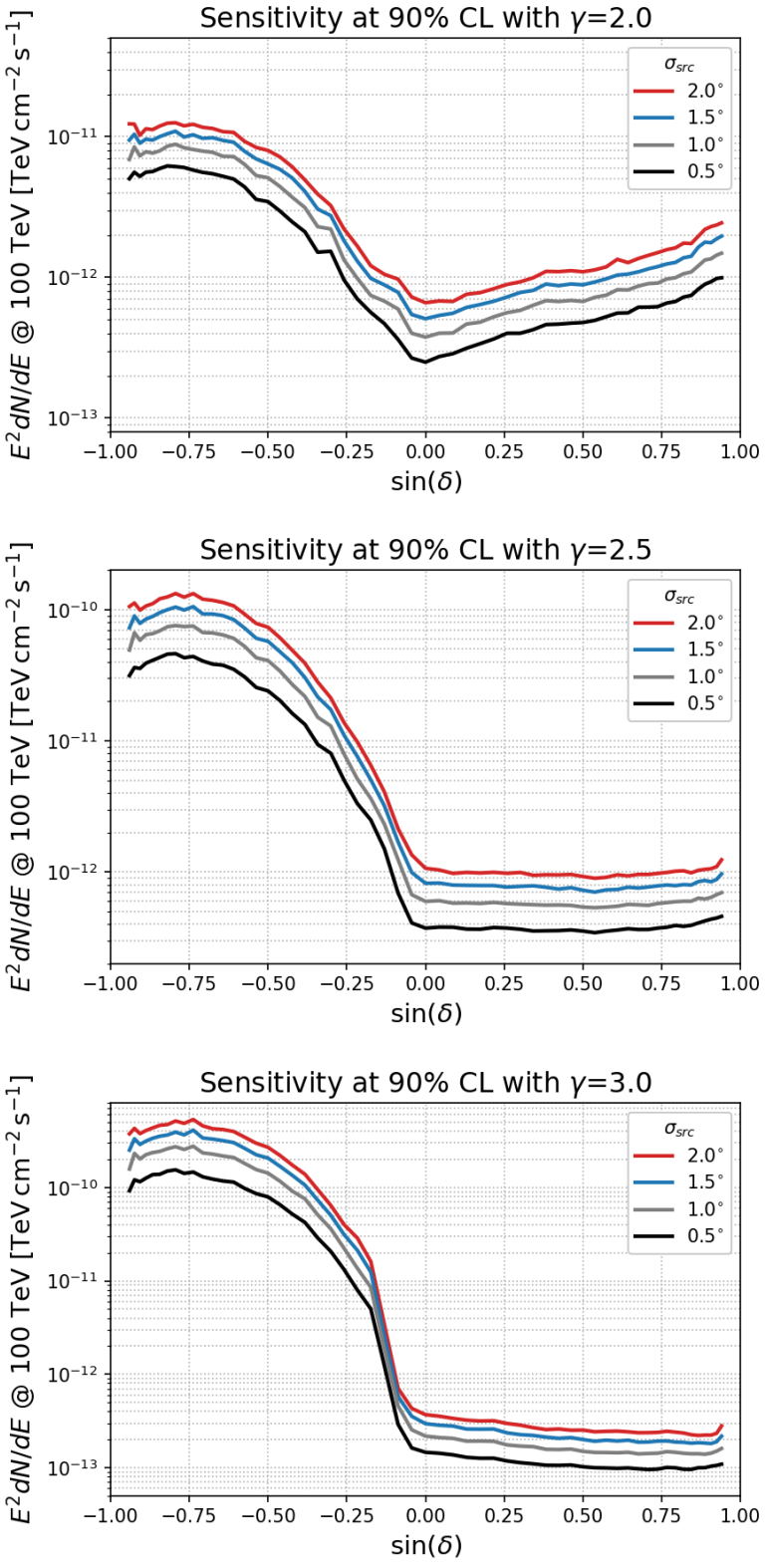

Figure 4.12: Sensitivity at 90% CL for all source extensions considered, ranging from 0.5° to 2.0°. Each plot is for a different spectral index: 2.0 (top), 2.5 (middle), and 3.0 (bottom).

hypothesis. Recalling Section 4.5, this means that sensitivity is calculated when $\alpha = 0.5$ and the power is $1-\beta = 0.9$. Sensitivity curves for this analysis are shown in Figure 4.12 for different source extensions and spectral indices. Sensitivity changes depending on the source extension and spectral index that is used in the search as well as where in the sky the search is being conducted. Sensitivity is worse in the southern hemisphere ($\sin\delta < -0.09$) due to the high background rates from cosmic-ray air showers. As the source extension increases, the sensitivity worsens. In addition, as you change spectral index, the sensitivity will improve or worsen depending on the declination. As mentioned, the background rate in the southern hemisphere is high due to cosmic-ray air showers, which have a spectral index ~ 2.7. Atmospheric muons and neutrinos that come from cosmic-ray air showers are typically one power steeper, at a spectral index of ~ 3.7. As the spectral index for the sensitivity tests tend towards the softer end of the spectrum, the sensitivity in the southern hemisphere worsens because the background that is observed is more energetically similar to the signal hypothesis.

Discovery potential represents the flux required to result in a 5σ discovery with 50% probability. This means that discovery potential at 5σ is calculated when $\alpha = 5\sigma$ and the power is $1 - \beta = 0.5$. The background TS will be larger than the observed TS at the 5σ level (probability of $\sim 3 \times 10^{-7}$) while the signal TS is above the observed TS only 50% of the time. Discovery potential curves for this analysis are shown in Figure 4.13 for different source extensions and spectral indices. Like sensitivity, discovery potential curves follow the same trends over different declinations, source extensions, and spectral indices.

4.7 Fit Bias

In this analysis, the two parameters that will be fitted are the number of signal particles, n_s, and the spectral index, γ. In order to test whether the fitting algorithm is behaving as expected, fit bias tests are performed. For these tests, a number of particles, n_{inj}, are injected at a specified spectral index. The fit is run with these input parameters, and the outputs, n_s and γ, are computed. If the software and the analysis run perfectly, one would expect that the correct number of particles is

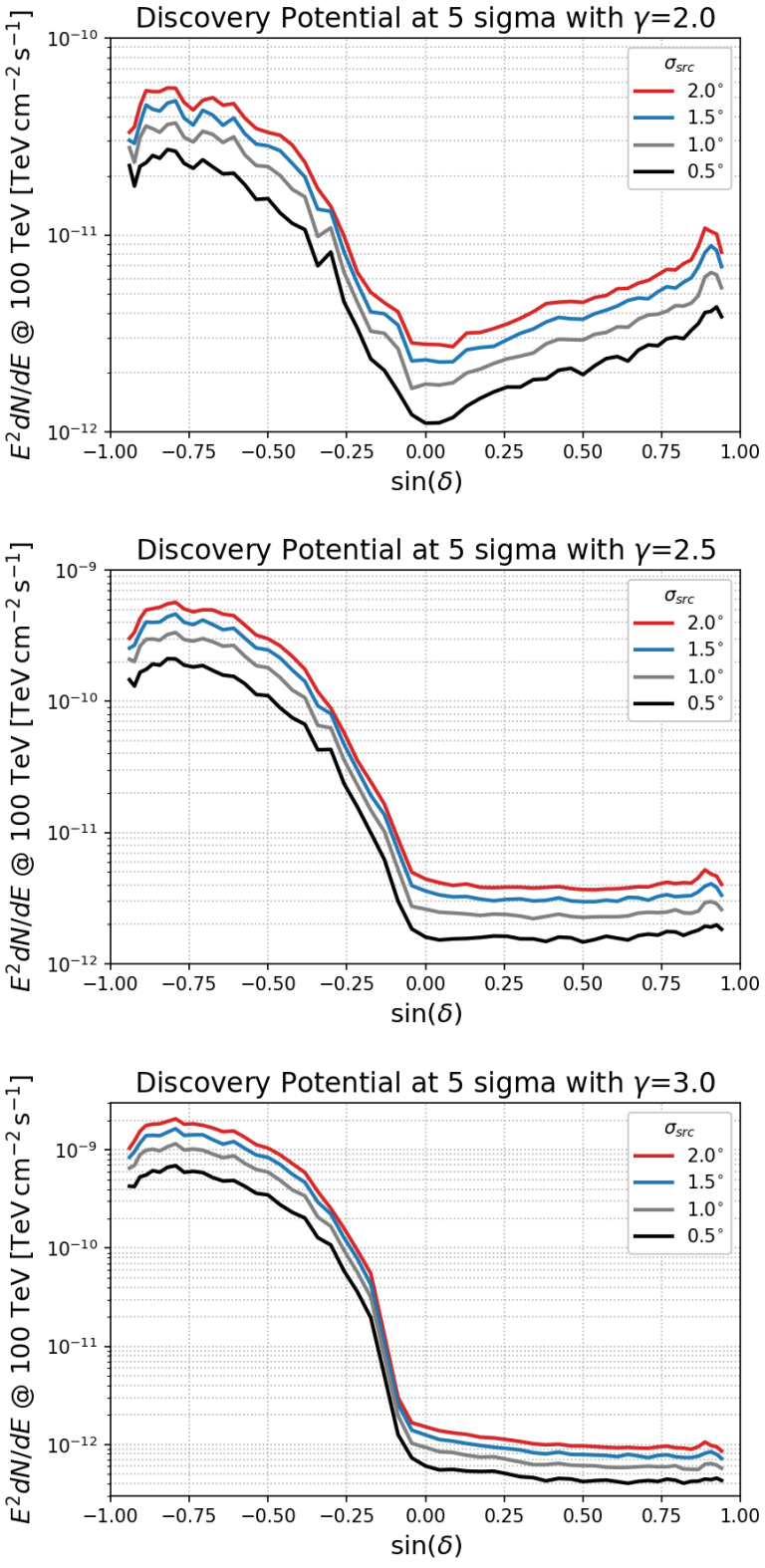

Figure 4.13: Discovery potential at 5σ for all source extensions considered, ranging from 0.5° to 2.0°. Each plot is for a different spectral index: 2.0 (top), 2.5 (middle), and 3.0 (bottom).

recovered ($n_s = n_{\text{inj}}$) as well as the spectral index.

Before running this analysis with the background estimation method of source masking, the method of signal subtraction was tested (both methods discussed in Section 4.4). Signal subtraction is used widely in the IceCube community; therefore we decided to run quick tests to see how signal subtraction performs with this analysis. The signal subtraction tests were run with seven years of IceCube track data, as discussed in Section 4.2, for extensions ranging from $0^\circ - 5^\circ$.

Fit bias tests performed with signal subtraction can be seen in Figure 4.14 for declinations of -30°, 0°, and 30° and Figure 4.15 for declinations of -70° and 70°. All fit bias tests shown in the plots had the source injected with a source extension of 1.0°, but the results for other extensions were similar. Three different spectral indices were tested: 2.0, 2.5, and 3.0. While fitting for n_s remains relatively unbiased for most declinations (excluding -70°), fitting harder spectral indices like 2.0 is consistently unreliable. Fit bias tests performed at even harder spectral indices like 1.0 and 1.5 also proved to be strongly biased, not just when fitting γ, but also when fitting n_s. An example of the fit bias at spectral indices close to the bound of the fit for the spectral index of [1,4] is shown in Figure 4.16. The test was done at a declination of 0° and a source extension of 1.0°. It can be seen that both the n_s and γ fits become unreliable for hard spectral indices when using signal subtraction.

4.8 Systematic Uncertainties

Systematic uncertainties for this type of analysis can come from many different places. The background for this analysis is estimated by scrambling IceCube data in right ascension. Since the background is created by randomizing the data in right ascension, it is not affected by systematic uncertainties because it cannot show any discrepancies from underlying distributions of the data. However, in order to relate observed events to neutrino fluxes, Monte Carlo simulations are used to inject hypothetical neutrino sources into the background, and therefore are affected by systematic uncertainties. The flux is dependent on the effective area of the detector and the angular uncertainty of events, which are modeled by Monte Carlo simulations. It is not feasible to produce a dedicated

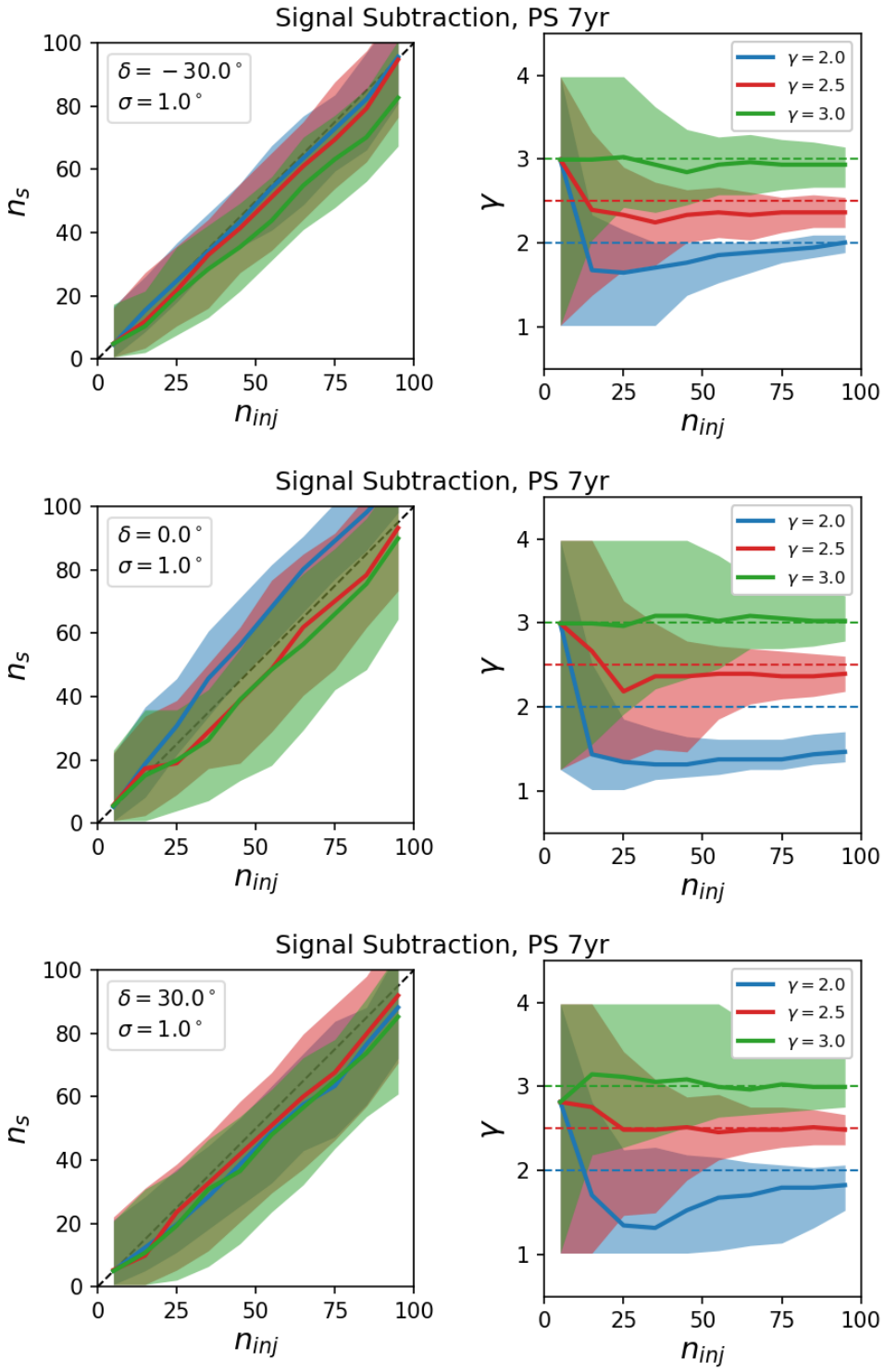

Figure 4.14: Fit bias tests using signal subtraction at declinations of -30° (top), 0° (middle), and 30° (bottom) with a source extension of 1.0° for spectral indices of 2.0 (blue), 2.5 (red), and 3.0 (green). The number of events recovered from the fit (left) and the fitted spectral index γ (right) are shown as a function of injected events n_{inj} for different declinations: $\delta = -30^\circ$ (top), $\delta = 0^\circ$ (middle), $\delta = 30^\circ$ (bottom).

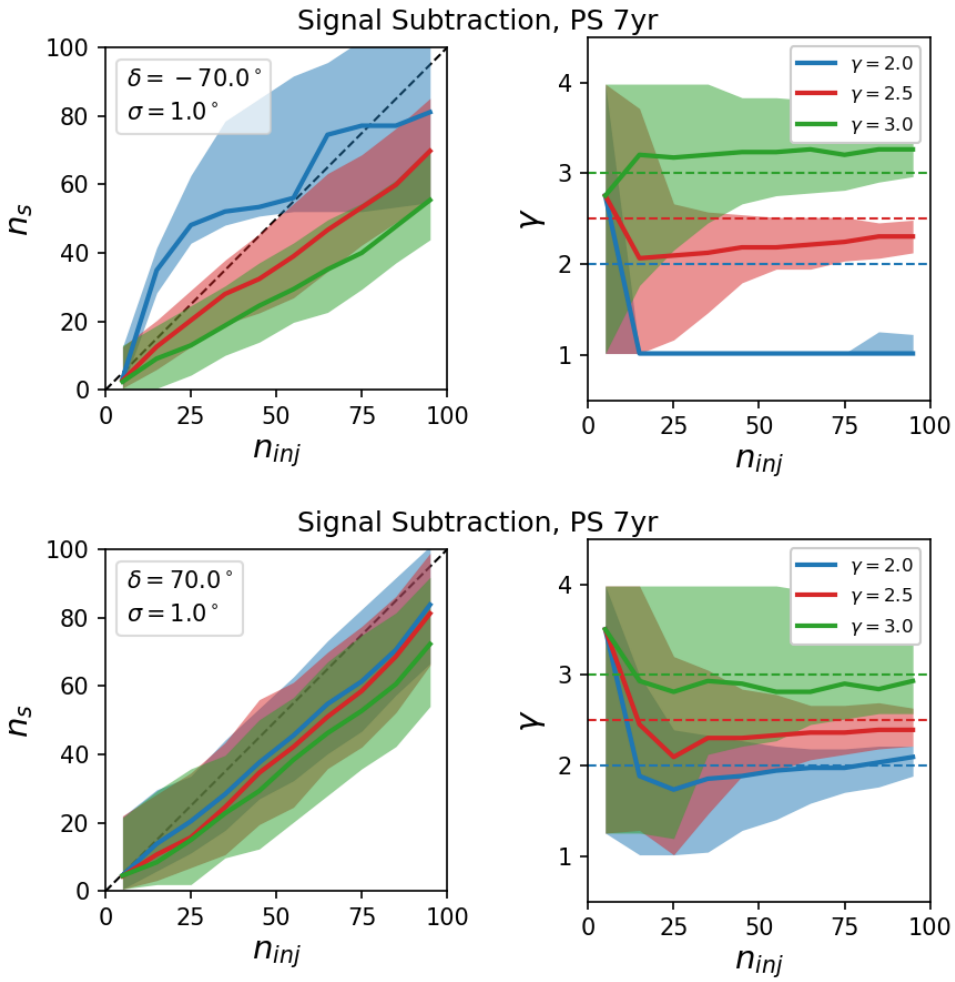

Figure 4.15: Fit bias tests using signal subtraction at declinations of -70° (top) and 70° (bottom) with a source extension of 1.0° for spectral indices of 2.0 (blue), 2.5 (red), and 3.0 (green). The number of events recovered from the fit (left) and the fitted spectral index γ (right) are shown as a function of injected events n_{inj} for different declinations: $\delta = -70^\circ$ (top) and $\delta = 70^\circ$ (bottom).

set of systematically varied Monte Carlo simulations for this analysis due to the time it would take to run those simulations and the relatively minor impact of systematic uncertainties on the final results. However, systematic uncertainties have been evaluated for the 7-year PS sample [118] and are summarized below.

The strongest systematic effects on Monte Carlo simulations are (1) the optical properties of the Antarctic ice [121], such as the scattering and absorption lengths, (2) the DOM optical efficiency [122], and (3) different photo-nuclear interaction models of high-energy muons [10, 123, 124, 125, 126, 127, 128]. Changing the scattering and absorption length of photons in ice by 10% resulted

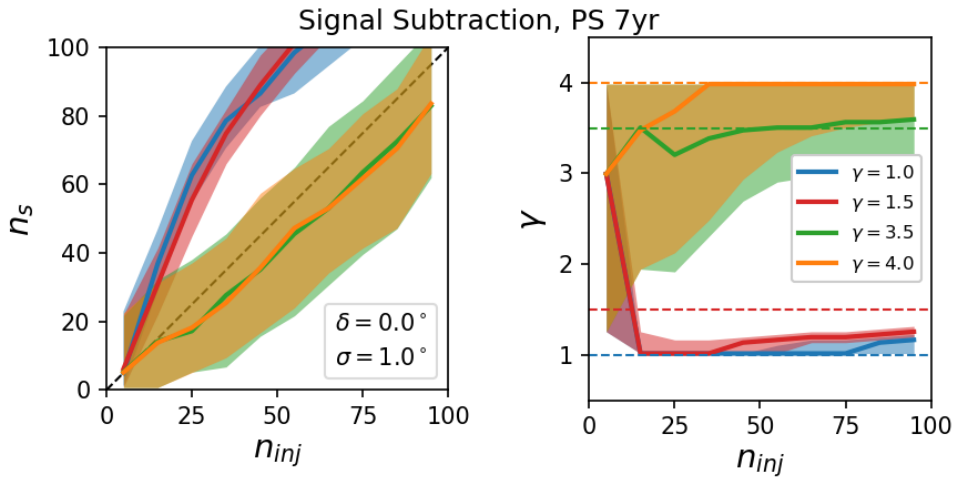

Figure 4.16: An example of fit bias tests at spectral indices close to the bounds of the spectral index fit of [1,4] using signal subtraction at a declinations of 0° with a source extension of 1.0°. The spectral indices included in this test were 1.0 (blue), 1.5 (red), 3.5 (green), and 4.0 (orange). The number of events recovered from the fit (left) and the fitted spectral index γ (right) are shown as a function of injected events n_{inj}.

in a flux uncertainty of 5.6%. Changing the DOM optical efficiency by ±10% resulted in a flux uncertainty of 7.5%. And finally, changing the photo-nuclear interaction model affected the flux as much as 5.9%. Overall, the combined systematic uncertainty on $\nu_\mu + \bar{\nu}_\mu$ flux values corresponding to a given number of events is 11% [118] for the 7-year PS data sample, and is assumed to be similar for the IC86v4 data set used in this analysis.

4.9 Galactic Plane Search

4.9.1 Motivation

The search for Galactic extended neutrino sources is performed with two different approaches. First, blind scans across the entire Galactic plane are performed searching for extended regions of neutrino emission. As discussed in Section 4.1, there have been many extended sources that have been detected in the gamma-ray sky along the Galactic plane. Searches for neutrino sources along the Galactic plane have been performed in IceCube as well as general extended neutrino source searches (not restricted to the Galactic plane) [41, 129, 130, 131]. The previous dedicated

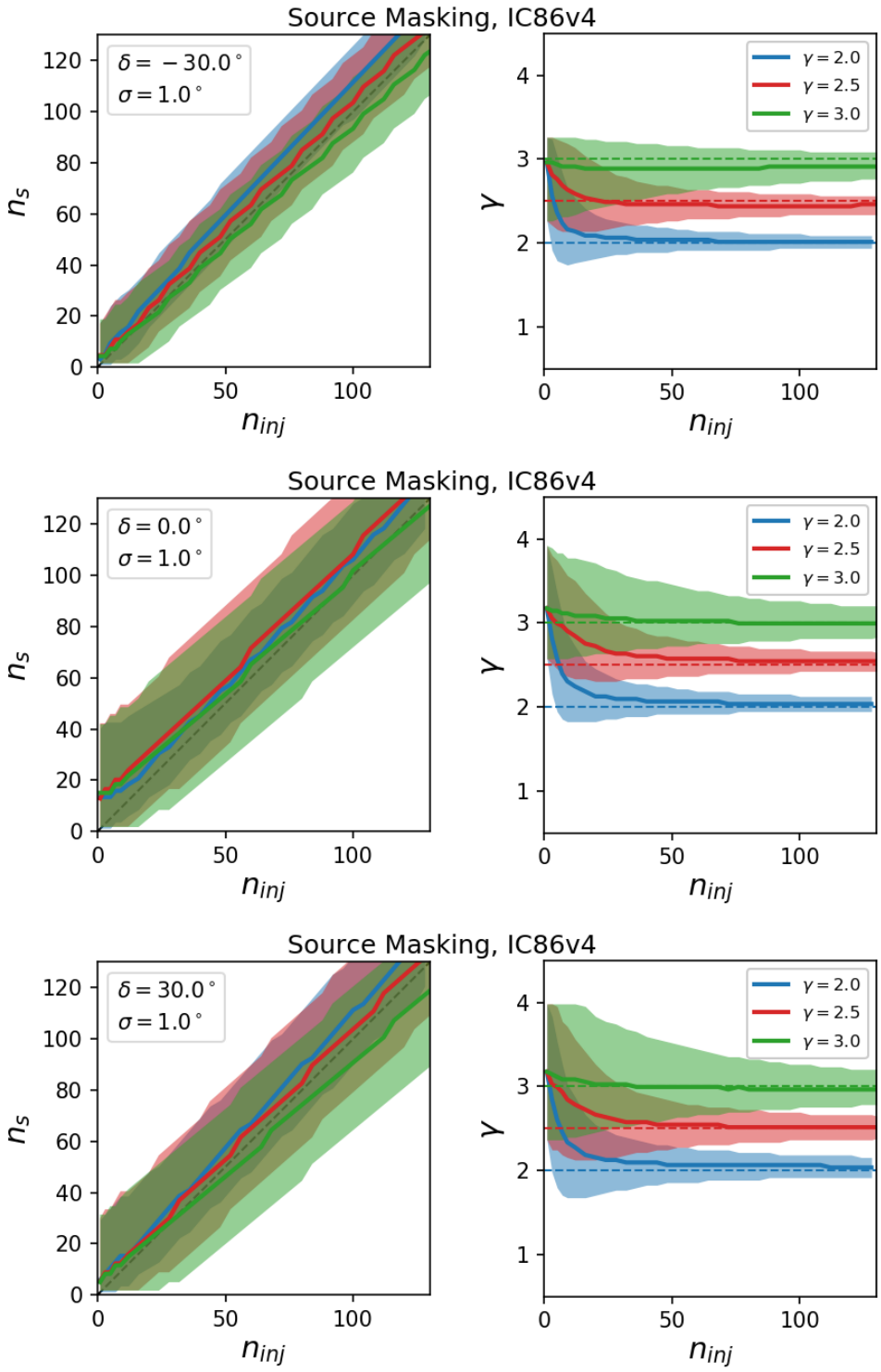

Figure 4.17: Fit bias tests using source masking at declinations of -30° (top), 0° (middle), and 30° (bottom) with a source extension of 1.0° for spectral indices of 2.0 (blue), 2.5 (red), and 3.0 (green). The number of events recovered from the fit (left) and the fitted spectral index γ (right) are shown as a function of injected events n_{inj} for different declinations: $\delta = -30^\circ$ (top), $\delta = 0^\circ$ (middle), $\delta = 30^\circ$ (bottom).

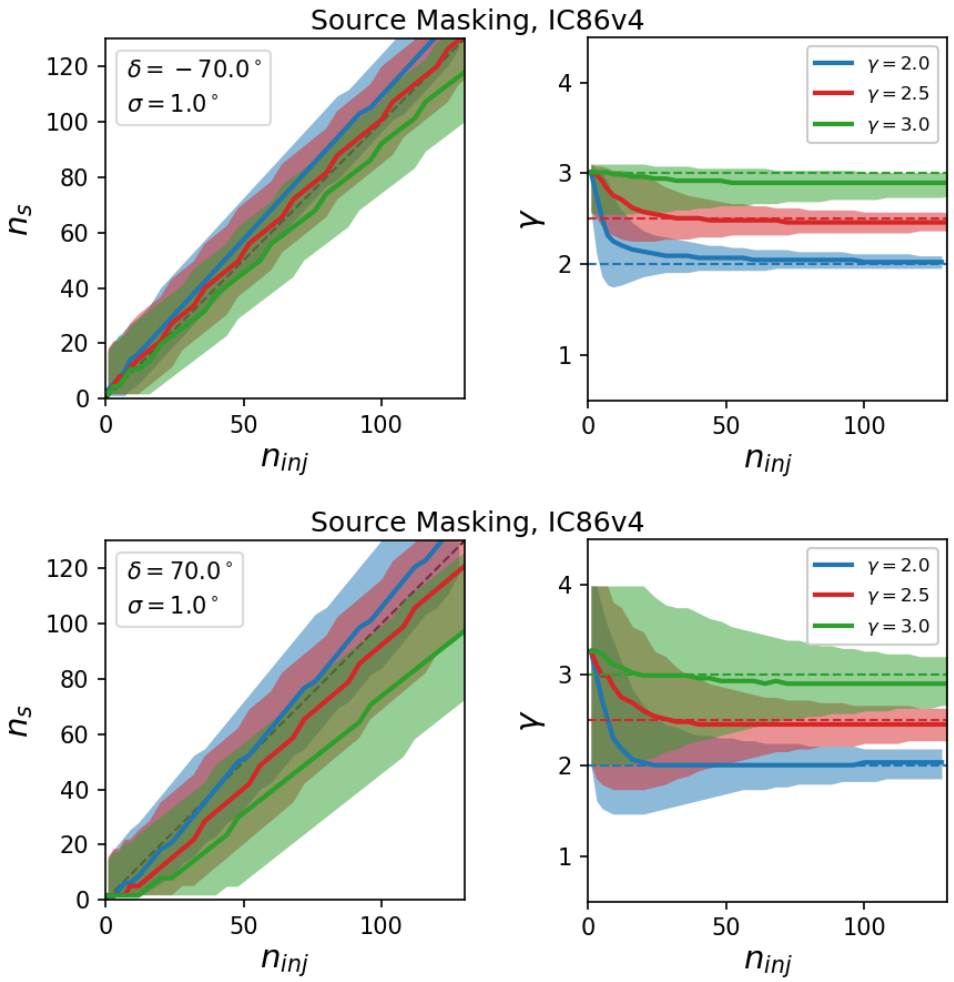

Figure 4.18: Fit bias tests using source masking at declinations of -70° (top) and 70° (bottom) with a source extension of 1.0° for spectral indices of 2.0 (blue), 2.5 (red), and 3.0 (green). The number of events recovered from the fit (left) and the fitted spectral index γ (right) are shown as a function of injected events n_{inj} for different declinations: $\delta = -70^\circ$ (top) and $\delta = 70^\circ$ (bottom).

extended source searches performed in IceCube used four years of IceCube data [129], seven years of IceCube data [130], and 16 years of combined ANTARES and IceCube data [131]. In addition, these searches were performed over the full sky or the southern sky. The search in this paper is an extended source search just along the Galactic plane, where extended sources are expected to be found due to their proximity. Sources outside of the Galaxy are more likely to appear to be point-like. Reducing the search area from the full sky (or southern sky) to just the Galactic plane reduces the look-elsewhere effect, which will be discussed in the next section. The IceCube searches that have been performed along the Galactic plane usually rely on detailed models of known sources

in the Galaxy, such as their source morphology or spectrum. The search in this paper aims to be as model-independent as possible. This search scans blindly across the Galactic plane for possible extended neutrino sources or regions, with no a priori knowledge or templates of expected Galactic emission.

4.9.2 Procedure

The analysis is performed using nine years of IceCube data, all collected with the full 86-string detector (IC86v4). Data was collected from May 13, 2011 to May 29, 2020, totalling in 3184.2 days and 1,133,364 events. Galactic latitudes within $-5^\circ < b < 5^\circ$ are included in the search, with individual scans being performed for the source extensions of 0.5°, 1.0°, 1.5°, and 2.0°. Prior to unblinding, it was decided that if hotspots in the sky are detected above a threshold significance of 3σ, a localized search around the hotspot would be performed.

To produce a significance map of the Galactic plane, each location along the Galactic plane must be evaluated. To do this, the Galactic plane is split into pixels using a HEALPix map [132]. The HEALPix map used in this analysis generally has 3,145,728 pixels; however, since only the Galactic plane within latitudes $[-5^\circ, 5^\circ]$ is being evaluated, this cuts the number of pixels in the map down to 274,176. The mean spacing of the pixels is $\sim 0.115^\circ$. At each of these pixels, the likelihood (as described in Equation 4.2) is minimized and a TS is calculated using Equation 4.8. This TS is compared to the background TS distribution at that point to calculate the pre-trial p-value. Distributions of 50,000 background test statistics have been produced for declinations between $[-70^\circ, 70^\circ]$ in steps of 2.5°. Each pixel uses the background TS distributions from the nearest smaller and larger declinations, computes observed pre-trial p-values for each one, and then linearly interpolates the result to the declination of the specified pixel. The result is a skymap of observed pre-trial p-values for each source extension.

Pre-trial p-values have to be corrected for the fact that nearly 3×10^5 fits are performed. Due to the large area being searched and the number of minimizations performed, there is an increased possibility that a statistically significant observation would occur by chance. This phenomenon

is known as the look-elsewhere effect. To properly account for the look-elsewhere effect and the probability that a significant observation could occur by chance, a post-trial procedure is followed. For each extension, 5,000 scrambled background skymaps are produced. The smallest pre-trial p-value from each of those 5,000 background skymaps are put into a distribution. The observed pre-trial p-value for each extension in the real data is then compared to the distribution of background pre-trial p-values to obtain the observed post-trial p-value.

4.9.3 Results

The Galactic plane scans for source extensions of 0.5°, 1.0°, 1.5°, and 2.0° are shown in Figures 4.19, 4.20, 4.21, and 4.22 respectively. The scans show the pre-trial p-values for each pixel across the Galactic plane for the corresponding source extension. The hottest pre-trial p-value is obtained for each skymap, as well as the corresponding location, the observed number of signal events, $\hat{n}_s$, and its associated spectral index, $\hat{\gamma}$. These values can be seen in Table 4.3. The hotspot in each skymap corresponds to the same location of the sky, with slight differences in RA and declination between the 0.5°/1.0° maps and the 1.5°/2.0° arising from the hottest pixel in that region shifting slightly. The hottest spots in each skymap can be seen in Figure 4.24.

Extension (°)	RA (°)	DEC (°)	$\hat{n}_s$	$\hat{\gamma}$	p_{pre} (σ_{pre})	p_{post} (σ_{post})
0.5°	296.98°	27.45°	80.28	3.10	5.48×10^{-5} (3.87σ)	2.70×10^{-1} (0.61σ)
1.0°	296.98°	27.45°	111.38	3.00	9.06×10^{-5} (3.74σ)	1.59×10^{-1} (1.00σ)
1.5°	297.42°	27.53°	150.47	3.03	6.61×10^{-5} (3.82σ)	6.30×10^{-2} (1.53σ)
2.0°	297.42°	27.53°	182.27	3.09	1.14×10^{-4} (3.69σ)	8.02×10^{-2} (1.40σ)

Table 4.3: Summary of results from the scans along the Galactic plane for different extensions. The location of the hottest spot in each skymap is given, as well as the observed number of signal events ($\hat{n}_s$), the spectral index ($\hat{\gamma}$), and pre-trial and post-trial p-values for the hottest spot.

Post-trial p-values are calculated using the background pre-trial p-value distributions shown in Figure 4.23. In each background pre-trial p-value distribution, the observed pre-trial p-value is shown with a black, dashed line. The post-trial p-value is determined by calculating how many times scrambled background skymaps obtain a pre-trial p-value smaller than the observed pre-trial

p-value. The obtained percentage is the post-trial p-value. The most significant result obtained in this search is a post-trial p-value of 0.06 for a source extension of 1.5°. This corresponds to a significance of 1.53σ.

For each hotspot in the four different skymaps, the upper limit on the number of signal events $n_{s,90\%}$ for which the background TS exceeds the observed TS 90% of the time is calculated. an associated 90% confidence level upper-limit flux is calculated. The number of signal events, $n_{s,90\%}$, is then converted to a flux assuming a simple power law spectrum with the observed spectral index and a pivot energy of 1 TeV. This flux is defined as:

$$\frac{dN_{\nu_\mu+\bar{\nu}_\mu}}{dE_\nu} = \phi_{90\%} \cdot \left(\frac{E_\nu}{\text{TeV}}\right)^{-\gamma} \quad \text{TeV}^{-1}\,\text{cm}^{-2}\,\text{s}^{-1} \tag{4.12}$$

where γ is the observed spectral index and $\phi_{90\%}$ is the normalization of the muon neutrino and anti-neutrino differential flux at a pivot energy of 1 TeV. The upper limit fluxes for the hotspot in each skymap is shown in Table 4.4. These values are also compared to the sensitivity at 90% CL and discovery potential at 5σ which was discussed in Section 4.6. Since each hotspot was

Extension (°)	$\hat{n}_s$	$\hat{\gamma}$	$\phi_{90\%}$ ($\text{TeV}^{-1}\,\text{cm}^{-2}\,\text{s}^{-1}$)
0.5°	80.28	3.10	5.13×10^{-11}
1.0°	111.38	3.00	6.29×10^{-11}
1.5°	150.47	3.03	6.61×10^{-11}
2.0°	182.27	3.09	1.04×10^{-10}

Table 4.4: Summary of 90% CL upper limit fluxes of the hottest spot in each scan along the Galactic plane for different extensions. The observed number of signal events ($\hat{n}_s$) and the spectral index ($\hat{\gamma}$) of each hotspot are given. The 90% CL upper limit flux is the normalization flux at 1 TeV. A pivot energy of 1 TeV was used to calculate the upper limit fluxes.

fit to a spectral index at or slightly above three, the upper limit fluxes are compared to sensitivity and discovery potential with energy spectra following E^{-3} as shown in Figures 4.12 and 4.13 respectively. The comparison of the upper limits and the sensitivity and discovery potential curves at E^{-3} are shown in Figure 4.25.

Although the hotspots found in the scans across the Galactic plane are insignificant, it is of interest to see what, if any, known gamma-ray sources are nearby those hotspots. Since the hottest

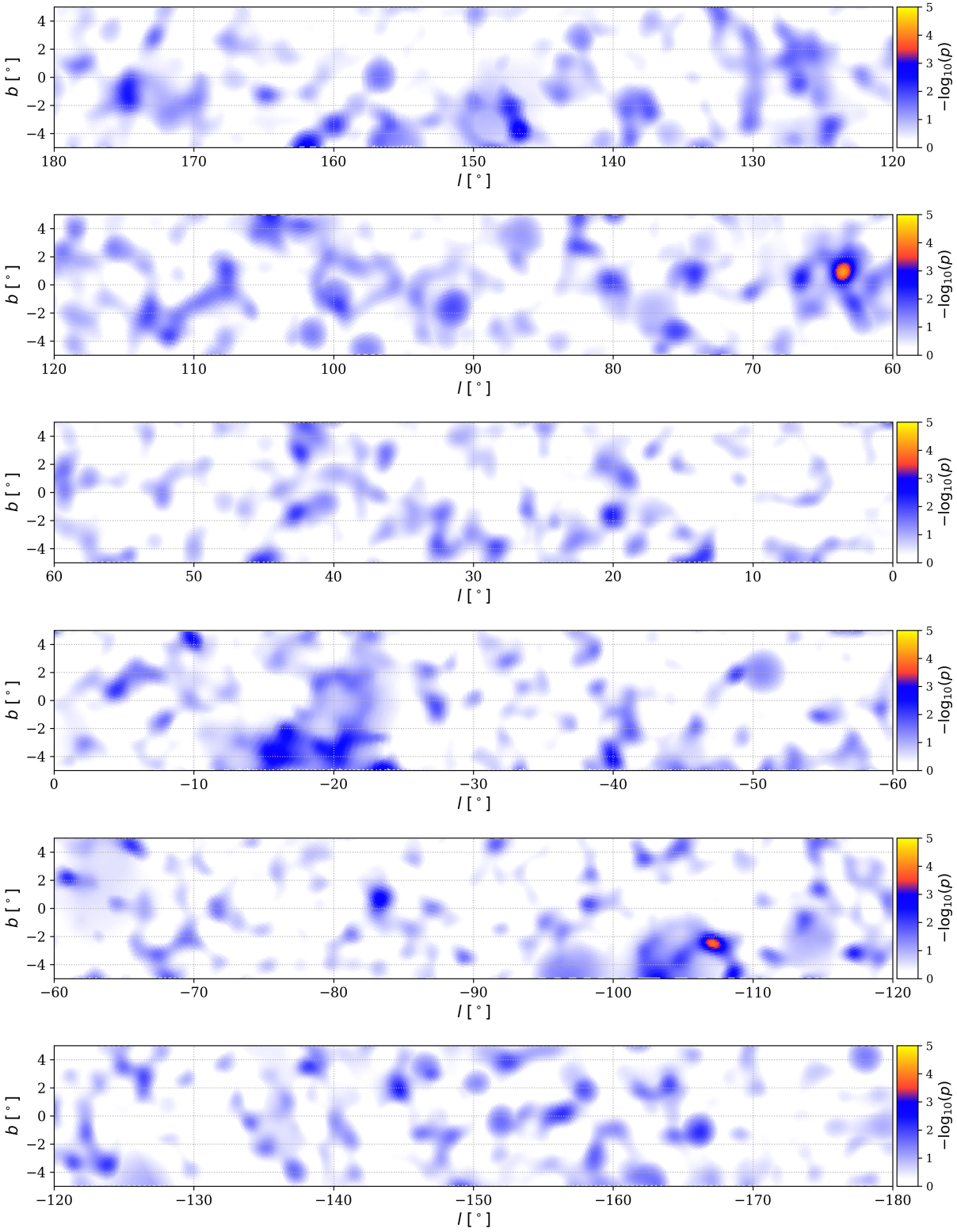

Figure 4.19: Skymap of pre-trial p-values of the Galactic plane for a 0.5° source extension.

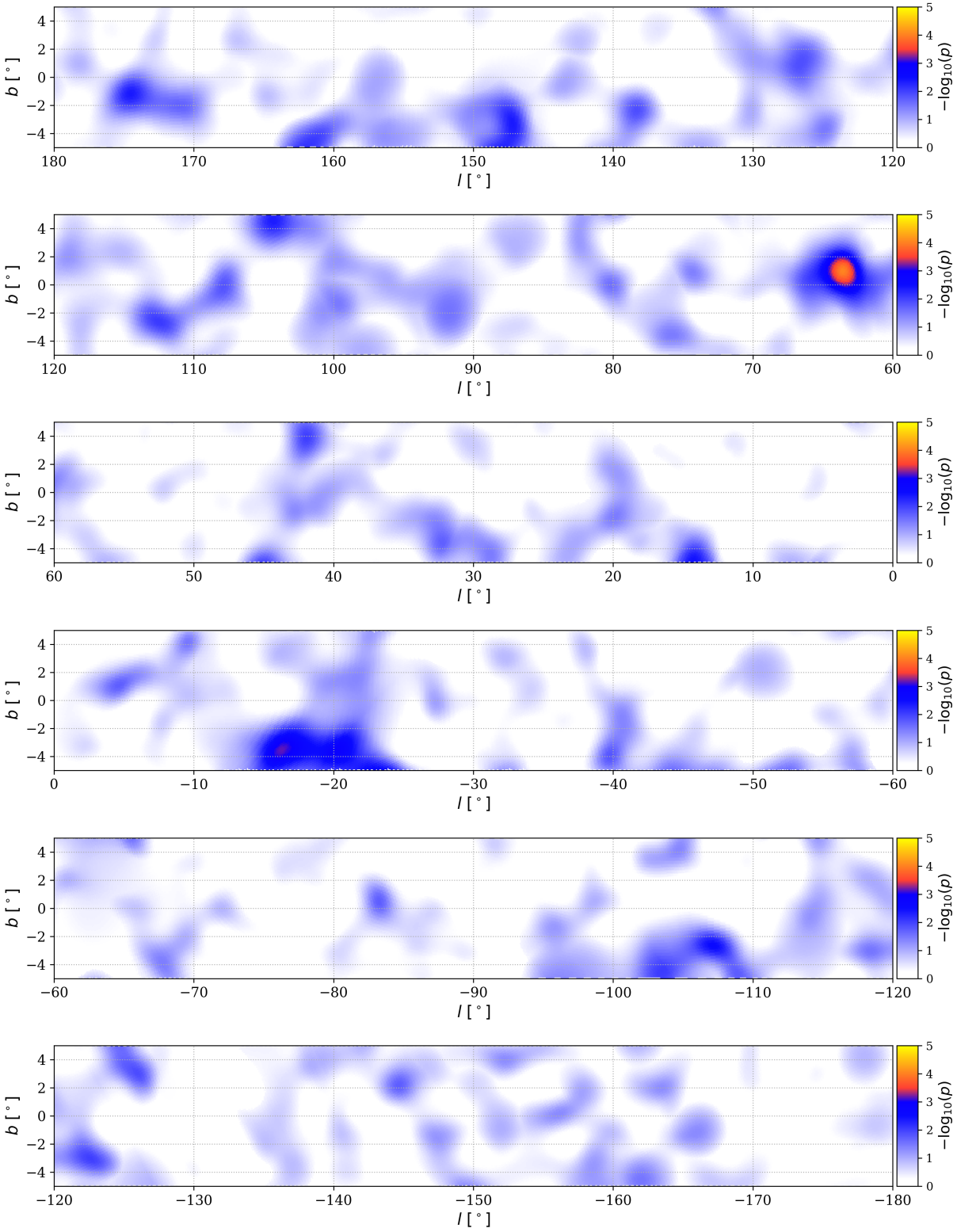

Figure 4.20: Skymap of pre-trial p-values of the Galactic plane for a 1.0° source extension.

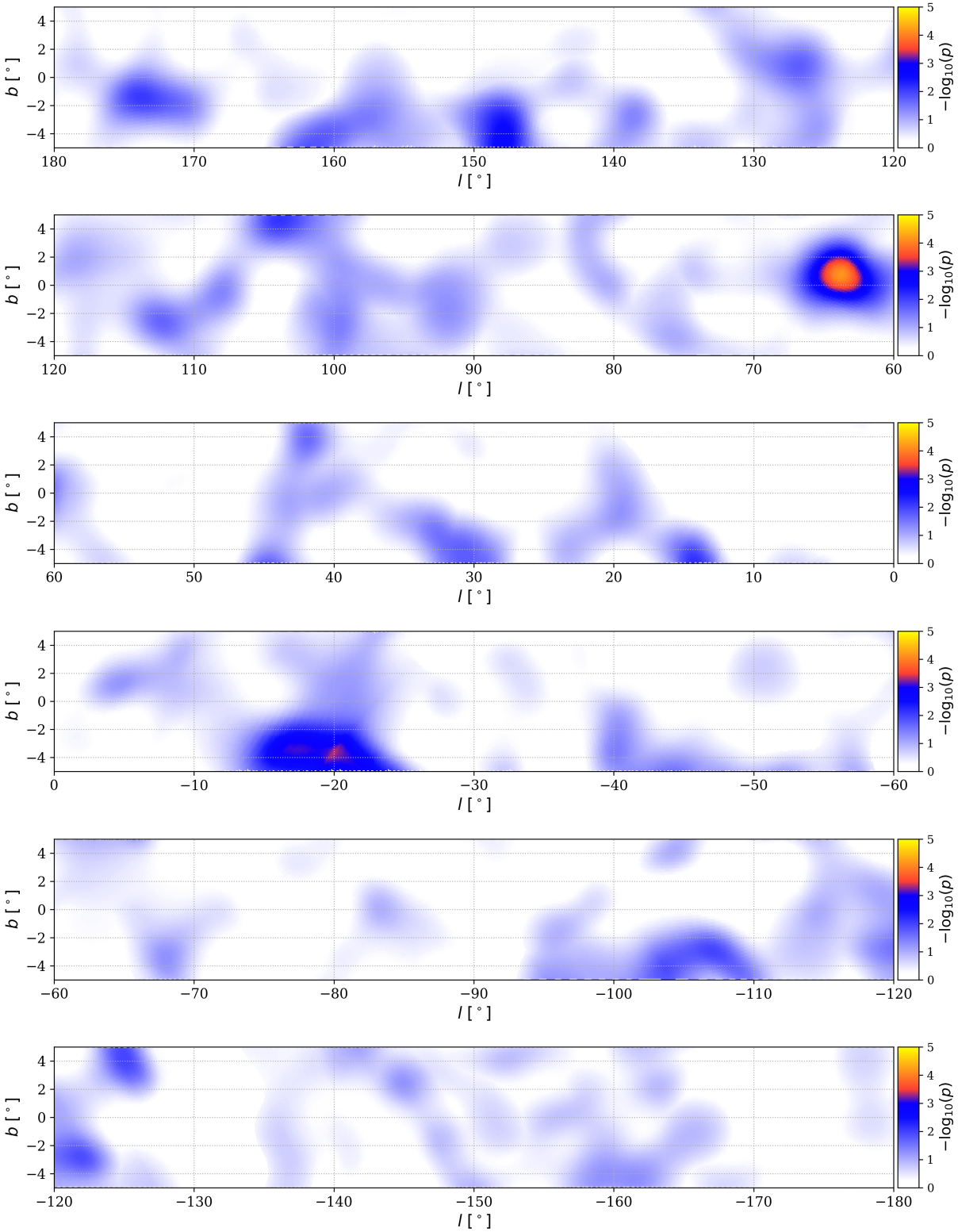

Figure 4.21: Skymap of pre-trial p-values of the Galactic plane for a 1.5° source extension.

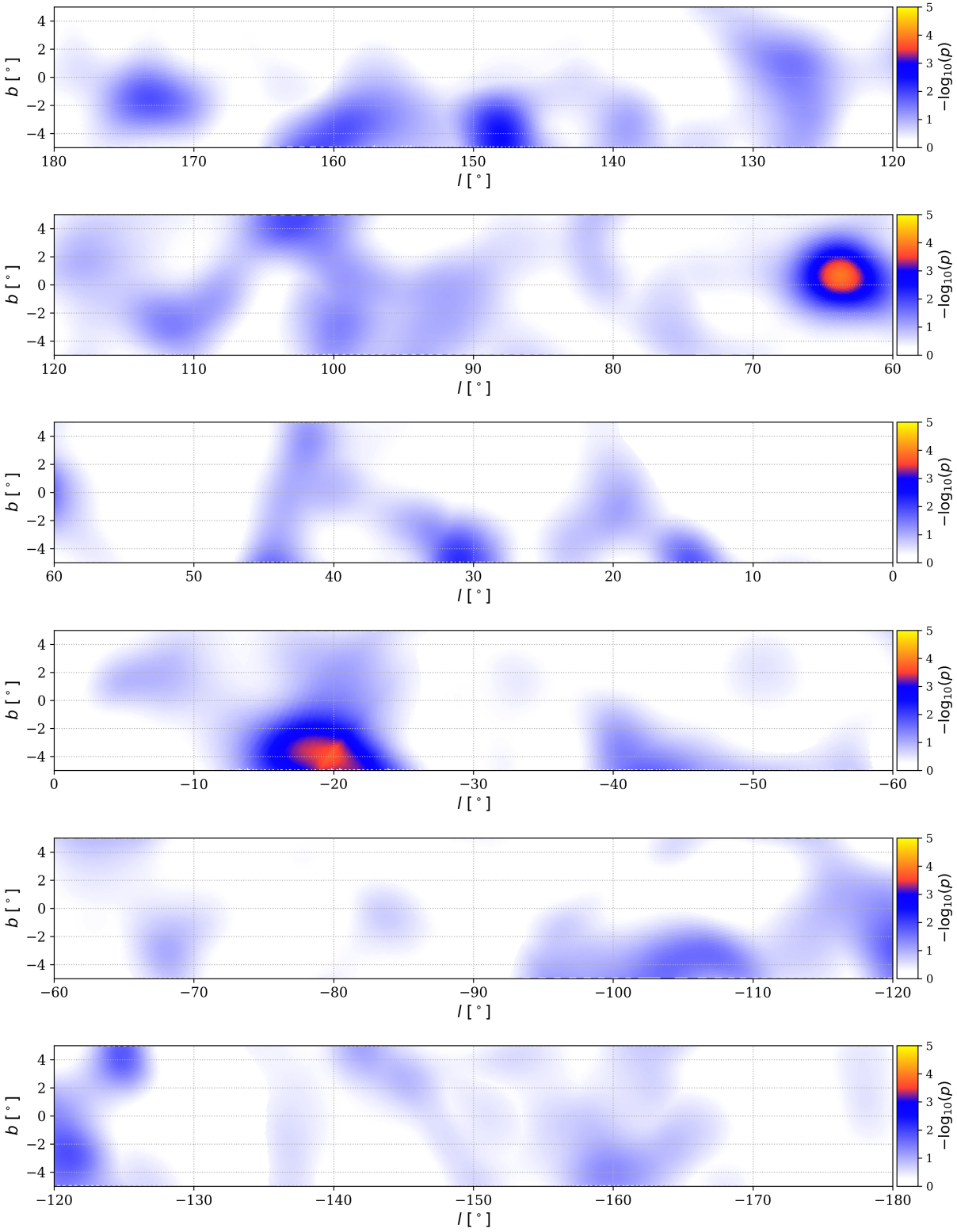

Figure 4.22: Skymap of pre-trial p-values of the Galactic plane for a 2.0° source extension.

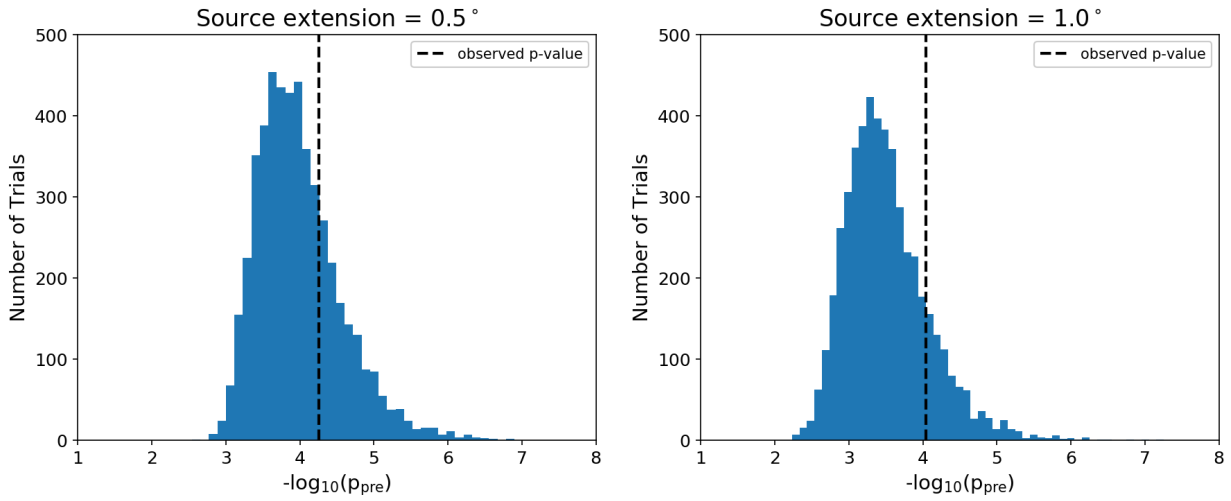

(a) Post-trial p-value: 0.27

(b) Post-trial p-value: 0.16

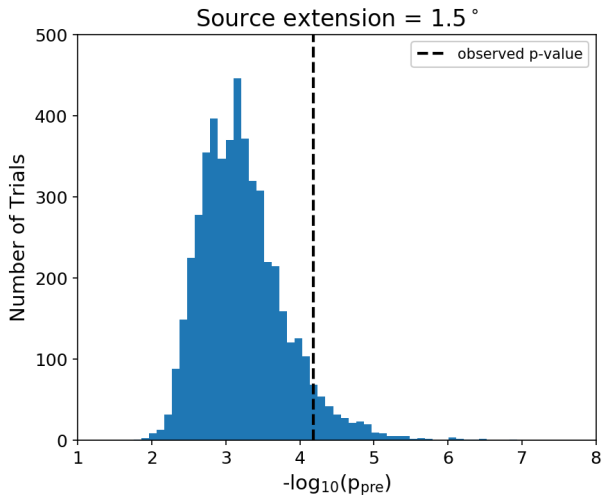

(c) Post-trial p-value: 0.06

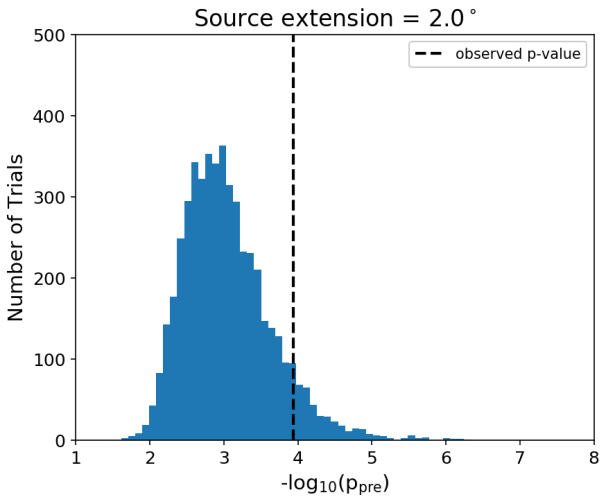

(d) Post-trial p-value: 0.08

Figure 4.23: Distribution of pre-trial p-values of the hottest spot in 5,000 background scrambled skymaps for each extension. The observed signal pre-trial p-value is marked by a dashed, black line. The observed signal post-trial p-value is calculated by evaluation how many times a background scrambled skymap would get a hotspot with a significance greater than or equal to the observed signal p-value.

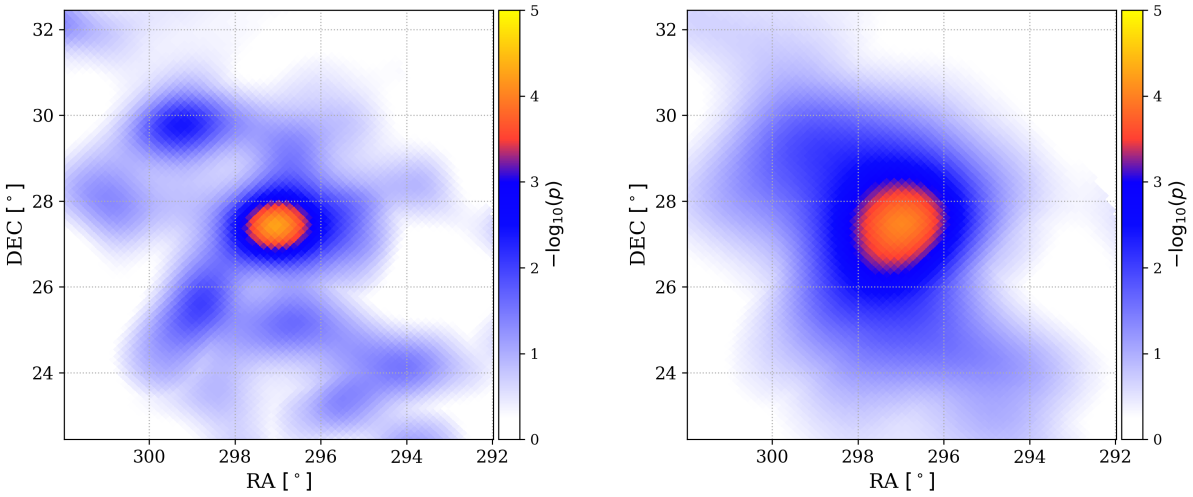

(a) Post-trial p-value: 0.27

(b) Post-trial p-value: 0.16

(c) Post-trial p-value: 0.06

(d) Post-trial p-value: 0.08

Figure 4.24: The map of the hottest spot in each skymap with source extensions of 0.5° (a), 1.0° (b), 1.5° (c), and 2.0° (d) measured in pre-trial p-values. The post-trial p-value of the hottest pixel in each skymap is given.

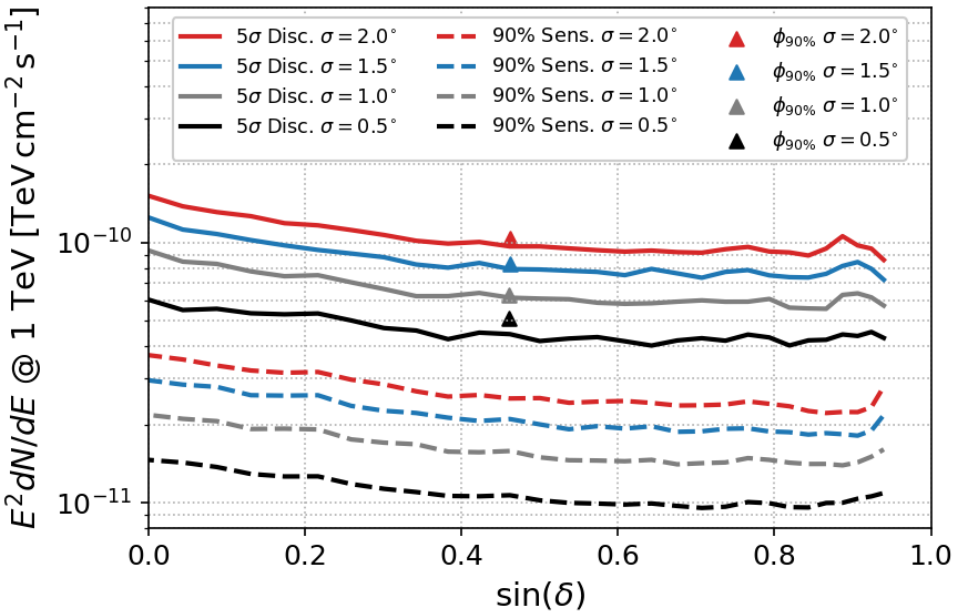

Figure 4.25: The 90% CL sensitivity (dashed lines) and the 5σ discovery potential (solid lines) as a function of declination are shown for neutrino sources with an energy spectrum of E^{-3} and source extension of 0.5° (black), 1.0° (gray), 1.5° (blue), and 2.0° (red). The 90% upper limit fluxes from Table 4.4 are shown for each source extension as triangular markers.

spot in each skymap was the same location, the following discussion will focus on the hottest spot in the 2.0° source extension map. Additional interesting features also appeared in the 0.5° and 2.0° source extension maps in Figures 4.19 and 4.22 respectively. Each map included a second location with pre-trial p-values less than 0.001, aside from the main hotspot that has been discussed thus far. While the hottest spot in each map lay in the northern sky, these secondary hotspots in the 0.5° and 2.0° source extension maps were in the southern sky. Because of this, they will be referred to the 0.5° southern hotspot and the 2.0° southern hotspot.

Several different catalogs of gamma-ray sources were considered when seeing if any sources were near the three hotspot locations. The second part of the analysis in this paper discusses a search for neutrino sources in locations which were chosen a priori, which is discussed in Section 4.10. The catalogs included in the analysis discussed in that section are also included in this search for sources near the hotspots in the Galactic plane scans. In addition to those catalogs, the Third Catalog of

Source Name	Separation (°)	Extension (°)	TeVCat Assoc	Source Type
3HWC J1951+266	1.017	0.5	-	-
3FHL J1954.3+283	1.478	-	-	PSR
3HWC J1954+286	1.572	-	2HWC J1955+285 (UNID)	-
LHAASO J1956+284	1.883	0.3	2HWC J1955+285 (UNID)	PSR/SNR
3HWC J1951+293	1.933	-	2HWC J1953+294 (PWN)	-
3FHL J1958.6+284	2.340	-	-	PWN
3HWC J1957+291	2.372	-	2HWC J1955+285 (UNID)	-
3HWC J1950+242	3.285	-	2HWC J1949+244 (UNID)	-
3FHL J1958.1+243	3.463	-	-	-
3HWC J1940+237	4.331	-	2HWC J1938+238 (UNID)	-

Table 4.5: The gamma-ray sources nearby the hottest spot in Figure 4.26. The distance separating each source and the hotspot is measured in degrees. Each source's extension, TeVCat association (TeVCat source type) and source type have been given if any have been reported in their respective catalogs. The following source types are included in this table: PSR (pulsar), PWN (pulsar wind nebula), SNR (supernova remnant), and UNID (unidentified).

Hard Fermi-LAT Sources (3FHL) is incorporated as well [133]. The Large Area Telescope (LAT) on the Fermi Gamma-ray Space Telescope [134] observed over 1,000 sources of gamma rays in the 10 GeV-2 TeV energy range. In addition, the TeVCat catalog of gamma-ray sources above 50 GeV is also included [135]. With all of these gamma-ray sources in mind, a search in the area of the three hotspots will be performed.

First, the location of the hottest spot in each map will be evaluated. Since the hottest spot is in the same location across the four skymaps, the area surrounding the hottest spot in the 2.0° source extension map will be used. The hotspot and the surrounding sources can be seen in Figure 4.26. The sources in the area are further discussed in Table 4.5. The closest source to the hotspot is 3HWC J1951+266, which is over 1° away from the hotspot. The area around the hotspot contains several different source types, including a pulsar, pulsar wind nebula, and a supernova remnant. Although none of these sources are within the region of the hotspot, it is possible that cosmic rays in the region may be interacting with matter such as a dense molecular cloud in the area of these sources, producing neutrinos over an extended region. Future work will be required to evaluate this hypothesis.

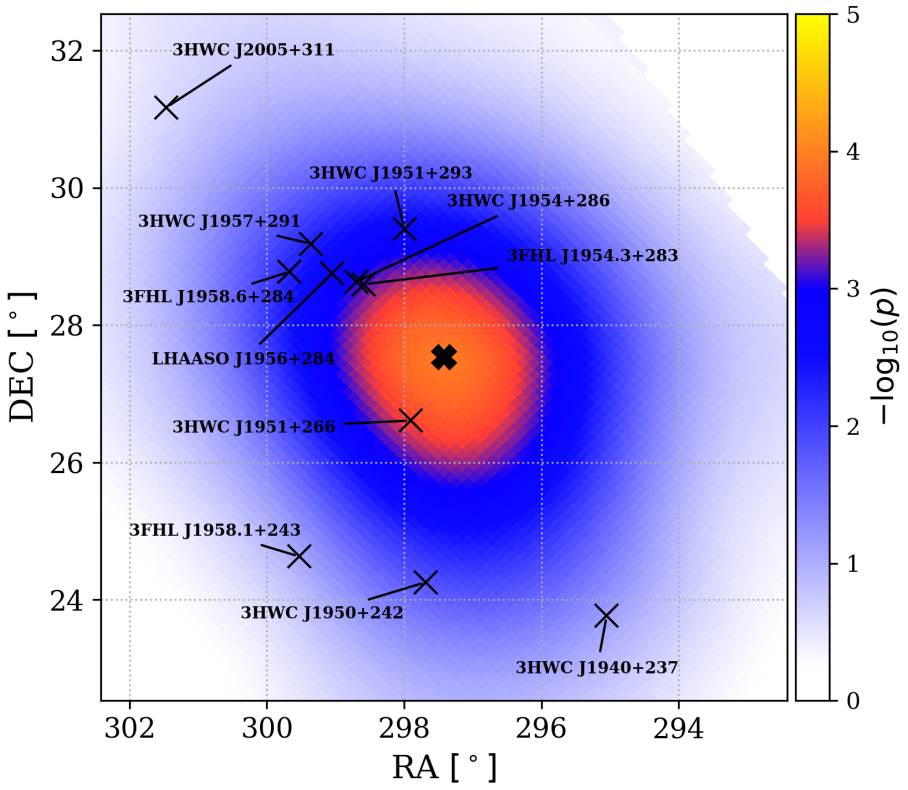

Figure 4.26: The area around the hottest spot in all skymaps (shown in the 2.0° source extension skymap) is evaluated. Known gamma-ray sources in the area have been labeled and are discussed in Table 4.5. The hotspot location is marked with a bold x in the map.

The secondary 0.5° southern hotspot and the surrounding sources can be seen in Figure 4.27. The sources in the area are further discussed in Table 4.6. The closest source to the 0.5° southern hotspot is 3FHL J0804.0-362, which is 0.299° away from the hotspot. This source has been identified as a BL Lac blazar, an extra-galactic source. While the aim of the Galactic plane search was to search for sources within the Galaxy, it is possible the 0.5° southern hotspot is due to an extra-galactic source such as the BL Lac the Fermi-LAT observatory has detected.

The secondary 2.0° southern hotspot and the surrounding sources can be seen in Figure 4.27. The sources in the area are further discussed in Table 4.6. The closest source to the 2.0° southern hotspot is 3FHL J1657.6-465, which is over 1.5° away from the hotspot. Like the hottest spot in each map, the secondary 2.0° is surrounded by several gamma-ray sources, but no sources are

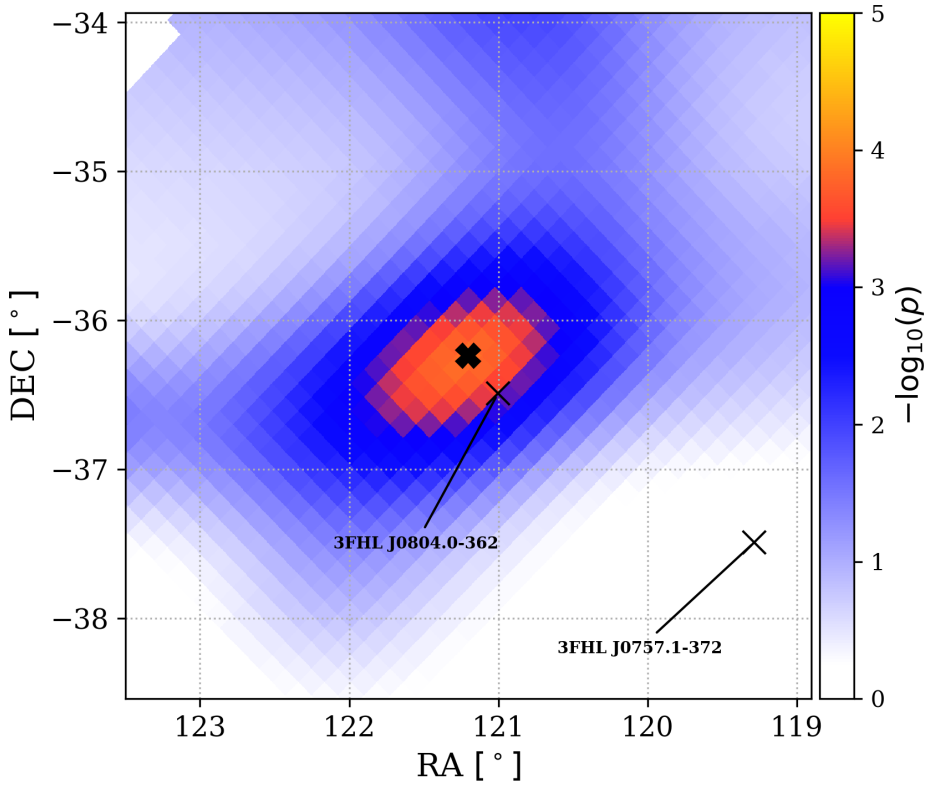

Figure 4.27: The area around the secondary 0.5° southern hotspot is evaluated. Known gamma-ray sources in the area have been labeled and are discussed in Table 4.6. The hotspot location is marked with a bold x in the map.

Source Name	Separation (°)	Extension (°)	TeVCat Assoc	Source Type
3FHL J0804.0-362	0.299	-	-	BLL
3FHL J0757.1-372	1.979	-	-	BLL

Table 4.6: The gamma-ray sources nearby the 0.5° southern hotspot in Figure 4.27. The distance separating each source and the hotspot is measured in degrees. Each source's extension, TeVCat association (TeVCat source type) and source type have been given if any have been reported in their respective catalogs. The only source type included in this table is BLL (BL Lac blazar).

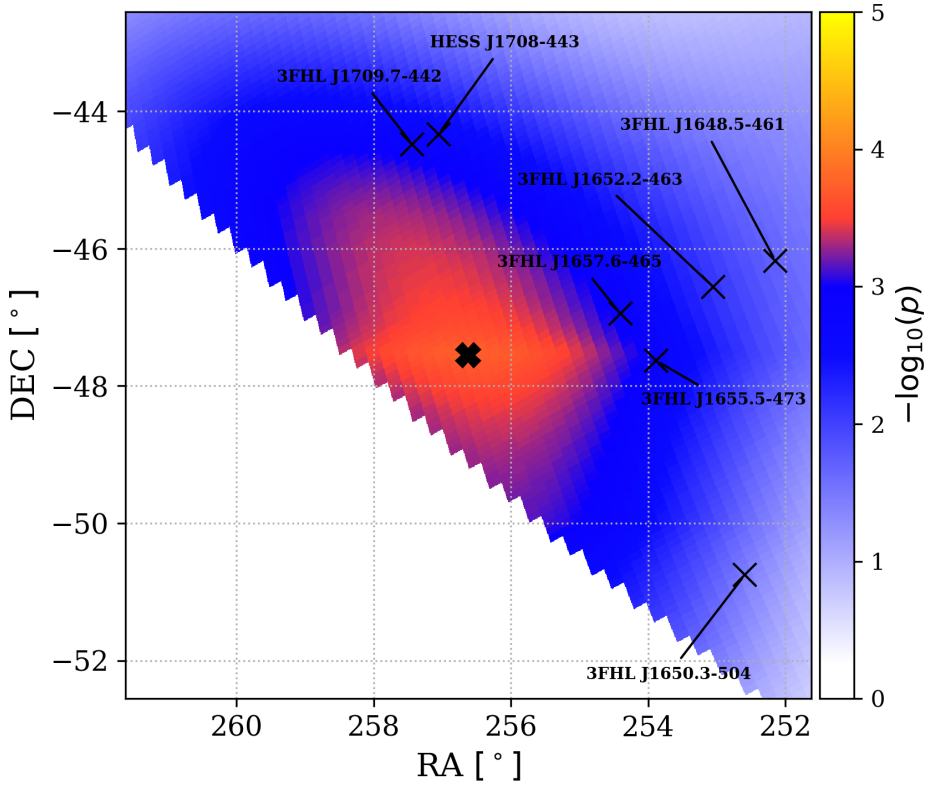

Figure 4.28: The area around the secondary 2.0° southern hotspot is evaluated. Known gamma-ray sources in the area have been labeled and are discussed in Table 4.7. The hotspot location is marked with a bold x in the map.

within the hotspot's significant extended region. With several gamma-ray sources nearby (some associated with a pulsar), it is possible that cosmic rays interact with matter and produce neutrinos in that extended region.

The 0.5° and 2.0° skymaps are overlaid with the sources in the catalog search discussed in Section 4.10, shown in Figure 4.29 and Figure 4.30 respectively. These maps were also overlaid with the entire 3HWC catalog, which can be seen in Figure 4.31 and Figure 4.32 respectively. The skymaps show no obvious correlations with sources in these catalogs.

The results of the Galactic plane scans for source extensions of 0.5°, 1.0°, 1.5°, and 2.0° are all consistent with background, with the highest post-trial significance being 1.53σ for the 1.5° source extension map. However, this significance is lowered even further considering that four

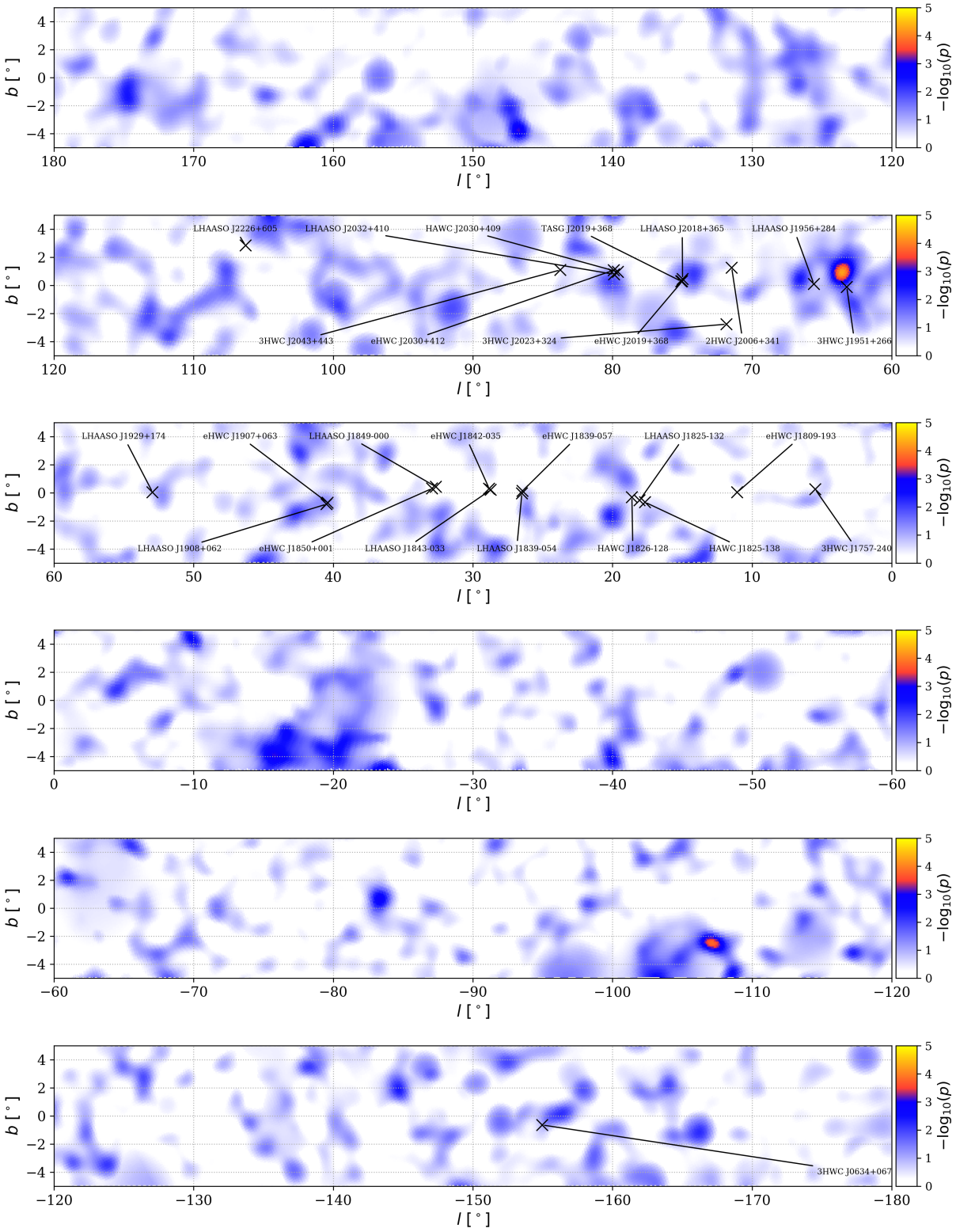

Figure 4.29: Skymap of pre-trial p-values of the Galactic plane for a 0.5° source extension with ROI source locations discussed in Section 4.10.

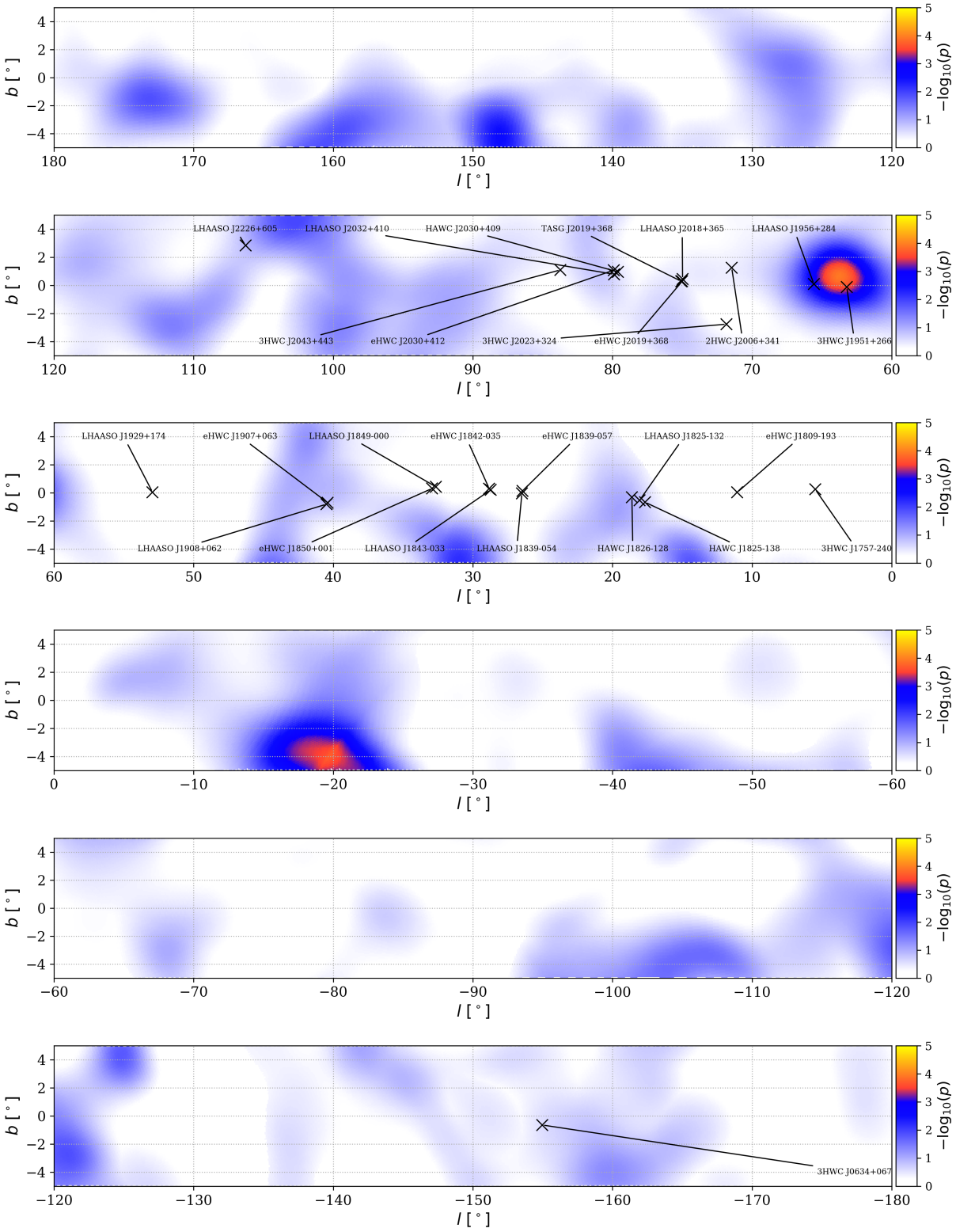

Figure 4.30: Skymap of pre-trial p-values of the Galactic plane for a 2.0° source extension with ROI source locations discussed in Section 4.10.

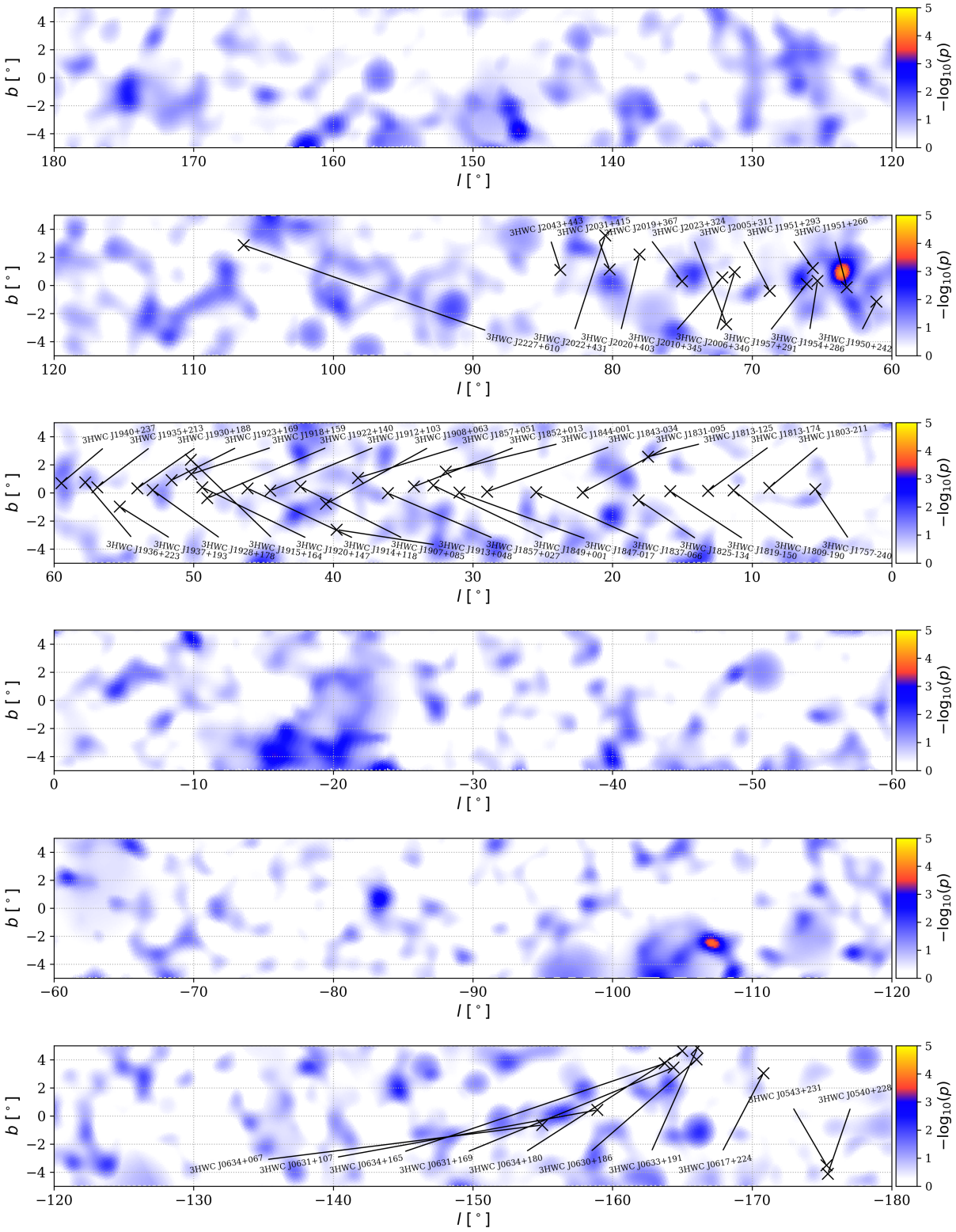

Figure 4.31: Skymap of pre-trial p-values of the Galactic plane for a 0.5° source extension with 3HWC source locations.

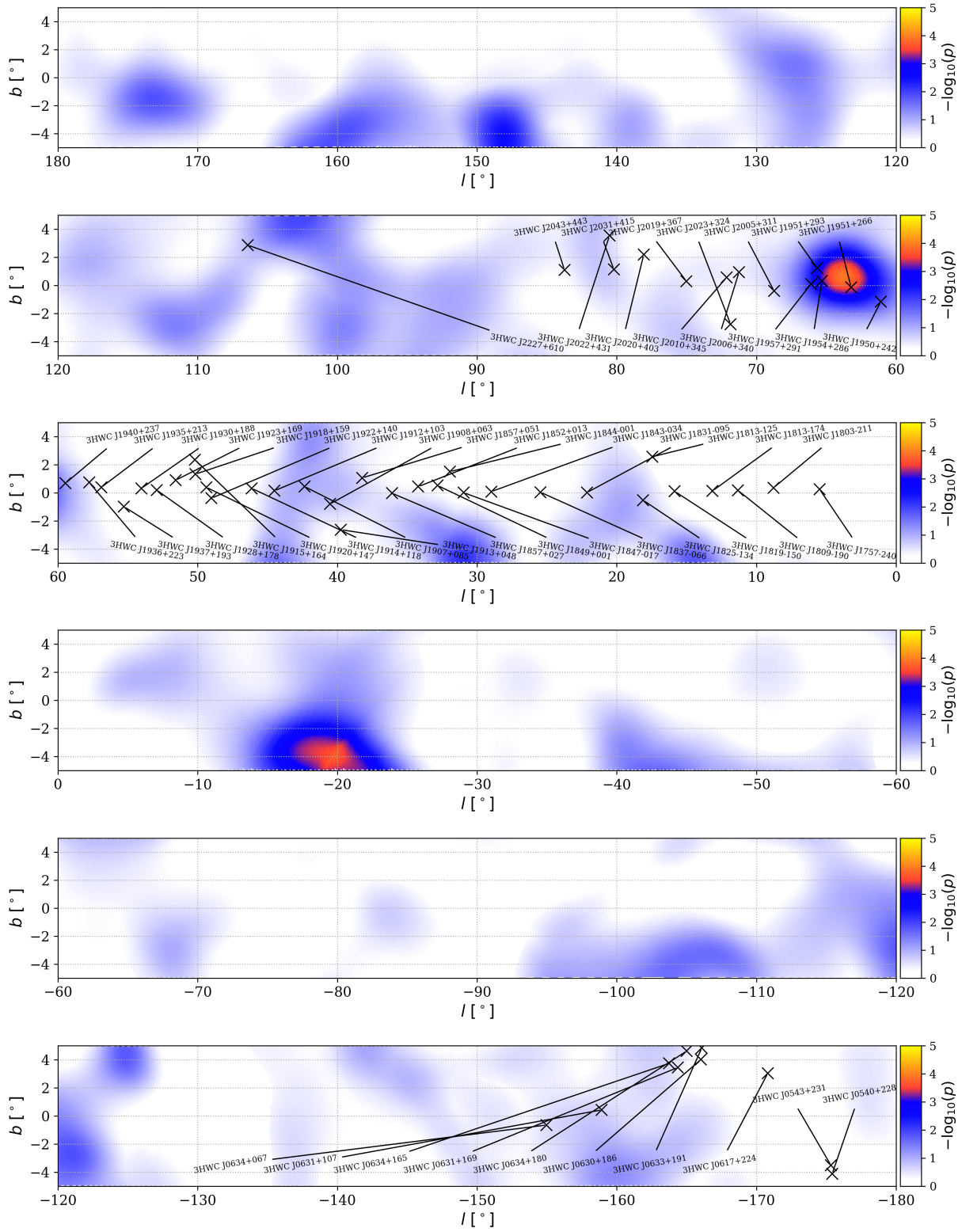

Figure 4.32: Skymap of pre-trial p-values of the Galactic plane for a 2.0° source extension with 3HWC source locations.

Source Name	Separation (°)	Extension (°)	TeVCat Assoc	Source Type
3FHL J1657.6-465	1.620	-	-	-
3FHL J1655.5-473	1.847	0.334	-	-
3FHL J1652.2-463	2.625	0.718	-	-
3FHL J1709.7-442	3.122	-	-	PSR
HESS J1708-443	3.234	0.28	PSR B1706-44 (PSR)	-
3FHL J1648.5-461	3.352	-	-	PSR
3FHL J1650.3-504	4.142	-	-	BCU

Table 4.7: The gamma-ray sources nearby the 2.0° southern hotspot in Figure 4.28. The distance separating each source and the hotspot is measured in degrees. Each source's extension, TeVCat association (TeVCat source type) and source type have been given if any have been reported in their respective catalogs. The following source types are included in this table: PSR (pulsar) and BCU (blazar candidate of unknown type).

skymaps were considered. The 90% CL upper limit fluxes of the hottest spot in each map have been reported. In addition, the location of the hottest spot, as well as two secondary southern hotspots, have been checked in order to find correlation to known gamma-ray sources in several different catalogs. No direct correlations were found for any hotspots, although they were surrounded by several different gamma-ray sources. One possibility is that cosmic rays from these sources are interacting with matter such as a dense molecular cloud in the region, producing neutrinos from an extended region within the area of these sources. Additional analyses in different wavelengths along the electromagnetic spectrum would need to be done in order to determine if an extended object is in the region.

4.10 Source Catalog Search

The Galactic plane scans are blind searches across a broad area of the sky. No prior knowledge of sources are taken into account. However, because a large area of the sky is searched, the end results suffer from the look-elsewhere effect. Performing a search in a few chosen locations would reduce the look-elsewhere effect significantly. This different approach performs more localized searches at a priori locations that will be discussed. This second type of search will be called the source catalog search.

4.10.1 Criteria for Catalog

For this approach, known sources were selected if they were located within the Galaxy, if their gamma-ray emission was extended, and their emission was observed at >TeV energies. There are a few different gamma-ray experiments that have source catalogs that fit these criteria.

HAWC has published numerous different catalogs of high-energy gamma-ray sources as well as in-depth studies of regions of gamma-ray emission along the Galactic plane. The newest, most up-to-date and sensitive catalog of TeV gamma-ray sources from HAWC is the 3HWC catalog discussed in [22]. This catalog is an update to its predecessor, the 2HWC catalog [120]. HAWC has also published a more selective, high-energy catalog of sources emitting in energies above 56 TeV and 100 TeV [136]. This catalog denotes sources with the prefix of eHWC (energy-HAWC). A few different sources in these catalogs had more detailed studies following their discovery, such as 3HWC J1825-134 [137] and 2HWC J2006+341 [138], and larger regions like the Cygnus Cocoon [107].

The Large High Altitude Air Shower Observatory (LHAASO) is a new experiment in the Sichuan province of China that aims to study the gamma-ray sky from 100 GeV to PeV energies [139]. LHAASO discovered multiple different Galactic sources of up to PeV energies [140]. The experiment has also seen extended gamma-ray emission surrounding the pulsar PSR J0622+3749 [141].

Finally, the Tibet air-shower (AS) array in Yangbajing, Tibet, has been observing gamma-rays above TeV energies since 1990. The Tibet AS array has published an in-depth study of the Cygnus region in the 100 TeV energy region [142]. Given the Cygnus region is located in our Galaxy, it is a location to be considered in this catalog. Tibet AS labels their sources as TASG.

4.10.2 Final Catalog

Several different sources matched these criteria, and are shown in Table 4.8. There are a few locations where two or more reported sources (although possibly from the same origin) are too close to distinguish with IceCube's angular resolution. To avoid possible confusion, any sources

that are within a spatial separation of 0.5° or less are combined into one region of interest (ROI). The midpoint between the sources in the ROI is used as the ROI's location. For ROIs that have only one source associated with them, that source is used as the ROI's location.

For the source catalog search, the analysis scans through a range of source extensions (0.5°, 1.0°, 1.5°, 2.0°) at the locations of 20 ROIs discussed in Table 4.8. Therefore, only the source locations are being used for the search. The reported source extensions for each individual source are noted in Table 4.8 only for reference and are not used in the search in an attempt to remain as model-independent and blind as possible. If any ROI has a significance above 2.5σ for any of the four extensions, it was decided in advance that a finer search around that extension would be performed in steps of 0.1°.

Similar to the Galactic plane scan, the pre-trial p-values obtained in the catalog search must take into account the number of tests that are performed. While the Galactic plane scan needed to correct for nearly 3×10^5 tests, the catalog search only needs to account for tests done at 20 different locations for four different extensions. To do this, 50,000 scrambled background skymaps are produced for each extension. The hottest p-value out of the 20 ROI locations and four extensions are put into a background pre-trial p-value distribution. The observed pre-trial p-values are then compared to this distribution to obtain the post-trial p-value.

4.10.3 Initial Results

The pre-trial p-values for each ROI location for the extensions of 0.5°, 1.0°, 1.5°, and 2.0° are shown in Table 4.9. The hottest pre-trial p-value is highlighted in each extension column. For each extension, the hottest pre-trial p-value occurred at the location of ROI-13. Post-trial p-values for these four values were calculated by scrambling 50,000 background skymaps. For each extension, the hottest scrambled pre-trial p-value per extension out of the 20 ROI locations were put into the background pre-trial p-value distributions shown in Figures 4.33a - 4.33d. The four post-trial p-values, as well as their associated extensions, $\hat{n}_s$, and $\hat{\gamma}$ can be seen in the top of Table 4.10. The post-trial significances of the 1.0°, 1.5°, and 2.0° source extension searches for ROI-13 are all

Region of Interest	Right Ascension (°)	Declination (°)	Possible Sources and Associated Extension
ROI-1	95.32	38.21	3HWC J0621+382 (0.5°) [22]
ROI-2	95.47	37.92	LHAASO J0621+3755 (0.4°) [141]
ROI-3	98.66	6.73	3HWC J0634+067 (0.5°) [22]
ROI-4	269.3	-24.09	3HWC J1757-240 (1.0°) [22]
ROI-5	272.46	-19.34	eHWC J1809-193 (0.34°) [136]
ROI-6	276.42	-13.66	HAWC J1825-138 (0.47°) [137] LHAASO J1825-1326 (0.3°) [140]
ROI-7	276.5	-12.86	HAWC J1826-128 (0.2°) [137]
ROI-8	279.86	-5.73	eHWC J1839-057 (0.34°) [136] LHAASO J1839-0545 (0.3°) [140]
ROI-9	280.73	-3.58	eHWC J1842-035 (0.39°) [136] LHAASO J1843-0338 (0.3°) [140]
ROI-10	282.47	0.05	eHWC J1850+001 (0.37°) [136] LHAASO J1849-0003 (0.3°) [140]
ROI-11	286.98	6.34	eHWC J1907+063 (0.67°) [136] LHAASO J1908+0621 (0.3°) [140]
ROI-12	292.25	17.75	LHAASO J1929+1745 (0.3°) [140]
ROI-13	297.9	26.61	3HWC J1951+266 (0.5°) [22]
ROI-14	299.05	28.75	LHAASO J1956+2845 (0.3°) [140]
ROI-15	301.55	34.35	2HWC J2006+341 (0.72°) [138]
ROI-16	304.90	36.82	eHWC J2019+368 (0.3°) [136] LHAASO J2018+3651 (0.3°) [140] TASG J2019+368 (0.28°) [142]
ROI-17	305.81	32.44	3HWC J2023+324 (1.0°) [22]
ROI-18	307.81	41.07	eHWC J2030+412 (0.18°) [136] LHAASO J2032+4102 (0.3°) [140] HAWC J2030+409 (2.13°) [107]
ROI-19	310.89	44.3	3HWC J2043+443 (0.5°) [22]
ROI-20	336.75	60.95	LHAASO J2226+6057 (0.3°) [140]

Table 4.8: Locations of the regions of interest that will be evaluated along with possible sources that could produce astrophysical neutrinos.

above 2.5σ.

In order to calculate the best overall observed p-value, post-trial corrections have to account

for not only the 20 different ROI locations searched, but also the four extensions searched as well. The best pre-trial p-value was observed at ROI-13 for a source extension of 1.5°. The hottest p-value over all ROI locations and source extensions was taken in each of the 50,000 scrambled skymaps. The background pre-trial p-value distribution accounting for all 20 ROI locations and all four source extensions can be seen in Figure 4.33e. The observed pre-trial p-value at ROI-13 for a source extension of 1.5° was compared to this distribution, and an overall post-trial p-value was obtained. This can be seen in the bottom part of Table 4.10. The overall hottest post-trial p-value at the location of ROI-13 for a source extension of 1.5° results in a significance of 2.63σ.

Region of Interest	p_{pre} for $\sigma_s = 0.5°$	p_{pre} for $\sigma_s = 1.0°$	p_{pre} for $\sigma_s = 1.5°$	p_{pre} for $\sigma_s = 2.0°$
ROI-1	6.49×10^{-1}	6.70×10^{-1}	6.81×10^{-1}	6.87×10^{-1}
ROI-2	6.43×10^{-1}	6.66×10^{-1}	6.76×10^{-1}	6.86×10^{-1}
ROI-3	1.05×10^{-1}	1.33×10^{-1}	2.01×10^{-1}	2.81×10^{-1}
ROI-4	3.08×10^{-1}	3.04×10^{-1}	7.14×10^{-1}	7.28×10^{-1}
ROI-5	5.08×10^{-1}	5.36×10^{-1}	5.97×10^{-1}	6.39×10^{-1}
ROI-6	3.38×10^{-1}	1.72×10^{-1}	1.44×10^{-1}	1.58×10^{-1}
ROI-7	2.87×10^{-1}	1.03×10^{-1}	8.64×10^{-2}	1.09×10^{-1}
ROI-8	5.64×10^{-1}	8.47×10^{-1}	7.89×10^{-1}	7.15×10^{-1}
ROI-9	5.14×10^{-1}	5.73×10^{-1}	6.76×10^{-1}	7.26×10^{-1}
ROI-10	7.12×10^{-1}	7.57×10^{-1}	7.07×10^{-1}	6.33×10^{-1}
ROI-11	6.29×10^{-2}	1.00×10^{-2}	1.20×10^{-1}	1.67×10^{-1}
ROI-12	1.38×10^{-1}	3.42×10^{-1}	6.70×10^{-1}	6.54×10^{-1}
ROI-13	$\mathbf{1.07 \times 10^{-2}}$	$\mathbf{3.87 \times 10^{-4}}$	$\mathbf{1.40 \times 10^{-4}}$	$\mathbf{2.53 \times 10^{-4}}$
ROI-14	1.15×10^{-1}	7.26×10^{-3}	1.69×10^{-3}	1.44×10^{-3}
ROI-15	5.52×10^{-1}	6.19×10^{-1}	4.45×10^{-1}	3.93×10^{-1}
ROI-16	5.92×10^{-2}	1.21×10^{-1}	2.69×10^{-1}	3.46×10^{-1}
ROI-17	6.08×10^{-1}	6.70×10^{-1}	6.85×10^{-1}	6.37×10^{-1}
ROI-18	7.82×10^{-2}	1.20×10^{-1}	2.15×10^{-1}	2.81×10^{-1}
ROI-19	4.21×10^{-1}	5.79×10^{-1}	5.35×10^{-1}	4.50×10^{-1}
ROI-20	6.45×10^{-1}	3.51×10^{-1}	1.74×10^{-1}	1.26×10^{-1}

Table 4.9: Summary of observed pre-trial p-values for each ROI for the four different source extensions evaluated. The smallest p-value for each extension is reported in bold in the table. The smallest p-value for each extension occurs at the location of ROI-13. Post-trial corrections will be applied for these four p-values as well as the overall smallest p-value of 1.40×10^{-4} for a source extension of 1.5° at ROI-13.

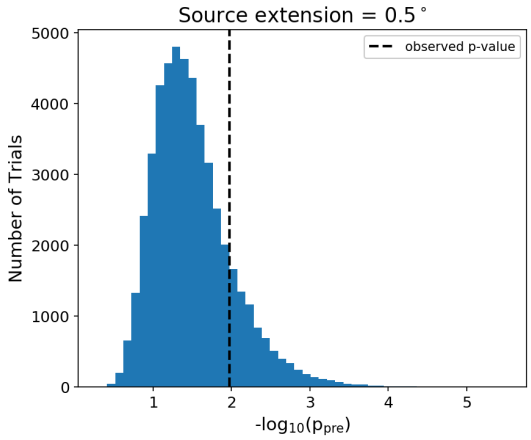

(a) Post-trial p-value: 1.60×10^{-1}

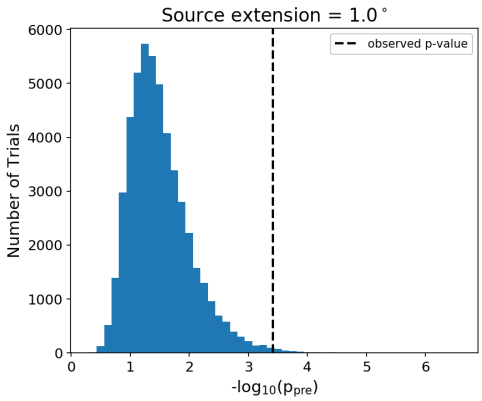

(b) Post-trial p-value: 5.30×10^{-3}

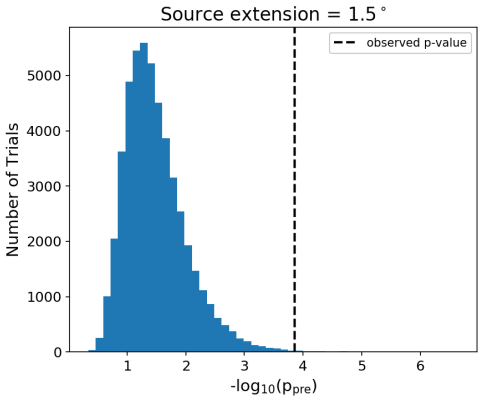

(c) Post-trial p-value: 1.92×10^{-3}

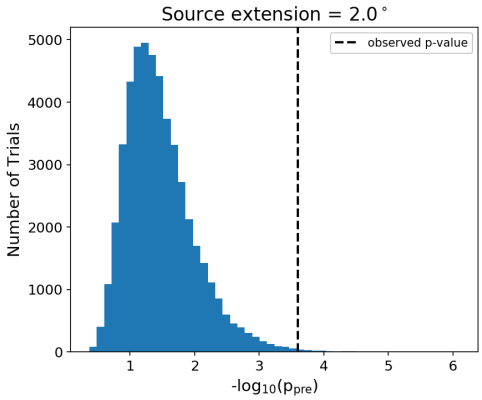

(d) Post-trial p-value: 2.94×10^{-3}

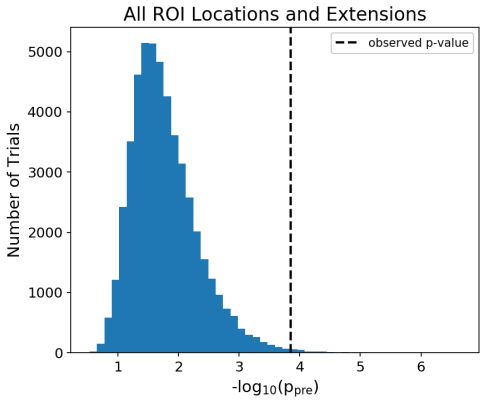

(e) Post-trial p-value: 4.32×10^{-3}

Figure 4.33: Distribution of the hottest ROI location in 50,000 background scrambled skymaps for each extension (Figures 4.33a - 4.33d). The hottest extension in each of the 50,000 background scrambled skymaps is then obtained to create the distribution of the hottest ROI location and extension in the 50,000 background scrambled skymaps (Figure 4.33e).

Region of Interest	Extension (°)	$\hat{n}_s$	$\hat{\gamma}$	p_{pre} (σ_{pre})	p_{post} (σ_{post})
ROI-13	0.5°	49.11	2.96	1.07×10^{-2} (2.30σ)	1.60×10^{-1} (0.99σ)
ROI-13	1.0°	99.33	3.03	3.87×10^{-4} (3.36σ)	5.30×10^{-3} (2.56σ)
ROI-13	1.5°	141.52	3.07	1.40×10^{-4} (3.63σ)	1.92×10^{-3} (2.89σ)
ROI-13	2.0°	175.29	3.14	2.53×10^{-4} (3.48σ)	2.94×10^{-3} (2.75σ)
ROI-13	1.5°	141.52	3.07	1.40×10^{-4} (3.63σ)	4.32×10^{-3} (2.63σ)

Table 4.10: Summary of the best observed pre-trial p-values for each source extension evaluated (top). Post trials corrections were applied by obtaining the hottest ROI location in 50,000 background scrambled skymaps for each extension (see Figures 4.33a - 4.33d). Finally, the hottest extension in each of the 50,000 background scrambled skymaps was obtained to calculate the overall best post-trial p-value for all ROIs and extensions (bottom). The pre-trial p-values of those 50,000 background scrambles can be seen in Figure 4.33e. The observed number of signal events, $\hat{n}_s$ and the spectral index, $\hat{\gamma}$, are also reported for all cases.

4.10.4 Further Investigation of ROI-13

At the location of ROI-13, the source extensions of 1.0°, 1.5°, and 2.0° all have a post-trial significance above the threshold significance of 2.5σ. A finer search in extension at the location of ROI-13 was performed in accordance with the prescription decided on prior to unblinding the data. ROI-13 was fit to source extensions ranging from 1.0° to 2.0° in steps of 0.1° in order to determine the most significant extension. Extensions below 1.0° were not analyzed to save processing time. The pre-trial p-values, as well as the fitted $\hat{n}_s$ and $\hat{\gamma}$, for the 11 extensions for ROI-13 can be seen at the top of Table 4.11. The hottest pre-trial p-value obtained is 1.27×10^{-4} at a source extension of 1.7°.

In order to properly perform post-trial corrections, the 20 different ROI locations must be accounted for as well as all of the possible source extensions. Since it was possible that a source extension of 0.5° could have had a post-trial significance above the threshold significance of 2.5σ, there are 16 possible extensions that could have been measured in the finer grid search. The possible source extensions range from 0.5° to 2.0° in steps of 0.1°. To calculate the post-trial p-value and significance of the finer scan through source extension, the hottest pre-trial p-value over all ROI locations and 16 source extensions from 50,000 background scrambled skymaps are

Extension (°)	$\hat{n}_s$	$\hat{\gamma}$	p_{pre} (σ_{pre})
1.0°	99.33	3.03	3.87×10^{-4} (3.36σ)
1.1°	108.27	3.03	3.80×10^{-4} (3.37σ)
1.2°	116.95	3.04	2.67×10^{-4} (3.46σ)
1.3°	125.43	3.05	2.07×10^{-4} (3.53σ)
1.4°	133.63	3.06	2.07×10^{-4} (3.53σ)
1.5°	141.52	3.07	1.40×10^{-4} (3.63σ)
1.6°	149.03	3.08	1.73×10^{-4} (3.58σ)
1.7°	**156.12**	**3.10**	$\mathbf{1.27 \times 10^{-4}}$ **(3.66σ)**
1.8°	163.06	3.12	2.27×10^{-4} (3.51σ)
1.9°	169.44	3.13	1.67×10^{-4} (3.59σ)
2.0°	175.29	3.14	2.53×10^{-4} (3.48σ)
Extension (°)	$\hat{n}_s$	$\hat{\gamma}$	p_{post} (σ_{post})
1.7°	156.12	3.10	4.50×10^{-3} (2.61σ)

Table 4.11: Summary of the observed pre-trial p-values for each source extension evaluated at the location of ROI-13: (RA,DEC)=(297.9°, 26.61°) (top). The observed number of signal events, $\hat{n}_s$ and the spectral index, $\hat{\gamma}$, are also reported. A post-trial p-value was obtained for the hottest extension (1.7°) by taking into account all 20 ROI locations and 16 possible extensions in the finer scan, ranging from 0.5° to 2.0° in steps of 0.1°.

considered. The distribution of these background pre-trial p-values can be seen in Figure 4.34. Comparing the hottest observed pre-trial p-value at source extension of 1.7° to this distribution, one obtains the observed post-trial p-value seen in the bottom of Table 4.11. The resulting final post-trial significance for ROI-13 with a source extension of 1.7° is 2.61σ. This result is interesting, considering that the location of ROI-13 is about 1.0° away from the hotspot in the Galactic plane scan for a source extension of 1.5°. If a dedicated search in this region were to be performed, the reduced trials factor and improved analysis techniques may push the significance above 3σ, suggesting evidence of a neutrino source, and therefore, a source of cosmic rays.

4.10.5 Binomial Test for Sub-Threshold Populations in Catalog

If search results are consistent with background, p-values should distribute uniformly between 0 and 1. However, if there is a small population of sources slightly below the threshold of detection,

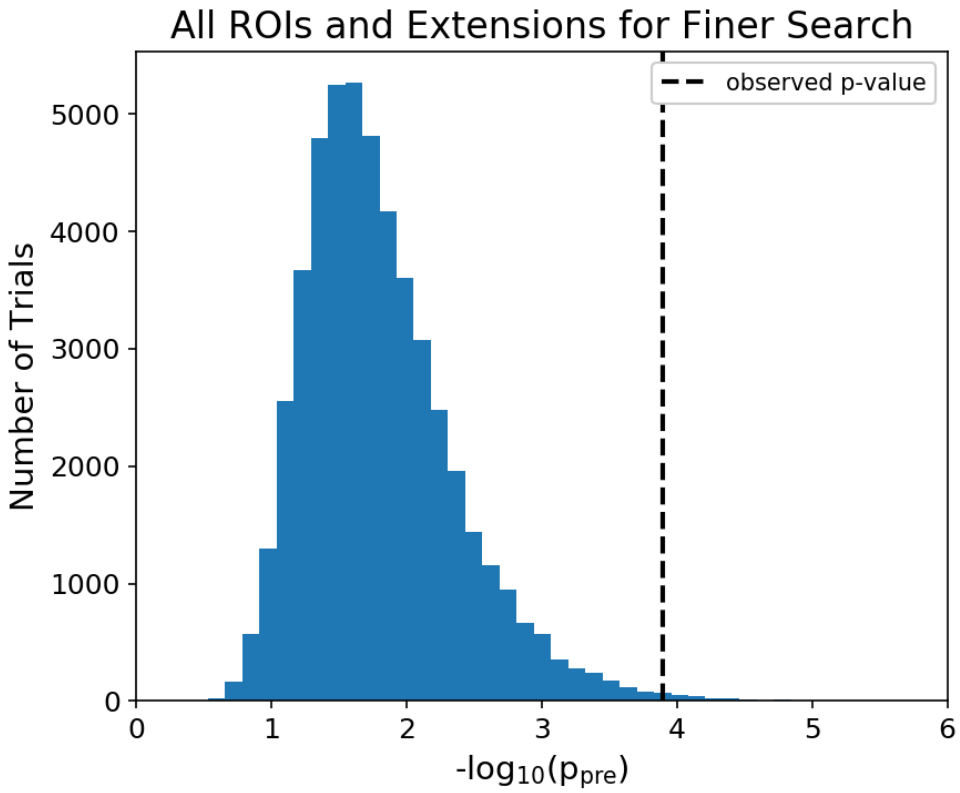

Figure 4.34: Distribution of pre-trial p-values of the hottest extension in 50,000 background scrambled skymaps for all 20 ROI locations and all 16 extensions considered, ranging from 0.5° to 2.0° in steps of 0.1°. The hottest observed pre-trial p-value in Table 4.11 can be seen by the dashed black line and is compared to the distribution to obtain an observed post-trial p-value.

then there will be a excess of small p-values over the background expectation. The p-value at the k-th source in a list of N sources is defined as p_k. The probability that background would have k or more locations with p-values less than p_k is defined as p_{bkg}. Since this results in counting how many times a p-value is less than p_k, p_{bkg} can be calculated with the binomial distribution:

$$p_{\text{bkg}} = \sum_{i=k}^{N} \binom{N}{i} p_k^i \, (1 - p_k)^{N-1} \, . \tag{4.13}$$

Since the catalog of 20 ROIs was tested at four different extensions, the extension that produced the smallest p-value for each ROI is used for the binomial test. The pre-trial p-value at each ROI is then trials-corrected to account for the four different extensions that were tested. The post-trial p-values for the catalog are then sorted and fed into the binomial distribution.

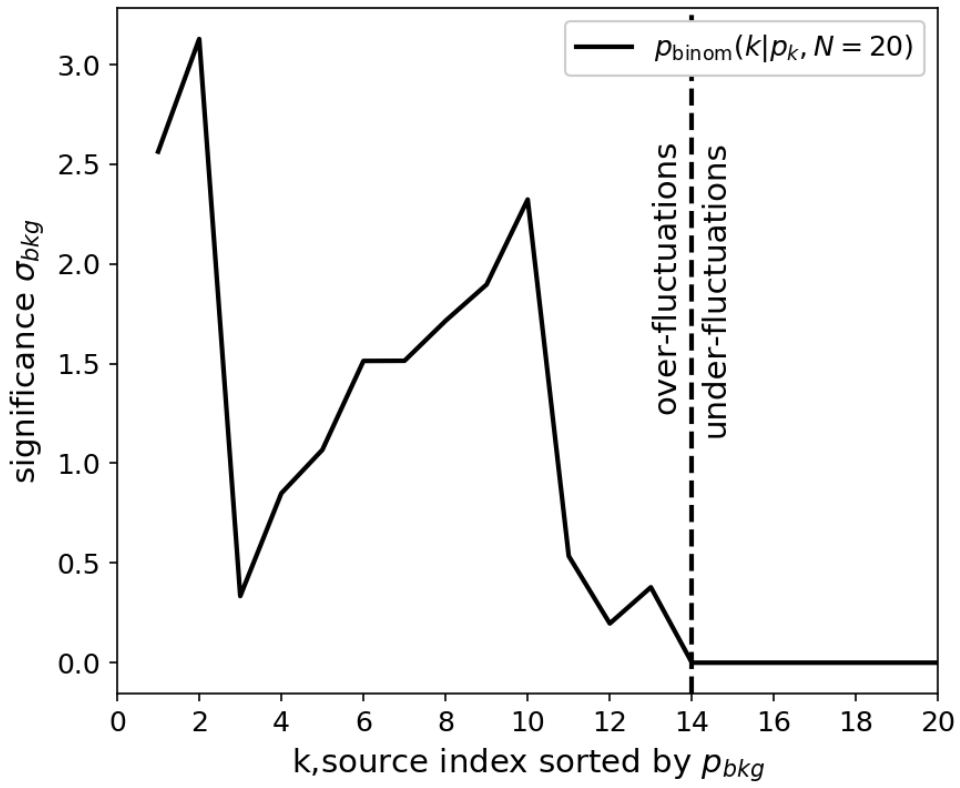

Figure 4.35: Significances of the pre-trial binomial p-values obtained for k sources that have p-values lower than p_k. The highest significance of 3.13σ is obtained when $k = 2$. A source index of $k = 14$ represents the first source which had $\hat{n}_s = 0$ and represents under-fluctuations. Every source index after $k = 14$ is automatically set to a significance 0σ.

The results of the binomial test are shown in Figure 4.35. The first source index where the fit resulted in an observed $\hat{n}_s = 0$ is $k = 14$. Above that source index, the binomial test is unable to give indication of a sub-threshold population as the observed number of events is at or below the estimated background level. Because of this, the significance at these values is automatically set to zero. The value of p_{bkg} that achieves the largest significance occurs at a source index of $k = 2$, with $p_{\text{bkg}} = 8.80 \times 10^{-4}$ which corresponds to a significance of 3.13σ.

The binomial distribution is calculated at 20 different ROI locations for the best-fitting source extension per ROI. To account for all the tests conducted at the different locations and extensions, 50,000 background scrambled skymaps were produced for each extension. The best-fitting extension was chosen for each of the 20 locations, were fed into the binomial distribution for each of

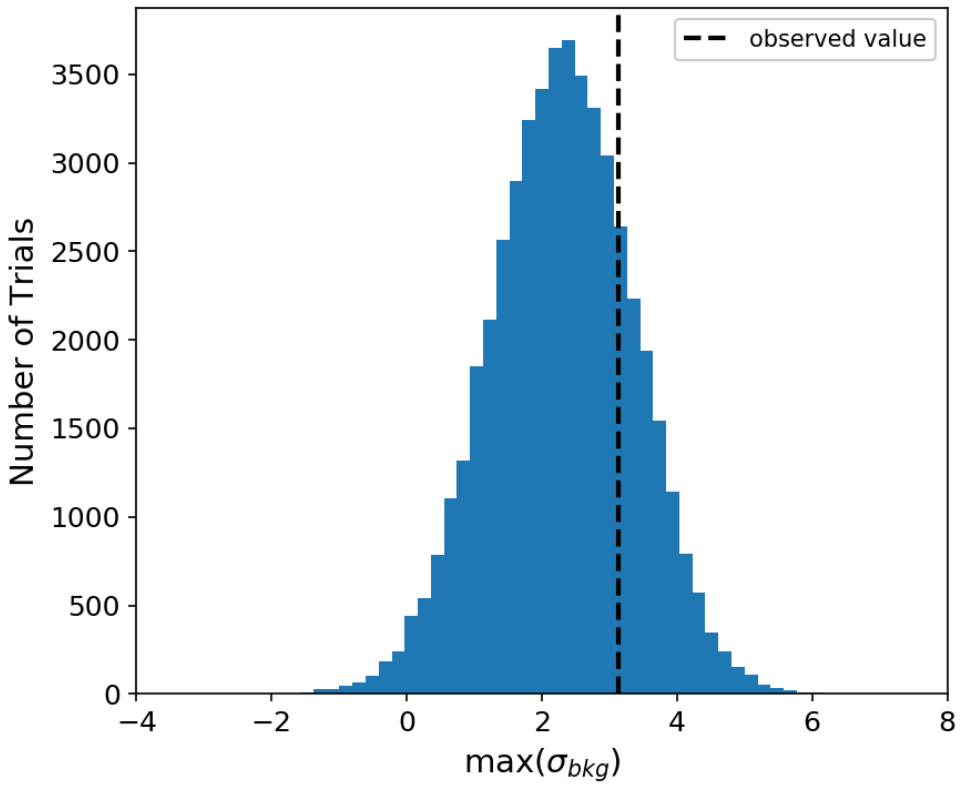

Figure 4.36: The maximum significance obtained from the binomial distribution for each of the 50,000 background scrambled skymaps. The observed maximum pre-trial significance is shown by the dashed vertical line. With the background distribution given, the resulting observed post-trial significance is 0.78σ.

the 50,000 background skymaps. This results in 50,000 pure-background binomial distributions. The most significant σ_{bkg} for each of the 50,000 background binomial distributions can be seen in Figure 4.36. The observed pre-trial significance of 3.13σ is shown by the dashed vertical line. The observed post-trial significance is obtained by calculating the probability of a pure-background binomial distribution resulting in a significance higher than the observed pre-trial significance. With the background significances shown in Figure 4.36, the observed post-trial p_{bkg} is 0.22, which corresponds to an observed post-trial significance of 0.78σ.

The results of the binomial test are compatible with background and show that there is no evidence of a small population of sources slightly below the detection threshold. The two ROI regions that contribute to the pre-trial significance of 3.13σ are ROI-13 and ROI-14, which are

2.37° apart. Correlations between source locations due to their proximity to each other were taken into account with the 50,000 background scrambled skymaps used to perform post-trial calculations.

4.10.6 Upper Limit on the Neutrino Flux from the ROIs

The results from the catalog search are consistent with background observations. However, upper limits can be placed on the neutrino emission from the 20 different ROI locations. Since four extensions were tested for each ROI location, upper limits will be calculated for the extensions with the smallest and largest pre-trial p-value for each ROI. Upper limits are calculated the same way as described in Section 4.9.3, except now at a pivot energy of 50 TeV.

The 90% upper-limit fluxes for the source extensions that achieve the smallest and largest pre-trial p-values for each ROI are seen in Figures 4.37 and 4.38 respectively. The upper limits are compared to the sensitivities discussed in Section 4.6. The values of the 90% upper-limit fluxes and their associated extension, fitted number of signal particles $\hat{n}_s$, and their fitted spectral index $\hat{\gamma}$ are shown in Tables 4.12 and 4.13 for the extensions with the smallest and largest pre-trial p-value respectively.

The 90% upper-limt fluxes can be compared to the expected neutrino emission from the gamma-ray sources that were selected to form the catalog of 20 ROIs. As discussed in Section 1.2.2, cosmic rays can interact with gas or radiation fields near their source, producing neutral and charged pions. The decays of these pions are what produce gamma rays and neutrinos. In radiation fields, the $p\gamma$ interactions produce pions at a ratio of $\pi^{\pm} : \pi^0 = 1 : 1$. For pp interactions, pions are produced at a ratio of $\pi^{\pm} : \pi^0 = 2 : 1$. Since pp interactions are believed to be the dominant hadronic process within the Galaxy for producing gamma-rays, the theoretical neutrino fluxes will be calculated under the assumption that the gamma-ray flux from the sources in the catalog is purely from pp interactions.

The gamma-ray differential flux and its associated spectral index are defined as ϕ_γ and γ. Under the assumption of 100% hadronic emission from pp interactions, the neutrino differential flux from

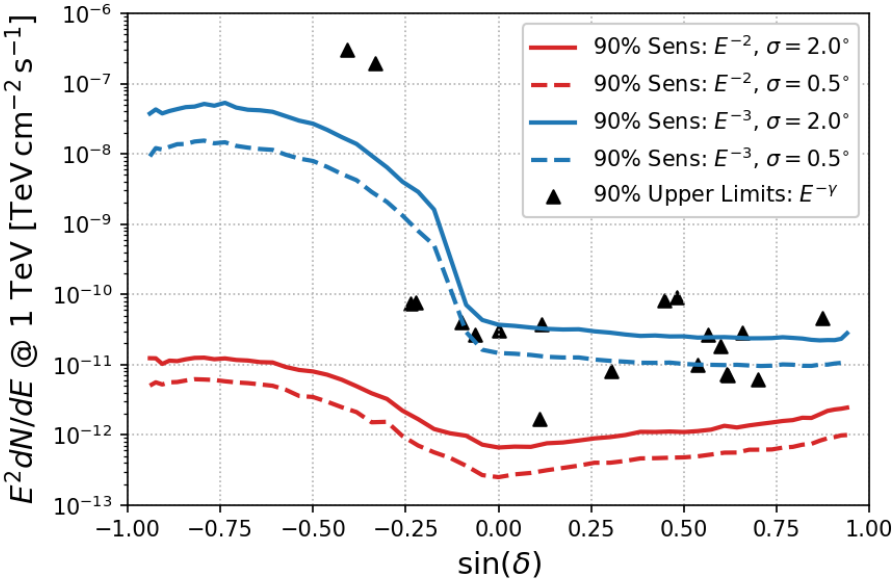

Figure 4.37: The 90% upper-limit fluxes at a pivot energy of 1 TeV for the source extensions with the smallest pre-trial p-value for each ROI, shown as the black triangles. The upper limits are compared to the 90% CL sensitivity curves with source extensions of 0.5° (dashed lines) and 2.0° (solid lines) at spectral indices of 2.0 (red lines) and 3.0 (blue lines).

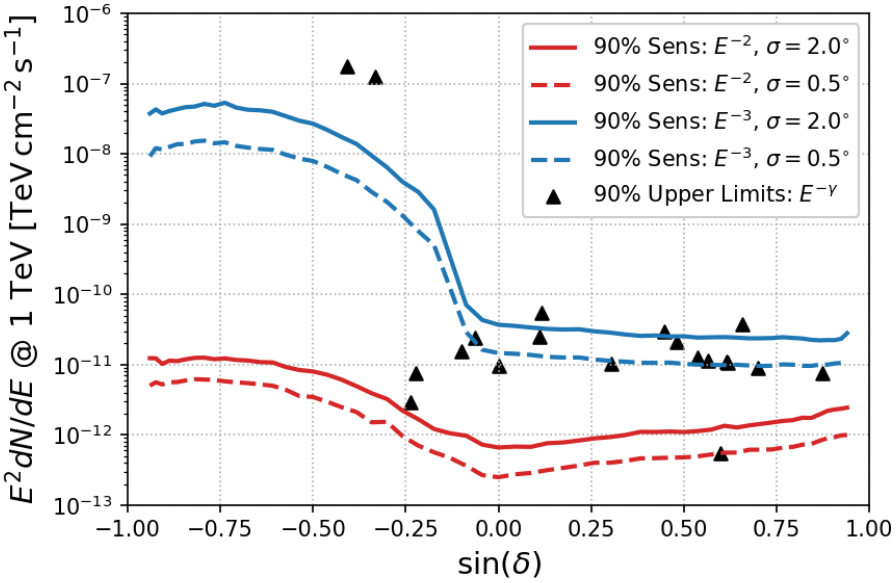

Figure 4.38: The 90% upper-limit fluxes at a pivot energy of 1 TeV for the source extensions with the largest pre-trial p-value for each ROI, shown as the black triangles. The upper limits are compared to the 90% CL sensitivity curves with source extensions of 0.5° (dashed lines) and 2.0° (solid lines) at spectral indices of 2.0 (red lines) and 3.0 (blue lines).

Region of Interest	Extension (°)	$\hat{n}_s$	$\hat{\gamma}$	$\phi_{90\%}$ at 50 TeV ($\mathrm{TeV}^{-1}\mathrm{cm}^{-2}\mathrm{s}^{-1}$)
ROI-1	0.5°	0.0	3.00	5.64×10^{-17}
ROI-2	0.5°	0.0	3.00	5.79×10^{-17}
ROI-3	0.5°	32.9	3.56	3.39×10^{-17}
ROI-4	1.0°	14.1	3.54	2.92×10^{-13}
ROI-5	0.5°	0.0	3.75	8.19×10^{-14}
ROI-6	1.5°	7.0	2.39	6.54×10^{-15}
ROI-7	1.5°	9.2	2.40	6.48×10^{-15}
ROI-8	0.5°	9.3	3.08	2.34×10^{-16}
ROI-9	0.5°	0.6	4.00	4.30×10^{-18}
ROI-10	2.0°	18.9	3.07	1.82×10^{-16}
ROI-11	0.5°	7.8	2.14	3.90×10^{-16}
ROI-12	0.5°	18.6	2.54	3.87×10^{-16}
ROI-13	1.5°	141.5	3.07	4.91×10^{-16}
ROI-14	2.0°	149.5	3.18	3.59×10^{-16}
ROI-15	2.0°	31.2	4.00	4.23×10^{-18}
ROI-16	0.5°	24.7	2.83	2.76×10^{-16}
ROI-17	0.5°	1.9	3.21	3.51×10^{-17}
ROI-18	0.5°	30.6	3.52	2.93×10^{-17}
ROI-19	0.5°	6.5	2.63	2.05×10^{-16}
ROI-20	2.0°	85.0	3.38	8.11×10^{-17}

Table 4.12: The 90% upper-limit fluxes at a pivot energy of 50 TeV for the source extensions with the smallest pre-trial p-value for each ROI. The associated extension, fitted number of signal particles $\hat{n}_s$, and the fitted spectral index $\hat{\gamma}$ are shown.

a source can be calculated. Since muon neutrinos are used in this analysis due to their pointing resolution, the theoretical muon neutrino differential flux will be presented. At the same energy, the muon neutrino flux can be calculated as [143]:

$$\phi_\nu(E_\nu) = 2^{1-\gamma}\phi_\gamma(E_\gamma) \tag{4.14}$$

where $E_\nu = E_\gamma$ and γ is the spectral index of the gamma-ray emission. The conversion between muon neutrino and gamma-ray flux can be simplified to [143]:

$$\phi_\nu(E_\nu) = 2\phi_\gamma(E_\gamma) \tag{4.15}$$

Region of Interest	Extension (°)	$\hat{n}_s$	$\hat{\gamma}$	$\phi_{90\%}$ at 50 TeV ($\mathrm{TeV}^{-1}\mathrm{cm}^{-2}\mathrm{s}^{-1}$)
ROI-1	2.0°	0.0	2.75	2.29×10^{-16}
ROI-2	2.0°	0.0	2.75	2.32×10^{-16}
ROI-3	2.0°	50.9	3.59	4.27×10^{-17}
ROI-4	2.0°	0.0	3.50	2.01×10^{-13}
ROI-5	2.0°	0.0	3.50	1.42×10^{-13}
ROI-6	0.5°	1.4	2.09	8.05×10^{-16}
ROI-7	0.5°	2.3	2.22	1.29×10^{-15}
ROI-8	1.0°	0.0	3.25	4.57×10^{-17}
ROI-9	2.0°	0.0	4.00	3.91×10^{-18}
ROI-10	1.0°	0.0	3.00	7.79×10^{-17}
ROI-11	2.0°	41.4	2.58	1.01×10^{-15}
ROI-12	1.5°	0.0	2.75	2.19×10^{-16}
ROI-13	0.5°	49.1	2.96	2.74×10^{-16}
ROI-14	0.5°	29.0	3.05	1.39×10^{-16}
ROI-15	1.0°	4.3	4.00	1.83×10^{-18}
ROI-16	2.0°	4.7	1.76	5.49×10^{-16}
ROI-17	1.5°	0.0	3.00	1.01×10^{-16}
ROI-18	2.0°	42.6	3.20	1.37×10^{-16}
ROI-19	1.0°	3.7	2.78	1.70×10^{-16}
ROI-20	0.5°	3.7	3.08	4.35×10^{-17}

Table 4.13: The 90% upper-limit fluxes at a pivot energy of 50 TeV for the source extensions with the largest pre-trial p-value for each ROI. The associated extension, fitted number of signal particles $\hat{n}_s$, and the fitted spectral index $\hat{\gamma}$ are shown.

when $E_\nu = E_\gamma/2$. Using these conversions, the theoretical muon neutrino flux from the gamma-ray sources included to create the ROI catalog are obtained.

The 90% upper-limit fluxes from the extensions with the smallest and largest pre-trial p-values are compared to the theoretical muon neutrino fluxes in Tables 4.14 and 4.15 respectively. Both the upper limits and the theoretical fluxes are at a pivot energy of 50 TeV. By comparing the upper limits to the theoretical fluxes, information about the sources can be inferred. If $\phi_{90\%} > \phi_\nu$, this means that the experiment is not sensitive enough to deduce that the gamma-ray emission from

that source is 100% hadronic. If $\phi_{90\%} < \phi_\nu$, the non-observation of muon neutrinos by IceCube can constrain a scenario where the emission was 100% hadronic. Under this condition, it can be assumed that the gamma-ray emission from that source is not 100% hadronic, and at least part of its emission comes from leptonic origins. Several ROIs fall under this category, meaning that the emission of the gamma-ray sources for those locations is not 100% hadronic. For ROI-13, the most significant region in the catalog, $\phi_{90\%} > \phi_\nu$ for both upper limits at extensions with the smallest and largest pre-trial p-values. IceCube has yet to be sensitive enough to probe the physics in this region. If the results for ROI-13 were weak evidence of a real flux, it is possible that the region is opaque to gamma rays.

4.11 Summary

This chapter describes a search for extended neutrino sources along the Galactic plane with nine years of IceCube data. Extended gamma-ray emission has been detected in the Galaxy, and neutrinos are expected from these gamma-ray sources if the emission is hadronic in origin. The Galaxy is filled with clouds of gas and radiation fields that can be large in comparison to sources. If cosmic rays interact in these regions, extended neutrino emission is expected.

This analysis introduced the method of source masking to reduce signal contamination in the background, as opposed to the signal subtraction method widely used in IceCube. Source masking is able to remove signal from multiple different sources at once, making it ideal to use for a Galactic plane analysis where multiple sources are expected. The search for extended neutrino sources along the Galactic plane was performed two different ways. First, blind scans across the Galactic plane were performed, searching for sources with extensions ranging from 0.5° to 2.0°. Secondly, extended sources were searched for at a priori locations. These locations were chosen due to their proximity to known extended gamma-ray sources within the Galaxy. Each location was fit to a range of extensions unassociated with the extension of gamma-ray emission.

The results of the Galactic plane scan and the catalog search were presented in Sections 4.9 and 4.10 respectively. No significant evidence for extended neutrino sources were found in either

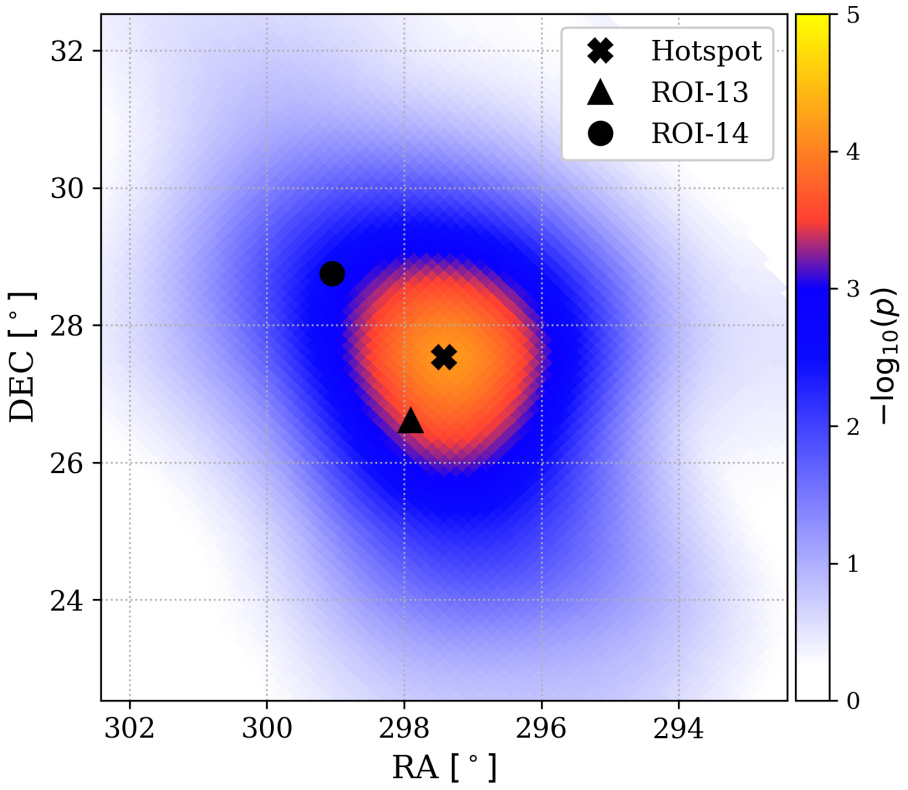

Figure 4.39: The location of the hottest spot in the Galactic plane scan searching for neutrino sources with an extension of 1.5°. The locations of the two most significant ROIs in the catalog search are marked with a triangle (ROI-13) and a circle (ROI-14).

search. However, the most significant location in the blind scans across the plane is 1.017° away from the most significant location in the catalog, ROI-13. The second-most significant location in the catalog is ROI-14, which is 1.883° away from the hostpot location in the Galactic plane scan. The hotspot along with the locations of ROI-13 and ROI-14 can be seen in Figure 4.39. With the most significant locations in both searches being within a few degrees of each other, follow-up searches in this location are of interest. With improved analysis techniques such as a multi-messenger search or including different profiles of source extension other than the standard 2D Gaussian, a search dedicated to this location could have a significant post-trial result.

Region of Interest	Possible Sources and Associated Extension	ϕ_ν from pp Collisions $\left(\text{TeV}^{-1}\,\text{cm}^{-2}\,\text{s}^{-1}\right)$	$\phi_{90\%}$ at 50 TeV $\left(\text{TeV}^{-1}\text{cm}^{-2}\text{s}^{-1}\right)$	$\frac{\phi_{90\%}}{\phi_\nu}$
ROI-1	3HWC J0621+382 [22]	2.93×10^{-17}	5.64×10^{-17}	1.92
ROI-2	LHAASO J0621+3755 [141]	4.28×10^{-17}	5.79×10^{-17}	1.35
ROI-3	3HWC J0634+067 [22]	4.30×10^{-17}	3.39×10^{-17}	7.87×10^{-1}
ROI-4	3HWC J1757-240 [22]	8.41×10^{-17}	2.92×10^{-13}	3.48×10^{3}
ROI-5	eHWC J1809-193 [136]	4.86×10^{-16}	8.19×10^{-14}	1.68×10^{2}
ROI-6	HAWC J1825-138 [137] LHAASO J1825-1326 [140]	1.80×10^{-14} 4.36×10^{-16}	6.54×10^{-15}	3.64×10^{-1} 1.50×10^{1}
ROI-7	HAWC J1826-128 [137]	5.54×10^{-14}	6.48×10^{-15}	1.17×10^{-1}
ROI-8	eHWC J1839-057 [136] LHAASO J1839-0545 [140]	3.04×10^{-16} 8.54×10^{-17}	2.34×10^{-16}	7.70×10^{-1} 2.74
ROI-9	eHWC J1842-035 [136] LHAASO J1843-0338 [140]	3.04×10^{-16} 8.91×10^{-17}	4.30×10^{-18}	1.42×10^{-2} 4.82×10^{-2}
ROI-10	eHWC J1850+001 [136] LHAASO J1849-0003 [140]	2.23×10^{-16} 9.03×10^{-17}	1.82×10^{-16}	8.19×10^{-1} 2.02
ROI-11	eHWC J1907+063 [136] LHAASO J1908+0621 [140]	4.95×10^{-16} 1.66×10^{-16}	3.90×10^{-16}	7.86×10^{-1} 2.35
ROI-12	LHAASO J1929+1745 [140]	4.64×10^{-17}	3.87×10^{-16}	8.36
ROI-13	3HWC J1951+266 [22]	3.20×10^{-17}	4.91×10^{-16}	1.53×10^{1}
ROI-14	LHAASO J1956+2845 [140]	5.00×10^{-17}	3.59×10^{-16}	7.18
ROI-15	2HWC J2006+341 [138]	8.37×10^{-19}	4.23×10^{-18}	5.05
ROI-16	eHWC J2019+368 [136] LHAASO J2018+3651 [140] TASG J2019+368 [142]	3.82×10^{-16} 6.10×10^{-17} 1.79×10^{-16}	2.76×10^{-16}	7.23×10^{-1} 4.52 1.54
ROI-17	3HWC J2023+324 [22]	2.10×10^{-17}	3.51×10^{-17}	1.67
ROI-18	eHWC J2030+412 [136] LHAASO J2032+4102 [140] HAWC J2030+409 [107]	1.82×10^{-16} 6.59×10^{-17} 3.88×10^{-16}	2.93×10^{-17}	1.61×10^{-1} 4.45×10^{-1} 7.55×10^{-2}
ROI-19	3HWC J2043+443 [22]	3.95×10^{-17}	2.05×10^{-16}	5.19
ROI-20	LHAASO J2226+6057 [140]	1.28×10^{-16}	8.11×10^{-17}	6.33×10^{-1}

Table 4.14: The theoretical neutrino fluxes from gamma-ray sources assuming 100% hadronic emission from pp interactions are compared with 90% upper-limit fluxes from the extension with the smallest pre-trial p-value. Both the theoretical neutrino fluxes and the 90% upper limits are at a pivot energy of 50 TeV.

Region of Interest	Possible Sources and Associated Extension	ϕ_ν from pp Collisions $\left(\text{TeV}^{-1}\,\text{cm}^{-2}\,\text{s}^{-1}\right)$	$\phi_{90\%}$ at 50 TeV $\left(\text{TeV}^{-1}\text{cm}^{-2}\text{s}^{-1}\right)$	$\frac{\phi_{90\%}}{\phi_\nu}$
ROI-1	3HWC J0621+382 [22]	2.93×10^{-17}	2.29×10^{-16}	7.83
ROI-2	LHAASO J0621+3755 [141]	4.28×10^{-17}	2.32×10^{-16}	5.42
ROI-3	3HWC J0634+067 [22]	4.30×10^{-17}	4.27×10^{-17}	9.92×10^{-1}
ROI-4	3HWC J1757-240 [22]	8.41×10^{-17}	2.01×10^{-13}	2.39×10^{3}
ROI-5	eHWC J1809-193 [136]	4.86×10^{-16}	1.42×10^{-13}	2.93×10^{2}
ROI-6	HAWC J1825-138 [137] LHAASO J1825-1326 [140]	1.80×10^{-14} 4.36×10^{-16}	8.05×10^{-16}	4.48×10^{-2} 1.85
ROI-7	HAWC J1826-128 [137]	5.54×10^{-14}	1.29×10^{-15}	2.33×10^{-2}
ROI-8	eHWC J1839-057 [136] LHAASO J1839-0545 [140]	3.04×10^{-16} 8.54×10^{-17}	4.57×10^{-17}	1.50×10^{-1} 5.35×10^{-1}
ROI-9	eHWC J1842-035 [136] LHAASO J1843-0338 [140]	3.04×10^{-16} 8.91×10^{-17}	3.91×10^{-18}	1.29×10^{-2} 4.39×10^{-2}
ROI-10	eHWC J1850+001 [136] LHAASO J1849-0003 [140]	2.23×10^{-16} 9.03×10^{-17}	7.79×10^{-17}	3.50×10^{-1} 8.62×10^{-1}
ROI-11	eHWC J1907+063 [136] LHAASO J1908+0621 [140]	4.95×10^{-16} 1.66×10^{-16}	1.01×10^{-15}	2.04 6.08
ROI-12	LHAASO J1929+1745 [140]	4.64×10^{-17}	2.19×10^{-16}	4.73
ROI-13	3HWC J1951+266 [22]	3.20×10^{-17}	2.74×10^{-16}	8.56
ROI-14	LHAASO J1956+2845 [140]	5.00×10^{-17}	1.39×10^{-16}	2.79
ROI-15	2HWC J2006+341 [138]	8.37×10^{-19}	1.83×10^{-18}	2.19
ROI-16	eHWC J2019+368 [136] LHAASO J2018+3651 [140] TASG J2019+368 [142]	3.82×10^{-16} 6.10×10^{-17} 1.79×10^{-16}	5.49×10^{-16}	1.44 9.00 3.07
ROI-17	3HWC J2023+324 [22]	2.10×10^{-17}	1.01×10^{-16}	4.81
ROI-18	eHWC J2030+412 [136] LHAASO J2032+4102 [140] HAWC J2030+409 [107]	1.82×10^{-16} 6.59×10^{-17} 3.88×10^{-16}	1.37×10^{-16}	7.50×10^{-1} 2.07 3.52×10^{-1}
ROI-19	3HWC J2043+443 [22]	3.95×10^{-17}	1.70×10^{-16}	4.31
ROI-20	LHAASO J2226+6057 [140]	1.28×10^{-16}	4.35×10^{-17}	3.40×10^{-1}

Table 4.15: The theoretical neutrino fluxes from gamma-ray sources assuming 100% hadronic emission from pp interactions are compared with 90% upper-limit fluxes from the extension with the largest pre-trial p-value. Both the theoretical neutrino fluxes and the 90% upper limits are at a pivot energy of 50 TeV.

CHAPTER 5

ATMOSPHERIC CHERENKOV TELESCOPES AS A POTENTIAL VETO ARRAY FOR NEUTRINO ASTRONOMY

This chapter is a paper previously published with the author of this thesis as the corresponding author of the paper. “Atmospheric Cherenkov Telescopes as a Potential Veto Array for Neutrino Astronomy" by D. Rysewyk *et al.* was published in *Astroparticle Physics* Volume 117, Page 102417 (2020) [144].

IceCube has revealed the existence of sources of high-energy astrophysical neutrinos. However, identification of the sources is challenging because astrophysical neutrinos because astrophysical neutrinos are difficult to separate from the background of atmospheric neutrinos produced in cosmic-ray air showers. The search for extended Galactic neutrino sources presented in Chapter 4 concluded in results consistent with background. This may have not been the case if IceCube had additional veto methods to reduce background, increasing IceCube’s sensitivity to astrophysical neutrino sources. The following chapter discusses the feasibility of utilizing Imaging Air Cherenkov Telescopes (IACTs) as a potential veto array for neutrino astronomy.

5.1 Introduction

A flux of high-energy neutrinos from astrophysical sources was discovered by the IceCube Neutrino Observatory in 2013 [145]. Although evidence has been presented for several possible multi-messenger correlations [146, 147, 148, 149], the only source identified with high confidence to date is the blazar TXS 0506+056 [65, 64]. However, IceCube limits on the total contribution of GeV blazars to the observed astrophysical neutrino flux [66] imply that the majority of the neutrino flux is produced in other, as-yet-unidentified class(es) of sources.

If blazars are not the primary sources of the neutrino flux, it is challenging to reconcile IceCube measurements of the neutrino flux below 200 TeV with the diffuse extra-galactic gamma-ray background measured by Fermi at GeV scales [150]. Most models of astrophysical neutrino sources

predict that the neutrinos are produced in the decay of $\pi^{\pm}$ and $K^{\pm}$ mesons. Neutral mesons will be produced alongside the charged mesons, and decay to produce gamma rays. Although high-energy gamma rays can be reprocessed through interaction with the cosmic backgrounds of infrared and microwave photons, the integrated energy emitted in high-energy photons and neutrinos is tightly coupled. The soft spectral index observed with IceCube at energies below 200 TeV [151, 152] implies a higher bolometric neutrino luminosity than can be accommodated easily in the non-blazar component of the Fermi diffuse gamma-ray background [153]. Options for resolving this tension include a sharp break in the neutrino spectrum at energies just below those currently accessible to IceCube; the existence of a significant but currently unidentified Galactic component in the IceCube flux; neutrino production in some currently unknown class of objects with opacity large enough to process the photons to energies below the gamma-ray band (or via new physics such as dark matter); or considerable errors in the fraction of either neutrinos or gamma rays attributed to blazars [154, 155, 156, 157, 158, 159, 160, 161, 162, 163, 164, 165, 166, 167, 168, 169, 170]. Speculation regarding the possibility of features in the neutrino energy spectrum in the 10–100 TeV range [171, 172, 173, 174], and the possibility of using the inelasticity of events observed at a few tens of TeV to measure the neutrino/anti-neutrino ratio and thus determine whether astrophysical neutrinos are generated in hadronuclear (pp) or photonuclear ($p\gamma$) processes in their sources [175, 176, 177, 178, 179, 180, 181, 182, 183], further contribute to the interest in improved measurements in this energy range.

Improved methods for identifying astrophysical neutrinos and reducing backgrounds at energies below the 100 TeV scale are thus of considerable interest. Neutrino telescopes such as IceCube [184], ANTARES [185], the Baikal Neutrino Observatory [186] as well as the planned Baikal-GVD [187] and KM3NeT [188] use photomultiplier tubes (PMTs) to detect Cherenkov radiation from charged leptons produced through neutrino interactions in the surrounding ice or water. Charged-current (CC) muon neutrino interactions produce track-like events in a neutrino telescope. Charged-current electron and tau neutrino interactions, as well as neutral-current (NC) neutrino interactions of any flavor, produce cascade-like events. Cherenov light emission from a cascade

is nearly spherically symmetric, while tracks are elongated due to the muon path length, which is typically several kilometers for TeV-scale muons in ice or water.

The main backgrounds in searches for extraterrestrial neutrinos are "atmospheric" muons and neutrinos, which are produced in cosmic-ray-induced particle cascades in the atmosphere known as air showers. The classic technique to reject atmospheric muons is to search for particles coming upward through the Earth from the opposite hemisphere, so that only neutrinos can reach the detector. However, this method cannot distinguish atmospheric neutrinos from those produced in astrophysical sources, except on a probabilistic basis based on the typically softer energy spectrum of atmospheric neutrinos.

A second technique for rejecting atmospheric backgrounds is to use entering atmospheric muons detected in the outer region of the neutrino telescope as indicators of air showers, enabling both muons and downward-going atmospheric neutrinos to be vetoed [189, 190, 191]. This is the method exploited by the IceCube Collaboration to first discover the diffuse astrophysical neutrino flux [145]. A variation of this method is to detect the air shower itself with a separate array of detectors at the surface. In IceCube, this approach has been demonstrated using the IceTop array of (frozen) water Cherenkov particle detectors on the surface above IceCube [192], but only above a cosmic-ray energy threshold[1] of 1 PeV and over a relatively small field of view.

In this paper, a potential array of Imaging Air Cherenkov Telescopes (IACTs) as a dedicated surface air shower detector array for IceCube is evaluated. The ability for IACTs to perform as a veto array with an efficiency and energy threshold that is relevant for neutrino astronomy is assessed. IACTs detect air showers by measuring Cherenkov light emitted from the particles during an extended air shower. Although the requirement of dark, clear skies (to reduce background and

[1]The energy of an atmospheric neutrino is a fraction of the energy of the primary cosmic ray. Although neutrino production peaks later in the shower development, the highest-energy neutrinos arise from mesons produced in the first generations of the air shower. The steeply falling cosmic-ray spectrum implies that for a given neutrino energy E_ν, cosmic rays with energies E_p only a few times higher than E_ν contribute significantly. As a rough rule of thumb, for an array with a cosmic-ray energy threshold of E_p, atmospheric neutrinos can be vetoed efficiently above an energy $E_\nu \gtrsim E_p/3$.

boost signal) will limit the duty cycle of such an array, IACTs offer the potential advantages of a lower energy threshold and larger ground coverage per station compared to direct particle detection with surface arrays such as IceTop. To be relevant for neutrino astronomy, the array must be capable of detecting high-energy cosmic-ray air showers with very high efficiency over a surface area of order 1 km^2 and a solid angle of at least a large fraction of a steradian. The ability to operate, even with reduced sensitivity, in harsh environments with bright Moon or aurora conditions is important to maximize the potential duty cycle.

The IACTs required to veto atmospheric neutrinos need not be as sophisticated as those used for gamma-ray astronomy, however. An IACT of ~ 0.5 m^2 collection area is easily capable of detecting air showers at or below the 100 TeV scale, which produce essentially all atmospheric neutrinos with energies above a few tens of TeV [193]. Angular resolution is not crucial: the Cherenkov radiation from air showers is strongly beamed, so only showers aimed generally at the IACT and the neutrino telescope below it will be detectable, and the potential transverse momentum of atmospheric neutrinos limits the utility of angular resolution better than a few degrees. Discrimination of gamma-induced and hadron-induced showers, a key performance metric for gamma-ray astronomy, is irrelevant in this context.

For this study, we consider an array of ground stations, each consisting of multiple small IACTs in a "fly's-eye" arrangement. We base performance assumptions on a design for an enclosed telescope with a camera of silicon photomultipliers (SiPMs), suitable for harsh environments and capable of operation in relatively high ambient light levels [194]. Prototypes of similar design have been operated at the South Pole in coincidence with IceCube [195].

This paper is structured as follows. Section 5.2 presents the conceptual design for the telescopes which make up the array. Section 5.3 describes air shower simulations used to characterize the performance of the telescope as an air shower detector. Section 5.4 outlines a possible veto array which could be installed at the IceCube Observatory. Section 5.5 discusses the potential impact of such an array on neutrino astronomy.

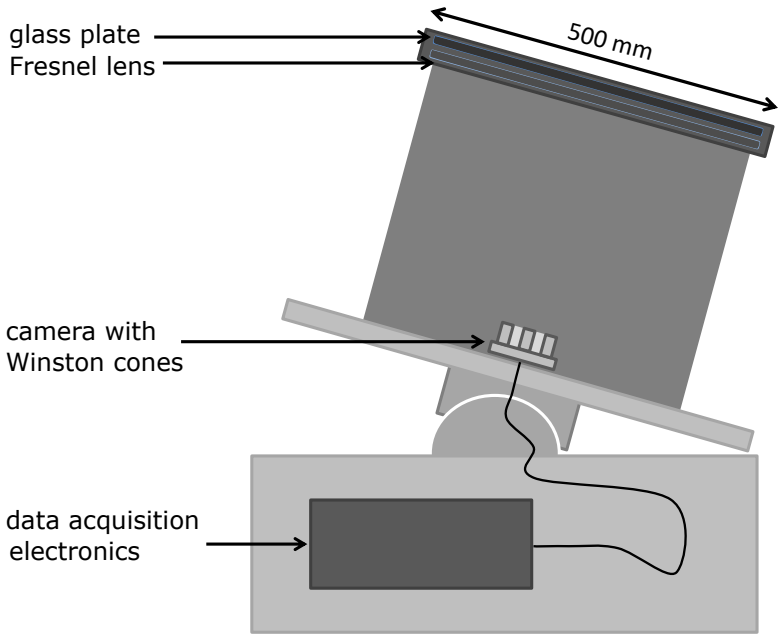

Figure 5.1: An example of a small-scale IACT adapted from [23]. It features a Fresnel lens and a camera based on 61 SiPMs with Winston cones.

5.2 Conceptual Design of a Small-Scale IACT

5.2.1 Optics and Photon Collection Efficiency

This study envisions an array of IACTs similar to the IceACT telescope [194, 23, 195], which has a light collection area of 0.237 m^2 and a field of view of 0.045 sr (roughly 14° diameter). An example diagram of one of these IACTs can be seen in Figure 5.1. It features a large Fresnel lens as imaging optics with a diameter of $D = 500$ mm and a numerical aperture, defined as the ratio of the focal length F to the diameter, of $F/D \sim 1$. The camera is based on 61 SiPMs, which have been widely explored as an alternative to classical PMTs in IACTs because they offer gain and quantum efficiency comparable to PMTs but can be operated under much brighter light conditions [196, 197]. Winston cones are used in the focal plane to increase the effective photon detection area [198, 199]. The total cost of such a telescope is estimated to be less than 10,000 euros [194].

Since IACTs can only operate in low light conditions, the telescopes can operate during astronomical night which corresponds to winter in the Southern hemisphere. At South Pole, these

conditions obtain for 4 months of the year, while the Sun is more than 12.6° below the horizon[2] [200]. Dark skies are required to detect air showers, although the SiPM-based camera will be capable of operating with the Moon above the horizon [201]. While very little precipitation falls at the South Pole, windblown snow crystals can also impact operations. Current prototypes are testing the effectiveness of resistive heating cables to improve snow removal during the winter months. We estimate that a winter duty factor of at least 60% (corresponding to 2.4 months of operation per year) will be possible, but this estimate must be confirmed based on the experience operating the IceACT prototype at the South Pole.

We assume that the telescope optics provide a photon collection efficiency of 60% between 300–650 nm. This is an estimate of the efficiency that could be possible with a system based on a commercially-available Fresnel lens, but is not based on detailed modeling of a specific telescope design. As a baseline for the camera we consider SensL-FJ (6 mm x 6 mm) SiPMs (MicroFJ-60035-TSV) with an overvoltage of 5 V. For these parameters, the quantum efficiency is close to 30% at 350 nm, as shown in Figure 5.2.

In addition to the usual diffuse night sky background (NSB), an IACT at the South Pole must also consider the aurora australis, discussed in detail in Section 5.3. For this study we assume that a filter made of Schott UG11 glass, with a peak efficiency for photons of ~90% around 325 nm, is added to the telescope to attenuate the longer wavelengths emitted by the aurora while retaining the shorter wavelengths which predominate in the Cherenkov spectrum.

The overall photon detection efficiency is the product of the efficiency of the telescope optics, the UG11 filter efficiency, and the SensL SiPM efficiency. The wavelength dependence of the efficiencies of various telescope elements, and the overall photon detection efficiency we assume in this study are given in Figure 5.2.

[2]Due to the lower aerosol content of the atmosphere over the Antarctic plateau, sky darkening occurs more rapidly than at most mid-latitude sites. Following Sims et al., we define astronomical night by the solar zenith distance at which the median moonless dark sky darkens by 0.5 mag.

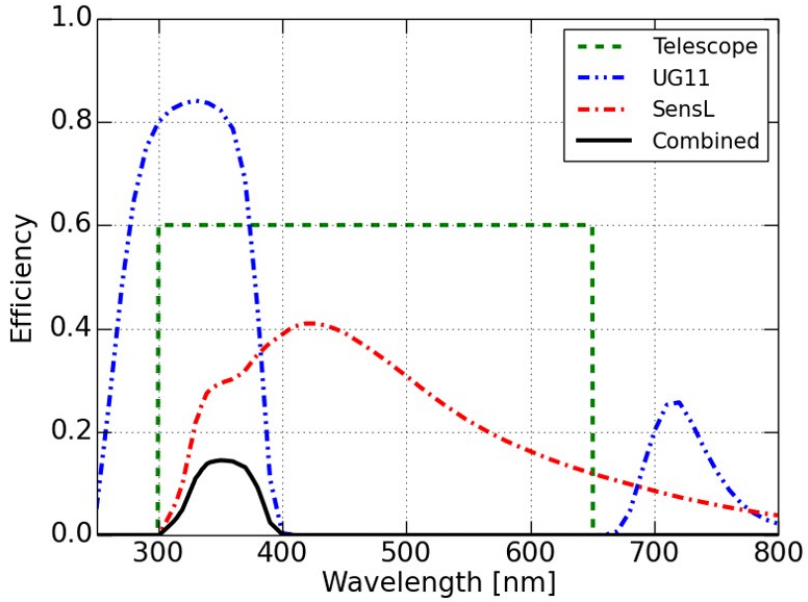

Figure 5.2: Performance of the various components of the telescope and their combined efficiency in the Cherenkov band. The dashed green line shows the photon collection efficiency assumed for the small-scale, wide field-of-view IACT. The dash-dotted red curve shows the photon detection efficiency (PDE) of the SensL SiPM, while the dash-double-dotted blue line shows the performance of the Schott UG11 filter. The black curve shows the overall efficiency of the telescope combining all of these components.

5.2.2 Electronics and Dark Noise

Temperature variations affect the gain of SiPMs at the level of about 10% per 10 °C. Ambient temperature is relatively stable over the Antarctic night, with typical variation of ±10 °C during the winter months and maximum recorded deviations ±25 °C. Gain variations due to temperature of the SiPM can be corrected by adjustment of the applied voltage [197], with residual gain variations at the 1% level. For the purpose of air shower detection, gain variation at this level is negligible compared to variations in ambient light levels.

Dark noise in the SiPMs does not pose a major problem at the temperatures typical of the South Pole winter. The single photon rate for SensL-J SiPMs is about 50 kHz/mm^2 at 20 °C, and falls by a factor of 3 for every 10 °C. Typical operating temperatures at the South Pole in winter are around -50 °C. The highest temperature recorded at the South Pole in winter is approximately -30 °C, corresponding to a noise rate of 0.2 kHz/mm^2. For a 61-pixel camera with 6 mm × 6 mm sensors

this corresponds to an overall dark count rate less than 450 kHz, or $\lesssim 10^{-2}$ per 10 ns (the time scale appropriate for Cherenkov light from air showers. Cross talk in the SiPMs can produce apparent 2–3 photon signals, but at rates 1–2 orders of magnitude lower than the single count rate. As these rates are more than two orders of magnitudes lower than the NSB levels discussed in Section 5.3, we do not consider dark noise further in this study. Bright stars in the field of view may also increase noise rates. We assume that the impact will be limited to individual pixels and that realistic trigger electronics would be able to exclude high-rate pixels temporarily as a star drifts across the field. As a detailed model of the trigger is beyond the scope of this study, we do not attempt to account for this effect.

To veto atmospheric neutrinos effectively, the telescopes in the array should be operated with the lowest possible trigger threshold. For this study, we do not attempt to design a complete data acquisition system, but only to model the performance of the telescopes at a conceptual design level. We assume the data acquisition electronics will be capable of recording single photoelectrons and implementing a simple coincidence logic which sums the total charge in the brightest three neighboring pixels of the telescope (the approximate size of an air shower in the camera) for the time windows of interest. Since information from the veto array is relevant only if the neutrino telescope below the array has detected a particle, we envision a system which relies primarily on the neutrino telescope trigger to define time windows of interest.

We assume that low-level trigger primitives from the IACTs can be stored in a look-back buffer until the neutrino telescope trigger is formed, and that the IACT data from the relevant time window would be examined for an excess signal above the background noise consistent with the presence of an air shower. While the rate of the trigger primitives may be very high, the actual trigger rate and data bandwidth would be throttled by the neutrino telescope trigger, which typically runs at a few kHz.

5.3 Detection of Air Showers

To investigate the feasibility of an IACT array as an air shower veto, we simulated the response of our conceptual IACT design to air showers produced by cosmic-ray primaries of different species, at energies ranging from 10 TeV to 200 TeV and zenith angles from 0° to 60°. Based on the Cherenkov light production and estimated background levels, we estimate the maximum distance from the shower axis at which our IACT concept could detect each shower, if it occurred within the IACT's field of view in a time window of interest identified by the neutrino telescope. In this feasibility study we do not include a detailed model of the IACT electronics or optics, but rather estimate detectability based on simple signal-to-noise considerations. In general, air showers may produce signals in multiple IACTs, particularly if the shower axis is approximately equidistant from multiple stations. This will tend to enhance the prospects for detection relative to the estimates presented here, which are based on the signals recorded in single telescopes. On the other hand, more detailed modeling of the backgrounds, trigger electronics and detector optics could reduce the estimated efficiency compared to the idealized signal-to-noise calculation used in this initial study.

5.3.1 Cherenkov Light Production in Air Showers

The cosmic ray simulation program CORSIKA [111] version 7.4005 was used to simulate air showers, with QGSJet-01c [202] for high-energy interactions and FLUKA 2011.2c.1 [203, 204] for low-energy interactions. All Cherenkov photons between 300–600 nm were recorded over a 2 km by 2 km readout area on the ground around the shower core. Wavelength dependence of the Cherenkov emission angle was ignored, as it has been shown that this level of detail is normally not needed for Cherenkov telescopes [205]. The simulation used CORSIKA's South Pole August atmosphere model and an observation level of 2,834 m above sea level. Particles were tracked down to energy thresholds of 50 MeV for hadrons and muons and 0.3 MeV for electrons and gamma rays, well below the threshold for Cherenkov radiation at sea level ($\sim$ 20 MeV for electrons and $\sim$ 4 GeV

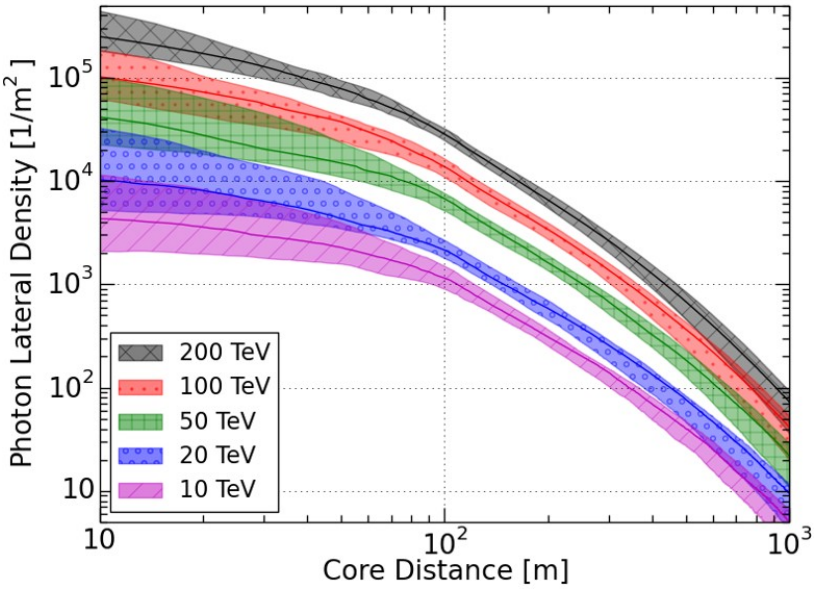

Figure 5.3: Mean lateral distribution of 300–600 nm Cherenkov photons for vertical proton primaries of different energies. A detector altitude of 2,834 m above sea level is assumed and effects of atmospheric absorption are not included. Each of the 30 showers is averaged in azimuth and the solid lines show the median of the averaged profiles. The shaded regions show the 15% and 85% percentiles for each energy.

for muons).

Vertical air showers were simulated for 300 proton, 20 oxygen and 50 iron primaries at 100 TeV. In addition, thirty 100 TeV proton showers were simulated at zenith angles between 10°–60° at 10° intervals to investigate the impact of zenith angle. Thirty vertical proton showers were simulated for primary energies 10 TeV, 20 TeV, 50 TeV and 200 TeV to assess energy dependence.

Figure 5.3 shows the mean lateral distribution of Cherenkov photons for vertical proton primaries of different energies. At energies below ~1 TeV the photon density is known to be relatively flat and exhibits a characteristic rim at approximately 120 m [205]. In the energy range of interest for the current study, the sharpness of this feature is greatly reduced, but a steepening in the rate of decline in photon density with distance can be seen. Typical Cherenkov photon densities for proton showers above 50 TeV are around 1,000 photons m^{-2} TeV^{-1} close to the core, and 30 photons m^{-2} TeV^{-1} at 200 m from the core. Relatively large fluctuations from the median profile are common close to the shower core, but shower-to-shower variations are smaller at radial distances of 100–300 m.

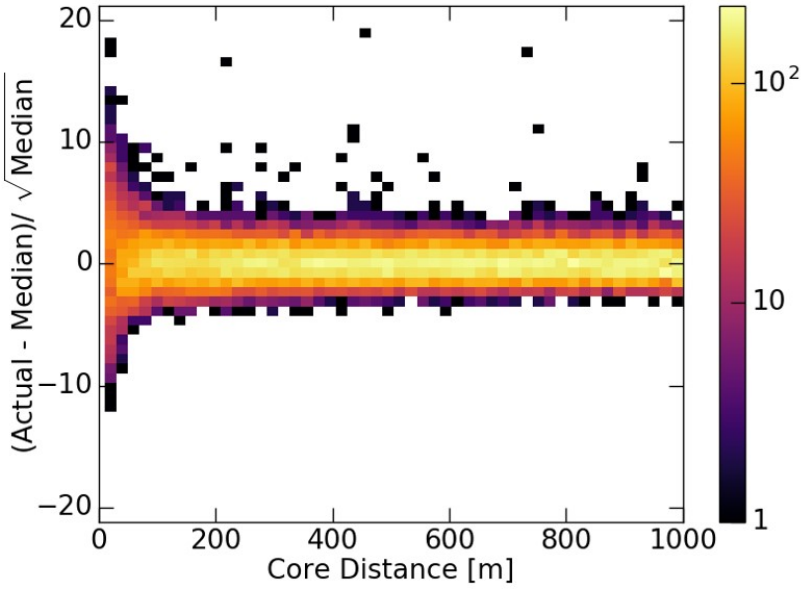

Figure 5.4: Azimuthal fluctuations of the lateral distribution of 300–600 nm Cherenkov photons for a single vertical proton shower at 100 TeV. In 5 degree steps around the shower core and every 2 m in radius, a 0.5 m times 0.5 m square on the ground is selected and the actual number of photons is compared to the median profile that is obtained by averaging over all azimuth angles. The result is divided by the square root of the median, to determine whether the fluctuations are Poisson distributed (see discussion in main text).

This effect is illustrated in Figure 5.4, which shows the azimuthal variability within a single shower. For a Poisson process, the fluctuations should have a typical scale of $\sqrt{N}$, where N is the expected number of photons. Close to the shower core, where the number of Cherenkov photons is not well described by a Poisson process, photon densities are well above the threshold for detection so large downward fluctuations are unimportant. At distances beyond about 100 m from the shower core, the photon density fluctuations are Poisson distributed, with the points in the plot having a mean close to 0 and a standard deviation close to 1. Small deviations caused by sub-structure in the air shower (e.g., energetic mesons with high transverse momenta p_T) create local fluctuations that are significantly higher than the expectation from the median profile, but downward fluctuations that could reduce detectability are well described by Poisson expectations. In this study we therefore assume Poisson distributions around the mean photon densities shown in Figure 5.3 for all Cherenkov photon counts.

5.3.2 Atmospheric Extinction

Some of the Cherenkov photons produced in air showers will be absorbed in the atmosphere before reaching ground level. The absorption probability depends on both the photon wavelength λ and the heights of production and detection, and is tabulated in CORSIKA for a general atmospheric model. For vertical proton showers at 100 TeV, about 13% of the Cherenkov photons between 300–600 nm are lost due to atmospheric extinction. This number varies between about 8% and 16% according to the first interaction height of the primary particle: a shower that starts higher in the atmosphere will suffer more absorption before it reaches the ground. The species of the primary particle also has some impact, since heavier primaries are less likely to penetrate deep into the atmosphere before the first interaction. For 30 vertical iron showers, the minimum and maximum atmospheric extinction are 15% and 18%. Shower inclination also affects the absorption due to the increasing path length through the atmosphere, with extinction rising to 20% for 100 TeV proton showers at 40° from zenith.

As discussed below in Section 5.3.5, the most challenging air showers to detect are vertical proton-induced showers which start deep in the atmosphere. Nonetheless, we conservatively assume a value of 18% extinction independent of energy and primary species. The resulting Cherenkov spectrum after atmospheric extinction is convolved with the total photon detection efficiency function shown in Figure 5.2 to determine the mean number of photoelectrons (PE) detected from each shower. After all effects are taken into account, the mean PE yield near the shower axis is ~550 PE m^{-2} of telescope area for vertical 100 TeV proton showers, or approximately 130 PE for our conceptual IACTs with 0.237 m^2 collection area.

5.3.3 Sky Brightness and Aurorae

The Antarctic plateau is one of the world's premier sites for optical, infrared, and submillimeter astronomy, and NSB levels on the Antarctic plateau have received considerable attention from the astronomical community. The plateau is a high-altitude desert with dark skies and relatively little cloud cover. However, the aurora australis presents unique challenges which must be taken into

account for an IACT veto array at the South Pole. Aurorae are created when solar wind particles collide with the Earth's atmosphere, producing a diffuse glow in optical wavelengths which covers portions of the sky. Fortunately, much of the auroral light is emitted at longer wavelengths which can be eliminated with a filter such as the Schott UG-11 glass included in our telescope model.

Detailed characterizations of the aurora australis at both the South Pole and Dome A, roughly 1,000 km away on the peak of the plateau, have been reported in [200] and [206]. Contributions to the NSB can be divided into two classes: line emission associated with the aurora australis, and continuum emission, including airglow, zodiacal light, starlight, diffuse galactic light, and quasi-continuous components of auroral emission ascribed to molecular bands of nitrogen and oxygen. Spectral models of airglow and auroral emission and detailed discussions of the physical processes involved are presented in [207, 208, 206, 200].

The intensity of the aurora vary considerably over the course of the year. We used the median auroral activity presented in [200] to calculate the impact of auroral activity on our telescopes. Auroral intensity is usually described in terms of the intensity of the characteristic green emission from the 557.7 nm [OI] line, with the spectrum presented in [200] representing an IBC3 aurora event with a 557.7 nm line intensity of 100 kR.[3] The six most dominant lines in the wavelength range of 300–650 nm are the 315.8, 337.0, 357.6, 391.4, 427.8, and 557.7 nm lines. We consider all other auroral lines in this wavelength range to be subdominant. We model the spectrum as scaling linearly with intensity, and normalize to the intensity of the 427.8 nm line:

$$I_{315.8} = 0.40\, I_{427.8} \quad I_{337.0} = 0.82\, I_{427.8} \quad I_{357.6} = 0.55\, I_{427.8}$$
$$I_{391.4} = 3.28\, I_{427.8} \quad I_{557.7} = 3.33\, I_{427.8}$$

Our model of the quasi-continuous component of the aurora is based on measurements from the Auroral Observatory in Fort Churchill, Manitoba [207, 208]. In the wavelength range of 310–470 nm, the continuum was found to have an intensity of 30 R/nm in reference to a 427.8 nm line intensity of 5 kR. In the wavelength range of 450-890 nm, the continuum intensity was 270 R/nm in

[3] 1 Rayleigh (R) = $(10^{10}/4\pi)$ photons / m^2 s sr.

reference to a 557.7 nm line intensity of 100 kR. For each of the benchmark auroral levels considered below, the continuum emission is dominated by these quasi-continuous auroral components. We therefore scale the continuum background with the auroral intensity as well as the lines, following [206].

In order to quantify the effect of the varying auroral conditions on the performance of the IACTs, we define three benchmark aurora levels. Observations of the brightness of the aurora australis were made at the South Pole Station during the winters of 1985 and 1990 [206], near solar minimum and maximum, respectively. Auroral levels vary with the solar cycle, with solar minimum leading to higher auroral activity than during solar maximum. The benchmark levels we consider are the mean auroral intensity during solar maximum, mean intensity during solar minimum, and the 90th percentile intensity during solar minimum to represent the highest intensities likely to be encountered on a regular basis.

The measured intensity of the 427.8 nm line at South Pole during both winters was reported in B mags arcsec^{-2}, which can be converted to an intensity I in photons m^{-2} s^{-1} sr^{-1} using the equation [206]

$$I = \frac{7.96 \times 10^8 \; K \; \Delta\lambda \; 10^{(20-m)/2.5}}{1.24 \times 10^6 \; \lambda}, \tag{5.1}$$

where m is the brightness in magnitudes/arcsec^2, λ is the central wavelength of the filter in m, and $\Delta\lambda$ is the filter bandwidth in nm. For the B band, $K = 42.6$, $\lambda = 436 \times 10^{-9}$ m, and $\Delta\lambda = 94$ nm. For the V band, $K = 36.4$, $\lambda = 556 \times 10^{-9}$ m, and $\Delta\lambda = 85$ nm.

The intensities of the 427.8 nm line at the three different benchmarks are 23.5 B mags/arcsec^2, 22.8 B mags/arcsec^2, and 21 B mags/arcsec^2 respectively. The intensities of the other five major auroral lines and the continuum were scaled along with the 427.8 nm line intensity for each benchmark level, as explained above. The background spectrum for the mean auroral intensity at solar maximum, including the continuum and six auroral lines, is shown in Figure 5.5 [4].

[4]Because the continuum has different intensities in different wavelength ranges, the different intensities were added together in a piecewise function at 450 nm based on [207] and [208]. However, since the UG11 filter cuts out higher wavelengths, continuum emission levels in the wavelength range from 450-890 nm do not affect our estimates.

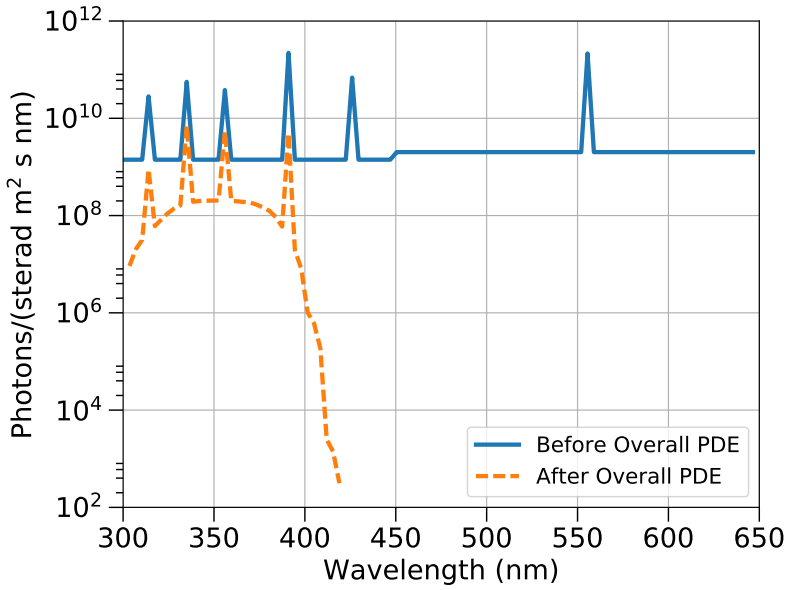

Figure 5.5: The spectrum of the NSB with mean-intensity aurora during solar maximum, before (solid blue line) and after (dashed orange line) applying the combined telescope photon detection efficiency from Figure 5.2.

Applying the combined photon detection efficiency (PDE) shown in Figure 5.2, the estimated sky background level at mean auroral intensity during solar maximum yields an average of 0.61 PE/ns detected across the full 61-pixel camera, for a 14° FoV and 0.237 m^2 collection area. This increases to 1.16 PE/ns for the background expected at the mean auroral intensity during solar minimum, and 6.1 PE/ns for the background from the 90th percentile intensity aurora during solar minimum. Measurements from the IceACT prototypes are required to validate these estimates.

5.3.4 Triggering

Cherenkov photons from an air shower show dispersion in time of a few ns near the shower core. The distribution gets wider in time further from the shower core. For a given time distribution of photons, we identify the optimal start and stop times for a trigger window by maximizing the signal over the square root of the expected continuum background (during solar maximum). This was repeated for 40 vertical proton showers. For distances of 140–160 m from the shower core, the optimal window was found to be 10 ns. The optimal time window retains 75% of the original

signal. For 190–210 m, the optimal window increases to 20 ns, with a similar fraction of signal retained.

A complete design of the trigger electronics is beyond the scope of this study. We assume that each telescope will form simple trigger primitives, and buffer the data from the corresponding time window until an external trigger decision is received from the neutrino telescope. We model a simple coincidence logic that considers the total charge in the brightest three neighboring pixels of the telescope during the optimal time window identified above. The charge threshold for the trigger primitives is determined by the need to limit accidental triggers due to background photons to a reasonable rate, which we define as less than 1 kHz.

A toy Monte Carlo was used to calculate the coincident three-pixel PE distribution in a 20 ns time window for a telescope size of 0.237 m^2, assuming that the background photons are uniformly distributed across the camera.[5] For a given trigger threshold, we computed the probability of accidental triggers based on the background levels calculated in Section 5.3.3 for the three different auroral benchmark levels. The probability of an accidental trigger in a 20 ns window with a threshold of ≥ 9 PE in three adjacent camera pixels for the lowest benchmark level (mean intensity during solar maximum) was found to be 5.3×10^{-6}, corresponding to a rate of 265 Hz. The thresholds required to keep accidental trigger rates below 1 kHz for the mean and the 90th percentile intensity aurorae at solar minimum are found to be $\geq$11 PE and $\geq$24 PE respectively.

For air showers, the Cherenkov photon density at ground level scales approximately linearly with the shower energy, as shown in Figure 5.3. Comparison of these trigger thresholds thus implies that even very bright aurorae should shift the veto energy threshold only by a factor of two to three. It should be noted that when bright aurorae are present, they often fill only a portion of the sky. As high-energy atmospheric neutrinos are well aligned with their parent air showers and are reconstructed to degree-scale accuracy in IceCube, an IACT veto could remain effective over much of the sky even with bright aurorae obscuring air showers in some directions. Experience

[5] We anticipate that pixels with elevated rates, e.g. from a bright star transiting the field of view, would be temporarily excluded from the trigger. Such effects are not included in this toy Monte Carlo.

with operating IACTs at the South Pole will be crucial for validating these expectations.

5.3.5 Air Shower Sensitivity

From the Corsika simulation we obtain the number of Cherenkov photons per unit area as a function of distance from the shower axis. The photon counts are scaled down to account for atmospheric extinction before reaching ground level and the telescope optical efficiency. We assume that 75% of the photons will arrive within the trigger window and be collected within the three brightest camera pixels (each of which has a field of view of 1.5°). For each simulated shower, the lateral distribution of photons is used to calculate the maximum distance from the shower core at which the expected signal in the trigger window of a single IACT equals 9 PE, the required trigger threshold for typical operation during solar maximum. This is the maximum distance from the telescope at which the simulated shower is considered detectable, which sets the maximum spacing between telescopes in a surface veto array.

Figure 5.6 plots the maximum detection distance for vertical showers of different energies and primary species against the height of the initial cosmic-ray interaction above the ground. As seen in Figure 5.6a, the most important factor affecting detectability is the interaction height. For cosmic rays which interact high in the atmosphere, the maximum distance at which showers of a given energy can be detected is generally consistent to roughly ±25%. The most difficult showers to detect are those in which the primary cosmic ray penetrates deeply into the atmosphere before interacting. In such cases, the maximum detection distance is limited because there is not enough time for the air shower to develop fully and the Cherenkov light pool to expand laterally before reaching the ground. Inclined showers are thus more reliably detected, as the increased slant depth through the atmosphere reduces the probability of very low interaction heights and the increased distance to the ground give more space for the Cherenkov pool to spread out.[6]

[6]Projection effects also improve the prospects for detecting inclined showers. The telescope axis must be nearly parallel to that of the shower to observe the Cherenkov emission, so the density of photons in the telescope camera plane is essentially unaffected. But the distance between telescopes in the plane perpendicular to the shower axis is smaller than in the ground plane, reducing the average projected distance from the shower axis to the nearest telescope.

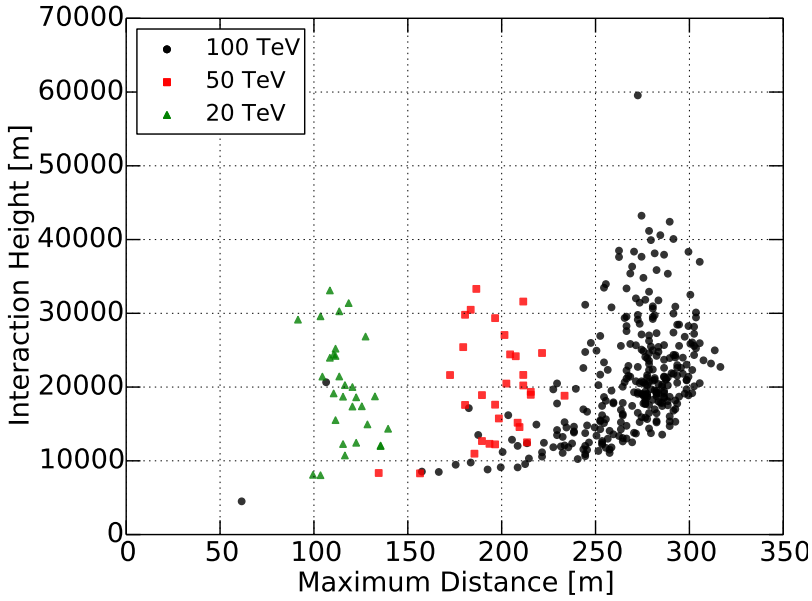

(a) Maximum distance for detection vs. first interaction height for 300 vertical proton-induced air showers at 100 TeV, compared to thirty showers each at 20 TeV and 50 TeV.

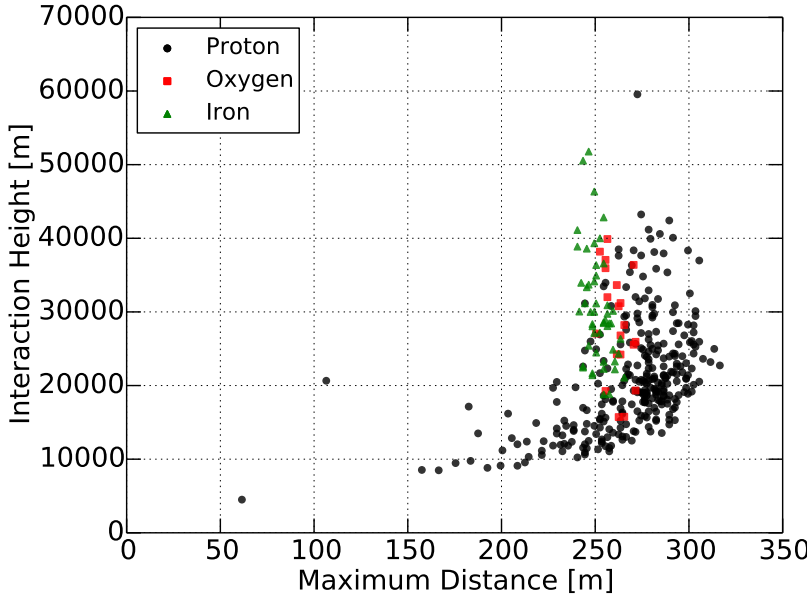

(b) Maximum distance for detection vs. first interaction height for different primary species. Heavier nuclei are slightly dimmer but less likely to penetrate deeply into the atmosphere.

Figure 5.6: Maximum distance from telescope at which vertical air showers can be detected for a trigger threshold of 9 PE, plotted against the height of the first cosmic-ray interaction above the surface. Showers that penetrate deeply into the atmosphere are the hardest to detect.

For similar reasons, showers produced by heavier primaries are more reliably detected than those produced by protons. As shown in Figure 5.6b, the larger cross sections on air increase the typical height of first interaction, compared to proton primaries. In addition, the air showers produced by heavy primaries develop more rapidly and more regularly than proton showers, so the Cherenkov light pool has more time to expand before reaching ground level. Both effects cause the distance at which showers induced by heavy primaries of a given energy can be detected to be significantly more consistent than for protons.

As shown in Figure 5.6, at primary energies of 100 TeV, ~99% of the vertical showers can be detected (and vetoed) up to 150 m away from the telescope. Even at energies as low as $E_p = 50$ TeV, the detection/veto rate is >95% for vertical proton showers. Similar detection rates are also possible at 150 m from the telescope when the threshold is increased to ≥11 PE. However, if the threshold is increased to ≥24 PE, these detection rates are only achieved for showers up to 100 m from the telescope. It should be noted that these efficiencies are for detection of the most challenging class of air showers: perfectly vertical proton-induced showers. Detection rates for inclined showers and those produced by heavy nuclei will be higher than for this class of events. We therefore conclude that our IACT concept should be able to detect air showers, and veto the associated atmospheric neutrinos, with at least 99% efficiency to a radius of approximately 150 m above an threshold of 50–100 TeV. This corresponds to an atmospheric neutrino energy threshold of approximately 15–30 TeV.

We note that there may be correlations between atmospheric neutrino production in air showers and characteristics which enhance or suppress detectability by the IACT array at ground level. For example, protons which penetrate too deeply into the atmosphere before first interaction may not leave enough time for energetic mesons to decay and produce neutrinos before reaching ground level, which would enhance prospects for detecting the showers producing high-energy atmospheric neutrinos. Conversely, if a large fraction of the primary cosmic ray's energy is carried away by a neutrino, the electromagnetic component of the air shower may produce less Cherenkov light and be more difficult to detect. More detailed air shower and telescope response simulations with

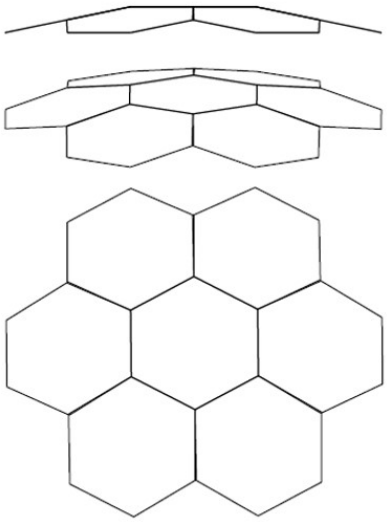

Figure 5.7: Schematic arrangement of a telescope station (side view to top view). Each telescope has a hexagonal FoV of 14°. Seven telescopes are arranged in a fly's eye array. The center telescope points straight up at 0° zenith. The six surrounding telescopes point at 14° zenith. With all seven telescopes, the station has a FoV of 36°.

higher statistics will be required to quantify these effects and further refine this estimate of the effective atmospheric neutrino energy threshold for veto efficiency.

5.4 A Potential Air Shower Veto Array

Based on these studies, we consider how one might implement an IACT-based surface veto array for the IceCube Neutrino Observatory. To assist in the discovery of new neutrino sources, the veto array must cover a relatively large section of the sky. This can be achieved by grouping multiple telescopes together into stations at different points above IceCube. Each individual IACT has a ~14° wide hexagonal FoV, and a station consists of up to seven telescopes arranged in a "fly's eye" configuration: one telescope pointing straight up, and six surrounding telescopes each pointing at a 14° angle from zenith. With this arrangement, each station would have a FoV of up to 36° (i.e., extending to 17° from zenith). Figure 5.7 illustrates the geometry of a station with seven telescopes.

A single station would have an effective coverage radius of 150 m in most light conditions, whereas IceCube has a footprint of a square kilometer. We performed calculations to determine the

total number of telescopes and stations required to cover the full IceCube array over the 36° field of view. A hexagonal array of seven-telescope stations with a distance between stations of ~260 m ensures that no point within the array is more than 150 m from the nearest station. Note that for air showers near this maximum distance from the nearest station, there will be several telescopes at comparable distances. This provides several chances to detect the shower in an individual telescope, as well as the possibility of combining information from multiple stations to improve detection efficiency. To ensure coverage of the full field of view, the IACT array should extend several hundred meters beyond the edge of the IceCube footprint, as shown in Figure 5.8.

The full complement of seven telescopes is not required at each station. For each telescope in each station, we calculated how many of IceCube's digital optiocal modules (DOMs) are located in the opposite direction of the telescope's FoV (i.e., how many DOMs the telescope would "protect"). The results are shown in Figure 5.8, with the color of each telescope hexagon representing the number of DOMs behind the IACT. A telescope array with a FoV of 36° and a telescope station spacing of ~ 260 m would include a total of 253 telescopes distributed among 83 stations. This includes all telescopes that cover at least one DOM in their FoV. At an estimated cost of around 10,000 euros per telescope, this corresponds to an investment of order 3 million euros. It would be possible to reduce the number of telescopes and stations required by eliminating telescopes protecting only the edges of the IceCube array, but detailed simulations of both the air showers and the IceCube detector response would be required to quantify the impact on veto efficiency.

The array shown in Figure 5.8 would cover a field of view of 0.27 sr (17° from zenith). Based on estimates that at least several hundred sources contribute to the astrophysical neutrino flux observed by IceCube [209], this field of view should contain a number of as-yet-unidentified neutrino sources. The field of view could be increased to 0.83 sr (30° from zenith, one fifteenth of the sky) by adding another ring to the fly's eye configuration at each station, increasing the number of potential telescopes at each station to 19. For this scaled-up telescope array, a total of 723 telescopes distributed over 151 stations would be needed to cover the footprint of IceCube using the same assumptions above. The estimated cost of this expanded array would still be less than 10

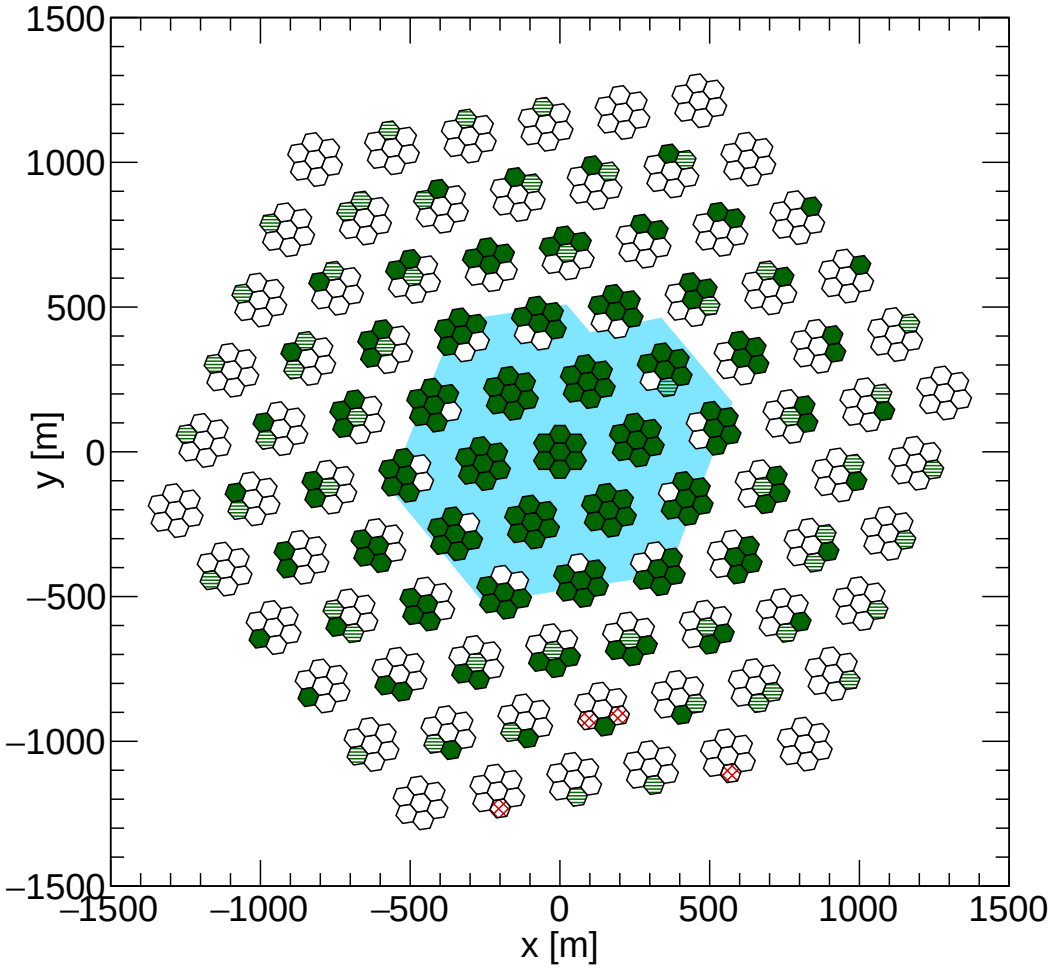

Figure 5.8: Top view of a telescope array with 36° FoV and a telescope station spacing of 260 m. The shaded blue region indicates the IceCube footprint. Each telescope in a station is colored according to how many DOMs are behind the telescope's FoV, from solid green (>50 DOMs) to green horizontal lines (11-50 DOMs), red crosshatched lines (1-10 DOMs) and white (none).

million euros.

5.5 Impact on Neutrino Astronomy

The standard IceCube search for neutrinos from the overhead sky [145] employs a veto cut that excludes the outer volume of the detector in order to veto atmospheric muons. This reduces the fiducial volume in which neutrinos are allowed to interact by approximately 40%. With a veto based on an IACT telescope array, neutrinos interacting anywhere inside the full volume of IceCube

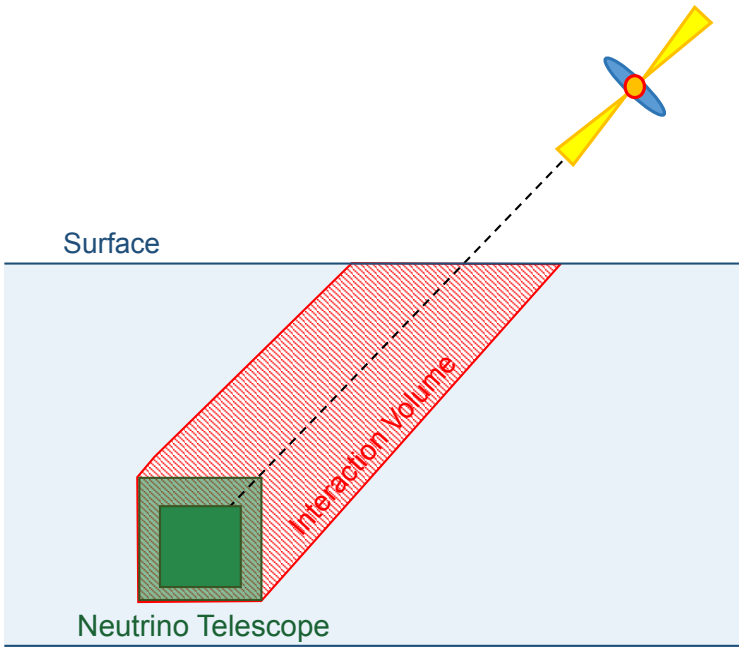

Figure 5.9: Volumes for accepted neutrino interactions for a source at a given zenith angle. For the standard starting event analysis, using the outer region of the detector as a veto, all neutrinos must interact in the fiducial volume indicated by the solid shaded region. With a surface veto array, neutrinos interacting in the outer (shaded) region of the detector can also be accepted. For long tracks from ν_μ CC events, the allowed interaction volume could be extended to the ice above the detector as well.

could be used, providing a full km^3 fiducial volume for cascades (charged current $\nu_{e,\tau}$ and neutral current $\nu_{e,\mu,\tau}$ events). For charged current ν_μ interactions, which produce long muon tracks, the usable interaction volume would include ice above the detector as well as the full IceCube detector volume, as shown in Figure 5.9. This would increase the available interaction volume for tracks, and thus the event rate from an overhead neutrino source, by a factor of 4–5, depending on the zenith angle.

To illustrate the increase in sensitivity to neutrino sources obtained by adding an IACT telescope array to IceCube, we consider a source located at a zenith angle of 15°, and assume a flux similar to that emitted by the TXS 0506+056 blazar in 2015–16 [64]. The average $\nu_\mu + \bar{\nu}_\mu$ flux observed from TXS 0506+056 over a 158 day period had a normalization at 100 TeV of $\Phi_{100} = 1.6 \times 10^{-18}$ GeV^{-1} cm^{-2} s^{-1} and a spectral index of 2.2.

We estimate that a surface array such as that outlined in Section 5.4 would detect air showers effectively above a cosmic-ray energy threshold of 50 TeV, corresponding to an atmospheric neutrino energy threshold of roughly 15 TeV. For comparison, the neutrino energy threshold above which the atmospheric background is generally absent in the standard IceCube high-energy starting event analysis (using the periphery of the detector as a veto) is around 100 TeV [145]. For the purposes of this study we assume that atmospheric neutrino backgrounds are reduced to negligible levels above this threshold; detailed simulations with high statistics will be required to quantify the exact atmospheric background rate surviving the veto. Complete elimination of the atmospheric background is not necessary to provide substantially improved sensitivity to astrophysical neutrino sources. A realistic analysis would likely weight individual events according to their likelihoods of being missed by the IACT veto, and would exploit neutrinos at energies below the threshold given here. Our model of the veto efficiency as a step function at a precise energy threshold is intended only as a simplistic first estimate of the potential benefits of the array.

The numbers of astrophysical neutrinos observed above the veto threshold from a point source at a zenith of 15° emitting a $\nu_\mu + \bar{\nu}_\mu$ flux of $1.6 \times 10^{-7}\ E_\nu^{-2.2}$ GeV^{-1}cm^{-2}s^{-1} over two different durations are shown in Figure 5.10. Tracks refer to charged current ν_μ events. Cascades include charged current $\nu_{e,\tau}$ and neutral current $\nu_{e,\mu,\tau}$ events. Because the source is in the Southern sky, neutrino interactions must take place within the 0.6 km^3 fiducial volume to pass the standard veto analysis; without the IACT veto array, tracks entering from outside the volume are always assumed to be atmospheric. With the IACT veto, tracks produced by neutrinos interacting in the ice above the detector can also be accepted since the lack of an air shower indicates they are not of atmospheric origin. [7]

[7] This assumes that atmospheric muons as well as atmospheric neutrinos can be vetoed effectively by the IACT array. Atmospheric muons should be easier to veto than neutrinos, for several reasons. Since over half of the muon energy will be deposited in the ice before reaching the detector, the minimum muon energy required to reach the neutrino telescope with at least 15 TeV (and thus the air shower energy threshold) is higher. Atmospheric muons are produced in high-multiplicity bundles, which are distinguishable in neutrino telescopes from the single muons produced in ν_μ CC interactions, so the neutrino telescope response can be incorporated to improve the veto efficiency. However, since the atmospheric muon rate is considerably higher than that of atmospheric neutrinos,

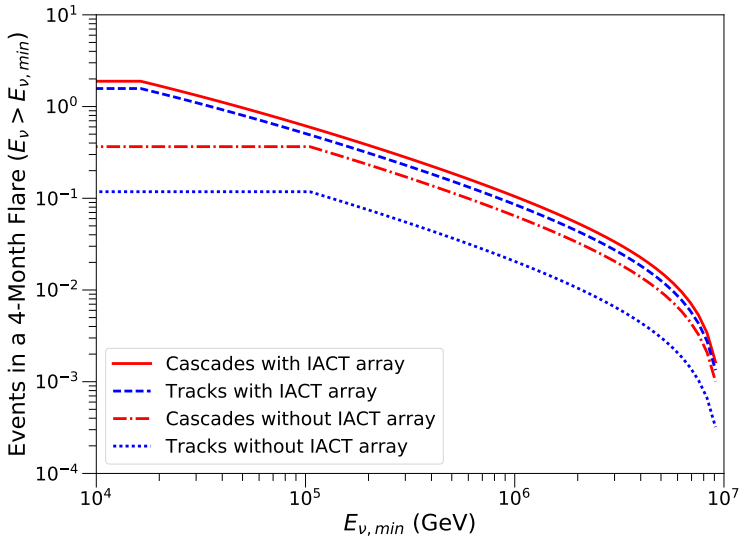

(a) Number of identified neutrino events during a 4-month flare during the winter when the IACT surface array has a 60% duty cycle.

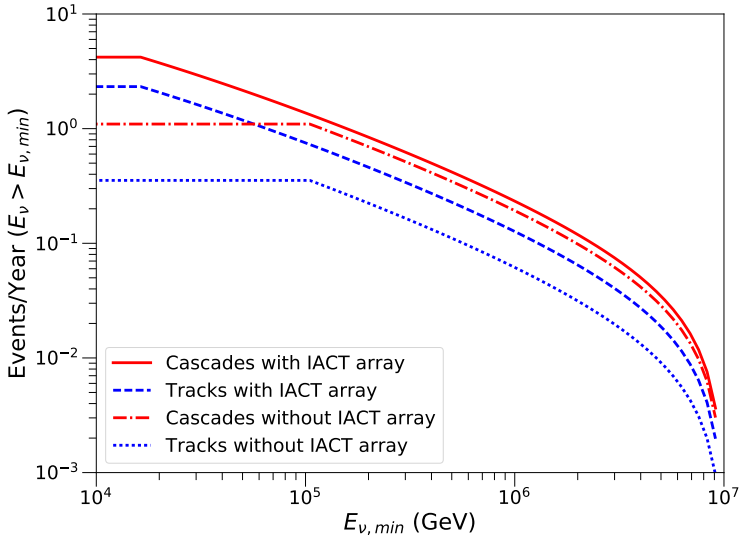

(b) Number of identified neutrino events during a year-long flare when the IACT surface array has a 20% duty cycle.

Figure 5.10: Number of neutrino events passing the veto for a point source similar to TXS 0506+056 at a zenith of 15°. $E_{\nu,min}$ is the minimum neutrino energy emitted by the source. When the detector veto energy threshold is above the minimum emitted energy, the number of events is independent of $E_{\nu,min}$. The IACT surface array primary energy threshold is taken to be 50 TeV, corresponding to a neutrino energy of 15 TeV, and the neutrino energy threshold for the standard veto is 100 TeV.

Figure 5.10a shows the number of neutrinos observed from the source over a 4-month flare during the winter, when the telescopes have a duty cycle of 60%. During this type of flare, around a factor of 13 more tracks and a factor of 5 more cascades would be observed with the IACT surface array than without it. Although only a few events of each flavor are expected, two factors should be borne in mind. First, the actual event rates will be Poisson-distributed around the means shown in Figure 5.10; higher numbers of events would be observed from a substantial fraction of actual flares. Second, the discovery of TXS 0506+056 was initiated by a single neutrino event. Two high-energy tracks from the same location in a relatively short period of time, with evidence from the IACT veto favoring non-atmospheric origin, would be enough to initiate multi-messenger follow-up observations and enable potential discoveries. Figure 5.10b shows the number of neutrinos from a TXS 0506+056-like source during a year-long flare when the telescopes have an overall duty cycle of 20%. During this type of flare, around a factor of 6.5 more tracks and a factor of 3.8 more cascades would be identified with the IACT surface array than without it.

5.6 Conclusions

An array of small, $O(0.25\ \mathrm{m}^2)$, wide field of view Cherenkov telescopes would provide an efficient detector of air showers for the purpose of vetoing atmospheric neutrinos in a high-energy neutrino telescope. The air Cherenkov technique is complementary to extensive air shower arrays (e.g. IceTop), which offer higher duty cycle, but have difficulty detecting lower energy ($E_p \lesssim 300$ TeV) air showers or those produced high in the atmosphere. With a camera based on silicon photomultipliers (SiPMs), an array deployed above the IceCube Neutrino Observatory would be capable of taking data during the four months of astronomical night available at South Pole including periods with bright moon or aurora australis. Filters selecting UV light would greatly reduce the impact of the aurora, enabling operation in most auroral conditions. An overall duty cycle, accounting for periods of poor visibility, of 20%–25% (2.5 to 3 months per year) is

this assumption remains to be validated with a detailed, high-statistics simulation of IceCube operating in conjunction with the IACT array. If sufficiently high atmospheric muon veto efficiency cannot be achieved, the relative gains for track events will be similar to those for cascades.

expected to be possible.

First estimates of the telescope response to air showers indicate that with a telescope spacing of approximately 260 m, efficient air shower detection is expected above primary cosmic-ray energies of 50–100 TeV, corresponding to rejection of atmospheric neutrinos above energies of 15–30 TeV. These thresholds could be tuned by changing the spacing between stations in the array. More detailed simulations of the telescopes in conjunction with the buried neutrino detector are required to refine these estimates further. The IceCube telescope could be covered with a field of view of 36° (i.e., zenith angles up to 17°) by an array consisting of approximately 250 telescopes at 80 stations. Approximately three times as many telescopes and twice as many stations would be required to extend the field of view to 30° from zenith.

At a cost scale of several million euros, such an array would significantly enhance the atmospheric neutrino veto capabilities of IceCube at energies as low as tens of TeV. This would greatly aid measurements of the lower end of the astrophysical neutrino spectrum, which have significant impact on understanding of the neutrino-gamma ray energy budget and the contributions of accelerators other than blazars to the neutrino sky. In addition, reduction of the atmospheric neutrino background would enhance the sensitivity of IceCube to neutrino emission from astrophysical objects, particularly transient multi-messenger emission such as that observed from the blazar TXS 0506+056.

CHAPTER 6

CONCLUSIONS

IceCube has been taking data with the full detector of 86 strings since its completion in 2010, with the goals of observing astrophysical neutrinos and their origins. In 2013, IceCube realized its first goal with the detection of the astrophysical neutrino flux. The origin of the astrophysical neutrino flux remained a mystery until 2017 which IceCube observed a neutrino from the direction of the flaring blazar TXS 0506+056. However, it has been shown that blazars cannot contribute the majority of the neutrino flux that IceCube has detected. Therefore, the origin of the majority of the astrophysical neutrino flux still remains a mystery.

The total contribution of Galactic sources to the astrophysical neutrino flux is expected to be no more than 14% above 1 TeV. However, no potential Galactic sources of neutrinos have been found by IceCube yet. A search for extended neutrino sources within the Galaxy has been performed with nine years of IceCube data using a new background estimation technique called source masking. The search was performed in two different ways: blind scans across the Galactic plane for neutrino sources with extensions between 0.5° and 2.0° and a search for extended neutrino sources at a priori locations chosen by their proximity to known extended Galactic gamma-ray sources. The results from the two types of searches were consistent with the background expectation. However, the most significant locations in the scans across the plane and the catalog search were within two degrees of each other. If follow-up searches focus on this location, the reduced trials factor and additional data may prove to produce significant results.

One of the main battles IceCube faces is the reduction of the large background of atmospheric muons and neutrinos. This background is significantly worse in the southern sky, where the Earth cannot be used as a shield against atmospheric muons. These muons are produced in air showers when cosmic-rays interact with particles in the atmosphere. The ability to observe air showers that are coincident with events seen in IceCube can reduce the background from particles produced in the air showers. A dedicated IACT array of 250 to 750 telescopes would effectively detect cosmic-ray

air showers down to primary energies of 50-100 TeV, which would further reduce the atmospheric background and improve IceCube's sensitivity to astrophysical neutrinos. With the continuation of data-taking, improvements to techniques used in neutrino source searches, and enhancements to the IceCube detector such as additional veto arrays or the expansion of the existing in-ice detector, the discovery of the origin of the astrophysical neutrino flux and cosmic rays may be within reach.

BIBLIOGRAPHY

BIBLIOGRAPHY

[1] M. G. Aartsen et al. (IceCube), "Time-Integrated Neutrino Source Searches with 10 Years of IceCube Data", Phys. Rev. Lett. vol. 124 (5) p. 051103 (2020), doi:10.1103/PhysRevLett.124.051103, 1910.08488

[2] C. Grupen et al., Astroparticle Physics, Springer (2005), URL https://books.google.com/books?id=wlVGJ4X1BKkC

[3] P.A. Zyla et al. (Particle Data Group), "Review of Particle Physics", PTEP vol. 2020 (8) p. 083C01 (2020), doi:10.1093/ptep/ptaa104

[4] M. Spurio, Particles and Astrophysics, Springer International Publishing Switzerland (2015)

[5] Luis Anchordoqui, Thomas Cantzon Paul, Stephen Reucroft, and John Swain, "Ultrahigh-energy cosmic rays: The State of the art before the Auger Observatory", Int. J. Mod. Phys. A vol. 18 pp. 2229–2366 (2003), doi:10.1142/S0217751X03013879, hep-ph/0206072

[6] Paolo S. Coppi and Felix A. Aharonian, "Constraints on the VHE emissivity of the universe from the diffuse GeV gamma-ray background", Astrophys. J. Lett. vol. 487 pp. L9–L12 (1997), doi:10.1086/310883, astro-ph/9610176

[7] Leif Rädel, Measurement of High-Energy Muon Neutrinos with the IceCube Neutrino Observatory, Ph.D. thesis, RWTH Aachen U. (2017), doi:10.18154/RWTH-2017-10054

[8] Amanda Cooper-Sarkar, Philipp Mertsch, and Subir Sarkar, "The high energy neutrino cross-section in the Standard Model and its uncertainty", JHEP vol. 08 p. 042 (2011), doi:10.1007/JHEP08(2011)042, 1106.3723

[9] René Reimann, Search for the sources of the astrophysical high-energy muon-neutrino flux with the IceCube neutrino observatory, Ph.D. thesis, RWTH Aachen U. (2019), doi:10.18154/RWTH-2019-11012

[10] J. H. Koehne et al., "PROPOSAL: A tool for propagation of charged leptons", Comput. Phys. Commun. vol. 184 pp. 2070–2090 (2013), doi:10.1016/j.cpc.2013.04.001

[11] IceCube, "IceCube Gallery", (2021 [Online]), URL https://gallery.icecube.wisc.edu/internal/main.php

[12] R. Abbasi et al. (IceCube), "IceTop: The surface component of IceCube", Nucl. Instrum. Meth. vol. A700 pp. 188–220 (2013), doi:10.1016/j.nima.2012.10.067, 1207.6326

[13] R. Abbasi et al. (IceCube), "The IceCube Data Acquisition System: Signal Capture, Digitization, and Timestamping", Nucl. Instrum. Meth. A vol. 601 pp. 294–316 (2009), doi:10.1016/j.nima.2009.01.001, 0810.4930

[14] M. G. Aartsen et al. (IceCube), "The IceCube Neutrino Observatory: Instrumentation and Online Systems", JINST vol. 12 (03) p. P03012 (2017), doi:10.1088/1748-0221/12/03/P03012, 1612.05093

[15] Hamamatsu Photonics, "About PMTs | Photomultiplier tubes (PMTs)", (September 29, 2021 [Accessed]), URL https://www.hamamatsu.com/us/en/product/optical-sensors/pmt/about_pmts/index.html

[16] IceCube MasterClass, "The Detection of Neutrinos in IceCube", (September 30, 2021 [Accessed]), URL https://masterclass.icecube.wisc.edu/en/learn/detecting-neutrinos

[17] Jöran Benjamin Stettner, Measurement of the energy spectrum of astrophysical muon-neutrinos with the IceCube Observatory, Ph.D. thesis, RWTH Aachen U. (2021), doi:10.18154/RWTH-2021-01139

[18] Till Neunhoffer, "Estimating the angular resolution of tracks in neutrino telescopes based on a likelihood analysis", Astropart. Phys. vol. 25 pp. 220–225 (2006), doi:10.1016/j.astropartphys.2006.01.002, astro-ph/0403367

[19] IceCube, "Ice models", (October 3, 2021 [Accessed]), URL https://wiki.icecube.wisc.edu/index.php/Ice_models

[20] Markus Ahlers, Klaus Helbing, and Carlos Pérez de los Heros, "Probing Particle Physics with IceCube", Eur. Phys. J. C vol. 78 (11) p. 924 (2018), doi:10.1140/epjc/s10052-018-6369-9, 1806.05696

[21] L. Martínez, "Equatorial Coordinate System", The Quantum Red Pill (2013. [Online]), URL https://quantumredpill.wordpress.com/2013/01/16/equatorial-coordinate-system/

[22] A. Albert et al. (HAWC), "3HWC: The Third HAWC Catalog of Very-High-Energy Gamma-ray Sources", Astrophys. J. vol. 905 (1) p. 76 (2020), doi:10.3847/1538-4357/abc2d8, 2007.08582

[23] Jan Auffenberg (IceCube Gen2), "IceAct: Imaging Air Cherenkov Telescopes with SiPMs at the South Pole for IceCube-Gen2", PoS vol. ICRC2017 p. 1055 (2018), doi:10.22323/1.301.1055

[24] Alessandro de Angelis, "Atmospheric ionization and cosmic rays: studies and measurements before 1912", Astroparticle Physics vol. 53 p. 19–26 (2014), doi:10.1016/j.astropartphys.2013.05.010

[25] Victor Hess, "On the Observations of the Penetrating Radiation during Seven Balloon Flights", ArXiv e-prints (1912), 1808.02927

[26] Dieter Fick and Dieter Hoffmann, "Werner Kolhörster (1887–1945): The German pioneer of cosmic ray physics", Astroparticle Physics vol. 53 pp. 50–54 (2014), doi:https://doi.org/10.1016/j.astropartphys.2013.09.007

[27] T.K. Gaisser, Cosmic Rays and Particle Physics, Cambridge University Press (1990), URL https://books.google.com/books?id=qJ7Z6oIMqeUC

[28] W. D. Apel et al. (KASCADE Grande), "Kneelike structure in the spectrum of the heavy component of cosmic rays observed with KASCADE-Grande", Phys. Rev. Lett. vol. 107 p. 171104 (2011), doi:10.1103/PhysRevLett.107.171104, 1107.5885

[29] Thomas K. Gaisser, "Spectrum of cosmic-ray nucleons, kaon production, and the atmospheric muon charge ratio", Astropart. Phys. vol. 35 pp. 801–806 (2012), doi:10.1016/j.astropartphys.2012.02.010, 1111.6675

[30] Karl-Heinz Kampert and Peter Tinyakov, "Cosmic rays from the ankle to the cutoff", Comptes Rendus Physique vol. 15 pp. 318–328 (2014), doi:10.1016/j.crhy.2014.04.006, 1405.0575

[31] G. T. Zatsepin and V. A. Kuzmin, "Upper limit of the spectrum of cosmic rays", JETP Lett. vol. 4 pp. 78–80 (1966)

[32] Kenneth Greisen, "End to the cosmic ray spectrum?", Phys. Rev. Lett. vol. 16 pp. 748–750 (1966), doi:10.1103/PhysRevLett.16.748

[33] G. T. Zatsepin and V. A. Kuzmin, "Upper limit of the spectrum of cosmic rays", JETP Lett. vol. 4 pp. 78–80 (1966)

[34] Enrico Fermi, "On the Origin of the Cosmic Radiation", Phys. Rev. vol. 75 pp. 1169–1174 (1949), doi:10.1103/PhysRev.75.1169

[35] A. M. Hillas, "The Origin of Ultrahigh-Energy Cosmic Rays", Ann. Rev. Astron. Astrophys. vol. 22 pp. 425–444 (1984), doi:10.1146/annurev.aa.22.090184.002233

[36] Fred L. Wilson, "Fermi's Theory of Beta Decay", Am. J. Phys. vol. 36 (12) pp. 1150–1160 (1968), doi:10.1119/1.1974382

[37] Frederick Reines and Clyde L. Cowan, "The neutrino", Nature vol. 178 pp. 446–449 (1956), doi:10.1038/178446a0

[38] C. L. Cowan et al., "Detection of the Free Neutrino: a Confirmation", Science vol. 124 (3212) pp. 103–104 (1956), doi:10.1126/science.124.3212.103, http://science.sciencemag.org/content/124/3212/103.full.pdf, URL http://science.sciencemag.org/content/124/3212/103

[39] H. Athar, M. Jezabek, and O. Yasuda, "Effects of neutrino mixing on high-energy cosmic neutrino flux", Phys. Rev. D vol. 62 p. 103007 (2000), doi:10.1103/PhysRevD.62.103007, hep-ph/0005104

[40] M. G. Aartsen et al. (IceCube), "A combined maximum-likelihood analysis of the high-energy astrophysical neutrino flux measured with IceCube", Astrophys. J. vol. 809 (1) p. 98 (2015), doi:10.1088/0004-637X/809/1/98, 1507.03991

[41] M. G. Aartsen et al. (IceCube), "Constraints on Galactic Neutrino Emission with Seven Years of IceCube Data", Astrophys. J. vol. 849 (1) p. 67 (2017), doi:10.3847/1538-4357/aa8dfb, 1707.03416

[42] Julia K. Becker, "High-energy neutrinos in the context of multimessenger physics", Phys. Rept. vol. 458 pp. 173–246 (2008), doi:10.1016/j.physrep.2007.10.006, 0710.1557

[43] Stephen P. Reynolds, "Supernova Remnants at High Energy", Annual Review of Astronomy and Astrophysics vol. 46 (1) pp. 89–126 (2008), doi:10.1146/annurev.astro.46.060407.145237

[44] M. Ackermann et al. (Fermi-LAT), "Detection of the Characteristic Pion-Decay Signature in Supernova Remnants", Science vol. 339 p. 807 (2013), doi:10.1126/science.1231160, 1302.3307

[45] A. Giuliani et al. (AGILE), "Neutral pion emission from accelerated protons in the supernova remnant W44", Astrophys. J. Lett. vol. 742 p. L30 (2011), doi:10.1088/2041-8205/742/2/L30, 1111.4868

[46] Stefano Gabici et al., "The origin of Galactic cosmic rays: challenges to the standard paradigm", Int. J. Mod. Phys. D vol. 28 (15) p. 1930022 (2019), doi:10.1142/S0218271819300222, 1903.11584

[47] J. G. Learned and K. Mannheim, "High-energy neutrino astrophysics", Ann. Rev. Nucl. Part. Sci. vol. 50 pp. 679–749 (2000), doi:10.1146/annurev.nucl.50.1.679

[48] F. Aharonian et al. (H.E.S.S.), "Discovery of very high energy gamma-rays associated with an x-ray binary", Science vol. 309 pp. 746–749 (2005), doi:10.1126/science.1113764, astro-ph/0508298

[49] Felix A. Aharonian, Luis A. Anchordoqui, Dmitry Khangulyan, and Teresa Montaruli, "Microquasar LS 5039: A TeV gamma-ray emitter and a potential TeV neutrino source", J. Phys. Conf. Ser. vol. 39 pp. 408–415 (2006), doi:10.1088/1742-6596/39/1/106, astro-ph/0508658

[50] Amir Levinson and Eli Waxman, "Probing microquasars with TeV neutrinos", Phys. Rev. Lett. vol. 87 p. 171101 (2001), doi:10.1103/PhysRevLett.87.171101, hep-ph/0106102

[51] C. Distefano, D. Guetta, E. Waxman, and A. Levinson, "Neutrino flux predictions for known galactic microquasars", Astrophys. J. vol. 575 pp. 378–383 (2002), doi:10.1086/341144, astro-ph/0202200

[52] W. Bednarek, "Neutrinos from the pulsar wind nebulae", Astron. Astrophys. vol. 407 pp. 1–6 (2003), doi:10.1051/0004-6361:20030929, astro-ph/0305430

[53] Irene Di Palma, Dafne Guetta, and Elena Amato, "Revised predictions of neutrino fluxes from Pulsar Wind Nebulae", Astrophys. J. vol. 836 (2) p. 159 (2017), doi:10.3847/1538-4357/836/2/159, 1605.01205

[54] A. Abramowski et al. (H.E.S.S.), "Diffuse Galactic gamma-ray emission with H.E.S.S", Phys. Rev. D vol. 90 (12) p. 122007 (2014), doi:10.1103/PhysRevD.90.122007, 1411.7568

[55] A. A. Abdo et al., "A Measurement of the Spatial Distribution of Diffuse TeV Gamma Ray Emission from the Galactic Plane with Milagro", Astrophys. J. vol. 688 pp. 1078–1083 (2008), doi:10.1086/592213, 0805.0417

[56] Amid Nayerhoda et al. (HAWC), "Gamma Ray Diffuse Emission from the GalacticPlane with HAWC Data", PoS vol. ICRC2019 p. 750 (2020), doi:10.22323/1.358.0750

[57] Meng Su, Tracy R. Slatyer, and Douglas P. Finkbeiner, "Giant Gamma-ray Bubbles from Fermi-LAT: AGN Activity or Bipolar Galactic Wind?", Astrophys. J. vol. 724 pp. 1044–1082 (2010), doi:10.1088/0004-637X/724/2/1044, 1005.5480

[58] Roland M. Crocker et al., "Steady-State Hadronic Gamma-Ray Emission from 100-Myr-Old Fermi Bubbles", Astrophys. J. Lett. vol. 791 p. L20 (2014), doi:10.1088/2041-8205/791/2/L20, 1312.0692

[59] Cecilia Lunardini and Soebur Razzaque, "High Energy Neutrinos from the Fermi Bubbles", Phys. Rev. Lett. vol. 108 p. 221102 (2012), doi:10.1103/PhysRevLett.108.221102, 1112.4799

[60] Cecilia Lunardini, Soebur Razzaque, Kristopher T. Theodoseau, and Lili Yang, "Neutrino Events at IceCube and the Fermi Bubbles", Phys. Rev. D vol. 90 (2) p. 023016 (2014), doi:10.1103/PhysRevD.90.023016, 1311.7188

[61] S. Adrian-Martinez et al. (ANTARES), "A Search for Neutrino Emission from the Fermi Bubbles with the ANTARES Telescope", Eur. Phys. J. C vol. 74 (2) p. 2701 (2014), doi:10.1140/epjc/s10052-013-2701-6, 1308.5260

[62] H. Abdalla et al. (HESS), "Characterising the VHE diffuse emission in the central 200 parsecs of our Galaxy with H.E.S.S", Astron. Astrophys. vol. 612 p. A9 (2018), doi:10.1051/0004-6361/201730824, 1706.04535

[63] C. Megan Urry and Paolo Padovani, "Unified schemes for radio-loud active galactic nuclei", Publ. Astron. Soc. Pac. vol. 107 p. 803 (1995), doi:10.1086/133630, astro-ph/9506063

[64] M. G. Aartsen et al. (IceCube), "Neutrino emission from the direction of the blazar TXS 0506+056 prior to the IceCube-170922A alert", Science vol. 361 (6398) pp. 147–151 (2018), doi:10.1126/science.aat2890, 1807.08794

[65] M. G. Aartsen et al. (IceCube, Fermi-LAT, MAGIC, AGILE, ASAS-SN, HAWC, H.E.S.S., INTEGRAL, Kanata, Kiso, Kapteyn, Liverpool Telescope, Subaru, Swift NuSTAR, VERITAS, VLA/17B-403), "Multimessenger observations of a flaring blazar coincident with high-energy neutrino IceCube-170922A", Science vol. 361 (6398) p. eaat1378 (2018), doi:10.1126/science.aat1378, 1807.08816

[66] M. G. Aartsen et al. (IceCube), "The contribution of Fermi-2LAC blazars to the diffuse TeV-PeV neutrino flux", Astrophys. J. vol. 835 (1) p. 45 (2017), doi:10.3847/1538-4357/835/1/45, 1611.03874

[67] Peter Meszaros, "Gamma-Ray Bursts", Rept. Prog. Phys. vol. 69 pp. 2259–2322 (2006), doi:10.1088/0034-4885/69/8/R01, astro-ph/0605208

[68] Francis Halzen and Dan Hooper, "High-energy neutrino astronomy: The Cosmic ray connection", Rept. Prog. Phys. vol. 65 pp. 1025–1078 (2002), doi:10.1088/0034-4885/65/7/201, astro-ph/0204527

[69] M. G. Aartsen et al. (IceCube), "Search for Prompt Neutrino Emission from Gamma-Ray Bursts with IceCube", Astrophys. J. Lett. vol. 805 (1) p. L5 (2015), doi:10.1088/2041-8205/805/1/L5, 1412.6510

[70] M. G. Aartsen et al. (IceCube), "An All-Sky Search for Three Flavors of Neutrinos from Gamma-Ray Bursts with the IceCube Neutrino Observatory", Astrophys. J. vol. 824 (2) p. 115 (2016), doi:10.3847/0004-637X/824/2/115, 1601.06484

[71] M. G. Aartsen et al. (IceCube), "Extending the search for muon neutrinos coincident with gamma-ray bursts in IceCube data", Astrophys. J. vol. 843 (2) p. 112 (2017), doi:10.3847/1538-4357/aa7569, 1702.06868

[72] Abraham Loeb and Eli Waxman, "The Cumulative background of high energy neutrinos from starburst galaxies", JCAP vol. 05 p. 003 (2006), doi:10.1088/1475-7516/2006/05/003, astro-ph/0601695

[73] M. Ackermann et al. (Fermi-LAT), "GeV Observations of Star-forming Galaxies with \textitFermi LAT", Astrophys. J. vol. 755 p. 164 (2012), doi:10.1088/0004-637X/755/2/164, 1206.1346

[74] Keith Bechtol et al., "Evidence against star-forming galaxies as the dominant source of IceCube neutrinos", Astrophys. J. vol. 836 (1) p. 47 (2017), doi:10.3847/1538-4357/836/1/47, 1511.00688

[75] Francesco Miniati et al., "Properties of cosmic shock waves in large scale structure formation", Astrophys. J. vol. 542 pp. 608–621 (2000), doi:10.1086/317027, astro-ph/0005444

[76] Kohta Murase, Susumu Inoue, and Shigehiro Nagataki, "Cosmic Rays Above the Second Knee from Clusters of Galaxies and Associated High-Energy Neutrino Emission", Astrophys. J. Lett. vol. 689 p. L105 (2008), doi:10.1086/595882, 0805.0104

[77] J. A. Formaggio and G. P. Zeller, "From eV to EeV: Neutrino Cross Sections Across Energy Scales", Rev. Mod. Phys. vol. 84 pp. 1307–1341 (2012), doi:10.1103/RevModPhys.84.1307, 1305.7513

[78] Raj Gandhi, Chris Quigg, Mary Hall Reno, and Ina Sarcevic, "Ultrahigh-energy neutrino interactions", Astropart. Phys. vol. 5 pp. 81–110 (1996), doi:10.1016/0927-6505(96)00008-4, hep-ph/9512364

[79] Sheldon L. Glashow, "Resonant Scattering of Antineutrinos", Phys. Rev. vol. 118 pp. 316–317 (1960), doi:10.1103/PhysRev.118.316

[80] M. G. Aartsen et al. (IceCube), "Detection of a particle shower at the Glashow resonance with IceCube", Nature vol. 591 (7849) pp. 220–224 (2021), doi:10.1038/s41586-021-03256-1, [Erratum: Nature 592, E11 (2021)]

[81] Askhat Gazizov and Marek P. Kowalski, "ANIS: High energy neutrino generator for neutrino telescopes", Comput. Phys. Commun. vol. 172 pp. 203–213 (2005), doi:10.1016/j.cpc.2005.03.113, astro-ph/0406439

[82] A. M. Dziewonski and D. L. Anderson, "Preliminary reference earth model", Phys. Earth Planet. Interiors vol. 25 pp. 297–356 (1981), doi:10.1016/0031-9201(81)90046-7

[83] Edgar Bugaev, Teresa Montaruli, Yuri Shlepin, and Igor A. Sokalski, "Propagation of tau neutrinos and tau leptons through the earth and their detection in underwater / ice neutrino telescopes", Astropart. Phys. vol. 21 pp. 491–509 (2004), doi:10.1016/j.astropartphys.2004.03.002, hep-ph/0312295

[84] P. B. Price and K. Woschnagg, "Role of group and phase velocity in high-energy neutrino observatories", Astropart. Phys. vol. 15 pp. 97–100 (2001), doi:10.1016/S0927-6505(00)00142-0, hep-ex/0008001

[85] I. M. Frank and I. E. Tamm, "Coherent visible radiation of fast electrons passing through matter", Compt. Rend. Acad. Sci. URSS vol. 14 (3) pp. 109–114 (1937), doi:10.3367/UFNr.0093.196710o.0388

[86] Dmitry Chirkin and Wolfgang Rhode, "Propagating leptons through matter with Muon Monte Carlo (MMC)", arXiv (2004), hep-ph/0407075

[87] R. Abbasi et al. (IceCube), "An improved method for measuring muon energy using the truncated mean of dE/dx", Nucl. Instrum. Meth. A vol. 703 pp. 190–198 (2013), doi:10.1016/j.nima.2012.11.081, 1208.3430

[88] Donald E. Groom, Nikolai V. Mokhov, and Sergei I. Striganov, "Muon stopping power and range tables 10-MeV to 100-TeV", Atom. Data Nucl. Data Tabl. vol. 78 pp. 183–356 (2001), doi:10.1006/adnd.2001.0861

[89] Claudio Kopper, Performance Studies for the KM3NeT Neutrino Telescope, Ph.D. thesis, Erlangen - Nuremberg U. (2010)

[90] Donald Groom, "Atomic and nuclear properties of water (ice)", (October 5, 2021 [Accessed]), URL https://pdg.lbl.gov/2020/AtomicNuclearProperties/HTML/water_ice.html

[91] M. G. Aartsen et al. (IceCube), "Evidence for High-Energy Extraterrestrial Neutrinos at the IceCube Detector", Science vol. 342 p. 1242856 (2013), doi:10.1126/science.1242856, 1311.5238

[92] M. G. Aartsen et al. (IceCube, Fermi-LAT, MAGIC, AGILE, ASAS-SN, HAWC, H.E.S.S., INTEGRAL, Kanata, Kiso, Kapteyn, Liverpool Telescope, Subaru, Swift NuSTAR, VERITAS, VLA/17B-403), "Multimessenger observations of a flaring blazar coincident with

high-energy neutrino IceCube-170922A", Science vol. 361 (6398) p. eaat1378 (2018), doi: 10.1126/science.aat1378, 1807.08816

[93] M. G. Aartsen et al. (IceCube), "Neutrino emission from the direction of the blazar TXS 0506+056 prior to the IceCube-170922A alert", Science vol. 361 (6398) pp. 147–151 (2018), doi:10.1126/science.aat2890, 1807.08794

[94] M. G. Aartsen et al. (IceCube), "Measurement of South Pole ice transparency with the IceCube LED calibration system", Nucl. Instrum. Meth. A vol. 711 pp. 73–89 (2013), doi:10.1016/j.nima.2013.01.054, 1301.5361

[95] M. G. Aartsen et al. (IceCube), "Measurement of the cosmic ray energy spectrum with IceTop-73", Phys. Rev. D vol. 88 (4) p. 042004 (2013), doi:10.1103/PhysRevD.88.042004, 1307.3795

[96] R. Abbasi et al. (IceCube), "Calibration and Characterization of the IceCube Photomultiplier Tube", Nucl. Instrum. Meth. A vol. 618 pp. 139–152 (2010), doi:10.1016/j.nima.2010.03.102, 1002.2442

[97] M. G. Aartsen et al. (IceCube), "Energy Reconstruction Methods in the IceCube Neutrino Telescope", JINST vol. 9 p. P03009 (2014), doi:10.1088/1748-0221/9/03/P03009, 1311.4767

[98] J. Ahrens et al. (AMANDA), "Muon track reconstruction and data selection techniques in AMANDA", Nucl. Instrum. Meth. A vol. 524 pp. 169–194 (2004), doi:10.1016/j.nima.2004.01.065, astro-ph/0407044

[99] M. G. Aartsen et al., "Improvement in Fast Particle Track Reconstruction with Robust Statistics", Nucl. Instrum. Meth. A vol. 736 pp. 143–149 (2014), doi:10.1016/j.nima.2013.10.074, 1308.5501

[100] P. B. Price, K. Woschnagg, and D. Chirkin, "Age vs depth of glacial ice at South Pole", Geophysical Research Letters vol. 27 (14) pp. 2129–2132 (2000), doi:https://doi.org/10.1029/2000GL011351, https://agupubs.onlinelibrary.wiley.com/doi/pdf/10.1029/2000GL011351, URL https://agupubs.onlinelibrary.wiley.com/doi/abs/10.1029/2000GL011351

[101] The IceCube Collaboration, "South Pole glacial climate reconstruction from multi-borehole laser particulate stratigraphy", Journal of Glaciology vol. 59 (218) p. 1117–1128 (2013), doi:10.3189/2013JoG13J068

[102] P. B. Price, "Kinetics of conversion of air bubbles to air hydrate crystals in Antarctic ice", Science vol. 267 p. 1802 (1995), doi:10.1126/science.267.5205.1802, astro-ph/9501073

[103] Martin Rongen, Calibration of the IceCube Neutrino Observatory, Ph.D. thesis, RWTH Aachen U. (2019), doi:10.18154/RWTH-2019-09941, 1911.02016

[104] M. G. Aartsen et al. (IceCube), "The IceCube Neutrino Observatory Part VI: Ice Properties, Reconstruction and Future Developments", in "33rd International Cosmic Ray Conference", (2013), 1309.7010

[105] J. A. Hinton (H.E.S.S.), "The Status of the H.E.S.S. project", New Astron. Rev. vol. 48 pp. 331–337 (2004), doi:10.1016/j.newar.2003.12.004, astro-ph/0403052

[106] A. U. Abeysekara et al., "Observation of the Crab Nebula with the HAWC Gamma-Ray Observatory", Astrophys. J. vol. 843 (1) p. 39 (2017), doi:10.3847/1538-4357/aa7555, 1701.01778

[107] A. U. Abeysekara et al., "HAWC observations of the acceleration of very-high-energy cosmic rays in the Cygnus Cocoon", Nature Astron. vol. 5 (5) pp. 465–471 (2021), doi:10.1038/s41550-021-01318-y, 2103.06820

[108] A. A. Abdo et al., "Milagro Observations of TeV Emission from Galactic Sources in the Fermi Bright Source List", Astrophys. J. Lett. vol. 700 pp. L127–L131 (2009), doi:10.1088/0004-637X/700/2/L127, [Erratum: Astrophys.J.Lett. 703, L185 (2009), Erratum: Astrophys.J. 703, L185 (2009)], 0904.1018

[109] Ali Kheirandish and Joshua Wood (IceCube, HAWC), "IceCube Search for Galactic Neutrino Sources based on HAWC Observations of the Galactic Plane", PoS vol. ICRC2019 p. 932 (2020), doi:10.22323/1.358.0932, 1908.08546

[110] M. G. Aartsen et al. (IceCube), "Observation and Characterization of a Cosmic Muon Neutrino Flux from the Northern Hemisphere using six years of IceCube data", Astrophys. J. vol. 833 (1) p. 3 (2016), doi:10.3847/0004-637X/833/1/3, 1607.08006

[111] D. Heck et al., CORSIKA: A Monte Carlo Code to Simulate Extensive Air Showers., Forschungszentrum Karlsruhe GmbH, Karlsruhe, Germany (1998)

[112] C. Kopper, "CLSim", (November 7, 2021 [Accessed]), URL https://github.com/claudiok/clsim

[113] R. Abbasi et al. (IceCube), "First Neutrino Point-Source Results From the 22-String IceCube Detector", Astrophys. J. Lett. vol. 701 pp. L47–L51 (2009), doi:10.1088/0004-637X/701/1/L47, 0905.2253

[114] R. Abbasi et al. (IceCube), "Time-Integrated Searches for Point-like Sources of Neutrinos with the 40-String IceCube Detector", Astrophys. J. vol. 732 p. 18 (2011), doi:10.1088/0004-637X/732/1/18, 1012.2137

[115] M. G. Aartsen et al. (IceCube), "Search for Time-independent Neutrino Emission from Astrophysical Sources with 3 yr of IceCube Data", Astrophys. J. vol. 779 p. 132 (2013), doi:10.1088/0004-637X/779/2/132, 1307.6669

[116] Kai Schatto, Stacked searches for high-energy neutrinos from blazars with IceCube, Ph.D. thesis, Johannes Gutenberg University Mainz (2014), (http://doi.org/10.25358/openscience-2897)

[117] M. G. Aartsen et al. (IceCube), "Searches for Extended and Point-like Neutrino Sources with Four Years of IceCube Data", Astrophys. J. vol. 796 (2) p. 109 (2014), doi:10.1088/0004-637X/796/2/109, 1406.6757

[118] M. G. Aartsen et al. (IceCube), "All-sky Search for Time-integrated Neutrino Emission from Astrophysical Sources with 7 yr of IceCube Data", Astrophys. J. vol. 835 (2) p. 151 (2017), doi:10.3847/1538-4357/835/2/151, 1609.04981

[119] T. P. Li and Y. Q. Ma, "Analysis methods for results in gamma-ray astronomy", Astrophys. J. vol. 272 pp. 317–324 (1983), doi:10.1086/161295

[120] A. U. Abeysekara et al., "The 2HWC HAWC Observatory Gamma Ray Catalog", Astrophys. J. vol. 843 (1) p. 40 (2017), doi:10.3847/1538-4357/aa7556, 1702.02992

[121] M. G. Aartsen et al. (IceCube), "Measurement of South Pole ice transparency with the IceCube LED calibration system", Nucl. Instrum. Meth. A vol. 711 pp. 73–89 (2013), doi:10.1016/j.nima.2013.01.054, 1301.5361

[122] R. Abbasi et al. (IceCube), "Calibration and Characterization of the IceCube Photomultiplier Tube", Nucl. Instrum. Meth. A vol. 618 pp. 139–152 (2010), doi:10.1016/j.nima.2010.03.102, 1002.2442

[123] Edgar Bugaev, Teresa Montaruli, Yuri Shlepin, and Igor A. Sokalski, "Propagation of tau neutrinos and tau leptons through the earth and their detection in underwater / ice neutrino telescopes", Astropart. Phys. vol. 21 pp. 491–509 (2004), doi:10.1016/j.astropartphys.2004.03.002, hep-ph/0312295

[124] L B Bezrukov and E V Bugaev, "Nucleon shadowing effects in photonuclear interactions", Sov. J. Nucl. Phys.; (United States) vol. 33 (1195) (1981), URL https://www.osti.gov/biblio/5909968

[125] E. V. Bugaev and Yu. V. Shlepin, "Photonuclear interactions of super-high energy muons and tau-leptons", Nucl. Phys. B Proc. Suppl. vol. 122 pp. 341–344 (2003), doi:10.1016/S0920-5632(03)80414-0

[126] E. V. Bugaev and Yu. V. Shlepin, "Photonuclear interaction of high-energy muons and tau leptons", Phys. Rev. D vol. 67 p. 034027 (2003), doi:10.1103/PhysRevD.67.034027, hep-ph/0203096

[127] H. Abramowicz, E. M. Levin, A. Levy, and U. Maor, "A Parametrization of sigma-T (gamma* p) above the resonance region Q**2 >= 0", Phys. Lett. B vol. 269 pp. 465–476 (1991), doi:10.1016/0370-2693(91)90202-2

[128] H. Abramowicz and A. Levy, "The ALLM parameterization of sigma(tot)(gamma* p): An Update", arXiv (1997), hep-ph/9712415

[129] M. G. Aartsen et al. (IceCube), "Searches for Extended and Point-like Neutrino Sources with Four Years of IceCube Data", Astrophys. J. vol. 796 (2) p. 109 (2014), doi:10.1088/0004-637X/796/2/109, 1406.6757

[130] E. Pinat, The IceCube Neutrino Observatory: search for extended sources of neutrinos and preliminary study of a communication protocol for its future upgrade, Ph.D. thesis, Université Libre de Bruxelles (2017), (http://web.iihe.ac.be/publications/Elisa-Pinat.pdf)

[131] A. Albert et al. (ANTARES, IceCube), "ANTARES and IceCube Combined Search for Neutrino Point-like and Extended Sources in the Southern Sky", Astrophys. J. vol. 892 p. 92 (2020), doi:10.3847/1538-4357/ab7afb, 2001.04412

[132] K. M. Gorski et al., "HEALPix - A Framework for high resolution discretization, and fast analysis of data distributed on the sphere", Astrophys. J. vol. 622 pp. 759–771 (2005), doi:10.1086/427976, astro-ph/0409513

[133] M. Ajello et al. (Fermi-LAT), "3FHL: The Third Catalog of Hard Fermi-LAT Sources", Astrophys. J. Suppl. vol. 232 (2) p. 18 (2017), doi:10.3847/1538-4365/aa8221, 1702.00664

[134] W. B. Atwood et al. (Fermi-LAT), "The Large Area Telescope on the Fermi Gamma-ray Space Telescope Mission", Astrophys. J. vol. 697 pp. 1071–1102 (2009), doi:10.1088/0004-637X/697/2/1071, 0902.1089

[135] S. P. Wakely and D. Horan, "TeVCat: An online catalog for Very High Energy Gamma-Ray Astronomy", International Cosmic Ray Conference vol. 3 pp. 1341–1344 (2008)

[136] A.U. Abeysekara et al. (HAWC), "Multiple Galactic Sources with Emission Above 56 TeV Detected by HAWC", Phys. Rev. Lett. vol. 124 (2) p. 021102 (2020), doi:10.1103/PhysRevLett.124.021102, 1909.08609

[137] A. Albert et al., "Evidence of 200 TeV photons from HAWC J1825-134", Astrophys. J. Lett. vol. 907 (2) p. L30 (2021), doi:10.3847/2041-8213/abd77b, 2012.15275

[138] A. Albert et al. (HAWC), "HAWC and Fermi-LAT Detection of Extended Emission from the Unidentified Source 2HWC J2006+341", Astrophys. J. Lett. vol. 903 (1) p. L14 (2020), doi:10.3847/2041-8213/abbfae, 2010.06670

[139] G. Di Sciascio (LHAASO), "The LHAASO experiment: from Gamma-Ray Astronomy to Cosmic Rays", Nucl. Part. Phys. Proc. vol. 279-281 pp. 166–173 (2016), doi:10.1016/j.nuclphysbps.2016.10.024, 1602.07600

[140] Zhen Cao et al., "Ultrahigh-energy photons up to 1.4 petaelectronvolts from 12 γ-ray Galactic sources", Nature vol. 594 (2021), doi:10.1038/s41586-021-03498-z

[141] F. Aharonian et al. (LHAASO), "Extended Very-High-Energy Gamma-Ray Emission Surrounding PSR J0622+3749 Observed by LHAASO-KM2A", Phys. Rev. Lett. vol. 126 (24) p. 241103 (2021), doi:10.1103/PhysRevLett.126.241103, 2106.09396

[142] M. Amenomori et al. (Tibet ASγ), "Gamma-Ray Observation of the Cygnus Region in the 100-TeV Energy Region", Phys. Rev. Lett. vol. 127 (3) p. 031102 (2021), doi:10.1103/PhysRevLett.127.031102, 2107.01064

[143] Markus Ahlers and Kohta Murase, "Probing the Galactic Origin of the IceCube Excess with Gamma-Rays", Phys. Rev. D vol. 90 (2) p. 023010 (2014), doi:10.1103/PhysRevD.90.023010, 1309.4077

[144] D. Rysewyk et al., "Atmospheric Cherenkov Telescopes as a Potential Veto Array for Neutrino Astronomy", Astropart. Phys. vol. 117 p. 102417 (2020), doi:10.1016/j.astropartphys.2019.102417, 1908.10865

[145] M. G. Aartsen et al. (IceCube), "Evidence for High-Energy Extraterrestrial Neutrinos at the IceCube Detector", Science vol. 342 p. 1242856 (2013), doi:10.1126/science.1242856, 1311.5238

[146] M. Kadler et al., "Coincidence of a high-fluence blazar outburst with a PeV-energy neutrino event", Nature Phys. vol. 12 (8) pp. 807–814 (2016), doi:10.1038/nphys3715,10.1038/NPHYS3715, 1602.02012

[147] P. Padovani et al., "Extreme blazars as counterparts of IceCube astrophysical neutrinos", Mon. Not. Roy. Astron. Soc. vol. 457 (4) pp. 3582–3592 (2016), doi:10.1093/mnras/stw228, 1601.06550

[148] F. Lucarelli et al. (AGILE Team), "AGILE detection of gamma-ray sources coincident with cosmic neutrino events", Astrophys. J. vol. 870 (2) p. 136 (2019), doi:10.3847/1538-4357/aaf1c0, 1811.07689

[149] S. Garrappa et al. (Fermi-LAT, ASAS-SN, IceCube), "Investigation of two Fermi-LAT gamma-ray blazars coincident with high-energy neutrinos detected by IceCube", Astrophys. J. vol. 880 p. 103 (2019), doi:10.3847/1538-4357/ab2ada, 1901.10806

[150] M. Ackermann et al. (Fermi-LAT), "The spectrum of isotropic diffuse gamma-ray emission between 100 MeV and 820 GeV", Astrophys. J. vol. 799 p. 86 (2015), doi:10.1088/0004-637X/799/1/86, 1410.3696

[151] M. G. Aartsen et al. (IceCube), "A combined maximum-likelihood analysis of the high-energy astrophysical neutrino flux measured with IceCube", Astrophys. J. vol. 809 (1) p. 98 (2015), doi:10.1088/0004-637X/809/1/98, 1507.03991

[152] M. G. Aartsen et al. (IceCube), "Observation and Characterization of a Cosmic Muon Neutrino Flux from the Northern Hemisphere using six years of IceCube data", Astrophys. J. vol. 833 (1) p. 3 (2016), doi:10.3847/0004-637X/833/1/3, 1607.08006

[153] M. Ackermann et al. (Fermi-LAT), "Resolving the Extragalactic γ-Ray Background above 50 GeV with the Fermi Large Area Telescope", Phys. Rev. Lett. vol. 116 (15) p. 151105 (2016), doi:10.1103/PhysRevLett.116.151105, 1511.00693

[154] Kohta Murase, Markus Ahlers, and Brian C. Lacki, "Testing the Hadronuclear Origin of PeV Neutrinos Observed with IceCube", Phys. Rev. vol. D88 (12) p. 121301 (2013), doi:10.1103/PhysRevD.88.121301, 1306.3417

[155] Kohta Murase, Ranjan Laha, Shin'ichiro Ando, and Markus Ahlers, "Testing the Dark Matter Scenario for PeV Neutrinos Observed in IceCube", Phys. Rev. Lett. vol. 115 (7) p. 071301 (2015), doi:10.1103/PhysRevLett.115.071301, 1503.04663

[156] Kohta Murase, Dafne Guetta, and Markus Ahlers, "Hidden Cosmic-Ray Accelerators as an Origin of TeV-PeV Cosmic Neutrinos", Phys. Rev. Lett. vol. 116 (7) p. 071101 (2016), doi:10.1103/PhysRevLett.116.071101, 1509.00805

[157] Xiao-Chuan Chang and Xiang-Yu Wang, "The diffuse gamma-ray flux associated with sub-PeV/PeV neutrinos from starburst galaxies", Astrophys. J. vol. 793 (2) p. 131 (2014), doi:10.1088/0004-637X/793/2/131, 1406.1099

[158] Irene Tamborra, Shin'ichiro Ando, and Kohta Murase, "Star-forming galaxies as the origin of diffuse high-energy backgrounds: Gamma-ray and neutrino connections, and implications for starburst history", JCAP vol. 1409 p. 043 (2014), doi:10.1088/1475-7516/2014/09/043, 1404.1189

[159] Shin'ichiro Ando, Irene Tamborra, and Fabio Zandanel, "Tomographic Constraints on High-Energy Neutrinos of Hadronuclear Origin", Phys. Rev. Lett. vol. 115 (22) p. 221101 (2015), doi:10.1103/PhysRevLett.115.221101, 1509.02444

[160] Xiao-Chuan Chang, Ruo-Yu Liu, and Xiang-Yu Wang, "Star-forming galaxies as the origin of the IceCube PeV neutrinos", Astrophys. J. vol. 805 (2) p. 95 (2015), doi:10.1088/0004-637X/805/2/95, 1412.8361

[161] Joachim Kopp, Jia Liu, and Xiao-Ping Wang, "Boosted Dark Matter in IceCube and at the Galactic Center", JHEP vol. 04 p. 105 (2015), doi:10.1007/JHEP04(2015)105, 1503.02669

[162] Xiang-Yu Wang and Ruo-Yu Liu, "Tidal disruption jets of supermassive black holes as hidden sources of cosmic rays: explaining the IceCube TeV-PeV neutrinos", Phys. Rev. vol. D93 (8) p. 083005 (2016), doi:10.1103/PhysRevD.93.083005, 1512.08596

[163] Dan Hooper, "A Case for Radio Galaxies as the Sources of IceCube's Astrophysical Neutrino Flux", JCAP vol. 1609 (09) p. 002 (2016), doi:10.1088/1475-7516/2016/09/002, 1605.06504

[164] P. S. Bhupal Dev et al., "Heavy right-handed neutrino dark matter and PeV neutrinos at IceCube", JCAP vol. 1608 (08) p. 034 (2016), doi:10.1088/1475-7516/2016/08/034, 1606.04517

[165] Keith Bechtol et al., "Evidence against star-forming galaxies as the dominant source of IceCube neutrinos", Astrophys. J. vol. 836 (1) p. 47 (2017), doi:10.3847/1538-4357/836/1/47, 1511.00688

[166] Tim Linden, "Star-Forming Galaxies Significantly Contribute to the Isotropic Gamma-Ray Background", Phys. Rev. vol. D96 (8) p. 083001 (2017), doi:10.1103/PhysRevD.96.083001, 1612.03175

[167] Atri Bhattacharya, Raj Gandhi, Aritra Gupta, and Satyanarayan Mukhopadhyay, "Boosted Dark Matter and its implications for the features in IceCube HESE data", JCAP vol. 1705 (05) p. 002 (2017), doi:10.1088/1475-7516/2017/05/002, 1612.02834

[168] Peter B. Denton, Danny Marfatia, and Thomas J. Weiler, "The Galactic Contribution to IceCube's Astrophysical Neutrino Flux", JCAP vol. 1708 (08) p. 033 (2017), doi:10.1088/1475-7516/2017/08/033, 1703.09721

[169] Andrea Palladino and Walter Winter, "A multi-component model for observed astrophysical neutrinos", Astron. Astrophys. vol. 615 p. A168 (2018), doi:10.3204/PUBDB-2018-01376, 10.1051/0004-6361/201832731, 1801.07277

[170] Yicong Sui and P. S. Bhupal Dev, "A Combined Astrophysical and Dark Matter Interpretation of the IceCube HESE and Throughgoing Muon Events", JCAP vol. 1807 (07) p. 020 (2018), doi:10.1088/1475-7516/2018/07/020, 1804.04919

[171] Atri Bhattacharya, Mary Hall Reno, and Ina Sarcevic, "Reconciling neutrino flux from heavy dark matter decay and recent events at IceCube", JHEP vol. 06 p. 110 (2014), doi:10.1007/JHEP06(2014)110, 1403.1862

[172] Atri Bhattacharya, Arman Esmaili, Sergio Palomares-Ruiz, and Ina Sarcevic, "Probing decaying heavy dark matter with the 4-year IceCube HESE data", JCAP vol. 1707 (07) p. 027 (2017), doi:10.1088/1475-7516/2017/07/027, 1706.05746

[173] M. Chianese, G. Miele, and S. Morisi, "Dark Matter interpretation of low energy IceCube MESE excess", JCAP vol. 1701 (01) p. 007 (2017), doi:10.1088/1475-7516/2017/01/007, 1610.04612

[174] Marco Chianese, Gennaro Miele, and Stefano Morisi, "Interpreting IceCube 6-year HESE data as an evidence for hundred TeV decaying Dark Matter", Phys. Lett. vol. B773 pp. 591–595 (2017), doi:10.1016/j.physletb.2017.09.016, 1707.05241

[175] Luis A. Anchordoqui, Haim Goldberg, Francis Halzen, and Thomas J. Weiler, "Neutrinos as a diagnostic of high energy astrophysical processes", Phys. Lett. vol. B621 pp. 18–21 (2005), doi:10.1016/j.physletb.2005.06.056, hep-ph/0410003

[176] S. Hummer, M. Maltoni, W. Winter, and C. Yaguna, "Energy dependent neutrino flavor ratios from cosmic accelerators on the Hillas plot", Astropart. Phys. vol. 34 pp. 205–224 (2010), doi:10.1016/j.astropartphys.2010.07.003, 1007.0006

[177] Atri Bhattacharya, Raj Gandhi, Werner Rodejohann, and Atsushi Watanabe, "The Glashow resonance at IceCube: signatures, event rates and pp vs. $p\gamma$ interactions", JCAP vol. 1110 p. 017 (2011), doi:10.1088/1475-7516/2011/10/017, 1108.3163

[178] Zhi-zhong Xing and Shun Zhou, "The Glashow resonance as a discriminator of UHE cosmic neutrinos originating from p-gamma and p-p collisions", Phys. Rev. vol. D84 p. 033006 (2011), doi:10.1103/PhysRevD.84.033006, 1105.4114

[179] V. Barger et al., "Glashow resonance as a window into cosmic neutrino sources", Phys. Rev. vol. D90 p. 121301 (2014), doi:10.1103/PhysRevD.90.121301, 1407.3255

[180] Ian M. Shoemaker and Kohta Murase, "Probing BSM Neutrino Physics with Flavor and Spectral Distortions: Prospects for Future High-Energy Neutrino Telescopes", Phys. Rev. vol. D93 (8) p. 085004 (2016), doi:10.1103/PhysRevD.93.085004, 1512.07228

[181] Daniel Biehl et al., "Astrophysical Neutrino Production Diagnostics with the Glashow Resonance", JCAP vol. 1701 p. 033 (2017), doi:10.1088/1475-7516/2017/01/033, 1611.07983

[182] Hiroshi Nunokawa, Boris Panes, and Renata Zukanovich Funchal, "How Unequal Fluxes of High Energy Astrophysical Neutrinos and Antineutrinos can Fake New Physics", JCAP vol. 1610 (10) p. 036 (2016), doi:10.1088/1475-7516/2016/10/036, 1604.08595

[183] M. G. Aartsen et al. (IceCube), "Measurements using the inelasticity distribution of multi-TeV neutrino interactions in IceCube", Phys. Rev. vol. D99 (3) p. 032004 (2019), doi:10.1103/PhysRevD.99.032004, 1808.07629

[184] IceCube Collaboration et al., "First year performance of the IceCube neutrino telescope", Astroparticle Physics vol. 26 pp. 155–173 (2006), doi:10.1016/j.astropartphys.2006.06.007, astro-ph/0604450

[185] M. Ageron et al. (ANTARES), "ANTARES: the first undersea neutrino telescope", Nucl. Instrum. Meth. vol. A656 pp. 11–38 (2011), doi:10.1016/j.nima.2011.06.103, 1104.1607

[186] I. A. Belolaptikov et al. (BAIKAL), "The Baikal underwater neutrino telescope: Design, performance and first results", Astropart. Phys. vol. 7 pp. 263–282 (1997), doi:10.1016/S0927-6505(97)00022-4

[187] A. D. Avrorin et al. (Baikal-GVD), "Baikal-GVD: status and prospects", EPJ Web Conf. vol. 191 p. 01006 (2018), doi:10.1051/epjconf/201819101006, 1808.10353

[188] S. Adrian-Martinez et al. (KM3Net), "Letter of intent for KM3NeT 2.0", J. Phys. vol. G43 (8) p. 084001 (2016), doi:10.1088/0954-3899/43/8/084001, 1601.07459

[189] Stefan Schonert, Thomas K. Gaisser, Elisa Resconi, and Olaf Schulz, "Vetoing atmospheric neutrinos in a high energy neutrino telescope", Phys. Rev. vol. D79 p. 043009 (2009), doi:10.1103/PhysRevD.79.043009, 0812.4308

[190] Thomas K. Gaisser, Kyle Jero, Albrecht Karle, and Jakob van Santen, "Generalized self-veto probability for atmospheric neutrinos", Phys. Rev. vol. D90 (2) p. 023009 (2014), doi:10.1103/PhysRevD.90.023009, 1405.0525

[191] Carlos A. Argüelles et al., "Unified atmospheric neutrino passing fractions for large-scale neutrino telescopes", JCAP vol. 1807 (07) p. 047 (2018), doi:10.1088/1475-7516/2018/07/047, 1805.11003

[192] Delia Tosi and Hershal Pandya (IceCube), "Performance of IceTop as a veto for IceCube", PoS vol. ICRC2017 p. 967 (2018), doi:10.22323/1.301.0967

[193] J. Audehm et al. (HAWC), "HAWC's Eye - Implementing hybrid detection at the HAWC Gamma-Ray Observatory", PoS vol. ICRC2019 p. 636 (2019)

[194] T. Bretz et al., "A compact and light-weight refractive telescope for the observation of extensive air showers", JINST vol. 13 (07) p. P07024 (2018), doi:10.1088/1748-0221/13/07/P07024, 1804.01781

[195] M. G. Aartsen et al., "Design and Performance of a first IceACT Demonstrator at the South Pole", (2019), Submitted to JINST., 1611.03874

[196] H. Anderhub et al., "Design and operation of FACT - the first G-APD Cherenkov telescope", Journal of Instrumentation vol. 8 P06008 (2013), doi:10.1088/1748-0221/8/06/P06008, 1304.1710

[197] A. Biland et al., "Calibration and performance of the photon sensor response of FACT – The First G-APD Cherenkov telescope", JINST vol. 9 (10) p. P10012 (2014), doi:10.1088/1748-0221/9/10/P10012, 1403.5747

[198] Jan Paul Koschinsky, Development of a 61-Pixel Camera for the IceAct Imaging Air Cherenkov Telescope, Master's thesis, RWTH Aachen U. (2017), URL http://www.institut3b.physik.rwth-aachen.de/global/show_document.asp?id=aaaaaaaaaaxbjez

[199] Maurice Günder, Simulation of the Optics of the Imaging Air-Cherenkov Telescopes IceAct with Geant4, Master's thesis, RWTH Aachen U. (2019), URL http://www.institut3b.physik.rwth-aachen.de/global/show_document.asp?id=aaaaaaaaacridos

[200] Geoff Sims et al., "Airglow and Aurorae at Dome A, Antarctica", Publications of the Astronomical Society of the Pacific vol. 124 (916) p. 637 (2012), URL http://stacks.iop.org/1538-3873/124/i=916/a=637

[201] Max Ludwig Knoetig et al. (FACT), "FACT - Long-term stability and observations during strong Moon light", in "Proceedings, 33rd International Cosmic Ray Conference (ICRC2013): Rio de Janeiro, Brazil, July 2-9, 2013", p. 0695 (2013), 1307.6116

[202] N. N. Kalmykov, S. S. Ostapchenko, and A. I. Pavlov, "Quark-Gluon String Model and EAS Simulation Problems at Ultra-High Energies", Nucl. Phys. Proc. Suppl. vol. 52 pp. 17–28 (1997), doi:10.1016/S0920-5632(96)00846-8

[203] T. T. Böhlen et al., "The FLUKA Code: Developments and Challenges for High Energy and Medical Applications", Nuclear Data Sheets vol. 120 pp. 211–214 (2014), doi:10.1016/j.nds.2014.07.049

[204] A. Ferrari, P. R. Sala, A. Fassò, and J. Ranft, FLUKA: A Multi-Particle Transport Code (Program Version 2005), CERN, Geneva (2005)

[205] K. Bernlöhr, "Simulation of imaging atmospheric Cherenkov telescopes with CORSIKA and sim_ telarray", Astroparticle Physics vol. 30 pp. 149–158 (2008), doi:10.1016/j.astropartphys.2008.07.009, 0808.2253

[206] Dempsey, J. T. and Storey, J. W. V. and Phillips, A., "Auroral Contribution to Sky Brightness for Optical Astronomy on the Antarctic Plateau", Publications of the Astronomical Society of Australia vol. 22 (2) pp. 91–104 (2005), doi:{10.1071/AS04036}

[207] R. L. Gattinger and A. V. Jones, "Quantitative spectroscopy of the aurora. II - The spectrum of medium intensity aurora between 4500 and 8900 A", Canadian Journal of Physics vol. 52 pp. 2343–2356 (1974), doi:10.1139/p74-305

[208] A. V. Jones and R. L. Gattinger, "Quantitative spectroscopy of the aurora. III - The spectrum of medium intensity aurora between 3100 A and 4700 A", Canadian Journal of Physics vol. 53 pp. 1806–1813 (1975), doi:10.1139/p75-231

[209] Markus Ahlers and Francis Halzen, "Pinpointing Extragalactic Neutrino Sources in Light of Recent IceCube Observations", Phys. Rev. vol. D90 (4) p. 043005 (2014), doi:10.1103/PhysRevD.90.043005, 1406.2160